



# Structural studies on the Plasmodium falciparum myosins : search for inhibitors to stop parasite invasion

Dihia Moussaoui

## ► To cite this version:

Dihia Moussaoui. Structural studies on the Plasmodium falciparum myosins : search for inhibitors to stop parasite invasion. Cellular Biology. Sorbonne Université, 2020. English. NNT : 2020SORUS112 . tel-03902486

**HAL Id: tel-03902486**

**<https://theses.hal.science/tel-03902486>**

Submitted on 16 Dec 2022

**HAL** is a multi-disciplinary open access archive for the deposit and dissemination of scientific research documents, whether they are published or not. The documents may come from teaching and research institutions in France or abroad, or from public or private research centers.

L'archive ouverte pluridisciplinaire **HAL**, est destinée au dépôt et à la diffusion de documents scientifiques de niveau recherche, publiés ou non, émanant des établissements d'enseignement et de recherche français ou étrangers, des laboratoires publics ou privés.

# Sorbonne Université

ED 515 : Complexité du Vivant  
*Institut Curie, Équipe « Motilité Structurale »*

## Structural studies on the *Plasmodium falciparum* myosins: search for inhibitors to stop parasite invasion

*Thesis submitted by Dihia Moussaoui  
In candidacy for the degree of Philosophiae Doctor, PhD.*

*Supervised by Anne Houdusse and Julien Robert-Paganin*

Defended on the 14th of December 2020

Jury members:

**Dr. Isabelle CALLEBAUT**, DR2, IMPMC

Chair

**Dr. Chris TOSELAND**, Senior Lecturer, University of Sheffield

Reviewer

**Dr. Sébastien FRIBOURG**, DR2, IECB

Reviewer

**Dr. Geneviève MILON**, Emeritus Researcher, Institut Pasteur

Examiner

**Dr. Robert MOON**, Associate Professor, LSHTM

Examiner

**Dr. Anne HOUDUSSE**, DR1, Institut Curie

Supervisor

**Dr. Julien ROBERT-PAGANIN**, CR, Institut Curie

Co-supervisor



Except where otherwise noted, this work is licensed under  
<http://creativecommons.org/licenses/by-nc-nd/3.0/>



## **Remerciements**

*Je tiens tout d'abord à adresser mes vifs remerciements et ma reconnaissance profonde à **Anne Houdusse** de m'avoir offert l'opportunité de travailler dans son laboratoire « Motilité Structurale, UMR 144 » où j'ai acquis tant de connaissances en science que de maturité. Merci pour ton soutien, ton encadrement, ta patience, tes conseils et ton encouragement pour mener à bien ce travail de thèse. Tu m'as fait énormément évoluer et inculqué l'esprit critique en science. Je suis ravie de t'avoir rencontré dans le cadre personnel et professionnel, j'ai toujours été impressionnée par la manière dont tu gère plusieurs projets, tous les membres de ton équipe ainsi que toute l'administration. Je suis admirative !*

*J'adresse ensuite mes vifs remerciements à mon co-encadrant **Julien Robert-Paganin** qui m'a supporté tout le long de ma thèse et qui m'a apporté un précieux soutien scientifique et personnel. Ça a été un réel plaisir de travailler avec toi, même si ce n'était pas toujours facile, mais c'est grâce à ton exigence que j'ai réussi beaucoup de tâches. Ton sérieux, ton sens de l'éthique, ta passion pour la science sont des éléments qui font de toi un scientifique inspirant. Merci pour tout le temps que tu as consacré pour répondre à mes questions et pour encadrer ma thèse.*

*Je remercie beaucoup **Daniel Auguin** pour son travail impressionnant et tous les beaux résultats qu'il a obtenus dans le cadre de notre collaboration, je te remercie pour ta disponibilité et ton efficacité, merci pour tes bonnes ondes et ton encouragement !*

*Un grand merci aux différents membres de l'équipe d'**Anne Houdusse**, aux gens qui sont partis poursuivre leur aventure professionnelle ailleurs, je remercie particulièrement **Yannick Sourigues** qui était un soldat de l'ombre pour notre équipe, ta générosité et ton sens du partage nous a touché, merci ! tu m'as toujours donné de bons conseils scientifiques. Je remercie **Vicente Planelles-Herrero** qui m'as encadré durant mon stage M2 et qui m'a appris les premiers clonages, premières purifs...etc merci pour ta bonne humeur et tous les bons moments partagés ! Je remercie **Guillaume Jousset** pour sa contribution à mes projets scientifiques, merci pour ta bonne ambiance et ton sens de l'humour et surtout pour ton amitié. Je remercie également **Hussein Hammiche** pour sa bonne ambiance et pour les conseils qu'il m'a donné pour réussir mon projet de thèse.*

*Je remercie **Carlos Kikuti** pour sa gentillesse, d'avoir répondu à toutes mes questions techniques, de m'avoir aidé dans l'analyse des résultats MALS. Merci pour ta bonne humeur ! Je remercie également **Elena Sirkia** pour son aide et sa contribution dans mes projets scientifiques et pour sa patience d'avoir répondu à toutes mes questions de biochimie. Je remercie toute mon équipe de **Motilité structurale** qui ont contribué à des degrés divers, à la réalisation de ce travail.*

*Je remercie le **Dr. Geneviève Milon** et le **Dr. Rob Moon** d'avoir accepté d'examiner mon travail de thèse. Je remercie le **Dr. Sébastien Fribourg** et le **Dr. Chris Toseland** d'avoir accepté de reporter mon travail de thèse. Je remercie également le **Dr. Isabelle Callebaut** d'avoir accepté de présider les membres de jury de thèse. Je vous remercie particulièrement car vous étiez présente à tous mes comités de thèses et m'avez apporté de bons conseils et motivée pour continuer. Merci c'est un honneur pour moi de vous avoir tous à ma soutenance*

*de thèse. Par la même occasion je tiens à remercier chaleureusement mes deux autres membres du comité de thèse le **Dr. Pierre Legrand** mon tuteur de thèse qui m'a initié au traitement des données cristallographiques et m'a encouragé durant ma thèse et le **Dr. Isabelle Tardieux** qui m'a apporté des conseils précieux ainsi que de la motivation.*

*J'adresse mes plus vifs remerciements à mes chers parents mais les mots ne suffisent pas pour les remercier ! ainsi que tous les autres membres de ma famille et mes amis qui m'ont toujours encouragé à aller de l'avant.*

## ***Abstract***

Malaria is the deadliest parasitic disease (0.5 million deaths per year) and results from infection by Apicomplexan parasites from the genus *Plasmodium*. PfMyoA, an atypical class XIV myosin from *Plasmodium falciparum*, is essential both for parasite motility and infectivity. In this work, we combined X-ray crystallography, transient kinetics, molecular dynamics and parasitology to decipher the specificities of this motor. PfMyoA comprises an atypical N-terminal extension that acts as a switch allowing the motor to move at high speed when the extension is phosphorylated (during motile stages) or to produce more force when dephosphorylated (during invasion). The full-length structures of PfMyoA reveal that the specific light chains are involved in the stabilization of a more primed pre-power stroke through unforeseen motor domain/lever arm interactions. Interestingly, the atypical essential light chain of PfMyoA (PfELC) is also essential for the infectivity of the parasite. Altogether, these results define PfMyoA as a first order target to design a new generation of antimalarial compounds able to block motor function or light chains targeting to the lever arm.

**Keywords:** *P. falciparum*; PfELC; antimalarial drugs; erythrocytes invasion; infectious disease; malaria; microbiology; gliding motility; molecular biophysics; myosin A; structural biology.

## **Résumé**

La malaria est la maladie parasitaire la plus mortelle (0,5 million de morts par an), elle résulte de l'infection par un parasite Apicomplexe du genre *Plasmodium*. PfMyoA, une myosine de la classe XIV de *Plasmodium falciparum*, est essentielle à la fois pour la motilité et pour l'infectivité du parasite. Dans ce travail, nous avons combiné des expériences de cristallographie aux rayons X, de la cinétique transitoire, de la dynamique moléculaire et enfin de la parasitologie afin de décrypter les spécificités de ce moteur. PfMyoA comprend une extension N-terminale atypique qui agit comme un interrupteur permettant au moteur de se déplacer à haute vélocité lorsque l'extension est phosphorylée (pendant les stades mobiles) ou de produire plus de force lorsqu'elle est déphosphorylée (pendant l'invasion). Les structures de PfMyoA entière révèlent que ses chaînes légères spécifiques sont impliquées dans la stabilisation d'un état pre-powerstroke avec un bras de levier plus relevé que chez les autres myosines grâce à des interactions spécifiques entre le bras de levier et le domaine moteur. Étonnamment, la chaîne légère essentielle (PfELC) atypique joue aussi un rôle important pour l'infectivité du parasite. Ensemble, ces résultats définissent PfMyoA comme une cible thérapeutique de premier ordre pour concevoir une nouvelle génération de composés antipaludiques capables de bloquer la fonction du moteur ou l'association des chaînes légères au bras de levier.

**Mot clés :** *P. falciparum*; PfELC; anti-paludiques; invasion des érythrocytes; maladie infectieuse; malaria; microbiologie; motilité par glissement; biophysique moléculaire; myosine A; biologie structurale.

## Abbreviations

<b>ADP</b>	<i>adenosine diphosphate</i>
<b>ATP</b>	<i>adenosine triphosphate</i>
<b>ELC</b>	<i>essential light chain</i>
<b>F-actin</b>	<i>filamentous-actin</i>
<b>FL</b>	<i>full-length protein</i>
<b>g</b>	<i>grams or gravity</i>
<b>G-actin</b>	<i>globular (monomeric) actin</i>
<b>HPLC</b>	<i>high performance liquid chromatography</i>
<b>IPTG</b>	<i>isopropyl-<math>\beta</math>-D-thiogalactopyranoside</i>
<b>IQ</b>	<i>light chain binding motif</i>
<b>Kb</b>	<i>kilobases</i>
<b>kd</b>	<i>dissociation constant</i>
<b>kDa</b>	<i>kilo-Daltons</i>
<b>k rpm</b>	<i>thousands of rotations per minute</i>
<b>MALS</b>	<i>« Multiangle Light Scattering »</i>
<b>MD</b>	<i>« Motor Domain »</i>
<b>M</b>	<i>molar</i>
<b>MST</b>	<i>« Microscale Thermophoresis »</i>
<b>N</b>	<i>number of filaments</i>
<b>nm</b>	<i>nanometres</i>
<b>OD</b>	<i>optical density</i>
<b>PBS</b>	<i>phosphate buffered saline</i>
<b>PH</b>	<i>pleckstrin homology domain</i>
<b>Pi</b>	<i>inorganic phosphate</i>
<b>RLC</b>	<i>regulatory light chains</i>
<b>SAXS</b>	<i>« Small-angle X-ray Scattering »</i>
<b>SDS-PAGE</b>	<i>sodium dodecyl sulphate polyacrylamide gel electrophoresis</i>

## CONTENTS

Chapter I: Introduction and general notions on myosins .....	11
1. Introduction.....	12
1.1 The cytoskeleton and its molecular motors .....	12
1.2 Myosins.....	13
1.3 The structural diagram of a myosin .....	15
1.4 The motor cycle of myosins .....	18
1.5 Myosin-related diseases .....	21
1.6 Myosins, excellent therapeutical targets.....	22
1.7 Myosin XIV and Malaria.....	25
2. Problematics.....	29
2.1 Sequence divergence in the connectors of PfMyoA suggests compensatory mechanisms of force production.....	29
2.2 Sequence analysis suggested an atypical recognition of Light chains PfELC1 and MTIP.....	29
2.3 Role of PfMyoA in <i>P. falciparum</i> invasion was not clearly established .....	31
2.4 Development of a new generation of antimalarial drugs targeting myosins .....	31
3. Methodologies.....	32
3.1 Expression and purification of the PfMyoA / ELC / MTIP complex.....	32
3.2 Reconstruction of the motor cycle of PfMyoA.....	34
3.3 The effect of mutants on the functionality of PfMyoA .....	36
3.3.1 Unloaded in vitro motility assays.....	37
3.3.2 Loaded in vitro motility assays.....	37
3.3.3 ADP release assays.....	37
3.4 The dynamics of the lever arm .....	38
3.5 PfMyoA and PfELC are critical in parasite blood stages.....	38
Chapter II: Results .....	40
Articles	
Chapter III: PfMyoA motor domain.....	41
1. The conservation of the adaptations in Apicomplexa Phylum .....	42
2. The Glycine that plays a role of fulcrum is also replaced by a Serine in PfMyoB and TgMyoA .....	42
3. Sequence alignment of PfMyoA, PfMyoB and TgMyoA.....	44
4. Stabilization of the Converter by the N-term extension .....	46
5. Conservation of the adaptations stabilizing the Rigor conformation .....	49
6. Conservation of the adaptations within the connectors .....	50
Chapter IV: PfMyoA Full Length.....	52
1. The resolved atomic structures of PfMyoA in PR and PPS .....	53
2. The interface that stabilizes the priming of the lever arm.....	53
3. Recognition of light chains (LCs) by IQ motifs.....	55
5. MTIP recruits PfMyoA to the plasma membrane of the complex .....	59

6. Towards the production of a minimal glideosome .....	63
7. Association of GAP45 to the IMC and to MTIP.....	65
8. GAP45 phosphorylations and glideosome assembly .....	66
9. Approaches for the treatment against malaria .....	68
10. Three strategies to develop treatments targeting the acto-myosin complex of <i>P. falciparum</i> .....	71
10.1 Inhibition of PfMyoA activity .....	73
10.1.1 Blebbistatin – a myosin inhibitor .....	74
10.1.2 CK-571 – a myosin inhibitor.....	75
10.1.3 Halogenated pseudilins – myosin inhibitors .....	75
10.1.4 Mavacamten – a myosin inhibitor.....	76
10.1.5 Omecamtive mecarbil (OM) – a myosin activator.....	76
10.1.6 Specificity and efficiency of inhibitors against PfMyoA .....	77
10.2 Inhibiting the association of the light chains .....	77
10.3 Inhibiting the association of PfMyoA to the actin.....	78
<b>Conclusions .....</b>	<b>80</b>
<b>Perspectives .....</b>	<b>81</b>
I. Other <i>P.falciparum</i> myosins .....	81
II. PfMyoA effectors .....	81
<b>References .....</b>	<b>83</b>

## Tables and figures

<b>Figure 1-</b> Cytoskeletal motors and function in the cell	13
<b>Figure 2-</b> Phylogenetic tree of myosin motor domains based on sequence	15
<b>Figure 3-</b> The cartoon diagram representing the different elements of a myosin motor domain	16
<b>Figure 4-</b> Structural organization of myosin motor	17
<b>Figure 5-</b> Myosin force production cycle	20
<b>Figure 6-</b> Overview of three allosteric binding pockets in myosin II	24
<b>Figure 7-</b> Cartoon representation of the Glideosome components	27
<b>Figure 8-</b> Degenerated IQ motif	30
<b>Figure 9-</b> PfMyoA purification and characterization by in vitro motility assays	33
<b>Figure 10-</b> Structural states and motor cycle of PfMyoA	35
<b>Figure 11-</b> Crystallographic structures of PfMyoA FL	36
<b>Figure 12-</b> PfMyoA conditional knock down with Dicre system	39
<b>Figure 13-</b> Non-conservation of the fulcrum at the basis of the SH1-helix	43
<b>Figure 14-</b> Interactions that stabilize the rigor state in PfMyoA may be conserved in TgMyoA and PfMyoB	47
<b>Figure 15-</b> PfMyoA force generation	50
<b>Figure 16-</b> Interface that promotes the priming of the PfMyoA lever arm	54
<b>Figure 17-</b> Degeneration of IQ motif	57
<b>Figure 18-</b> Model of the PfMyoB and analysis of why PfELC is not interacting strongly on the 1 <sup>st</sup> IQ motif.	58
<b>Figure 19-</b> Interaction MTIP-lever arm	60
<b>Figure 20-</b> MTIP may anchor PfMyoB	62
<b>Figure 21-</b> Sequence alignment of MTIP from P.falciparum and MLC1 from T.gondii.	62
<b>Figure 22-</b> Glideosome localization in merozoite	64
<b>Figure 23-</b> MTIP Hydrophobic Cluster Analysis (HCA)	65
<b>Figure 24-</b> Sequence alignment of GAP45 in Plasmodium phylum	67
<b>Figure 25-</b> Existing treatments against malaria and different kind of novel approaches that are under development	70
<b>Figure 26-</b> Global strategy to target PfMyoA.	73
<b>Figure 27-</b> The Blebbistatin pocket in PfMyoA	75



**Figure 28-***Strategies to block the parasite infectivity.* \_\_\_\_\_ 79

**Table 1-** *List of recent and historic abbreviation of ELCs, RLCs and CaM*\_\_\_\_\_ 33

**Table 2-***Comparison of critical residues that play important role in force production of PfMyoA, PfMyoB and TgMyoA.* \_\_\_\_\_ 46

**Table 3-***Critical elements of the interface that stabilizes the lever arm priming* \_\_\_\_\_ 54

**Table 4-***The conservation of the residues that maintain the interactions between the ELC and the Heavy chain helix of the lever arm* \_\_\_\_\_ 57

**Table 5-***Current malaria vaccines stages* \_\_\_\_\_ 71

## **Chapter I: Introduction and general notions on myosins**

# 1. Introduction

## 1.1 The cytoskeleton and its molecular motors

The proper functioning of eukaryotic cells depends on the motility properties of nanomachines (molecular motors) which are capable of generating molecular movements. This is thanks to the combination system between molecular motors and polarized tracks ([Robert-Paganin et al., 2020](#)). Molecular motors act on the cytoskeleton to ensure the control and coordination of intracellular traffic, which is essential for carrying out most of the essential biological processes such as cell motility, muscle contraction, chromosomal segregation, intracellular organelle transport as well as endocytosis and exocytosis. These molecular motors interact with the cytoskeleton to generate forces and movements along those tracks, by harnessing the free energy of the ATP to generate mechanical forces. They have both structural functions, anchoring of organelles and organization of the cytoskeleton, as well as cargo transport functions, motility and contractility.

Cargo transport is ensured by three superfamilies of molecular motors: **kinesins** and **dyneins**, which move along microtubules to ensure rapid delivery of vesicles over long distances between the nucleus and the cell periphery ([Langford, 1995](#)). **Myosins**, on the other hand, associate with actin filaments to anchor organelles or transport cargos on short distances. However, this simple model has been recently debated as dispersion of melanosome and long range movements in oocytes seem to be linked to long-range transport by Myosin V towards the cell periphery without the need of microtubule transport ([Alzahofi et al., 2020](#)). However, the complementarity of these two addressing systems (**Figure 1**) ensures the delivery of the various cargo ships to the right place and in a well-defined time. The way in which several molecular motors cooperate to organize cell content remains poorly known today although it is essential for numerous cellular functions, including cell division ([Tab et al., 1998](#); [Gross et al., 2002](#); [Ross et al., 2008](#)).

The polarity is a characteristic of microtubules and actin filaments. The majority of kinesins and all myosins known to date, but one class, move towards the positive-end of these cytoskeleton filaments ([Buss & Kendrick-Jones 2007](#)). Myosin VI is the exception as it moves towards the negative-end of the actin filament ([Wells et al., 1999](#)). Conversely, all dyneins and one class of Kinesin (Kin14) move towards the negative-end of the microtubules.

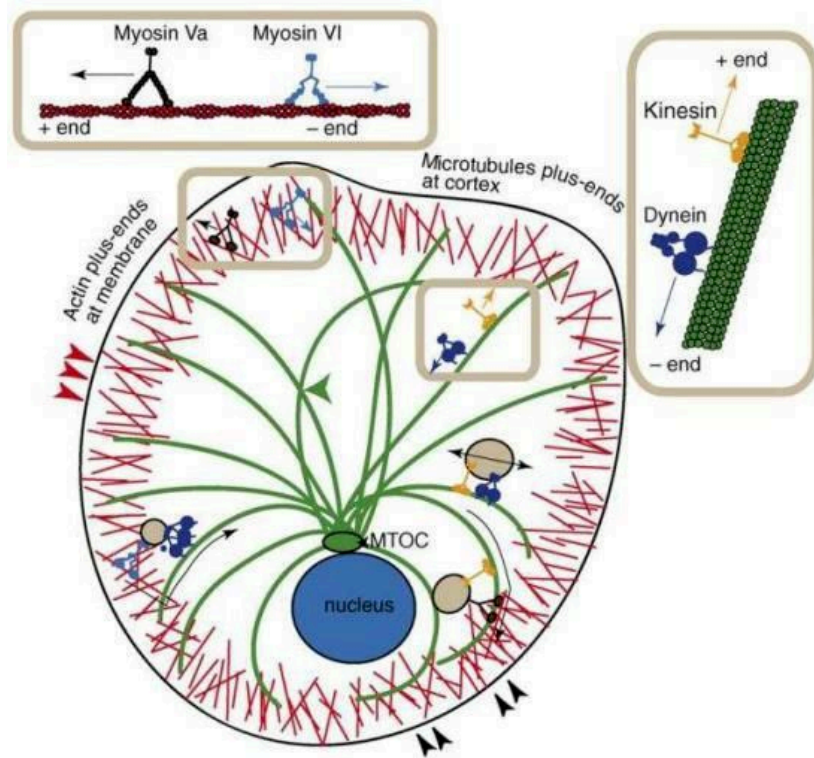


**FIGURE 1- Cytoskeletal motors and function in the cell**

Taken from (Ross et al., 2008). This simplified cartoon present different types of cytoskeletal motors involved in vesicles transport (in gray) and other cargoes into the different cell compartments. In orange kinesins and in dark blue dynein, moving on the microtubules. The myosins move along the actin filaments represented here in red. Myosins are present in particular in the cellular cortex. The myosin Va (in dark) moves towards the positive-end of the actin filament, while the myosin VI (in blue) moves towards the negative-end of the actin filament. The two types of filaments, actin and microtubule, are in contact in the cellular cortex (black arrows), which allows collaboration between the two systems.

## 1.2 Myosins

The myosin superfamily regroups actin-based motor proteins that use the energy derived from ATP hydrolysis to translocate actin filaments and to produce force (Coluccio, 2020). Progress has been made over the years to understand how these molecular motors couple the chemical energy derived from ATP hydrolysis to mechanical work, which allows a relative displacement of the motor along the actin filament. Moreover, myosins are essential for the formation and deformation of plasma membranes and therefore for the maintenance of cell morphology (Anitei & Hoflack, 2011). They are also involved in cytokinesis, phagocytosis, vesicular trafficking, extension of the growth cone, signal transduction as well as in the polymerization of actin (Berg et al., 2001). The human genome contains 39 known myosins divided into 45 different classes to date (Odrionitz & Kollmar., 2007) (Figure 2).

The myosin superfamily contains:

- i) **conventional myosins** (**Figure 2**), the first myosin to be characterized. Skeletal muscle myosin-II was isolated over 150 years ago. It was not until many years later, however, that myosin was recognized as the ATPase responsible for muscle contraction ([Coluccio, 2020](#); [Engelhardt & Ljubimowa 1939](#)), while acto-myosin was separated from one another revealing the existence of an actin system separated from muscular myosin class II. This class of myosins forms filaments (thick filaments) that are able to pool actin microfilaments (thin filaments). When involved in muscle contraction, these myosins are organized into sarcomeres. Other myosins of this class are involved in the formation of the contractile ring during cell division, they are present in all cells and are thus called non-muscle myosins II ([Wilhelm Kuhne. 1864](#); [Gordon et al., 2000](#)).
- ii) **Unconventional myosins** that do not form thick filaments and most often act as isolated molecules or dimers.

Myosins are associated with serious human pathologies. The dysfunction of these motors leads to cardiomyopathies, deafness, or Griscelli's disease which is a rare hereditary disorder characterized by hypopigmentation and can lead to death. The infectivity of parasites such as Apicomplexa relies on class XIV myosins (see section 1.7). It is therefore essential to understand the force generation mechanism of these motors in order to propose new therapeutic approaches when they are involved in diseases.

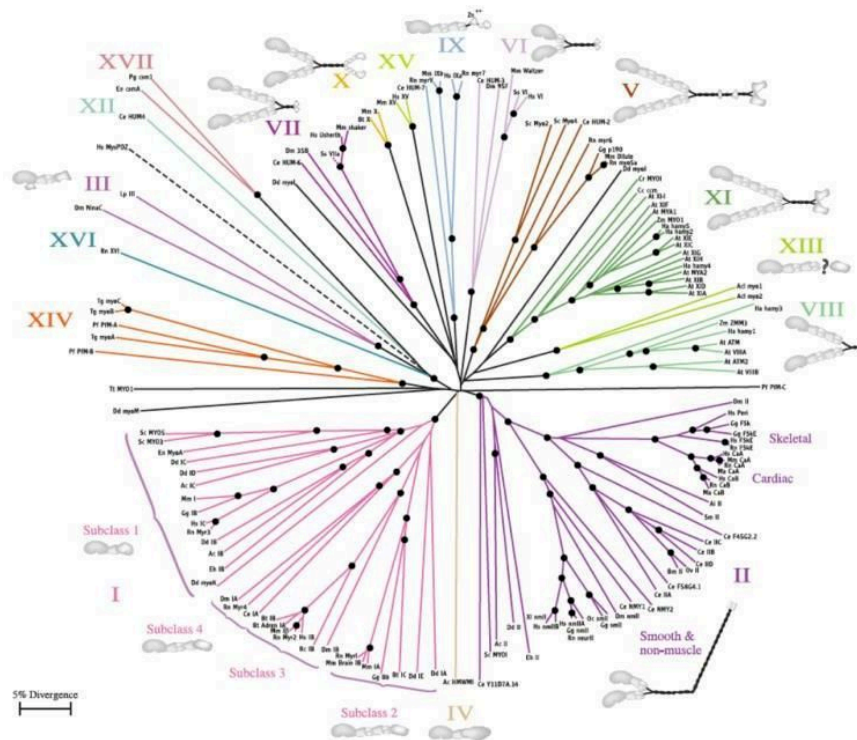


**FIGURE 2-Phylogenetic tree of myosin motor domains based on sequence**

(Hodge and Jamie. Cope 2000) The phylogenetic tree was constructed from the sequences of 1984 different myosin motor domains.

### 1.3 The structural diagram of a myosin

Myosin structure can be generally subdivided in three parts. A globular N-terminal domain called the **motor domain** which hydrolyzes ATP, followed by a **neck region** able to bind the light chains and finally, in C-terminus, **the tail domain** (Sweeney *et al.*, 2020).

#### 1.3.1 The motor domain

The motor domain carries the active site able to hydrolyze the ATP and the actin binding region that is composed of actin-binding loops as well as a helix-turn-helix region. Myosin motor domain consists of four subdomains (**Figure 3**): the **N-terminal** subdomain, the **upper 50-kDa (U50)** and the **lower 50-kDa (L50)** subdomains forming a large outer cleft that opens and closes depending of the nucleotidic state of the motor. The inner cleft near the **Switch-II** connector controls the phosphate release and closes to the active site where ATP is bound. The central beta-sheet called the **Transducer** plays a critical role by adopting specific conformations affecting the opening/closure of the inner cleft, but also affecting the conformation of the active site. In the other hand, the so-called **P-loop** (belonging to the N-terminal subdomain) and **Switch-I** (belonging to the Upper 50-kDa subdomain) control the release of the Mg.ADP from the active site. In the C-terminal region of the motor domain the

**Converter** plays the role of a movement amplifier. Two highly deformable connectors play an important role in motor mechano-chemical transduction: The **Relay** (an extension of the L50 subdomain) and the nearby **SH1-helix** (at the periphery of the N-term subdomain). These connectors transmit the small conformational changes that occur during the powerstroke (force production) to the converter (Reviewed by Robert-Paganin et al., 2020; Sweeney, Houdusse & Robert-Paganin, 2020).

The connectors of the motor domains of myosin are conserved in sequence. Moreover, it is in itself based on this conservation of the sequence of the motor domain that the classification of myosins was carried out (Foth et al., 2006).

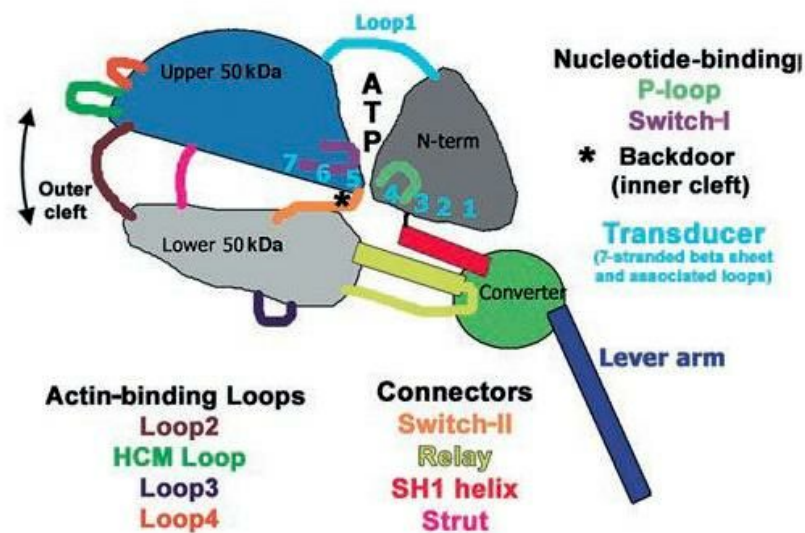


**FIGURE 3-***The cartoon diagram representing the different elements of a myosin motor domain*

(adapted from Sweeney, Houdusse 2010) . Structural elements of the myosin motor domain. The myosin motor domain consists of four subdomains and connectors that link these different subdomains. Subdomains are colored as follows: N-terminal (in dark grey), upper 50-kDa (in blue), lower 50-kDa (in light grey) and converter (in green). The actin-binding site is composed of Loop2,3,4 and the HCM Loop that belong to both the upper and lower 50 subdomains, near the outer cleft. The closure of the outer cleft controls the actin interface and thus actin affinity. Different connectors have been identified in the motor domain (Houdusse et al 1999) that are involved in controlling the lever arm orientation. Among them, switch-II in the active site is close to the inner cleft, next to where the gamma-phosphate of ATP is bound. It has been proposed that switch-II plays the role of doorkeeper whereas it opens a backdoor (★) to release hydrolysis product as phosphate upon actin binding (Llinas et al 2015).



### 1.3.2 The neck region

The neck region is a region that consists of a long helix of the heavy chain able to recognize partners called light chains, its length is variable amongst myosin classes (Provance & Mercer. 1999). The neck and the converter are called the lever arm since this part of the motor plays the role of an amplifier of the conformational changes required to produce force (Sweeney & Houdusse 2010; Robert-Paganin et al., 2020). It is a region composed of a variable number of **IQ motifs** whose consensus sequence is **[IQxxxRGxxxR]** that are able to bind calmodulins (CaM) or proteins homologous to calmodulin (essential or regulatory light chains) to stiffen its structure and regulate its activity (Houdusse and al. 1996; Sweeney & Houdusse 2010; Mukherjea et al., 2014). Extension of the lever arm by single alpha-helix (SAH) or other domain is also present in certain myosins such as Myo6 and Myo10 (Mukherjea et al., 2014; Ropars et al 2016).

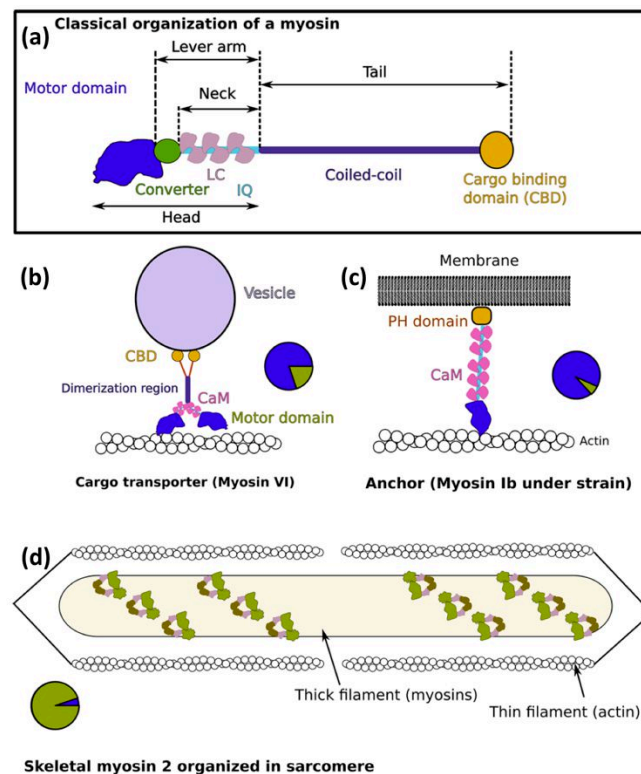


**FIGURE 4- Structural organization of myosin motor**

Taken from (Robert-Paganin et al., review 2019): (a) Schematic representation of a myosin. (b–d) Examples of myosin motors with different time spent on actin (duty ratio): dimeric myosin VI involved in cargo transport, monomeric myosin Ib anchoring membrane to the cytoskeleton, and the sarcomere in panel. Each of these examples represents a distinct duty ratio between weak (green) and strong (blue) binding states for actin of the overall motor cycle.



### 1.3.3 The tail region

The sequence and the topology of this region are very variable among myosin classes. It plays a role of adapter and regulator. This region allows the oligomerization of certain myosins (**Figure 4**), the binding to protein partners, phospholipids. In conventional myosins, the sequence form a long coiled-coil that promote the formation of the thick filament, an assembly of dimeric myosin molecules. Thanks to the interactions established by the tail, each myosin is addressed to the different compartments of the cell.

## 1.4 The motor cycle of myosins

Force production in myosin goes through several stages and states of low to high affinity for the actin filament. The state of hydrolysis of the nucleotide in the active site dictates the affinity for actin, thanks to the conformational changes resulting during force production. These rearrangements are transmitted to the lever arm, whose orientation is therefore nucleotide dependent. The generation of force and movements by myosins is established via sequential structural changes linked to ATP hydrolysis. The study of the myosin force production cycle through X-ray crystallography and electron microscopy have made possible to characterize distinct structural states and to reconstitute the kinematics of the motor cycle ([Sweeney & Houdusse, 2010](#)). However, this task has been quite complicated due to technical limitations. Indeed, actin cannot be crystallized due to its fibrous nature, and acto-myosin complexes *per se* have to be studied by electron microscopy (EM), a technique that has been able to provide medium to high resolution only recently with the cryo-electron microscopy (cryoEM) revolution ([reviewed by Robert-Paganin et al., 2020](#)).

The first structure that was solved at high resolution was that of chicken skeletal myosin, at 2,8 Å resolution ([Rayment et al., 1993](#)). This structure was the key to understand the structural features of myosins. At first, this structure was difficult to place in the motor cycle as it was not bound to nucleotide yet it was not clear that it would fit well into the low resolution electron microscopy (EM) maps of skeletal acto-myosin available at that time ([Rayment et al., 1993b](#)). Later, it was recognized as the state with ATP in which the myosin is dissociated from actin: the so-called **Post-Rigor state** (PR). Even if there was no nucleotide in the crystal, the sulfate was coordinated in the active site, thereby, mimicking the ATP state ([Houdusse et al., 2000](#)). Few years later, the structural study of *Dictyostelium*, smooth muscle myosin and scallop

myosin 2 revealed the **pre-powerstroke (PPS)**, with the lever arm up and complexed to Mg.ADP.Vanadate, an analogue of Mg.ADP.Pi (Smith & Rayment, 1996 ; Dominguez et al., 1998; Houdusse et al., 2000). A **Rigor-like** state, crystallized without actin, was finally identified with Myosin Va (Coureux et al., 2003). This state, with the actin binding cleft closed and the lever arm down, corresponds to the state of highest affinity for F-actin. Technological advances in cryoEM allowed to solve the structure of the acto-myosin complex of *Dictyostelium discoideum* myosin 1E at a resolution of 7.4 Å (Behrmann et al., 2012). But higher resolution cryoEM structures solved more recently were critical to establish that the rigor-like state solved with Myosin Va by crystallography is similar to the state populated when bound to F-actin at the end of the powerstroke (Von der Ecken et al., 2016; Gurel et al., 2017; Mentés et al., 2018). The crystallization of myosin VI in a state releasing the phosphate (Pi), the **Pi release**, demonstrated the existence of other myosin conformations and permitted a precise model for the chronology of events during the powerstroke, including how Pi is released from the active site and when the lever arm swings (Llinas et al., 2015). Finally, another state of high affinity for the actin filament, the **Strong ADP** state with MgADP in the active site was solved by cryoEM at medium resolution for Myosin Va (Wulf et al., 2016) and at higher resolution for Myosin 1b and Myosin VI (Gurel et al., 2017; Mentés et al., 2018).

Thanks to all these structures, the structural states of the myosin motor cycle were visualized. In the **Rigor** state (nucleotide-free state), the myosin binds strongly to the actin filament. ATP binding triggers the conformational changes in the transducer that cause the opening of the internal cleft, which facilitates the fast detachment of myosin from actin (Coureux et al., 2004), the myosin is thus in **PR** state. Myosin then undergoes an isomerization called **Recovery stroke** that leads to the **PPS** state, in which the lever arm is primed and in which ATP hydrolysis into ADP and Pi can occur. The PPS state associates only weakly with the actin filament. Actin binding induces conformational changes in the motor, which cause the release of the phosphate (Pi) from the active site, An intermediate state called **Pi Release** is populated to allow this release. After Pi release, rearrangements occur to populate the **strong ADP state**. They involve the closure of both the outer and inner cleft by the formation of the high affinity actin interface. In so doing, a large swing of the lever arm is produced to generate force. Finally, the release of MgADP induces other conformational changes in the active site which cause the tilt down of the lever arm and a reorientation of the N-term subdomain, the motor is now in the **Rigor state**. From this state, ATP binding can start a new cycle. So, the

motor cycle of myosins follows its course (**Figure 5**) (Sweeney & Houdusse, 2010; Robert-Paganin et al., 2020).

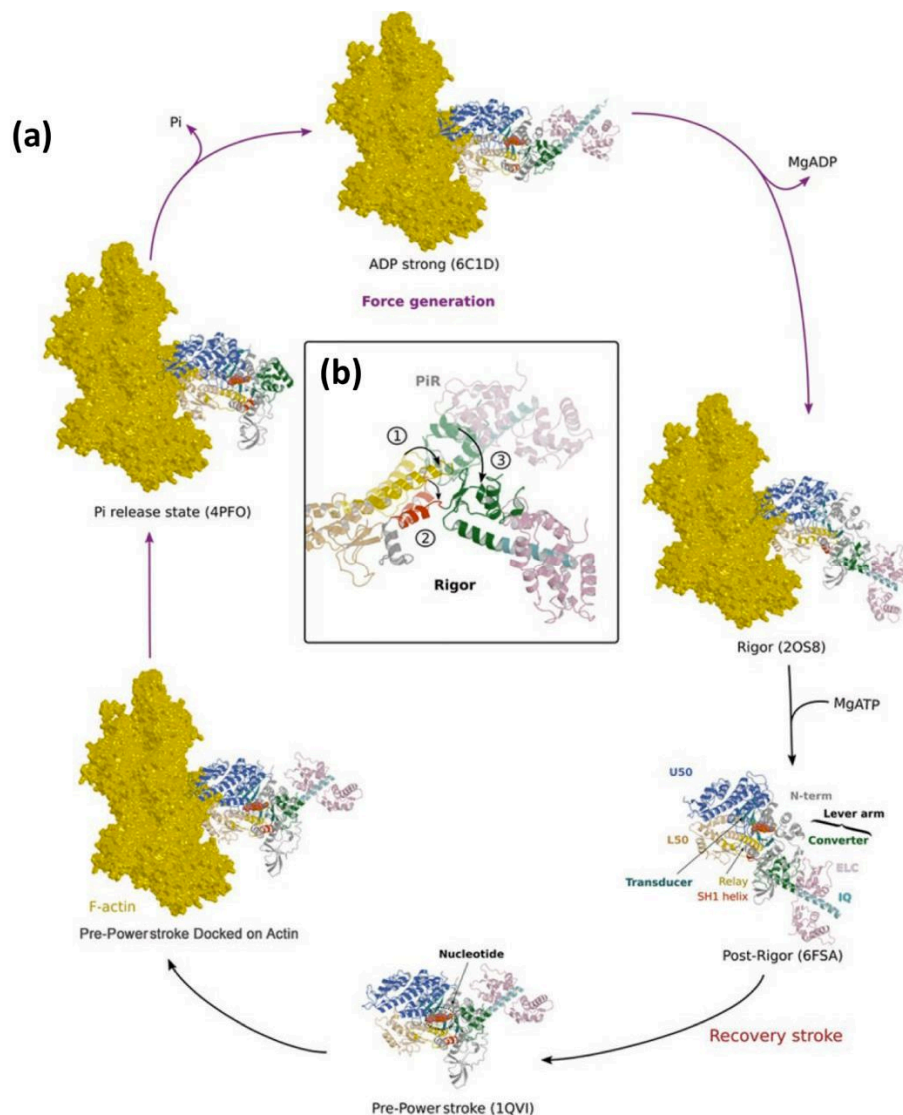


**FIGURE 5-Myosin force production cycle**

Taken from (Sweeney, Houdusse and Robert-Paganin. 2020). The actin-activated ATPase cycle of the myosin superfamily consists of three major nucleotide state dependent; these states differ in their affinity for the actin filament (actin is represented here in yellow spheres). **(a)** In the Rigor state, the myosin is strongly associated with actin filament with the outer cleft closed. The entry of ATP into the active site causes conformational changes to the motor, thus myosin is detached from F-actin, this state is called Post-rigor (PR). ATP hydrolysis along with the lever arm priming occur in the Recovery stroke transition that leads to the pre-powerstroke state (PPS). Reattachment of myosin to actin accelerates the release of the hydrolysis products (Pi first, then ADP) and involves conformational changes in the motor on actin, generating movement (powerstroke). **(b)** During the powerstroke, the unpriming of the Relay-helix and the piston-like movement of the SH1-helix are associated with the swing of the lever arm.

## 1.5 Myosin-related diseases

Myosins are critical for the achievement of different cellular processes. These motors power not only muscle contraction but also participate in cell division and polarization (myosin classes I and II) (Hartman et al., 2011). Other more specific myosin genus are responsible of cytokinesis, cells crawling on surfaces as well as formation of diverse forms of cellular protrusions, aspects of endo- and exocytosis, as well as Golgi function and maintenance of its shape (Titus MA. 2018; Berg et al., 2001). So, it is not surprising that the dysfunction of these molecular motors leads to various human diseases. These pathologies are often associated with mutations in myosin genes that affect the motor function and regulation. A close link between cancers and molecular motors has also been established, as well as with other serious illnesses.

One of the most frequent pathologies linked to myosin II are inherited cardiomyopathies that result from mutations in the  $\beta$ -cardiac myosin (Kaski et al., 2008; Morita et al., 2008). Hypertrophic cardiomyopathies (HCM) for example, can affect 1 individual among 500 (Maron, 2002), and remains so far an important public health problem in the world (WHO statistics 2016). The heart is a pump highly synchronized with nutritional and oxygen requirements of all other organs. So, the loss of this myosin or a mutation on its heavy chain (amino acid change) directly affects the average force involved in heart contractility. The effects of these mutations on the motor cycle of myosin has been studied in our laboratory (Robert-Paganin et al., 2018). The Non muscular myosin II (NM-II) also plays an essential role in the tumor invasion and metastasis (Martson et al. 2020). It was demonstrated that the genetic deletion of both isoforms NM-IIA and NM-IIB decreases tumor proliferation (Picariello et al., 2019). In most of the cases, the lack of information about the molecular consequences of these mutations on myosin functions constitutes a major obstacle in finding new treatments (Robert-Paganin et al., 2018).

Other myosin classes are overexpressed in cancers, such as Myosin VI that is overexpressed in glioblastomas, as well as in prostate and ovarian cancers (Dunn et al., 2006; Knudsen, 2006; Yoshida et al., 2004). Furthermore, its expression is regulated by p53 (Jung et al., 2006) and varies according to the stage of the tumor. Interestingly, cell partners of myosin VI, such as GIPC1 and the autophagy receptors Optineurin and NDP52, are also linked to tumorigenesis. Suppression of myosin VI in cancer cells decreases cell migration *in vitro* and suppression of GIPC1 in mouse reduces tumor development and has no negative effects on the

mouse (Chittenden et al., 2010; Fejzo et al., 2011). Another example is Myosin18a, which has an important role in the organization of the Golgi but is also involved in cell migration, adhesion, cytokinesis and transcription (Hartman & Spudich, 2012). Myosin 18a is also involved in the development of many cancers (Ouderkirk et al., 2014).

Another myosin class that is involved in other diseases is unconventional vertebrate myosin class IX. Myo9a plays a role in epithelial differentiation and morphology whereas Myo9b regulates the migration of macrophages and immune cells (Hanley et al., 2010; Ma et al; 2010). Defect of these motors is associated with neurological diseases (O'Connor et al., 2018) and immune disorders (as Crohn's disease), respectively (Nunez et al., 2007 ; Coluccio, 2020).

## **1.6 Myosins, excellent therapeutical targets**

As a consequence of being sophisticated nanomachines, myosins can be highly specific therapeutical targets. They constitute a safe alternative for the treatment of certain diseases by using small molecules capable of binding myosins and modulating their activity. The development of these small molecules is essential for the development of non-invasive treatments against the diseases in which myosins are involved.

The study of these small molecules in our laboratory constitutes a tool to **i)** deepen the understanding of the myosins force production mechanism, and **ii)** to identify new chemical entities of therapeutic interest. This approach has important advantages in cell biology experiments (such as reversibility) and is complementary to the suppression of genes by silencing RNA (SiRNA). For some human disease, such as cardiomyopathy, it can open new therapeutic potential for diseases for which the only solution is often heart transplant.

We can divide these modulators into two groups: **i)** The competitive modulators that bind to the nucleotide hydrophobic pocket (mostly conserved in myosins and close to ATP binding sites found in other proteins). Such modulators would prevent ATP binding, thus prevent motor activity. **ii)** The non-competitive modulators bind outside the active site and are more specific. These modulators are allosteric molecules that act on myosin activity, using different sites that are important in the mechanochemical coupling between critical remote sites in the motor (Manstein & Preller, 2020). The crystallographic X-ray structures of myosins with modulators (small molecules) have revealed four distinct modulator binding pockets in myosins

(Allingham et al., 2005; Fedorov et al., 2009; Preller et al., 2011; Sirigu et al., 2016; Planelles-Herrero et al., 2017).

The best known and characterized modulator is Blebbistatin that targets specifically class II Myosin (Straight et al., 2003). It binds to the hydrophobic pocket at the interface between the U50 and L50 subdomains (Figure 6). By stabilizing the PPS state of myosin (Allingham et al., 2005), it prevents release of Pi. Blebbistatin inhibits class II myosins with half maximal inhibitory concentration (IC<sub>50</sub>) of 0.50 to 80  $\mu$ M while myosins from classes I, V, and X have IC<sub>50</sub> > 150  $\mu$ M, demonstrating the specificity of this molecule (Limouze et al., 2004).

The other excellent identified small-molecule therapeutic against heart failure is *Omecamtiv Mecarbil* (OM) developed by the biopharma company Cytokinetics inc. and targeting human  $\beta$ -cardiac myosin. This small molecule represents a new generation of modulators. It increases the ejection fraction volume of the heart. Thus, used as a treatment against heart failure without any secondary effect below the maximum tolerated dose (0.5 mg/kg/h) (Malik et al., 2011; Cleland et al., 2011). It targets the motor domain near the SH1 helix and at the interface between the motor domain and the Converter (Planelles-Herrero et al., 2017) (Figure 6). Unlike other modulators already described here, this molecule plays the role of activator for the  $\beta$ -cardiac myosin since it accelerates the rate of Pi release in presence of actin (Malik et al., 2011; Liu et al., 2012; Swenson et al., 2017). The crystallographic structure of this modulator bound to cardiac myosin has been solved in our laboratory. It allowed to decipher the mechanism of action of OM. S1 fragment/OM crystallized in PPS revealing how OM shifts the hydrolysis equilibrium of MgATP towards the products, MgADP + Pi and favors the PPS state. OM thus increases the number of heads available to produce force and increases the force output of the heart (Planelles-Herrero et al., 2017), by increasing the amount of myosin heads in the PPS state. In addition, OM is not compatible with the resting state of cardiac myosin and its binding therefore makes more heads available for force production (Robert-Paganin et al., 2018). OM is currently in clinical phase III (8000 patients) to study its effect on patients with chronic cardiac insufficiency (Malik et al., 2011; Teerlink et al., 2016).

Mavacamten (Mava) is a selective inhibitor of human  $\beta$ -cardiac myosin (Green et al., 2016; Kawas et al., 2017). Mava is able to decrease the contractility of the heart and to suppress hypertrophy and cardiomyocyte disarray in mice (Green et al., 2015). Mava is currently in phase III clinical trials for treating obstructive HCM (Heitner et al., 2019).



These examples highlight the importance of structural studies to understand the mechanism of action of such modulators.

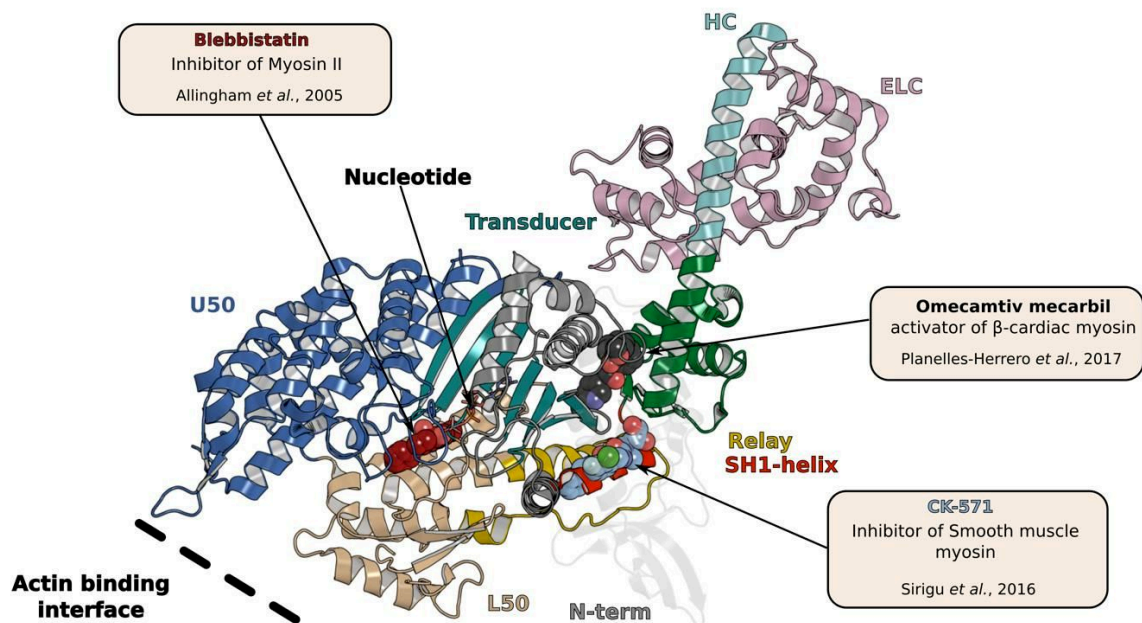


**FIGURE 6-Overview of three allosteric binding pockets in myosin II**

The binding sites were determined by co-crystallization of myosin in complex with Blebbistatin (PDB code 1yv3), CK-571 (PDB code 5t45), and OM (PDB code 5n69). The different structural elements of the motor domain are color coded and labeled in the diagram.

## 1.7 Myosin XIV and Malaria

### 1.7.1 Malaria

Malaria is an infectious disease caused by parasites of the genus *Plasmodium* transmitted to humans by a female mosquito bite of the genus *Anopheles*, previously infected. This disease is characterized by symptoms like fever, vomiting, diarrhea, headache and chills.

Malaria is the cause of death for about over then half a million people per year. Children under the age of five are the most vulnerable group affected by this disease (WHO, 2018). It mainly affects tropical regions and intertropical zones, several regions in Southeast Asia, South America, Oceania but especially in Africa and sub-Saharan Africa. Malaria is gaining more and more ground in the world, spreading over the dry regions of Africa (WHO, 2018). Europe is experiencing so-called imported malaria. In France, in 2011, 3,560 cases of imports were reported (source InVS).

Five species of *Plasmodium* cause malaria in humans: *Plasmodium falciparum*, *Plasmodium vivax*, *Plasmodium ovale*, *Plasmodium malaria* and *Plasmodium knowlesi*. *P.falciparum* is the most pathogenic species and accounts for 90% of human mortality.

Despite the efforts and the money invested in the fight against malaria, the parasite develops resistance to existing treatments currently used, such as chloroquine, sulfadoxine-pyrimethamine (SP) (Dhingra et al., 2019) and more recently to CATs (therapeutics combinations based on artemisinin) (Müller et al., 2019). Not only does the parasite become resistant to anti-malaria treatments, but also the *Anopheles* mosquitoes have developed resistance to insecticides which initially seemed a promising strategy to fight against malaria (WHO, 2018). Faced with this health crisis, a new approach to develop treatments against malaria is essential, hence the interest and motivation of our scientific project which aims to seek a new generation of treatment against malaria.

### 1.7.2 The Parasite's infectivity cycle

The Apicomplexa phylum includes parasites of the group protozoa which cause severe pathologies in both humans and animals. All Apicomplexans, including *Toxoplasma gondii* (responsible for toxoplasmosis, which affects up to one-third of the human population) and



*Plasmodium falciparum* have developed a motility system which facilitates their infectivity and their dissemination (Frénil et al., 2013). They use a mode of displacement unique to protozoa that allows them to invade host cells.

These organisms have complex and diverse life cycles alternating between different stages and different hosts. For example, *Toxoplasma gondii* carries its sexual portion in the intestines of cats (the definitive host) (Dubey et al., 2009) while *Plasmodium falciparum* carries its sexual portion in the intestines of mosquito of the genus *Anopheles*. Zygotes undergo meiosis to become sporozoites that infect human (Pietro Alano, 2007). Despite these differences, these parasites have in common to actively generate the force to invade their target cells, the driving force necessary for their internalization being essential for this invasion (Frénil et al., 2017).

The life cycle of the *Plasmodium spp.* starts with the bite of an infected female *Anopheles*, thus injecting sporozoites into the human dermis. The sporozoites travel to the blood vessels and migrate to the liver, where they migrate along the sinusoidal cells, enter and cross Kupffer cells, and finally traverse and invade hepatocytes. As it enters, the parasite induces the formation of a new intracellular compartment called parasitophorous vacuole (VP), in which it will be able to divide away from the immune system protected from fusion with endosomes and lysosomes of the host cell. The sporozoites multiply in hepatocytes (10-15 days) and form a schizonts (30-40µm) that releases thousands of merozoites into the bloodstream and infect host cells such as erythrocytes. Merozoites multiply in red blood cells by forming schizonts. A new generation of merozoites will be elaborated after the bursting of red blood cells and it is at this stage that the symptoms appear in the patient. The released merozoites will i) either infect new host cells ii) or will develop into gametocytes, which will be transmitted to the next *Anopheles* mosquito when it bites the person infected with malaria (Soullard et al., 2015; reviewed by Frénil et al., 2017).

### 1.7.3 The Glideosome, the war machine

Locomotion of apicomplexan parasites occurs through a process called gliding motility. This mode of displacement and the infectivity of the parasite are based on a macromolecular assembly called the **glideosome**, which is anchored in an internal membrane complex located approximately 25 nm below the plasma membrane of the parasite. The heart of the glideosome is composed of an atypical class XIV myosin A (PfMyoA) and a divergent actin (PfAct1).

PfMyoA is a short myosin with a conserved globular motor domain and a lever arm that associates with two light chains: an essential light chain (PfELC) (Green et al., 2017; Bookwalter et al., 2017) and MTIP (Myosin Tail Interacting Protein) (Münter et al., 2009; Crick et al., 2014). The N-terminal extension of MTIP binds to integral membrane proteins called GAP (proteins associated with glideosomes), which anchor myosin so that it can produce force when it interacts cyclically with actin (Meissner et al., 2002) (Figure 7). This model was proposed by (Bergman et al., 2003) but it is still mostly a schematic view of the assembly of these proteins, for which much remains unknown. PfMyoA is a critical molecule in the parasite's life cycle as it fuels the rapid motility ( $\sim 2 \mu\text{m.s}^{-1}$ ) required during the mobile stages of sporozoites (Andenmatten et al., 2013), and is essential for providing strength (up to 40 pN) necessary for the non-mobile stages of the parasite, such as the merozoite stage that invades erythrocytes (Frenal et al., 2013; Egarter et al., 2014).

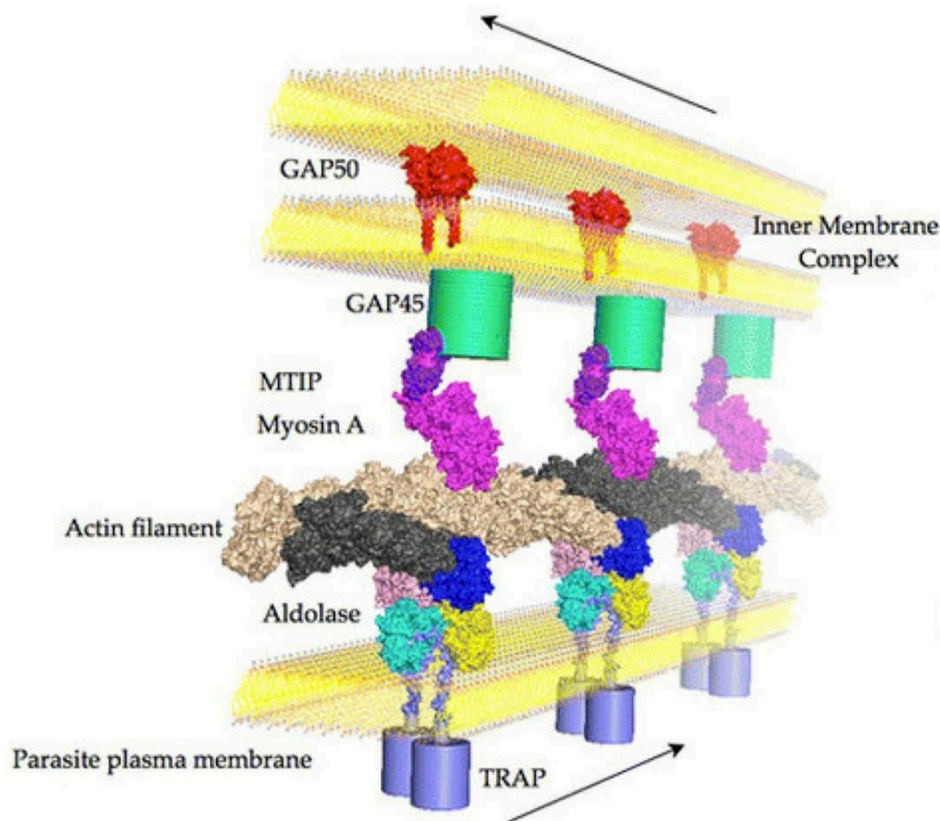


**FIGURE 7-Cartoon representation of the Glideosome components**

Taken from (Nemetski and al. 2015). The gliding machinery is located within the pellicle in the space between the parasite plasma membrane and the inner membrane complex (IMC). An actin-myosin system at the core of the glideosome is composed of a divergent actin (PfAct1) and a divergent myosin called PfMyoA. GAP45 (Green) recruits PfMyoA to the IMC. Aldolase mediates a bridging function between short actin filaments and thrombospondin related anonymous protein TRAP.

### 1.7.4 Myosin A is a promising therapeutic target

Unconventional class XIV myosins are myosins specific to Apicomplexa phylum. A total of six myosin genes are found in the genome of *Plasmodium* : class XIV Myosin A, Myosin B and Myosin E; class VI Myosin J and Myosin K; and class XXII Myosin F (Foth et al., 2006; Wall et al., 2019). Interestingly, only myosin A (MyoA; Class XIVa) is well- conserved across Apicomplexa, and a further three myosins, MyoF, MyoJ, and MyoK, are common between *Plasmodium* and *Toxoplasma* (Foth et al., 2006). Myosin A is also the best characterized to date. The structure and the role in the cycle of infectivity of the parasite played by Myosins B, E, F, J and K remains unknown.

Myosin A from *P. falciparum* (PfMyoA) is a tailless myosin consisting of only a motor domain and a light chain interaction domain. The light chains of conventional myosins are recognized by motifs whose consensus sequence is (IQ XXX RG XXX R), these motifs are generally conserved in classical myosins but are degenerate in the case of the atypical myosin PfMyoA. The degenerate patterns of PfMyoA: PfIQ1 and PfIQ2 recognize the light chains **i)** Essentiel Light Chain (PfELC) and **ii)** Myosin Tail Interacting Protein (MTIP), respectively (Figure 7). PfMyoA is also a divergent motor, sharing only 30% of sequence identity with class II myosins (Figure 7). Myosin A from *Toxoplasma gondii* (TgMyoA) has been implicated in the invasion and egress of host cells but also in the motility of the parasite (Meissner et al., 2002; Andenmatten et al., 2013). TgMyoA is however not essential for invasion and its function can be compensated by TgMyoB or TgMyoC (Egarter et al., 2014; Frénal et al., 2013). Interestingly, according to studies performed in *Plasmodium*, although forces are produced by the motors of the parasite to allow merozoites to invade erythrocytes, the host-cell has also a contribution during membrane wrapping, but it still has to be investigated (Dasgupta et al., 2014).

In the *Plasmodium* genus, the first experiments investigating the role of Myosin A have been carried with the mouse pathogen (*P. berghei* parasite) responsible of malaria in this animal. This study has demonstrated that myosin A (PbMyoA) is necessary for the motility of the parasite (Siden-Kiamos et al, 2006). More recently, studies made on *P. falciparum* have shown that inhibition of the expression of the GAP45 gene leads to the abolition of the invasion during the merozoite stage, but interestingly no role in the motility of the parasite was found (Perrin et al., 2018). While this study highlights a key role of the glideosome in the invasive

stage of *Plasmodium*, the structural role of Gap45 as well as its interaction with MyoA and their role together in the infectivity of the parasite remains unknown. Since MyoA is the motor at the heart of the glideosome, its importance in the different stages of the parasite's infectivity cycle was suspected for a long time and has recently been shown for invasion of merozoites (Robert-Paganin et al., 2019).

## 2. Problematics

### 2.1 Sequence divergence in the connectors of PfMyoA suggests compensatory mechanisms of force production

Myosin A is a very interesting myosin to study for various reasons: **i)** it shows sequence divergences comparing with other conventional myosins, it shares only 30% as best score of sequence identity with  $\beta$ -cardiac Myosin II **ii)** according to the sequence analysis of myosin A, the domain organizations is different from known human myosins: it comprises an extension in the N-terminal region predicted to be an alpha helix which is unique to Myosin A. However, the role of this N-terminal extension was unknown. In addition, based on sequence analysis the PfMyoA is shorter than the conventional myosins and devoid of a tail region. This region usually regulates certain myosins via its interaction with cellular partners which allow the recruitment of these motors in different biological processes. These specificities suggest that Myosin A has a different mode of regulation. **iii)** the other difference which is not at all negligible is the lack of glycine in the sequence of Myosin A SH1 helix. This glycine plays a role of a fulcrum which promotes the piston-like movement of the connector SH1 during the force generation. The mutation of this glycine in conventional myosins blocks their force production. Despite the lack of this glycine in myosin A, this motor is still capable to produce force and to move on the actin filament. This suggests a compensatory mechanism present in PfMyoA in order to allow force production. A structural study of the motor domain and of the motor cycle of this atypical motor was necessary to address this question.

### 2.2 Sequence analysis suggested an atypical recognition of Light chains PfELC1 and MTIP

Myosins bind to light chains via IQ motifs with conserved elements of the consensus (IQXXRGXXR) that are crucial for the interactions that maintain the anchoring of the light chains. In the case of Myosin A, the IQ motifs are completely degenerated (**Figure 8**), none of the consensus elements are conserved in the case of IQ1 motif that binds ELC. This is a first for

myosin, so we were wondering how myosin A is able to recognize its light chains. PfELC that was discovered recently by our collaborator Jake Baum and his team is very important for the functionality of the motor (Bookwalter et al., 2017), we will detail this point in the methodology section. To answer the question of how the PfELC is recognized by the degenerated IQ1 motif from the Myosin A lever arm, we needed to solve the atomic structure of Myosin A Full Length by X-ray crystallography.

**FIGURE 8-Degenerated IQ motif**

In *Plasmodium* zoites (Sporozoites and Merozoites) MTIP localizes to the periphery of the cell, MTIP compensates the lack of the tail domain in Myosin A and allows it to anchor the inner membrane complex (IMC) (Bergman et al., 2003). The atomic structure of the lever arm peptide complexed with MTIP was solved by (Bosch et al., 2006; Douse et al., 2012). TgMyosin and other structure recently solved for MLC1 and TgELC1 together complexed with the lever arm (Pzicki et al., 2020).



We wanted to understand how these specific light-chains could recognize the target degenerated IQ motifs of PfMyoA. For this purpose, a structural investigation on the lever arm was necessary.

### **2.3 Role of PfMyoA in *P. falciparum* invasion was not clearly established**

During malaria infection, the parasite spreads through blood vessels, thanks to the gliedosome complex it is endowed with a high speed which allows it to escape the immune system (Reviewed by [Tardieux & Baum, 2017](#)). In the other hand this complex provides the parasite with the necessary force to actively invade host cells ([Perrin et al., 2018](#)). The PfMyoA is at the core of this complex within a divergent actin. MyoA is critical but not essential to the invasion of host cells in *Toxoplasma gondii* ([Egarter et al., 2014](#)). Indeed, TgMyoA KO in *Toxoplasma gondii* leads to the diminution of the parasite invasion and egress but not to the complete blocking of one of these, due to the fact that there is a potential compensatory mechanism between MyoA and another *Toxoplasma* myosin, TgMyoC ([Egarter et al., 2014](#); [Frénal et al., 2013](#)). Since a recent study which showed that the disruption of the gliedosome blocks the invasion of the parasite at the merozoite stage ([Perrin et al., 2018](#)), we wanted to further study the role of PfMyoA in the parasite infectivity. To investigate the role of PfMyoA in *P. falciparum* asexual stages, we planned with our collaborator Jake Baum to delete the heavy chain of PfMyoA and evaluate the effect of this deletion to the infectivity of merozoites.

we used kinetics and parasitology studies which demonstrated the role of PfMyoA in both invasion and motility of the parasite.

### **2.4 Development of a new generation of antimalarial drugs targeting myosins**

Since recent studies suggested the role of PfMyoA in the parasite infectivity we start to view PfMyoA as an excellent therapeutic target. We planned to use strategies developed in our laboratory and already used to characterize a modulator able to block PfMyoA functions. Our lab has established strong collaborations to screen and to synthesize small molecules able to modulate myosin functions (see conclusions).

### 3. Methodologies

#### 3.1 Expression and purification of the PfMyoA / ELC / MTIP complex

The expression and purification of PfMyoA is carried out in collaboration with the laboratory of Dr. Kthleen Tribus at the University of Vermont. The long years of research by our collaborators into the production conditions of PfMyoA have borne fruit recently in (Bookwalter et al., 2017). Expression of PfMyoA occurs in baculovirus with an expression system in insect cells (*Sf9*) and requires specific UCS (UNC-45 / CRO1 / She4p) chaperones of the *Plasmodium* spp. genus (Bookwalter et al., 2017). These chaperones are required for the correct folding of myosin PfMyoA. Thanks to these results we were able to produce and purify PfMyoA-MD that we characterized later. Today If we manage to express, purify (Figure 9) and characterize the PfMyoA FL / PfELC / MTIP complex, it is thanks to the work of our collaborators who have led to the identification of the Essential Light Chain type (PfELC) which coexists with the PfMyoA motor isolated from the parasite lysate (Bookwalter et al., 2017). The major difficulty with which we are confronted in order to be able to purify a myosin is the identification of its light chains like the ELCs (see in Table 1 for a list of all the identified light-chains and historical nomenclature). In addition to that, there are myosins that can bind several ELCs as is the case for TgMyoA with ELC1 and ELC2 (Heissler & Sellers. 2015; Williams et al., 2015). PfELC from *Plasmodium falciparum* is very divergent from known ELCs including that of *T. gondii*. Surprisingly the binding of PfELC to the heavy chain requires the binding of MTIP, means that one can purify PfMyoA in complex with MTIP without PfELC but the opposite is not possible. *In vitro* motility assays done by collaborators have shown that when the two light chains PfELC and MTIP are bound to the heavy chain, the PfMyoA motor is capable of producing a speed of 3.8  $\mu\text{m} / \text{S}$ , therefore the presence of PfELC is necessary operation of the PfMyoA motor (Bookwalter et al., 2017).

With this strategy we purified (i) the PfMyoA Motor domain (1-768 residues) and its different mutants (ii) the construct PfMyoA FL associated with its two light chains in order to study their structure and function.

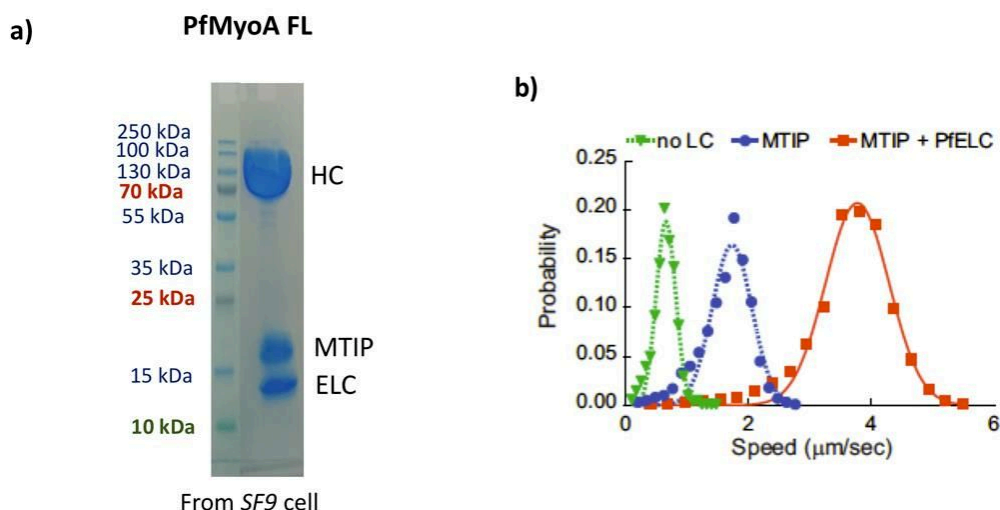


**FIGURE 9-PfMyoA purification and characterization by *in vitro* motility assays**

**a)** SDS-PAGE showing the purified PfMyoA FL with its light chains ELC and MTIP. The samples have been obtained in sufficient quantity and purity for structural studies by X-ray crystallography. **b)** *In vitro* motility assays. Speed distributions of PfMyoA FL with no light chain bound (green),  $0.670.16 \mu\text{m/s}$ , with MTIP bound (blue),  $1.750.32 \mu\text{m/s}$  and with both light chains MTIP and PfELC bound (red),  $3.780.52 \mu\text{m/s}$ , taken from (Bookwalter et al., 2017).

Light chain	Historic abbreviation
Essential (ELC)	LC17
	Alkali LC
	A1, A3
	g1, g3
	MLC1
	SH-LC
Regulatory (RLC)	LC20
	MLC1
	MRLC
	DTNB LC
	A2
	g2
	P-LC
Calmodulin (CaM)	CDR

**Table 1- List of recent and historic abbreviation of ELCs, RLCs and CaM. Taken from (Heissler and Sellers. 2015)**



### 3.2 Reconstruction of the motor cycle of PfMyoA

As we have seen before, the motor cycle of a myosin is composed of distinct structural states. Trapping these states is challenging, since the conformational changes involved in force generation are in the order of nano seconds (Nesmelov et al., 2011). Our laboratory has spent years developing strategies for the co-crystallization of myosins and developed approaches to trap each state. These approaches consist in the use of nucleotide hydrolysis product analogues, including the Mg.ADP and the VO<sub>4</sub> which is phosphate analogue that stays in the nucleotide pocket. The use of different nucleotide analogues allows to trap distinct states and thus to reconstitute the motor cycle.

Other techniques are used to crystallization and help in difficult cases. We can for example use limited proteolysis or seeding approaches. The principle of **limited proteolysis** is to co-crystallize the protein in presence of few amount of a protease such as the trypsin. The trypsin will digest and remove the flexible portions of the protein and thus help crystallization. **Seeding** approaches are used in order to improve the quality of the crystals. When for example we obtain poor quality crystals such as needles or microcrystals, the crystals are collected and crushed mechanically, leading to a solution of seeds. Seeds are small nuclei that will be serially diluted and put in the conditions to favor nucleation and the growth of larger crystals.

All the crystals are treated with a cryoprotectant (in our case glycerol) prior to freezing in order to avoid the formation of crystalline ice, and frozen in liquid nitrogen. All the crystals were analyzed at the SOLEIL Synchrotron (on lines Proxima-1 and Proxima-2 or to the ESRF (ID23a et ID30a-1 beamlines).

When I arrived in the team, Julien Robert-Paganin, a researcher in our team and co-supervisor of my PhD thesis project, had solved the structures of PfMyoA-MD in the PR and the Rigor-like states without any nucleotide in the crystal (nucleotide free) at a 2.8 Å resolution. The PPS state was recalcitrant to crystallize at this time. I finally identified a condition with poor quality crystals. Thanks to optimization in the buffer of the condition, I could improve the crystals. Finally, I get and solved the PPS structure of the PfMyoA at 3.49 Å which was missing to reconstitute and understand the force production cycle of this atypical motor (**Figure 10**).

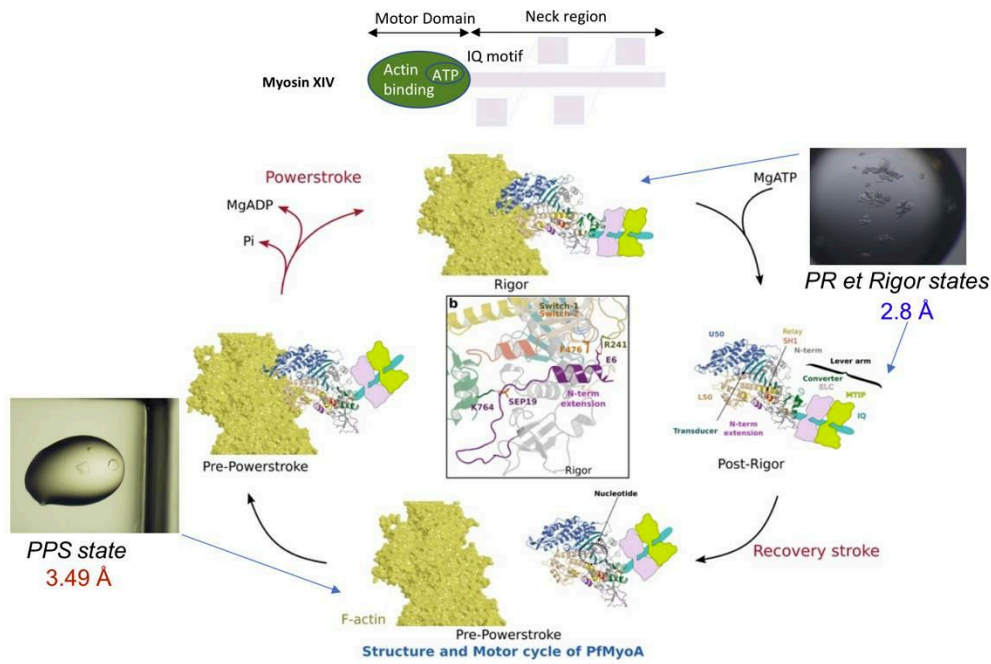


**FIGURE 10-Structural states and motor cycle of PfMyoA**

Modified from (Robert-Paganin et al., 2019). PfMyoA MD crystallized in different states in Rigor, PR and PPS. The lever arm is represented here in cartoon. In the square the zoom of the phosphorylated N-terminal extension (purple) that tunes the proprieties of this motor.

Once the motor domain was characterized, the crystallographic structures of the PfMyoA-FL was necessary for the study of the lever arm orientation during the force production and how the lights chains anchor the lever arm to contribute to its rigidity. Until here the information of the lever arm was missing because the ELC of PfMyoA (PfELC) was not identified. Once our collaborator Jake Baum could get this information (Bookwalter et al., 2017), the lab of Kathleen Trybus started to set up a purification protocol. As soon as we succeeded in producing PfMyoA-FL in collaboration with Dr. Kathleen Trybus laboratory, we proceeded crystallization trials with the full-length construct comprising the two light-chains.

The same crystallization strategy used for PfMyoA-MD was used for PfMyoA-FL. I succeeded to crystallize and solve the structure of PfMyoA-FL in PPS and PR state at a resolution of 2.6 Å and 3.9 Å, respectively (Figure 11). The PPS state was recalcitrant to crystallize and I identified a condition with microcrystals. I could improve the size and the quality of these crystals by a seeding approach. We did molecular replacement for solving both structures by using the structures motor domain and of MTIP bound to its IQ motif as target models (PDB code 4AOM), PfELC and its IQ were built manually.

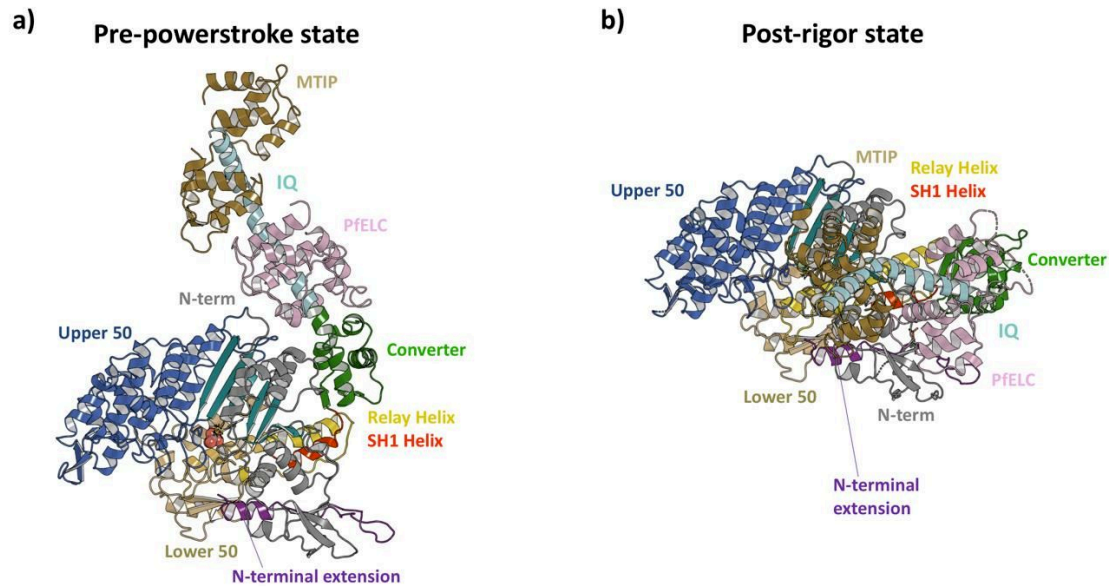


**FIGURE 11-Crystallographic structures of *PfMyoA FL***

Taken from (Moussaoui et al., 2020). Overall structures of the full length *PfMyoA* motor in the PPS and PR states, displayed so that their N-terminal subdomains adopt a similar orientation. As expected, the orientation of the Converter and lever arm differs in these two states.

Since the N-terminal extension was proven be involved in tuning force production of *PfMyoA*, see (Robert-Paganin et al., 2019), we designed construct deprived of the phosphorylated extension N-terminal in order to study the impact of N-terminal extension deletion on the structure of *PfMyoA-FL*. We succeeded to crystallize these mutant in PR and PPS states at 2.6 Å and 1.9 Å, there structures were solved by molecular replacement using the WT *PfMyoA-FL* models without the N-terminal extension (residues 1-19). Notes that for the PPS state, the crystallization conditions were different for the WT *PfMyoA* and truncated construct. To get these two crystals, we set off on new conditions that we found by screening and that we refined as described in the strategy cited above.

### 3.3 The effect of mutants on the functionality of *PfMyoA*

The crystallographic structures alone are not sufficient to study the role of a particular extension or a residue a connector in force production. That is why kinetics experiments are mandatory to conclude on these questions.

The myosin force production cycle is quite complex, hydrolysis products are indeed released in two steps: the state of Pi release and the state of ADP release are detailed in the text dedicated to the explanation of the motor cycle states (see **the motor cycle of myosins**). To study the functional proprieties of PfMyoA and the specific aspects of the states of the cycle, *in vitro* motility assay, transient kinetics and Actin-activated ATPase activity were done by our collaborator Kathleen Trybus laboratory.

**3.3.1 Unloaded *in vitro* motility assays** are used to measure the ability of the myosin to move actin. The principle consists in skeletal actin filaments labelled with Rhodamine phalloidin. Functionalized myosin containing a C-terminal biotin tag are fixed in a flow cell with streptavidin. Actin filaments were visualized and tracked using an inverted microscope. This set up allow to measure the speed of the PfMyoA WT and its mutants on actin.

**3.3.2 Loaded *in vitro* motility assays** are used to measure ensemble force produced by myosins functionalized in the flow cell. The only difference with unloaded motility assays is the addition of utrophin fused to a biotin tag. Utrophin binds actin filaments and add some mechanical resistance once the myosins pull on the actin filaments. The experiment is done with crescent utrophin concentrations and thus the speed of actin filaments is tracked with increasing mechanical load. In this experiment, it is assumed that the speed is linked to the force applied by the myosins to move loaded actin filaments.

**3.3.3 ADP release assays** are transient kinetics experiments that measure specifically the rate of ADP release. In a quenched-flow apparatus, actin is labeled with Pyrene, the acto-PfMyoA (MgADP) were mixed with a high concentration of MgATP to cause the dissociation of myosin from actin. The dissociation rate of PfMyoA were measured by light scattering at 295 nm. The fluorescence detected change depending of the cleft closure, whereas, when the affinity of the motor is weak to the actin (myosin detached from actin=> cleft opened) the fluorescence is detected means that ADP is released whereas in Rigor state (state with high affinity to the actin=> cleft closed) the fluorescence of the pyrene is quenched.

For each construct, steady-state actin activated ATPase assays are used to evaluate general effect on the cycle. Steady-state basal ATPase assays (measurement of the activity without actin) are used to evaluate the stability of the PPS state. ADP-release and *in vitro* motility assays are used as well to evaluate the effect of a mutation on specific aspects of the

cycle. This approach is highly powerful since it allows to study the function of a residue or a connector on a specific step or parameter of the motor cycle of the myosin. For more details see (Robert-Paganin et al., 2019).

### **3.4 The dynamics of the lever arm**

The possible conformations of the lever arm as well as the dynamics of the elements of the motor domain have been studied by molecular dynamic simulations in collaboration with Dr. Daniel Auguin from Université d'Orléans. The principle of the method is to use all-atom simulations performed with GROMACS (Charmm force field), during a time course of several hundreds of nanoseconds and to specifically inspect the dynamics of specific connectors or regions of the myosin. This approach is adapted to study movements and dynamics in myosins since it has been developed to investigate impact of HCM causing mutations on the flexibility of the lever arm of  $\beta$ -cardiac myosin (Robert-Paganin et al., 2018).

We used molecular dynamics to demonstrate the role of the N-terminal extension in stabilizing the Rigor orientation of the converter. The dynamics of the  $\Delta$ Nt-MD construct and phosphonul mutants have been compared to the WT, all in Rigor-like conformation. In this last experiment, the orientation of the converter has been inspected during all the time course of the simulations. The same experiments has been used to study the role of specific residues in stabilizing the atypical priming of the lever arm in the PPS state, the dynamics of the WT-construct has been compared to the dynamics of a variant with alanine mutants in three residues that were suspected to maintain the priming. We expected that the priming was not maintained in the triple mutant.

Molecular dynamics complements crystallography and is essential to understand the flexibility and the allostery underlying the progression during the motor cycle.

### **3.5 PfMyoA and PfELC are critical in parasite blood stages**

In order to confirm the essential role of PfMyoA and PfELC, respectively in the invasion of erythrocytes, we collaborated with the laboratory of Pr. Jake Baum who designed a conditional knock out (cKO) DiCre system inducible to Rapamycin treatment. Rapamycin induces a constitutively expressed DiCre recombinase that deletes the sequence between two loxP sites integrated either into the PfmyoA or in PfELC which leads to the expression of

truncated and non-functional fragments of PfMyoA and PfELC individually. Truncated proteins are expressed fused to GFP in our system.

Conditional KO are done in merozoites stages (**Figure 12**), which cause the symptomatic stages of the disease. Erythrocytic blood cells are infected by *P. falciparum* merozoites and parasitaemia is measured by flow-cytometry (FACS) as the proportion of red blood cells containing DNA (with SyBR green). Immunofluorescence allow to check the location of GAP45, PfMyoA and PfELC.

This technique has the great advantage to work on the specie infecting humans, *P. falciparum*. Indeed, a lot of experiments are done on *P. berghei* (Siden-Kiamos et al, 2006), a species infecting rodents, because it is easier to study in laboratory. Due to the high divergence amongst the Apicomplexan genus, data are stronger when they all come from the same species.

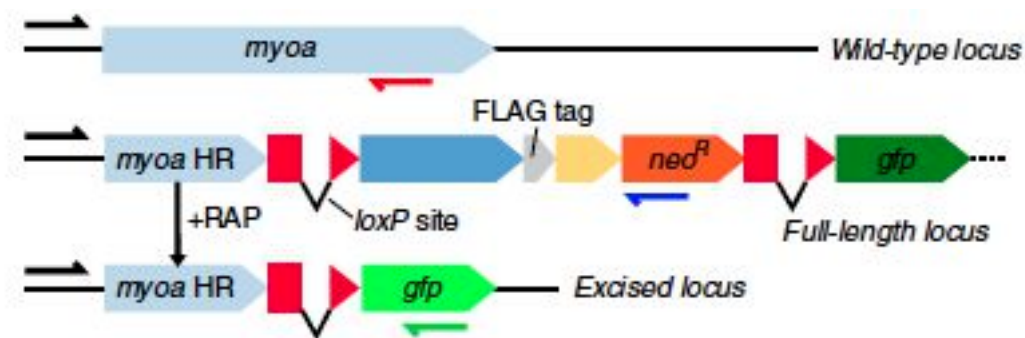


**FIGURE 12-*PfMyoA* conditional knock down with Dicre system**

Taken from (Robert-Paganin et al., 2019). Schematic showing replacement of the wild-type *myoa* locus with the full-length mutant locus by single crossover recombination in the *myoa* HR region using a T2A skip peptide (yellow box) to couple genomic integration to neomycin selection.




## **Chapter II: Results**

## ARTICLE

<https://doi.org/10.1038/s41467-019-11120-0>

OPEN

# Plasmodium myosin A drives parasite invasion by an atypical force generating mechanism

Julien Robert-Paganin<sup>1</sup>, James P. Robblee<sup>2</sup>, Daniel Auguin <sup>3</sup>, Thomas C. A. Blake<sup>4</sup>, Carol S. Bookwalter<sup>2</sup>, Elena B. Kremontsova<sup>2</sup>, Dihia Moussaoui<sup>1</sup>, Michael J. Previs<sup>2</sup>, Guillaume Jousset<sup>1</sup>, Jake Baum <sup>4</sup>, Kathleen M. Trybus<sup>2</sup> & Anne Houdusse <sup>1</sup>

*Plasmodium* parasites are obligate intracellular protozoa and causative agents of malaria, responsible for half a million deaths each year. The lifecycle progression of the parasite is reliant on cell motility, a process driven by myosin A, an unconventional single-headed class XIV molecular motor. Here we demonstrate that myosin A from *Plasmodium falciparum* (PfMyoA) is critical for red blood cell invasion. Further, using a combination of X-ray crystallography, kinetics, and in vitro motility assays, we elucidate the non-canonical interactions that drive this motor's function. We show that PfMyoA motor properties are tuned by heavy chain phosphorylation (Ser19), with unphosphorylated PfMyoA exhibiting enhanced ensemble force generation at the expense of speed. Regulated phosphorylation may therefore optimize PfMyoA for enhanced force generation during parasite invasion or for fast motility during dissemination. The three PfMyoA crystallographic structures presented here provide a blueprint for discovery of specific inhibitors designed to prevent parasite infection.

<sup>1</sup>Structural Motility, UMR 144 CNRS/Curie Institute, 26 rue d'ulm, 75258 Paris cedex 05, France. <sup>2</sup>Department of Molecular Physiology and Biophysics, University of Vermont, Burlington, VT 05405, USA. <sup>3</sup>Laboratoire de Biologie des Ligneux et des Grandes Cultures (LBLGC), Université d'Orléans, INRA, USC1328, 45067 Orléans, France. <sup>4</sup>Department of Life Sciences, Imperial College London, Exhibition Road, South Kensington, London SW7 2AZ, UK. Correspondence and requests for materials should be addressed to K.M.T. (email: [kathleen.trybus@uvm.edu](mailto:kathleen.trybus@uvm.edu)) or to A.H. (email: [anne.houdusse@curie.fr](mailto:anne.houdusse@curie.fr))



**M**alaria is a mosquito-borne disease caused by obligate protozoan parasites from the genus *Plasmodium*. Despite global efforts to control the disease, malaria is still responsible for half a million deaths each year, with the vast majority of mortality caused by *P. falciparum*<sup>1</sup>. During its complex life-cycle, the parasite transforms through motile and non-motile stages in its two hosts: human and mosquito (Supplementary Fig. 1a). The sporozoite stage that establishes infection, is injected into the dermis following the bite of an infected female mosquito from the genus *Anopheles*. This elongated and highly motile parasite form reaches dermal capillaries and is rapidly transported to the liver, where it targets and infects hepatocytes. Within hepatocytes the parasite grows and divides, eventually releasing tens of thousands of merozoite forms en masse into the blood stream. Merozoites, in contrast to sporozoites, are relatively non-motile stages that specifically target erythrocytes, where they develop and lead to all symptoms associated with malaria disease. Beyond this asexual replicative stage of development, some parasites switch commitment to develop into sexual forms (following an as yet unknown signal) producing male and female gametocytes that re-establish mosquito infection on the next bite<sup>2</sup> (Supplementary Fig. 1a). Whilst anti-malarials are available, resistance to all frontline drugs, including combination therapies based on artemisinin, continues to emerge<sup>3</sup> (Supplementary Fig. 1a), reinforcing the need to find drugs with new modes of action.

Force production and movement are essential for the progression at each stage of the parasite's two host life-cycle. Erythrocytic invasion by a merozoite, for example, involves a force of ~40 pN<sup>4</sup>, while sporozoites can move at a speed of 2  $\mu\text{m.s}^{-1}$ , an order of magnitude faster than the fastest human immune cells<sup>5</sup>. Like all Apicomplexa (the phylum to which *Plasmodium* belong), malaria parasites move using a substrate-dependent mechanism called gliding motility, a sophisticated substrate-dependent form of cell movement based on a macromolecular complex called the glideosome (Supplementary Fig. 1b). At the glideosome core is the single-headed class XIV myosin A (PfMyoA), and short and oriented filaments of a divergent actin (PfAct1). PfMyoA is a tailless myosin consisting only of a motor domain and light chain binding domain. The N-terminal region of one of the light chains (LC), called myosin tail interacting protein (MTIP), is believed to anchor the myosin to a membrane bound complex of glideosome associated proteins (GAP45-GAP50-GAP40) (Supplementary Fig. 1b). Several studies have investigated the role of myosin A in both the coccidian parasite *Toxoplasma gondii* and across the genus *Plasmodium*. In *Toxoplasma gondii*, Myosin A (TgMyoA) has been implicated in both invasion and egress of the parasite from the infected cell<sup>6,7</sup>. TgMyoA is not, however, essential for invasion and its function can be compensated for by TgMyoB or its splicing isoform TgMyoC<sup>8,9</sup>, or by active host cell-mediated internalization<sup>10</sup>. Although host cell membrane wrapping forces likely play a role in merozoite invasion of red blood cells<sup>11</sup>, their role has not been tested in the absence of a parasite motor. In the *Plasmodium* genus, initial experiments using the mouse malaria parasite *P. berghei*, showed that PbMyoA is required for cell motility and midgut colonization during parasite mosquito stages<sup>12</sup>. More recently, genetic ablation of GAP45 in *P. falciparum* blocked parasite invasion in merozoite stages, but not egress<sup>13</sup>. Whilst this study points to a critical role for the motor complex in blood stages of infection, the structural role GAP45 plays in apicomplexan cell architecture and glideosome function leaves the essential functionality of MyoA in the merozoite unresolved.

Given that the core of the glideosome is composed of divergent forms of both myosin and actin, the actomyosin system of *P. falciparum* is an attractive target for generation of new anti-malarial drugs. Actin is a highly conserved, ubiquitous

protein in all Eukaryotes, with yeast and human actins sharing 87% identity, in contrast to <80% identity of PfAct1 with canonical actins. The sequence of PfAct1 differs from canonical actins in regions implicated in inter-protomer interfaces of the actin filament<sup>14</sup>. Accordingly, high resolution cryo-electron microscopy (CryoEM) studies confirmed altered inter-strand and intra-strand contacts that provided a structural basis for the instability of PfAct1 filaments<sup>14,15</sup>. PfMyoA is also a divergent motor, sharing only 30% sequence identity with Class II myosins. Interestingly, important sequence differences are located precisely in structural elements predicted to be relaying parts of the allosteric communication pathway within the myosin motor domain. In Class XIV myosins, to which PfMyoA belongs, the sequence of critical canonical residues for the motor mechanism are not conserved, including a pivotal <sup>SH2-SH1</sup>Gly (G695 in scallop myosin 2) at the beginning of the SH1-helix. The connectors (Switch-2, the Relay helix, and the SH1-helix) are structural elements that coordinate rearrangements of the four motor subdomains, whose motions are amplified into a larger swing of the distal light chain binding lever arm (Supplementary Fig. 2). Mutations of this <sup>SH2-SH1</sup>Gly greatly impede motor activity in class 2 myosins (Myo2) by reducing the flexibility of the fulcrum<sup>16–18</sup>. Despite lacking this fulcrum, PfMyoA nonetheless displays robust motor activity<sup>19</sup>. Resolving this conundrum requires structural studies of MyoA in different nucleotide states to reveal the key compensatory intra-molecular rearrangements that are involved in guiding the lever arm. Such a force generation mechanism is likely to be unique to the apicomplexan class XIV myosins. Based on a recently solved crystal structure of only one state (Pre-powerstroke, PPS) of the TgMyoA motor domain with a disordered N-terminal region, Boulanger and coworkers could only speculate about how sequence adaptations in the Wedge, the Relay and the fulcrum (Supplementary Fig. 2) may compensate for this mechanism<sup>20</sup>.

By combining parasitological studies of MyoA in *P. falciparum* with structural, motility, and kinetic studies of the motor in vitro, we show that PfMyoA is critical for *P. falciparum* erythrocyte invasion, and that this atypical motor diverges significantly with regard to how force and motion is produced compared with conventional myosins. By solving three structural states of the PfMyoA motor domain, corresponding to three states of the motor cycle, we show how the unique class XIV N-terminal heavy chain extension and its interactions with other structural elements define motor function. We also show that Ser19 phosphorylation in this N-terminal extension substantially modulates the speed and force output generated by the motor. These insights allow us to propose a phosphorylation-dependent mechanism that tunes the motor for optimal invasion (high force) or dissemination (fast motility speed). Together, these insights provide a complete foundation from which to understand the non-canonical mechanism of force production in these globally significant parasites.

## Results

**PfMyoA is critical for erythrocytic invasion by merozoites.** Whilst GAP45 has been reported to be essential for erythrocytic invasion by merozoites<sup>13</sup> the role of the gliding motor itself, PfMyoA, in *Plasmodium* blood stages, has never been directly tested. To address this question, we generated a rapamycin (RAP) inducible PfMyoA KO<sup>21</sup> (Fig. 1a). Rapamycin treatment induces a constitutively expressed DiCre recombinase, leading to excision of the sequence between two loxP sites integrated into the *pfmyoa* gene<sup>22</sup>, deleting the last 543 bases and bringing *gfp* into frame as a truncated fusion protein (residues 1–638). The resulting truncated PfMyoA motor lacks the C-terminal residues predicted

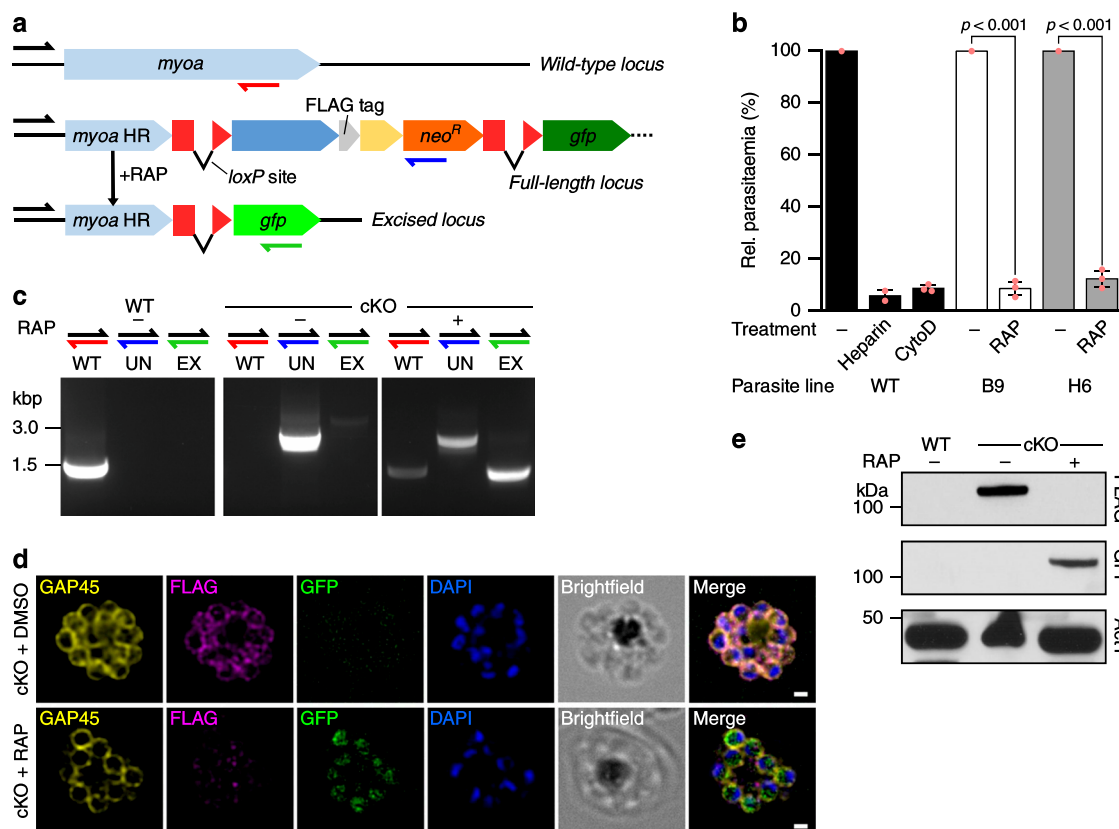


**Fig. 1** PfMyoA is critical for red blood cell invasion by merozoites. **a** Schematic showing replacement of the wild-type *myoA* locus with the full-length mutant locus by single crossover recombination in the *myoA* HR region using a T2A skip peptide (yellow box) to couple genomic integration to neomycin selection. **b** Treatment of two MyoA-cKO clones (B9 and H6) or WT with rapamycin (RAP) shows an almost complete invasion block (~90%) compared to DMSO treatment (-). This is comparable to the defect with known invasion inhibitors heparin and Cytochalasin D (CytoD) (90–95%). Parasitaemia was measured in the following cycle (cycle 1) by flow cytometry as the percentage of red blood cells (RBCs) that were DNA-positive by staining with SYBR Green I. Mean of three biological replicates (except for WT+heparin: two biological replicates), each three technical replicates,  $\pm$  standard deviation (S.D.) of biological replicates. Data from each biological replicate were normalized to the DMSO-treated sample for each parasite line. Significance assessed using parametric t-test (paired, two-tailed). **c** Genotyping PCR of WT or cKO parasites following DMSO (-) or RAP (+) treatment detecting the wild-type (WT, red half-arrow), unexcised (UN, blue half-arrow) and excised (EX, green half-arrow) *pfmyoA* loci. **d** Immunofluorescence analysis of cKO parasites following DMSO or RAP treatment. FLAG-tag is detectable in DMSO-treated schizonts fixed ~48 h post-treatment, colocalising with motor complex protein GAP45, while after RAP treatment GFP but not FLAG is detectable, and the signal is restricted to the cytosol, consistent with a non-functional truncated MyoA. Scale bar 1  $\mu$ m. Image stacks were deconvolved using the EpiDEMIC plugin for Icy, with a z-step size of 200 nm. **e** Western blot of WT and cKO parasites following DMSO (-) or RAP (+) treatment. Parasites were lysed ~40 h post-treatment, before the end of cycle 0. In DMSO-treated cKO parasites, the original FLAG-tag is detectable, but following RAP-treatment, only GFP is detectable. PfAct1 was used as a loading control. Representative blot shown from three biological replicates

to be required for the folding of the motor domain and would therefore be expected to be non-functional.

Two PfMyoA-cKO clones (B9 and H6) were compared with both WT and non-excised (DMSO treatment) controls to assess motor function. In addition, two known invasion inhibitors, heparin (that blocks cell-to-cell interactions) and CytoD (that blocks actin polymerization) served as positive controls<sup>23</sup> (Fig. 1b). Synchronized parasites were treated with 100 nM RAP and incubated for 16 h at the start of one cycle (cycle 0) to trigger truncation of *pfmyoA*. These were then tested for invasion of red blood cells (RBCs). Parasitaemia was measured in the following cycle (cycle 1) by flow cytometry as the percentage of RBCs that were DNA-positive by staining with SYBR Green I (Fig. 1b). Successful excision of the *loxP* section of *pfmyoA* was monitored by PCR (Fig. 1c), localization of PfMyoA by immunofluorescence (Fig. 1d) and western blotting (Fig. 1e), all confirming loss of the functional protein.

The KO of PfMyoA induced in the two PfMyoA-cKO clones demonstrated an almost complete block in invasion (~90%)

compared to DMSO treatment, comparable to rates of invasion detected with known invasion inhibitors heparin and CytoD (90–95%) (Fig. 1b). This confirms the long-held assumption that PfMyoA is directly involved in merozoite invasion of the erythrocyte in *P. falciparum*. Given the combined evidence that MyoA is critical for both invasion and for motility<sup>12</sup> in *Plasmodium* parasites, it would appear to be a bona fide first-order therapeutic target for preventing malaria parasite infection and disease progression.

**X-ray structures of three structural states of PfMyoA.** To define the motor cycle of PfMyoA, we determined the crystallographic structures of the motor domain (MD) of PfMyoA (1–768) in a nucleotide-free (NF) condition at 2.82 Å resolution (crystal type 1) (Supplementary Table 1, PDB code 6I7D) and complexed to ADP.Vanadate at 3.45 Å resolution (crystal type 2) (Supplementary Table 2, PDB code 6I7E). Four molecules are present in the asymmetric unit of crystal type 1, one of the motor domain is

in the Rigor-like state and three molecules adopt the Post-rigor (PR) state. These two structural states correspond, respectively to the state of highest affinity for F-actin<sup>24,25</sup> (Rigor-like) and to the state that allows detachment from F-actin but prior to the lever arm recovery stroke<sup>26</sup> (Post-rigor). The PfMyoA Rigor-like state adopts a fully closed cleft as found for non muscle Myo2c and Myo1b Rigor states<sup>25,27</sup> and is thus likely a good model of myosin XIV in the Rigor state.

The crystal type 2 contains one molecule per asymmetric unit. It corresponds to the Pre-powerstroke (PPS) state, a state with the lever arm up and able to dock to actin with electrostatic contacts. The resolution of the PPS state is poorer, but the electron density map is of good quality and allowed the entire motor domain to be built, including loops with good refinement statistics (Supplementary Table 2). Description of these three structural states for the PfMyoA motor provides a direct way to assess the major conformational changes that would occur during the motor cycle (Fig. 2a).

These structures enable visualization of the large conformational changes required for the powerstroke (PPS/Rigor), for detachment of the motor from actin (Rigor/PR), and for re-priming of the lever arm (PR/PPS). The amplitudes of the subdomain movements and converter swing are similar to that of other myosins<sup>28</sup> (Fig. 2a), but the stabilization of the states and the connector rearrangements differ. A key observation we made is the role of the unusual N-terminal (N-term) extension of PfMyoA (Fig. 2b, Supplementary Movie 1). This extension makes

conserved interactions with the N-term subdomain in all three structures, and consists of a helix followed by a linker that contains the phosphorylated Ser19 (SEP19) (Supplementary Fig. 3). Structural analysis presented in detail below shows an unforeseen compensatory mechanism that involves the N-term extension driving the PfMyoA powerstroke despite the lack of sequence conservation in canonical residues of the motor domain connectors (Fig. 3a).

**Motor mechanism in classical myosins.** During motor domain rearrangements required for the motor cycle, movement near the active site involves the connector Switch-2, and is transmitted to the lever arm through interactions between Switch-2 and an important structural element of the Lower 50 kDa (L50) subdomain called the Wedge (Fig. 3b, Supplementary Fig. 2, 4). To drive the lever arm swing in all myosins studied thus far (classical myosins), these Switch-2 rearrangements are coordinated with specific changes of two other connectors: the Relay helix kink straightening and a SH1-helix rotation<sup>28</sup> (Fig. 3c, Supplementary Fig. 4, Supplementary Movie 2). The highly conserved glycine (SH2-SH1Gly) acts as a fulcrum to promote the piston-like movement of the SH1-helix<sup>29</sup>. Conserved interactions between the Relay/SH1-helix and the Wedge/Switch-2 are critical for motor activity (Fig. 3, Supplementary Fig. 5, Supplementary Movies 2 and 3). In classical myosins, such as scallop myosin II (ScMyo2) (Supplementary Fig. 5a), the active site rearrangements

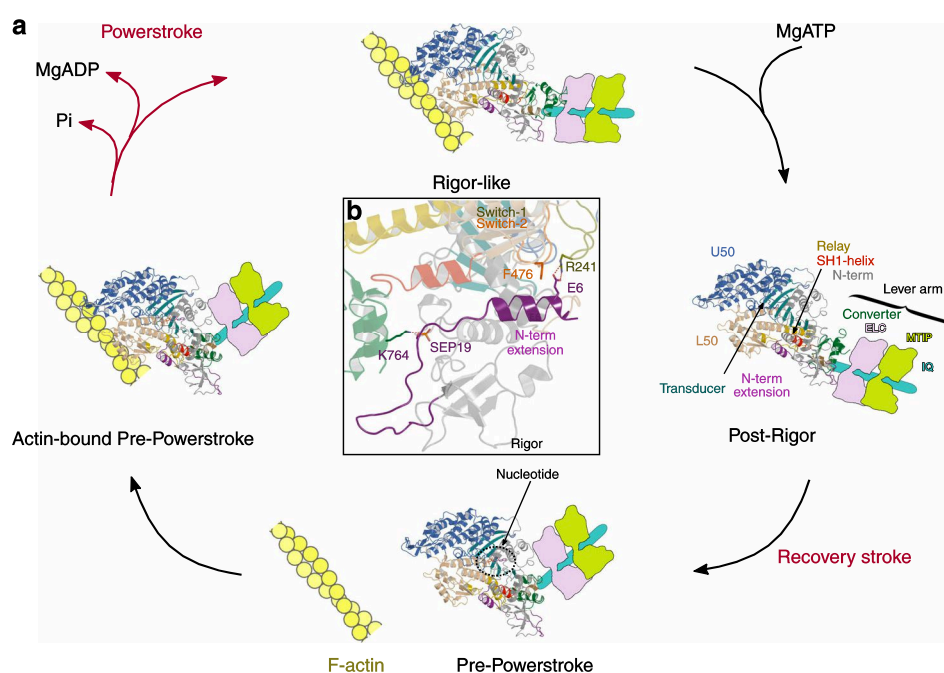


**Fig. 2** Structural states and motor cycle of PfMyoA. **a** The crystallographic structures of the three states of the motor cycle of PfMyoA are represented along the motor cycle: the Rigor-like and the Post-rigor (PR) states reveal how the motor detaches from F-actin upon ATP binding; the Pre-powerstroke (PPS) state corresponds to the state in which hydrolysis occurs and that rebinds to F-actin to trigger the powerstroke. The Rigor-like state is the conformation the motor adopts at the end of the powerstroke when hydrolysis products have been released. To appreciate the movement of the converter and how it can be amplified by the rest of the lever arm, the IQ region and the two LCs (PfELC and MTIP, Supplementary Fig. 1) are represented schematically in continuity of the last helix of the converter. PfMyoA displays the four canonical subdomains which are the hallmark of the myosin superfamily: N-terminus (N-term) (gray), Upper 50 kDa (U50) (marine blue), Lower 50 kDa (L50) (tint) and the converter (green) and central elements (including a beta-sheet) forming the transducer (dark cyan). During the motor cycle, rearrangements in the motor domain are allosterically transmitted through the Relay helix (yellow) and are amplified by the swing of the converter with the rest of the lever arm. **b** In the center diagram, a zoom of the Rigor-like structural state is presented to show the opposite side of the motor domain compared to **a**. Note the position of the unique N-terminal extension (purple) which is close to the connectors that direct rearrangements between motor subdomains (Switch-2 (orange), Relay (yellow) and SH1-helix (red)). PfMyoA employs an atypical motor mechanism in which the N-term extension (purple) compensates for non-canonical sequences in subdomain connectors essential for motor function



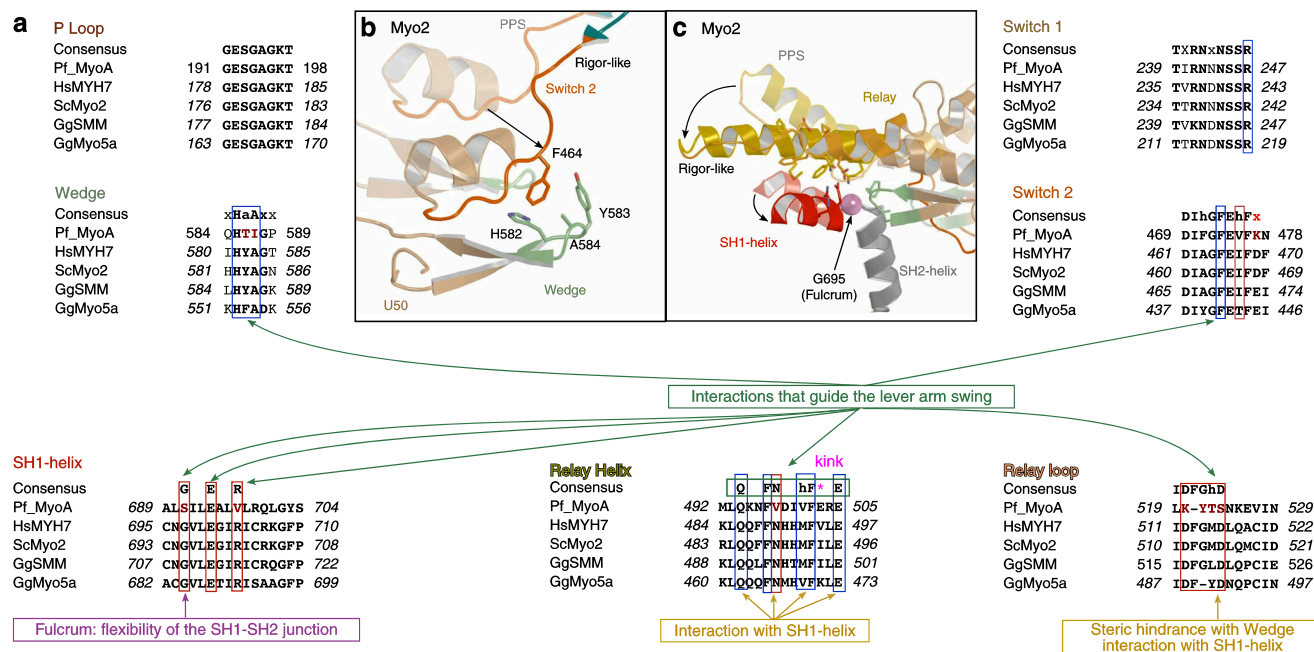


**Fig. 3** Sequence alignment of connectors essential in driving motor conformational changes—lack of canonical residues in PfMyoA. **a** Sequence comparison of several key elements involved in myosin mechanical transduction and allosteric communication. The consensus is represented on top of each sequence and the PfMyoA sequence is compared to other myosins. This comparison shows that the sequences of the Switch-2, Wedge, and Relay differ from the consensus. Consensus code: a is an aromatic residue, h a hydrophobic residue, x colored in red is an acidic residue. Residues important in allosteric communication in the motor are indicated in rectangles (blue rectangle if the residue is involved in a conserved interface, red rectangle if the residues are involved in interactions specific to PfMyoA). If the position is not conserved in PfMyoA, the residue is colored in dark red. To see how these residues affect the PfMyoA motor rearrangements along the cycle, see Fig. 4 and Supplementary Movie 2. **b** Switch-2/Wedge interactions in classical Myo2. **c** Conformational changes of two connectors before (PPS, transparent) and after (Rigor-like, plain) the powerstroke in Myo2. The Relay helix unkinks while the SH1-helix undergoes a piston-like movement using the canonical flexibility found at the fulcrum  $^{SH2-SH1}$ Gly (pink ball)

are linked to Switch-2 changes that are guided by hydrophobic interactions of Switch-2<sup>F464</sup> with canonical residues of the Wedge such as Wedge<sup>H582</sup> and Wedge<sup>A584</sup> (Supplementary Fig. 5b). In the PPS state, the Relay, the SH1-helix and the lever arm are in a “primed” conformation: the interactions between the Relay and the SH1-helix are mainly hydrophobic. Here the conserved Relay<sup>M514</sup> and SH1-helix<sup>E698</sup> are nearby (Supplementary Fig. 5b). During the powerstroke, release of hydrolysis products induces specific structural rearrangements in the active site, and specifically of Switch-2 that repositions the L50 subdomain. In so doing, the Wedge which belongs to the L50 subdomain becomes closer to the Relay/SH1-helix position. The steric hindrance caused by a conserved bulky aromatic, Wedge<sup>Y583</sup> with residues from the SH1-helix and the Relay, Relay<sup>M514</sup> and SH1-helix<sup>E698</sup>, drives the straightening of the Relay, the piston-like movement of the SH1-helix (Supplementary Fig. 5b, Supplementary Movies 2 & 3) and thus the lever arm swings because these two connectors interact strongly with the converter (Supplementary Fig. 5c). The movement of the SH1-helix and the Relay are defined by interactions between these two connectors which are not only hydrophobic but supplemented with electrostatic interactions between conserved residues in the Rigor-like state: the conserved SH1-helix<sup>R701</sup> binds Relay<sup>D515</sup>; SH1-helix<sup>E698</sup> binds Relay<sup>Q485</sup>; and Relay<sup>N489</sup> (Supplementary Fig. 5b).

**The atypical structural motor mechanism of PfMyoA.** In PfMyoA, the amplitude of the converter swing is similar to that observed for classical myosins, despite the absence of the canonical residues essential for allosteric movement in classical myosins. This occurs while the SH1-helix is mostly immobile (Fig. 4), rather than performing a piston-like movement previously described for

classical myosins (Supplementary Fig. 5, Supplementary Movies 2 and 3). As predicted from sequence alignments, the replacement of the conserved  $^{SH2-SH1}$ Glycine restrains the mobility of the SH1-helix. Several sequence adaptations are needed to compensate for the lack of mobility of the SH1-helix. First, the aromatic and bulky residue of the Wedge is absent in PfMyoA and replaced by a threonine (T586), and the nearby bulky methionine residue from the Relay (Relay<sup>511</sup>-DFGMD-515 in ScMyo2) is also absent and replaced by a threonine (T522) in PfMyoA (Relay<sup>520</sup>-KYTS-523) (compare Fig. 4b and Supplementary Fig. 5b; Supplementary Movie 4). The movement of the Wedge during the powerstroke results in less steric hindrance and is thus adapted to the lack of mobility of the SH1-helix which stays in position while the Relay kink resolves and the lever arm swings (Fig. 4b, c, Supplementary Movie 3). Second, the interaction between the Relay and the SH1-helix is mainly hydrophobic both in the PPS state and in the Rigor-like state, with the exception of an electrostatic bond between the Relay<sup>Q494</sup> and the fulcrum  $^{SH2-SH1}$ S691 that is present in the two states (Fig. 4b, Supplementary Movie 3). Third, the PfMyoA Rigor-like state is stabilized by atypical interactions of Wedge<sup>I587</sup> with Switch-2<sup>F473</sup>, Switch-2<sup>V475</sup>, SH2-helix<sup>H688</sup> and SH2-SH1<sup>S691</sup> (red circle in Fig. 4b). Additional interactions with the N-term extension further stabilize the Rigor-like state, including a strong salt bridge- $\pi$  interaction between the N-term.extension<sup>Glu6</sup>, Switch-1<sup>Arg241</sup> and Switch-2<sup>Phe476</sup> (Fig. 4c). In addition, electrostatic contacts directly stabilize the converter since Converter<sup>K764</sup> interacts with the phosphorylated N-term.extension<sup>SEP19</sup> (Fig. 4c).

We conclude from the structures that the electrostatic interactions with the N-term extension compensate for the absence of a piston-like movement of the SH1-helix, enabling force production by accelerating the transitions of the

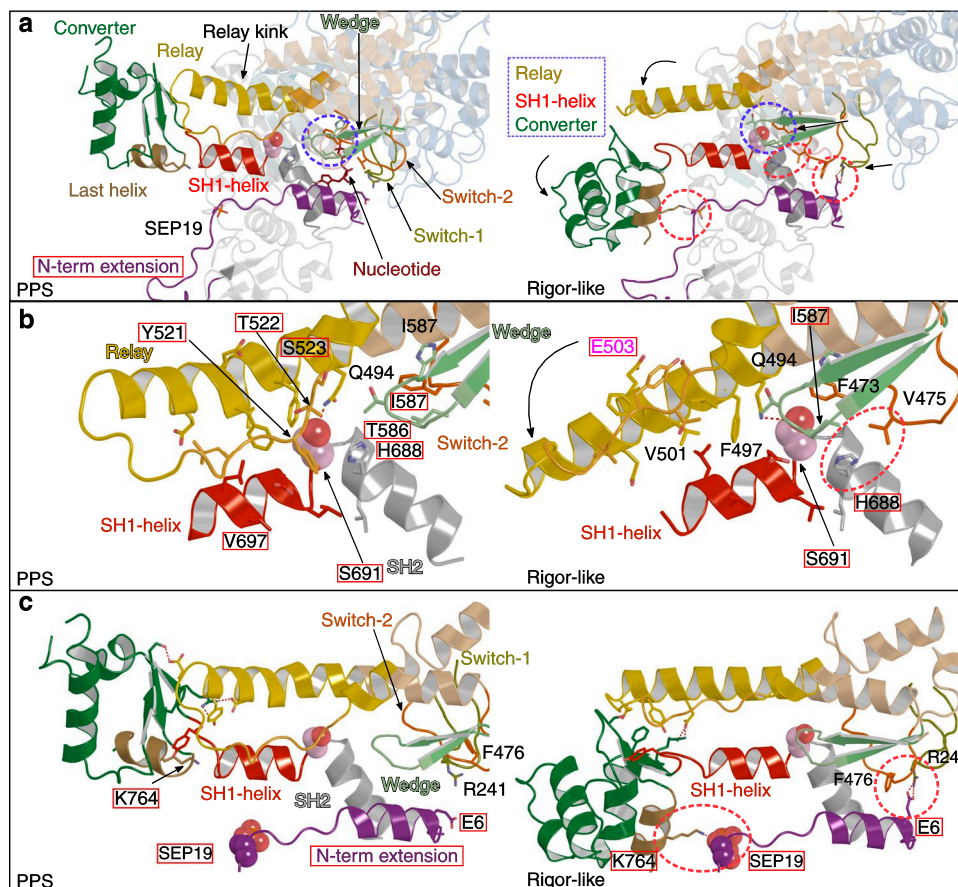


**Fig. 4** The unconventional mechanism of force production by PfMyoA. **a** Overall view of the mechanical communication within the PfMyoA motor domain during the powerstroke. In both the PPS and the Rigor-like states, interactions between Switch-2 and the Wedge are maintained (highlighted by dashed blue lines and detailed in **b**). The Rigor-like structure indicates that the sequential release of hydrolysis products upon the powerstroke triggers displacement of the Wedge which is associated with straightening of the Relay helix and the converter swing. The PfMyoA unconventional powerstroke requires sequence compensation near the Ser691 (blue dashed lines) since this residue is bulkier than the canonical SH<sub>2</sub>-SH<sub>1</sub>Gly found in classical myosins at this position. Thus, motor domain rearrangements are allowed by changes in the interactions between the Wedge and the Relay and SH1-helix connectors (details in **b**). Additional interactions (highlighted by dashed red lines) involving the N-term extension (purple) also stabilize the Rigor-like state and compensate for the immobility of the SH1-helix. (Details are shown using the same view in **c**). **b** Non-conserved residues are highlighted by a red rectangle. The SH1-helix lacks the conserved glycine SH<sub>2</sub>-SH<sub>1</sub>Gly at the fulcrum which is replaced by a serine (light pink spheres, S691). A hydrogen bond is formed between S691 and RelayQ494 in both the PPS and Rigor-like states. The presence of a less pliant fulcrum requires sequence adaptation in the Wedge and in the Relay and results in the immobility of the SH1-helix during the powerstroke. Switch-2V475 establishes hydrophobic interactions with SH<sub>2</sub>H688, helping to stabilize the Rigor-like position of the Switch-2 (red dashed lines). E503 (shown in pink) is a reporter to indicate the kink of the Relay. **c** In PfMyoA, the converter establishes a network of interactions with the Relay and the SH1-helix. Non-conserved residues are highlighted by a red rectangle. An electrostatic bond between phosphoserine 19 (SEP19) (N-term extension) and K764 (converter), as well as a salt bridge- $\pi$  interaction between the N-term extensionE6, Switch-1R241, Switch-2F476 (red dashed lines) stabilize the position of the converter in the Rigor-like conformation. For comparison with Myo2, see Supplementary Fig. 5 and Supplementary Movies 2 and 3

powerstroke. In particular, these interactions could accelerate ADP release which was slowed when the SH<sub>2</sub>-SH<sub>1</sub>Gly was mutated in a canonical Myo2 motor<sup>17,18</sup>.

**PfMyoA phosphorylation tunes its motor properties.** To further analyze the compensatory mechanism and more fully decipher the role of the N-term phosphorylation, we functionally characterized PfMyoA constructs with a 19 amino acid N-term deletion ( $\Delta$ N), or with point mutations that disrupt the N-term extension/converter interaction formed in the Rigor-like state (phospho-null S19A or K764E) (Figs. 4c, 5a). In agreement with the phosphorylated Ser (SEP19) observed in the crystallographic structures described above, we verified that PfMyoA was phosphorylated at Ser19 on the heavy chain during expression in *S*9 cells. Phosphoprotein gels qualitatively showed heavy chain phosphorylation, and mass spectrometry confirmed that  $96 \pm 1\%$

( $\pm$  SD,  $n = 6$ , 2 independent preparations) of the peptides found in the untreated sample were phosphorylated compared with a phosphatase-treated sample (Supplementary Fig. 6).

In vitro motility assays showed that the N-term extension and, specifically the Ser19 phosphorylation, are necessary for actin displacement at maximal speed ( $\sim 4 \mu\text{m.s}^{-1}$ ).  $\Delta$ N-PfMyoA reduced speed  $\sim 17$ -fold, while both the phospho-null (S19A) and charge reversal mutation in the converter (K764E) mutants slowed speed 2-fold to  $\sim 2 \mu\text{m.s}^{-1}$  (Fig. 5b, Supplementary Table 3). The phosphomimic S19E did not fully recapitulate the enhancing effect of bona fide phosphorylation on speed, moving actin at a value intermediate ( $\sim 2.8 \mu\text{m/s}$ ) between S19A and phosphorylated PfMyoA (Supplementary Fig. 7a).

The same pattern seen for in vitro motility was also observed for the maximal rate of the steady-state actin-activated ATPase activity (WT > S19A or K764E >  $\Delta$ N) (Fig. 5c). A linked assay with

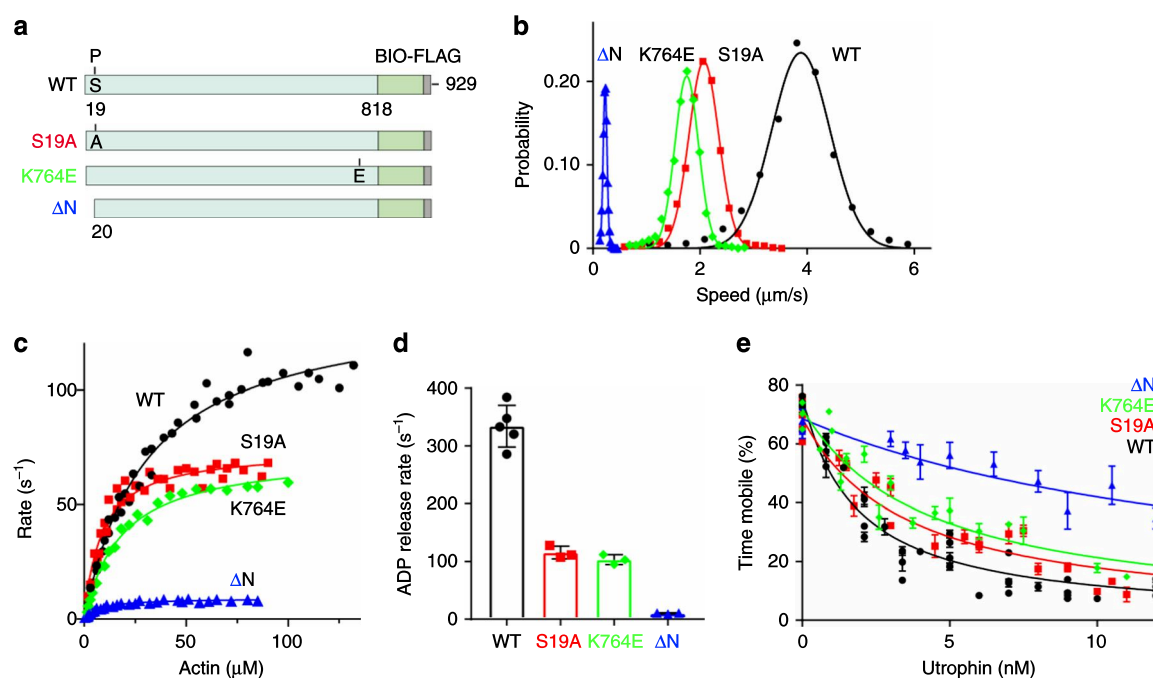


**Fig. 5** Functional properties of wild-type (WT) and mutant full-length PfMyoA constructs. **a** Schematic of constructs used for functional analysis. Ser19 is fully phosphorylated during protein expression in Sf9 cells (Supplementary Fig. 6). **b** Speed distributions from a representative in vitro motility assay. WT,  $3.88 \pm 0.54 \mu\text{m/s}$ ; S19A,  $2.07 \pm 0.28 \mu\text{m/s}$ ; K764E,  $1.75 \pm 0.22 \mu\text{m/s}$ ; and  $\Delta\text{N}$ ,  $0.23 \pm 0.04 \mu\text{m/s}$ . Values, mean  $\pm$  SD (Supplementary Table 3 shows data from multiple protein preparations). **c** Actin-activated ATPase activity for WT,  $V_{\text{max}} = 138 \pm 4 \text{ s}^{-1}$  and  $K_m = 30.3 \pm 2.3 \mu\text{M}$ ; S19A,  $V_{\text{max}} = 74.0 \pm 2.0 \text{ s}^{-1}$  and  $K_m = 8.5 \pm 1.0 \mu\text{M}$ ; K764E,  $V_{\text{max}} = 72.9 \pm 1.9 \text{ s}^{-1}$  and  $K_m = 18.2 \pm 1.4 \mu\text{M}$ ; and  $\Delta\text{N}$ ,  $V_{\text{max}} = 9.13 \pm 0.20 \text{ s}^{-1}$  and  $K_m = 7.34 \pm 0.67 \mu\text{M}$ . Data from 2 protein preparations and 3 experiments for each construct were fitted to the Michaelis-Menten equation. Error, SE of the fit. **d** ADP release rates from actin-PfMyoA. WT,  $334 \pm 36 \text{ s}^{-1}$ ; S19A,  $115.8 \pm 10.9 \text{ s}^{-1}$ ; K764E,  $103.5 \pm 8.6 \text{ s}^{-1}$ ;  $\Delta\text{N}$ ,  $10.32 \pm 0.91 \text{ s}^{-1}$ . Values, mean  $\pm$  SD. WT vs. any other construct,  $p < 0.0001$ ; S19A vs. K764E, NS; S19A or K764E vs.  $\Delta\text{N}$ ,  $p < 0.01$  (one way ANOVA followed by a Tukey's Honest Significant Difference post-hoc test). Data from at least 3 protein preparations of each construct at different temperatures are shown in Supplementary Table 4. **e** Ensemble force measurements using a utrophin-based loaded in vitro motility assay. A myosin that produces more force requires higher utrophin concentrations to arrest motion: WT,  $1.40 \pm 0.08 \text{ nM}$ ; S19A,  $2.42 \pm 0.17 \text{ nM}$ ; K764E,  $3.04 \pm 0.30 \text{ nM}$ ;  $\Delta\text{N}$ ,  $10.8 \pm 0.8 \text{ nM}$ . Error, SE of the fit. Data from two protein preparations and three experiments for each construct. Supplementary Fig. 7b shows these force data and fits extended to higher utrophin concentrations. Supplementary Fig. 7c–e shows  $\Delta\text{N}$  data shown with an expanded y-axis. Skeletal actin was used for all experiments. Temperature,  $30^\circ\text{C}$ . Source data are provided as a Source Data file

an ATP regenerating system was used to prevent ADP buildup during the course of the assay, which could potentially slow the ATPase rate. Transient kinetics were used to directly measure the rate of ADP release from actin-PfMyoA. A high concentration of MgATP was mixed with actin-PfMyoA (MgADP). Under these conditions, the rate of dissociation of PfMyoA from actin, as measured by light scattering, is limited by the rate of ADP release from the motor (Fig. 5d, Supplementary Table 4). For phosphorylated WT, S19A, and K764E, the rate of ADP release was faster than the steady-state ATPase rate. Interestingly, deletion of the N-term extension caused ADP release to become the rate-limiting step in the cycle ( $\sim 10 \text{ s}^{-1}$ ), a hallmark of high duty-ratio motors that spend the majority of their ATPase cycle in a state strongly bound to actin<sup>30</sup>.

Ensemble force measurements using a utrophin-based loaded motility assay and automated filament-tracking software<sup>31</sup> showed that  $\Delta\text{N}$  produced  $\sim 8$ -fold more force, and S19A and K764E produced  $\sim 2$ -fold more force than phosphorylated PfMyoA (Fig. 5e, Supplementary Fig. 7b). These results demonstrate that Ser19 phosphorylation, which has been shown to occur in vivo<sup>32</sup>, likely tunes PfMyoA motor properties. The absence of Ser19 phosphorylation, or removal of the N-term extension, enhances ensemble force at the expense of speed, confirming the role of this atypical extension in force generation.

The electrostatic bond between SEP19 and ConverterK764 stabilizes the Rigor-like conformation while it is unlikely to form in high ADP affinity states. The rate of the last

transition of the powerstroke (ADP release) is thus faster when Ser19 is phosphorylated. Faster ADP/ATP exchange and motor detachment from F-actin leads to higher speed by accelerating motor turn-over. The role of SEP19 in this transition was further investigated in silico using the mutant K764E. Molecular dynamic simulations on a 60 ns time-course further confirm the role of this electrostatic bond for the stability of the converter position, by comparing phosphorylated WT and K764E mutant in the Rigor-like state (Supplementary Fig. 8). In the WT phosphorylated motor domain, the converter is maintained in its Rigor-like position throughout the simulation (Supplementary Fig. 8a, c, d, Supplementary Movie 5). Conversely, in the K764E mutant, the converter position is not maintained and progressively deviates from its initial position together with the Relay, while the SH1-helix stays immobile (Supplementary Fig. 8b, c, d, Supplementary Movie 6). The in silico and in vitro results confirm that the electrostatic interaction between SEP19 and K764 stabilizes the Rigor-like state and is important for modulating ensemble force and the speed at which PfMyoA moves actin.

## Discussion

The divergent force production mechanism of PfMyoA, which we now show underpins the breadth of *Plasmodium* parasite lifecycle progression, is the result of sequence adaptations in which the N-term extension compensates for the absence of the SH1-SH2Gly fulcrum residue, shown as essential for the piston-like movement of the SH1-helix of canonical myosins<sup>18</sup>. By providing three



structural states of the PfMyoA motor, our data directly show the atypical mechanism of force production. While the sequence adaptation near the SH1-SH2Gly/Wedge was correctly predicted from the TgMyoA PPS structure as part of this mechanism<sup>20</sup>, the authors could not envisage that this would lead to a lack of piston-like movement of the SH1-helix as shown here. Other speculations in the study were incorrect because of an inability to visualize the N-term extension in the TgMyoA structure and the absence of a Rigor-like state structure. The details provided by the PfMyoA structures here, highlight how this N-term extension plays a direct and critical role in the force generation mechanism by direct interactions with Switch-2 and the converter.

The PfMyoA Rigor-like structure reveals how an interaction of the phosphorylated serine in the N-term extension with the converter is directly involved in the last step of the lever arm swing associated with ADP release. In so doing, phosphorylation directly controls the speed and force sensitivity of the PfMyoA motor by modulating the time spent strongly attached to F-actin. These insights into the PfMyoA mechanical cycle reveal that a specific phosphorylation event on class XIV myosins tunes their motor activity by a change in their duty ratio. This allows switching between an ability of the motor to generate force under loaded conditions, or to move actin for highest speed under unloaded conditions. The ATPase activity and unloaded in vitro motility speed of expressed PfMyoA were also recently measured by Green et al.<sup>33</sup>, but with values for both that were over 10-fold lower than reported here. Although part of this discrepancy (~2-fold) can be attributed to different assay temperatures (our study 30 °C, their study 23 °C), and part to not knowing the state of phosphorylation of their expressed myosin (dephosphorylation would slow values 2-fold), it is unclear why their values are considerably lower than reported here.

In mammalian Myo1b, ADP release has been shown to involve the N-terminal extension of the motor that docks at the motor domain/lever arm interface in the Rigor state but is free of interaction in the strong ADP state<sup>27,34</sup>. The position of the N-terminal extension and the location of the bonds that favor the Rigor-like state differ greatly between PfMyoA and Myo1b (Supplementary Fig. 10), although in both cases, the presence of the N-terminal extension increases ADP release by forming precise bonds stabilizing the Rigor state. No phosphorylation has been reported for the Myo1b N-terminal extension which contains two serine residues (Ser8, Ser9), so it is unknown whether the tuning of ADP release found by phosphorylation of PfMyoA might be recapitulated in other members of the myosin superfamily such as Myo1b. If phosphorylation on either of these Myo1b serines occurs, it would greatly perturb and likely prevent the docking of the N-terminal extension required for stabilizing the Rigor state. Thus, while both N-terminal extensions contribute to stabilizing the Rigor state, the nature of how this is done differs greatly between these myosins. The PfMyoA N-term extension, in contrast to that of Myo1b, is integral to the motor domain and directly influences the connectors that drive the lever arm swing in addition to the position of the converter. Depending on its phosphorylation state, the PfMyoA N-term extension stabilizes the Rigor state in a unique and tunable way to control the motor duty ratio.

The mechanism presented here provides new insights into how PfMyoA may modulate its motor properties and adapt for optimized *Plasmodium* parasite function across the lifecycle. Liver-stage sporozoites can move at speeds of  $>2 \mu\text{m.s}^{-1}$  across substrates or within extra-cellular space. This high speed is one of the fastest characterized for any eukaryotic cell. In contrast, blood stages merozoites, which are relatively immotile away from host cells, require the development of force (~40 pN) by the glideosome against the erythrocytes specifically for invasion<sup>4</sup>. Because it is now clear that PfMyoA is required for both motility and

invasion processes, Ser19 phosphorylation could provide a mechanism to optimize motor properties (speed vs. force) depending on parasite life-cycle stage (Fig. 6). From proteomic studies there is evidence of S19 phosphorylation in schizonts, merozoites<sup>32</sup> and salivary gland sporozoites<sup>35</sup> but further study with invasion-ready parasites will be required to show the extent of S19 phosphorylation in each stage. Motility studies with liver-stage sporozoites would be required to definitively test this hypothesis and how it relates to the subtleties of motor tuning.

All the Apicomplexan parasites differ in their life-cycle, as well as in the host organisms that they target. The function of myosin A amongst these organisms may differ too, as suggested by the differences found for the role and essentiality of MyoA in the genus *Plasmodium* vs. *Toxoplasma*. In *T. gondii*, TgMyoA is essential for egress<sup>6,7</sup> but not for host cell invasion<sup>8,9</sup>. Here, we demonstrate that PfMyoA is critical for erythrocytic invasion in *P. falciparum*, but the parasite is still able to egress in the absence of GAP45, the protein anchoring PfMyoA to the inner membrane complex<sup>13</sup>. This example shows likely key differences in the cellular basis of host cell entry and exit across Apicomplexan parasites, highlighting that caution should be used when extrapolating conclusions from one genus to another.

These results also raise the question about the conservation of the atypical and tunable mechanism of PfMyoA in other apicomplexan parasites. All the sequence adaptations described here are present in the recently solved PPS structural state of TgMyoA<sup>20</sup>: the G-to-S substitution at the SH2-SH1 fulcrum; the sequence adaptation to maintain the interaction between the Relay and the SH1-helix; the substitution of the aromatic residue of the Wedge by a threonine. In the TgMyoA converter there is a lysine (K766) equivalent to K764 in PfMyoA. Moreover, the TgMyoA N-term extension contains three serines that can be phosphorylated: S20, S21 that is equivalent to S19 in PfMyoA, and S29. An additional serine can be phosphorylated (S743) in the converter. Phosphomimetic mutants showed that the number of charged residues in the N-terminus modulates the speed at which TgMyoA moved actin filaments<sup>20</sup>, although we showed here that a phosphomimic does not recapitulate the full effect of a phosphorylated Ser. While the N-term extension was not defined in the electron density of the TgMyoA X-ray structure, the sequence conservation is sufficient to assume that it may form a helix and a turn, as found in our PfMyoA structures (Supplementary Fig. 3d, e). The basis of the tunable mechanism described here for PfMyoA is thus likely conserved in TgMyoA, although possibly more complex because it involves two additional phosphorylation sites in the N-term extension and one additional site in the converter. These differences in the possible tuning of PfMyoA and TgMyoA activity may result from variations of the requirement for the glideosome motor during the different life-cycles of the two parasites. Indeed, across its human host, *Plasmodium falciparum* alternates between the highly motile sporozoite and the invasive but relatively immobile merozoite. In contrast, the free stage of *Toxoplasma gondii* is the tachyzoite with a speed of  $5 \mu\text{m.s}^{-1}$ , similar to the maximum in vitro motility speed for TgMyoA when this myosin had three N-terminal phospho-mimic Asp residues<sup>20</sup>. Tachyzoites, however, can either undergo dissemination, invasion or egress. Thus, controlling the phosphorylation status of TgMyoA in tachyzoites could in principle modulate the speed and/or force developed by TgMyoA and thus adapt its motor properties depending on the need for either the dissemination, invasion or egress phases of the parasite. It may be possible to test this hypothesis with future studies on TgMyoA, permitting a direct comparison to the PfMyoA tuning mechanism revealed here.

Finally, we show here definitively for the first time that PfMyoA is critical for erythrocytic invasion. Myosin A is thus not only

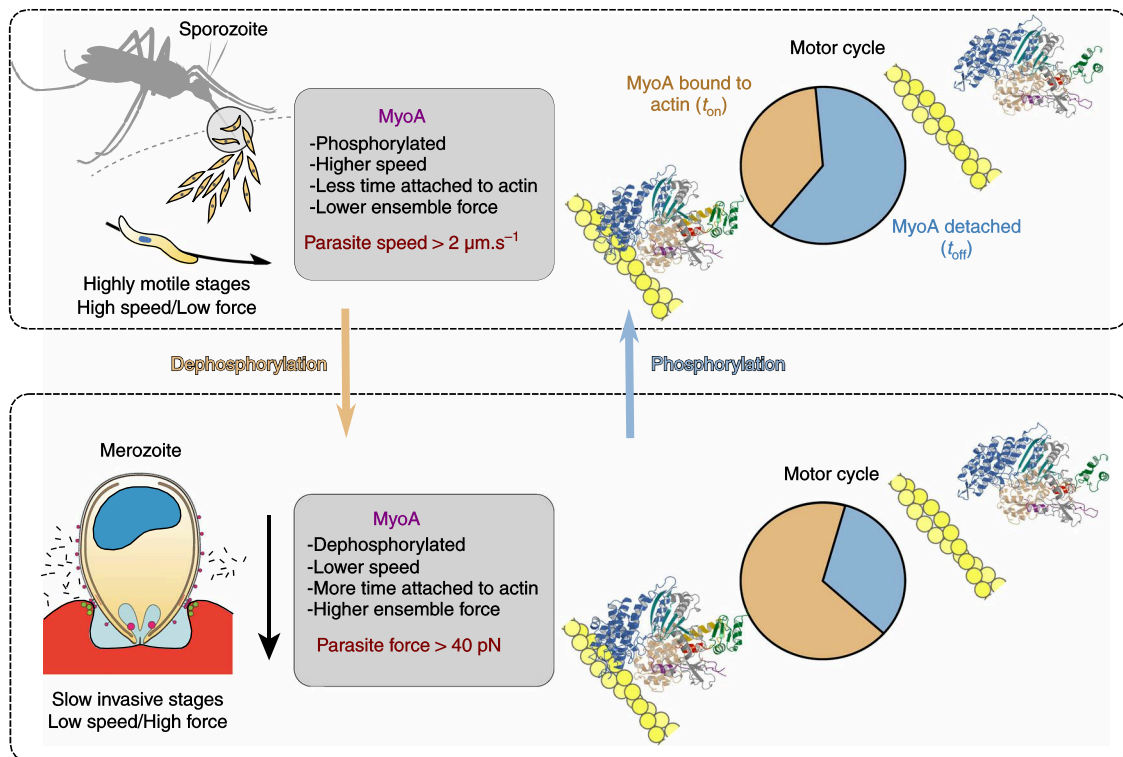


**Fig. 6** Phosphorylation of PfMyoA tunes its motor properties. Scheme representing how phosphorylation tunes PfMyoA motor properties and how this could optimize the motor for parasite motility or invasion at different stages of the parasite. In highly motile stages, sporozoites move at a speed higher than 2 μm/s. At this stage, phosphorylation of PfMyoA would allow the parasite to move actin at maximal speed but with low ensemble force. In merozoites, which lack continuous motility, but are instead adapted for erythrocyte invasion, dephosphorylation of PfMyoA localized at the invasion junction would result in active motors efficient in invasion. This merozoite PfMyoA motor would spend more of its total cycle time strongly bound to actin, thereby resulting in greater ensemble force output. The apparent duty ratio in the two phosphorylation states was estimated from the rate of ADP release divided by the total ATPase cycle time. The S19A, K764E and ΔN mutants would likely impair speed but not invasion, because their ensemble force is higher than phosphorylated, wild-type PfMyoA. Phosphorylation of the N-term extension of PfMyoA can thus act as a switch to tune motor activity depending on the needs of the parasite (high speed and low force for gliding, or higher force for the low speed invasion process)

required for motility in general in the *Plasmodium* genus but also for establishing blood stage infection during the symptomatic stages. The levels of reinvasion are commensurate with a complete block in invasion, as shown by comparison with CytoD and heparin. Nevertheless, there may be some residual invasion due to parasites with non-excised *pfmyoA* locus and there is a possibility of invasion by RBC membrane wrapping interactions alone<sup>11</sup>. However, the size of this residual population appears much smaller than found in *T. gondii* tachyzoites lacking TgMyoA<sup>9</sup> and would argue against redundancy in motor function like that seen in *Toxoplasma*.

In recent years, several small molecules targeting myosins have been developed as promising treatments for diverse pathologies such as cardiac diseases and asthma<sup>36–39</sup>. Amongst these modulators, CK-571 is able to selectively block smooth muscle myosin by trapping an intermediate of the recovery stroke<sup>38</sup>. The design of molecules able to block PfMyoA activity based on similar principles, such as that found for CK-571, would be a highly specific and efficient way to treat malaria. A ~1000-fold difference in IC<sub>50</sub> allows CK-571 to be tuned for inhibition of smooth muscle myosin compared with cardiac or skeletal muscle myosins, despite the fact that the allosteric drug binding pocket corresponds to conserved residues in sequence among these Myo2 motors. The divergence of PfMyoA in terms of sequence and mechanism would ensure an even higher selectivity for inhibitors of the recovery stroke. The atypical mechanism of PfMyoA described here and the structural blueprints provided should therefore enable the specific design of inhibitors that could stall the progression of malarial infection.

## Methods

**Expression constructs.** Full-length PfMyoA heavy chain (PlasmoDB ID PF3D7\_1342600/ GenBank accession number XM\_001350111.1), with Sf9 cell preferred codons, was cloned into the baculovirus transfer vector pFastbac (pFB). A 13 amino acid linker separates the C-terminus of the PfMyoA heavy chain from an 88 amino acid segment of the *Escherichia coli* biotin carboxyl carrier protein<sup>40</sup>, which gets biotinylated during expression in Sf9 cells, followed by a C-terminal FLAG tag for purification via affinity chromatography. The S19A or K764E mutated versions were generated using site directed mutagenesis. The ΔN version of full length PfMyoA heavy chain was made by removing residues Ala2 through Ser19. All PCR products were cloned into the baculovirus transfer vector pAcSG2 (BD Biosciences) to make recombinant virus for the Sf9 expression system. The mouse utrophin (NP\_035812) clone was a gift from Kathleen Ruppel and James Spudich. It was modified so that utrophin residues 1-H416 were followed by C-terminal biotin and FLAG tags. It was cloned into pFastbac for production of recombinant baculovirus and subsequent expression in Sf9 cells.

**Protein expression and purification.** The full-length PfMyoA heavy chain or mutant constructs (S19A, K764E, ΔN) were co-expressed with the chaperone PUNC and the light chains (PfMTIP and PfELC) in Sf9 cells as described in ref. <sup>19</sup>. The cells were grown for 72 h in medium containing 0.2 mg/ml biotin, harvested and lysed by sonication in 10 mM imidazole, pH 7.4, 0.2 M NaCl, 1 mM EGTA, 5 mM MgCl<sub>2</sub>, 7% (w/v) sucrose, 2 mM DTT, 0.5 mM 4-(2-aminoethyl)benzenesulfonyl fluoride, 5 μg/ml leupeptin, 2 mM MgATP. An additional 2 mM MgATP was added prior to a clarifying spin at 200,000×g for 40 min. The supernatant was purified using FLAG-affinity chromatography (Sigma). The column was washed with 10 mM imidazole pH 7.4, 0.2 M NaCl, and 1 mM EGTA and the myosin eluted from the column using the same buffer plus 0.1 mg/ml FLAG peptide. The fractions containing myosin were pooled and concentrated using an Amicon centrifugal filter device (Millipore), and dialyzed overnight against 10 mM imidazole, pH 7.4, 0.2 M NaCl, 1 mM EGTA, 55% (v/v) glycerol, 1 mM DTT, and 1 μg/ml leupeptin and stored at -20 °C. Utrophin purification was essentially the same as for myosin but without the MgATP steps. Skeletal muscle actin was purified from chicken skeletal muscle tissue essentially as described in<sup>41</sup>.



His-tagged PfMTIP and PfELC were bacterially expressed using BLR(DE3)-competent cells and the isopropyl  $\beta$ -D-thiogalactopyranoside induction system<sup>40</sup>. Pellets were lysed by sonication in 10 mM sodium phosphate, pH 7.4, 0.3 M NaCl, 0.5% (v/v) glycerol, 7% (w/v) sucrose, 7 mM  $\beta$ -mercaptoethanol, 0.5 mM 4-(2-aminoethyl)benzenesulfonfyl fluoride, and 5  $\mu$ g/ml leupeptin. The cell lysate was clarified at 26,000 $\times$ g for 30 min. The supernatant was boiled for 10 min in a double boiler, clarified at 26,000 $\times$ g for 30 min, and the supernatant loaded on a His-select nickel-affinity column (Sigma). The resin was washed in 10 mM sodium phosphate, pH 7.4, 0.3 M NaCl before being eluted in the same buffer containing 200 mM imidazole. The protein was concentrated and dialyzed overnight against 10 mM imidazole, pH 7.4, 150 mM NaCl, 1 mM EGTA, 1 mM MgCl<sub>2</sub>, 55% (v/v) glycerol, 1 mM DTT and stored at  $-20^{\circ}\text{C}$ .

**Crystallization and data processing.** Crystals of PfMyoA motor domain in Post-rigor and Rigor-like states (type 1 crystals) (10 mg.ml<sup>-1</sup>) were obtained at 4  $^{\circ}\text{C}$  by the hanging drop vapor diffusion method from a 1:1 mixture of protein with 2 mM EGTA and precipitant containing 18% PEG 3350; 100 mM glycine pH 8.6. Crystals of PfMyoA motor domain in Pre-powerstroke state (type 2 crystals) were obtained at 17  $^{\circ}\text{C}$  by the hanging drop vapor diffusion method from a 1:1 mixture of protein (21 mg.ml<sup>-1</sup>) with 2 mM MgADP.VO<sub>4</sub> and precipitant containing 0.6 M K-Phosphate dibasic and 0.7 M Na-Phosphate monobasic. Crystals were transferred in the mother liquor containing 30% glycerol before flash freezing in liquid nitrogen. X-ray diffraction data were collected at 100 K on the PX1 ( $\lambda = 0.906019$  Å) for type 1 crystals and on the PX2 ( $\lambda = 0.979384$  Å) for type 2 crystals, at the SOLEIL synchrotron. Diffraction data were processed using the XDS package<sup>42</sup> and AutoProc<sup>43</sup>. Data obtained from the crystal type 2 were anisotropic, processing has been performed with StarAniso<sup>44</sup>. The crystals type 1 belong to the P2<sub>1</sub> space group with four molecules per asymmetric unit. The type 2 crystals belong to the P6<sub>2</sub>22 space group with one molecule per asymmetric unit. The cell parameters and data collection statistics for these crystals are reported in Supplementary Tables 1 and 2, respectively.

**Structure determination and refinement.** Molecular replacement in type 1 crystals was performed with the motor domain (residues 66–688) of scallop myosin 2 in Post-rigor state (PDB code 1B7T) and in Rigor-like state (PDB code 2O58) without water and ligand with Phaser<sup>45</sup> from the CCP4i program suite. Manual model building was achieved using Coot<sup>46</sup>. Refinement was performed with Buster<sup>47</sup>. The statistics for most favored, allowed and outlier Ramachandran angles are 95.63, 3.97, and 0.4%, respectively. Structure determination indicated that this crystal form corresponds to three molecules in the Post-rigor state (chains A, B, C) and one molecule in the Rigor-like state (chain D). The final model has been deposited on the PDB (PDB code 6I7D). The procedure for structure determination and refinement for crystals type 2 was identical, using one molecule of PfMyoA in Post-rigor state without the converter (residues 2–704) and without water and ligand as search model for molecular replacement. The statistics for most favored, allowed and outlier Ramachandran angles are 82.49, 13.40, and 4.11%, respectively. Structure determination indicated that this crystal form corresponds to the Pre-powerstroke state. The final model has been deposited on the PDB (PDB code 6I7E).

**Molecular dynamics simulations.** The procedure used for molecular dynamics simulation is similar to what was described in<sup>48</sup>. Inputs were prepared with the CHARMM-GUI<sup>49</sup> with the Quick MD Simulator module<sup>50</sup>. The CHARMM36 force field<sup>51</sup> was used to describe the full systems in a box with explicit water (TIP3P model) and salt (KCl reaching 150 mM). The protocol provided in the Quick MD output was followed. Gromacs<sup>52</sup> (VERSION 5.0-rc1) was used to execute the 60 ns simulations. Each molecular dynamics simulation was analyzed with the Gromacs tools.

**Motor cycle reconstitution and visualization.** In this study, we reconstitute the motor cycle based on three structural states: Post-rigor (PR), Pre-powerstroke (PPS) and Rigor-like. To visualize structural changes during the powerstroke, we used a comparison between the PPS and the Rigor-like states. We have made some animations (Supplementary Movies 1–4) to compare the conformation of the different connectors in the PPS and in the Rigor-like in conventional myosins (ScMyo2) and in the atypical PfMyoA. Morphs were not used to illustrate the transition between the PPS and the Rigor-like states since the isomerization occurs through intermediate states<sup>53</sup> which are not known for these myosins, this kind of procedure would thus be misleading.

In order to visualize the powerstroke of a conventional class II myosin, we have used scallop myosin II (ScMyo2). The structures of the Pre-powerstroke (PPS) and of the Rigor-like states of ScMyo2 have been solved in different organisms: PPS of bay scallop (*Argopecten irradians*) ScMyo2 (PDB code 1QVI, resolution 2.54 Å) and Rigor-like state of Atlantic deep-sea scallop (*Placopecten magellanicus*) ScMyo2 (PDB code 2O58, resolution 3.27 Å). The sequence of ScMyo2 heavy chain in these two species is highly conserved for the motor domain (92% identity, 95% similarity) and the two structures can thus be used to reconstitute the powerstroke of ScMyo2.

**Unloaded and loaded in vitro motility measurements.** Before the assay, myosin heads that cannot release from actin upon binding MgATP were removed by a 20 min spin at 350,000 $\times$ g in the presence of 1.5 mM MgATP and a three-fold excess of skeletal actin. Myosin and utrophin (when applicable) concentrations were determined using the Bio-Rad Protein assay. The following solutions were added to a nitrocellulose-coated flow cell in 15  $\mu$ l volumes. 0.5 mg/ml biotinylated bovine serum albumin (BSA) in buffer A (150 mM KCl, 25 mM imidazole pH 7.5, 1 mM EGTA, 4 mM MgCl<sub>2</sub>, and 10 mM DTT) was added and incubated for 1 min. Three additions of 0.7 mg/ml BSA in buffer A and a 2 min wait prevent subsequent nonspecific binding of either the myosin or utrophin. 25  $\mu$ g/ml neutravidin (Thermo Fischer Scientific) in buffer A was added for 1 min and then rinsed three times with buffer A. 120  $\mu$ g/ml PfMyoA (and utrophin, when performing a loaded in vitro motility assay) was flowed into the cell and rinsed 3 times with buffer A after a 1 min wait. All myosin and utrophin constructs contained a C-terminal biotin tag for specific attachment to the neutravidin coated flow cell. Rhodamine-phalloidin labeled skeletal muscle actin was incubated for 30 s followed by one rinse with buffer A and one rinse with buffer B. Buffer B is buffer A plus 0.5% (w/v) methylcellulose, 25  $\mu$ g/ml PfELC and 25  $\mu$ g/ml PfMTIP and oxygen scavengers (50  $\mu$ g/ml catalase (Sigma), 125  $\mu$ g/ml glucose oxidase (Sigma), and 3 mg/ml glucose). Motility was initiated by adding buffer B containing 2 mM MgATP twice to the flow cell, and waiting 1 min for temperature equilibration (30  $^{\circ}\text{C}$ ) on the microscope.

Actin filaments were visualized using an inverted microscope (Zeiss Axiovert 10) equipped with epifluorescence, a Rolera MGI Plus digital camera, and a dedicated computer with the Nikon NIS Elements software package. Filaments were automatically tracked and analyzed, both under unloaded and loaded conditions, with the Fast Automated Spud Trekker analysis program (FAST, Spudich laboratory, Stanford University). This online software is available free for download (<http://spudlab.stanford.edu/fast-for-automatic-motility-measurements/>).

Speeds for all unloaded motility experiments were fit to a Gaussian curve. All loaded motility data sets were fitted to the equation:

$$\text{Time mobile} = \frac{K_s M_0}{K_s + M_0 [\text{utrophin}]}$$

Where  $M_0$  is percent mobile filaments in unloaded conditions,  $K_s$  is a pseudo actin-utrophin dissociation constant (in nM), that is sensitive to myosin ensemble force, and % time mobile is the total duration of filaments in the mobile state divided by the total duration of the combined stuck and mobile states (see ref. <sup>31</sup> for a detailed explanation).

**Actin-activated ATPase activity.** The actin-activated ATPase activity of all PfMyoA constructs was determined at 30  $^{\circ}\text{C}$  in 10 mM imidazole pH 7.5, 5 mM KCl, 1 mM MgCl<sub>2</sub>, 1 mM EGTA, 1 mM DTT, and 1 mM NaN<sub>3</sub> as a function of skeletal actin concentration. The salt concentration was kept low (5 mM) to minimize  $K_m$  values and reach  $V_{\text{max}}$  with actin concentrations that are compatible with this assay. Actin-activated ATPase activity was determined using a linked assay, which couples the regeneration of hydrolyzed ATP to the oxidation of NADH to NAD<sup>+</sup>. Pyruvate kinase (Sigma), in the presence of phosphoenolpyruvate (Sigma) and low ADP concentrations, regenerates ATP. In a subsequent reaction, pyruvate is converted to lactate by L-lactate dehydrogenase (Sigma) which oxidizes NADH (Sigma) to NAD<sup>+</sup>. The decrease in optical density at 340 nm as a function of time was measured on a Lambda 25 UV/VIS spectrophotometer (Perkin Elmer), with a 300 s data monitoring window sampled every 2 s. Data were fit to the Michaelis–Menten equation.

**Transient kinetics.** All kinetic experiments were performed in 10 mM 4-(2-hydroxyethyl)-1-piperazineethanesulfonic acid, pH 7.5, 50 mM KCl, 4 mM MgCl<sub>2</sub>, 1 mM EGTA, and 1 mM DTT at 30  $^{\circ}\text{C}$  using a KinTek stopped-flow apparatus (KinTek Corporation, model SF-2001). All concentrations stated are those after mixing in the stopped-flow cell. Light scattering at 295 nm was used to monitor the dissociation of the actomyosin.ADP complex (skeletal actin) by 2 mM MgATP. Light scattering of unlabeled acto-PfMyoA was observed with an incident beam of 295 nm and detected orthogonal to the incident beam with a 295 nm interference filter. All traces were analyzed using the software provided by KinTek and fit to single exponential fits. Typically, multiple (3–10) time courses were averaged before fitting to an exponential.

**Mass spectrometry.** The phosphorylation status of expressed PfMyoA was determined by liquid chromatography tandem mass spectrometry (LCMS/MS). Aliquots of PfMyoA heavy chain (104 kDa) and PfMyoA heavy chain treated with dephosphorylation with calf intestinal phosphatase (CIP; New England Biolabs, M0290S) were separated by SDS-PAGE, stained with Coomassie and excised from the gel. The bands were destained with 50% acetonitrile (ACN), dehydrated with 100% ACN and dried in a speed vacuum device. The bands were destained, reduced, alkylated and digested with 2  $\mu$ g of trypsin (Promega) as described<sup>19</sup>. The resultant peptides were dried in a speed vacuum device and then reconstituted in 0.05% trifluoroacetic acid. The peptides were separated on an Acquity UPLC HSS T3 column (100 Å, 1.8  $\mu$ m, 1 mm  $\times$  150 mm) (Waters) attached to a Dionex Ulti-Mate 3000 high pressure liquid chromatography system (HPLC) (Dionex). The

HPLC effluent was directly injected into a Q Exactive Hybrid Quadrupole-Orbitrap mass spectrometer through an electrospray ionization source (ThermoFisher). Data were collected in data-dependent MS/MS mode with the top 5 most abundant ions being selected for fragmentation.

Peptides were identified from the resultant MS/MS spectra using SEQUEST run via Proteome Discoverer 2.2 software (ThermoFisher). These searches were performed against a custom database that reflected the cloned gene (PfMyoA heavy chain) plus tags. Peptide oxidation was accounted for by addition of 15.99 and 31.99 Da to each methionine, carbamidomethylation was accounted for by addition of 57.02 Da to each cysteine, and phosphorylation was accounted for by adding 79.97 Da to each serine, threonine or tyrosine residue. All identifications were manually confirmed by inspection of the MS/MS fragmentation spectra. LC peak areas were quantified for each peptide using Proteome Discoverer 2.2. The LC peak areas were normalized using the median abundance of the top 5 most abundant PfMyoA peptides. The degree of phosphorylation was estimated from abundance of non-phosphorylated VSNVEAFDK peptide (containing serine 19) in the untreated PfMyoA samples relative to that in the samples dephosphorylated with CIP using a mass-balance approach<sup>54</sup>.

**DNA manipulation.** For generation of Myo-LP constructs, synthetic gene fragments were ordered (GENEWIZ or Thermo Scientific) comprising the re-codon optimized myosin sequence, *loxPint* module, tags and T2A skip peptide with 30 bp Gibson flanks. These were assembled with a ~700 bp long homology region (amplified from 3D7 genomic DNA) by Gibson assembly. The parent vector (pARL-FIKK10.1) was a gift of Dr Moritz Treeck (Crick Institute). Plasmids were purified from *E. coli* cultures using QIAGEN Plasmid Maxi kit.

**P. falciparum culture and transfection.** Strain B11<sup>13</sup>, which constitutively expresses inducible DiCre, was cultured in RPMI 1640 (Life Technologies) under standard conditions<sup>55</sup> at 4% hematocrit and synchronized with 5% sorbitol (Sigma)<sup>56</sup>. Parasites were grown to 5% at ring stage and electroporated with 100 µg of plasmid in 15 µL of sterile TE buffer added to 385 µL sterile Cytomix<sup>57</sup>. Plasmid uptake was selected for by adding fresh media with 3 nM WR9210 daily for 7 days, then every 2–3 days until parasite population re-established. Transfectants were grown to 2–4% parasitaemia and integration was selected for with 400 µg/mL G418<sup>21</sup>. Fresh media with G418 was added for 10 days before parasites were returned to drug-free media. MyoA-cKO parasites were cloned by limiting dilution.

**Genotyping, western blotting, and immunofluorescence assays.** DNA was extracted using the PureLink Genomic DNA Mini kit (Invitrogen) for genotyping. Schizonts at ~5% parasitaemia were lysed using 0.1% saponin/PBS (Sigma) and prepared for Western Blotting by standard methods. The presence of FLAG (F1804, Sigma) or GFP (Roche) was probed using primary antibody at 1:1000 dilution with the appropriate HRP-coupled secondary antibody added at 1:3000 dilution. Detection was performed with ECL (Amersham).

Schizonts at 5% parasitaemia or higher were treated with cysteine protease inhibitor E64 (10 µM) for 4–6 h to prevent egress, then fixed with 4% PFA/0.025% glutaraldehyde/PBS for 1 h, permeabilised with 0.1% Triton X-100/PBS for 10 min and blocked overnight at 4 °C in 3% BSA/PBS. Fixed cells were incubated with αFLAG (F1804, Sigma), αGAP45<sup>58</sup> and αGFP antibodies (Roche) at 1:500 dilution in 3% BSA/PBS for 2 h, then washed three times in PBS. Secondary antibodies were added at 1:1000 dilution in 3% BSA/PBS and incubated for 1 h, then cells were washed three times in PBS. The cells were resuspended to a hematocrit of 10% and mounted with DAPI-VECTASHIELD (Vectorlabs). Images were acquired with an OrcaFlash4.0 CMOS camera using a Nikon Ti Microscope (Nikon Plan Apo 100 × 1.4-N.A. oil immersion objective). Z-stacks were acquired with a step size of 0.2 µm and images were deconvoluted using the EpiDEMIC plugin with 50 iterations in Icy<sup>59</sup>. Subsequent image manipulations were carried out in ImageJ<sup>60–62</sup>.

**Conditional myosin knockout and quantification.** 30 ml of synchronous, late stage parasites at 5% parasitaemia were purified by density gradient centrifugation with 70% Percoll supplemented with sorbitol<sup>63</sup>. The purified schizonts were incubated with fresh RBCs at 1% hematocrit for 2–3 h, shaking at 100 rpm. Once new rings reached >10% parasitaemia the remaining schizonts were lysed by sorbitol treatment and rings were split equally into two 10 ml dishes at 2–4% parasitaemia, 4% hematocrit and incubated for 16 h with 0.05% DMSO or rapamycin (100 nM, Sigma), as well as heparin to prevent any further invasion (Pfizer, 1:25 dilution). Cultures were washed twice in complete media to remove heparin and DMSO/RAP, then transferred to 96 well plates in triplicate at 2% parasitaemia, 0.15% hematocrit for quantification, with invasion inhibitors heparin (1:25) or CytoD (500 nM) added to control samples. Parasites were allowed to proceed to the following cycle, and at 16–24 h post invasion were stained with SYBR Green I (Sigma) at 1:5000 dilution for 15 min. After three washes in PBS the parasites were analyzed by flow cytometry. Gates were set for RBCs, single cells and SYBR Green-positive cells (Supplementary Fig. 11).

**Reporting summary.** Further information on research design is available in the Nature Research Reporting Summary linked to this article.

## Data availability

All data are available from the corresponding author upon reasonable request. The crystallographic structures can be found on the Protein Data Bank (PDB codes 6I7D and 6I7E). The source data underlying Figs. 1e, 5b–e and Supplementary Fig 7 are provided as a Source Data file.

Received: 22 November 2018 Accepted: 11 June 2019

Published online: 23 July 2019

## References

- WHO. World Malaria Report 2017. World Health Organization [https://doi.org/10.1016/S0264-410X\(07\)01183-8](https://doi.org/10.1016/S0264-410X(07)01183-8) (2017).
- Frenal, K., Dubremetz, J.-F., Lebrun, M. & Soldati-Favre, D. Gliding motility powers invasion and egress in Apicomplexa. *Nat. Rev. Microbiol.* **15**, 645–660 (2017).
- Imwong, M. et al. The spread of artemisinin-resistant *Plasmodium falciparum* in the Greater Mekong subregion: a molecular epidemiology observational study. *Lancet Infect. Dis.* **17**, 491–497 (2017).
- Crick, A. J. et al. Quantitation of malaria parasite-erythrocyte cell-cell interactions using optical tweezers. *Biophys. J.* **107**, 846–853 (2014).
- Münter, S. et al. *Plasmodium* sporozoite motility is modulated by the turnover of discrete adhesion sites. *Cell Host Microbe* **6**, 551–562 (2009).
- Meissner, M., Schluter, D. & Soldati, D. Role of *Toxoplasma gondii* myosin A in powering parasite gliding and host cell invasion. *Science* **298**, 837–840 (2002).
- Andenmatten, N. et al. Conditional genome engineering in *Toxoplasma gondii* uncovers alternative invasion mechanisms. *Nat. Methods* **10**, 125–127 (2013).
- Frenal, K., Marq, J.-B., Jacot, D., Polonais, V. & Soldati-Favre, D. Plasticity between MyoC- and MyoA-glideosomes: an example of functional compensation in *Toxoplasma gondii* invasion. *PLoS Pathog.* **10**, e1004504 (2014).
- Egarter, S. et al. The *toxoplasma* Acto-MyoA motor complex is important but not essential for gliding motility and host cell invasion. *PLoS ONE* **9**, e91819 (2014).
- Bichet, M. et al. Genetic impairment of parasite myosin motors uncovers the contribution of host cell membrane dynamics to *Toxoplasma* invasion forces. *BMC Biol.* **14**, 97 (2016).
- Dasgupta, S. et al. Membrane-wrapping contributions to malaria parasite invasion of the human erythrocyte. *Biophys. J.* **107**, 43–54 (2014).
- Siden-Kiamos, I. et al. Stage-specific depletion of myosin A supports an essential role in motility of malarial ookinets. *Cell. Microbiol.* **13**, 1996–2006 (2011).
- Perrin, A. J. et al. The actinomyosin motor drives malaria parasite red blood cell invasion but not egress. *MBio* **9**, e00905–18 (2018).
- Vahokoski, J. et al. Structural differences explain diverse functions of *Plasmodium* actins. *PLoS Pathog.* **10**, e1004091 (2014).
- Pospich, S. & Raunser, S. Single particle cryo-EM—an optimal tool to study cytoskeletal proteins. *Curr. Opin. Struct. Biol.* **52**, 16–24 (2018).
- Kinose, F., Wang, S. X., Kidambi, U. S., Moncman, C. L. & Winkelmann, D. A. Glycine 699 is pivotal for the motor activity of skeletal muscle myosin. *J. Cell Biol.* **134**, 895–909 (1996).
- Kad, N. M., Patlak, J. B., Fagnant, P. M., Trybus, K. M. & Warshaw, D. M. Mutation of a conserved glycine in the SH1-SH2 helix affects the load-dependent kinetics of myosin. *Biophys. J.* **92**, 1623–1631 (2007).
- Preller, M. et al. Structural basis for the allosteric interference of myosin function by reactive thiol region mutations G680A and G680V. *J. Biol. Chem.* **286**, 35051–35060 (2011).
- Bookwalter, C. S. et al. Reconstitution of the core of the malaria parasite glideosome with recombinant *Plasmodium* class XIV myosin A and *Plasmodium* actin. *J. Biol. Chem.* **292**, 19290–19303 (2017).
- Powell, C. J. et al. Structural and mechanistic insights into the function of the unconventional class XIV myosin MyoA from *Toxoplasma gondii*. *Proc. Natl Acad. Sci. USA* **115**, E10548–E10555 (2018).
- Birnbaum, J. et al. A genetic system to study *Plasmodium falciparum* protein function. *Nat. Methods* **14**, 450–456 (2017).
- Jones, M. L. et al. A versatile strategy for rapid conditional genome engineering using loxP sites in a small synthetic intron in *Plasmodium falciparum*. *Sci. Rep.* **6**, 21800 (2016).
- Zuccala, E. S. et al. Quantitative phospho-proteomics reveals the *Plasmodium* merozoite triggers pre-invasion host kinase modification of the red cell cytoskeleton. *Sci. Rep.* **6**, 19766 (2016).
- Coureur, P.-D. et al. A structural state of the myosin V motor without bound nucleotide. *Nature* **425**, 419–423 (2003).
- von der Ecken, J., Heissler, S. M., Pathan-Chhatbar, S., Manstein, D. J. & Raunser, S. Cryo-EM structure of a human cytoplasmic actomyosin complex at near-atomic resolution. *Nature* **534**, 724–728 (2016).



26. Coureux, P.-D., Sweeney, H. L. & Houdusse, A. Three myosin V structures delineate essential features of chemo-mechanical transduction. *EMBO J.* **23**, 4527–4537 (2004).
27. Montes, A. et al. High-resolution cryo-EM structures of actin-bound myosin states reveal the mechanism of myosin force sensing. *Proc. Natl Acad. Sci.* **115**, 1292–1297 (2018).
28. Sweeney, H. L. & Houdusse, A. Structural and functional insights into the Myosin motor mechanism. *Annu. Rev. Biophys.* **39**, 539–557 (2010).
29. Koppole, S., Smith, J. C. & Fischer, S. The structural coupling between ATPase activation and recovery stroke in the myosin II motor. *Structure* **15**, 825–837 (2007).
30. De La Cruz, E. M. & Ostap, E. M. Relating biochemistry and function in the myosin superfamily. *Curr. Opin. Cell Biol.* **16**, 61–67 (2004).
31. Aksel, T., Choe Yu, E., Sutton, S., Ruppel, K. M. & Spudich, J. A. Ensemble force changes that result from human cardiac myosin mutations and a small-molecule effector. *Cell Rep.* **11**, 910–920 (2015).
32. Lasonder, E., Green, J., Grainger, M., Langsley, G. & Holder, A. A. Extensive differential protein phosphorylation as intraerythrocytic *Plasmodium falciparum* schizonts develop into extracellular invasive merozoites. *Proteomics* **15**, 2716–2729 (2015).
33. Green, J. L. et al. Compositional and expression analyses of the glideosome during the *Plasmodium* life cycle reveal an additional myosin light chain required for maximum motility. *J. Biol. Chem.* <https://doi.org/10.1074/jbc.M117.802769> (2017).
34. Greenberg, M. J., Lin, T., Shuman, H. & Ostap, E. M. Mechanochemical tuning of myosin-I by the N-terminal region. *Proc. Natl Acad. Sci. USA* **112**, E3337–E3344 (2015).
35. Swearingen, K. E. et al. Proteogenomic analysis of the total and surface-exposed proteomes of *Plasmodium vivax* salivary gland sporozoites. *PLoS Negl. Trop. Dis.* **11**, e0005791 (2017).
36. Malik, F. I. et al. Cardiac myosin activation: a potential therapeutic approach for systolic heart failure. *Science* **331**, 1439–1443 (2011).
37. Green, E. M. et al. A small-molecule inhibitor of sarcomere contractility suppresses hypertrophic cardiomyopathy in mice. *Science* **351**, 617–621 (2016).
38. Sirigu, S. et al. Highly selective inhibition of myosin motors provides the basis of potential therapeutic application. *Proc. Natl Acad. Sci. USA* **113**, E7448–E7455 (2016).
39. Planelles-Herrero, V. J., Hartman, J. J., Robert-Paganin, J., Malik, F. I. & Houdusse, A. Mechanistic and structural basis for activation of cardiac myosin force production by omecamtiv mecarbil. *Nat. Commun.* **8**, 190 (2017).
40. Cronan, J. E. J. Biotinylation of proteins in vivo. A post-translational modification to label, purify, and study proteins. *J. Biol. Chem.* **265**, 10327–10333 (1990).
41. Pardee, J. D. & Spudich, J. A. Purification of muscle actin. *Methods Enzymol.* [https://doi.org/10.1016/0076-6879\(82\)85020-9](https://doi.org/10.1016/0076-6879(82)85020-9) (1982).
42. Kabsch, W. XDS. *Acta Crystallogr. Sect. D. Biol. Crystallogr.* **66**, 125–132 (2010).
43. Vonrhein, C. et al. Data processing and analysis with the autoPROC toolbox. *Acta Crystallogr. D. Biol. Crystallogr.* **67**, 293–302 (2011).
44. Tickle, I. et al. STARANISO. Global Phasing Ltd., Cambridge, United Kingdom (2016). <https://doi.org/10.1002/anie.201305315>
45. McCoy, A. J. et al. Phaser crystallographic software. *J. Appl. Crystallogr.* **40**, 658–674 (2007).
46. Emsley, P. & Cowtan, K. Coot: model-building tools for molecular graphics. *Acta Crystallogr. Sect. D. Biol. Crystallogr.* **60**, 2126–2132 (2004).
47. Bricogne, G. et al. BUSTER version 2.10.2. Cambridge, United Kingdom Glob. Phasing Ltd. (2017).
48. Robert-Paganin, J., Auguin, D. & Houdusse, A. Hypertrophic cardiomyopathy disease results from disparate impairments of cardiac myosin function and auto-inhibition. *Nat. Commun.* **9**, 4019 (2018).
49. Jo, S., Kim, T., Iyer, V. G. & Im, W. CHARMM-GUI: a web-based graphical user interface for CHARMM. *J. Comput. Chem.* **29**, 1859–1865 (2008).
50. Jo, S. et al. CHARMM-GUI 10 years for biomolecular modeling and simulation. *J. Comput. Chem.* **38**, 1114–1124 (2017).
51. Huang, J. & MacKerell, A. D. J. CHARMM36 all-atom additive protein force field: validation based on comparison to NMR data. *J. Comput. Chem.* **34**, 2135–2145 (2013).
52. Abraham, M. J. et al. Gromacs: high performance molecular simulations through multi-level parallelism from laptops to supercomputers. *SoftwareX* **1–2**, 19–25 (2015).
53. Houdusse, A. & Sweeney, H. L. How myosin generates force on actin filaments. *Trends Biochem. Sci.* **41**, 989–997 (2016).
54. Previs, M. J. et al. Quantification of protein phosphorylation by liquid chromatography-mass spectrometry. *Anal. Chem.* **80**, 5864–5872 (2008).
55. Trager, W. & Jensen, J. B. Human malaria parasites in continuous culture. *Science* **193**, 673–675 (1976).
56. Lambros, C. & Vanderberg, J. P. Synchronization of *Plasmodium falciparum* erythrocytic stages in culture. *J. Parasitol.* **65**, 418–420 (1979).
57. Adjalley, S. H., Lee, M. C. S. & Fidock, D. A. A method for rapid genetic integration into *Plasmodium falciparum* utilizing mycobacteriophage Bxb1 integrase. *Methods Mol. Biol.* **634**, 87–100 (2010).
58. de Chaumont, F. et al. Icy: an open bioimage informatics platform for extended reproducible research. *Nat. Methods* **9**, 690–696 (2012).
60. Schindelin, J., Rueden, C. T., Hiner, M. C. & Eliceiri, K. W. The ImageJ ecosystem: an open platform for biomedical image analysis. *Mol. Reprod. Dev.* **82**, 518–529 (2015).
61. Schindelin, J. et al. Fiji: an open-source platform for biological-image analysis. *Nat. Methods* **9**, 676–682 (2012).
62. Rueden, C. T. et al. ImageJ2: ImageJ for the next generation of scientific image data. *BMC Bioinforma.* **18**, 529 (2017).
63. Radfar, A. et al. Synchronous culture of *Plasmodium falciparum* at high parasitemia levels. *Nat. Protoc.* **4**, 1899–1915 (2009).

## Acknowledgements

We thank Margaret Titus for critical reading of the paper. We are grateful to beamline scientists of PX1 and PX2A (SOLEIL synchrotron) for excellent support during data collection. We thank Kathleen Ruppel and James Spudich (Stanford University) for the utrophin DNA. We thank Linda Makhlof for experimental support. This work was funded by National Institutes of Health grant AI 132378 (A.H. and K.M.T.), and HL 124041 (M.J.P.). Parasite work was funded through an Investigator Award (100993/Z/13/Z, J.B.) and PhD studentship (109007/Z/15/A, T.B.) from Wellcome and through a program grant from the Human Frontier Science Program (RGY0066/2016, A.H. and J.B.). We thank Dr. Stéphane Réty for his advice and help to process the dataset of PfMyoA PPS.

## Author contributions

J.R.P., J.P.R., J.B., K.M.T., and A.H. designed the research. J.R.P., G.J., and D.M. crystallized PfMyoA in the different states. J.R.P. solved the structures and performed refinement. D.A. performed molecular dynamics. J.P.R. and C.S.B. performed in vitro functional assays. E.B.K. expressed and purified protein for crystallization. M.J.P. performed mass spectrometry analysis. T.B. generated conditional PfMyoA knockout. J.R.P., J.P.R., J.B., K.M.T., and A.H. discussed the results and wrote the paper with the help of D.A. and D.M.

## Additional information

**Supplementary Information** accompanies this paper at <https://doi.org/10.1038/s41467-019-11120-0>.

**Competing interests:** The authors declare no competing interests.

**Reprints and permission** information is available online at <http://npg.nature.com/reprintsandpermissions/>

**Peer review information:** Nature Communications thanks Stefan Raunser and the other, anonymous, reviewer(s) for their contribution to the peer review of this work. Peer reviewer reports are available.

**Publisher's note:** Springer Nature remains neutral with regard to jurisdictional claims in published maps and institutional affiliations.

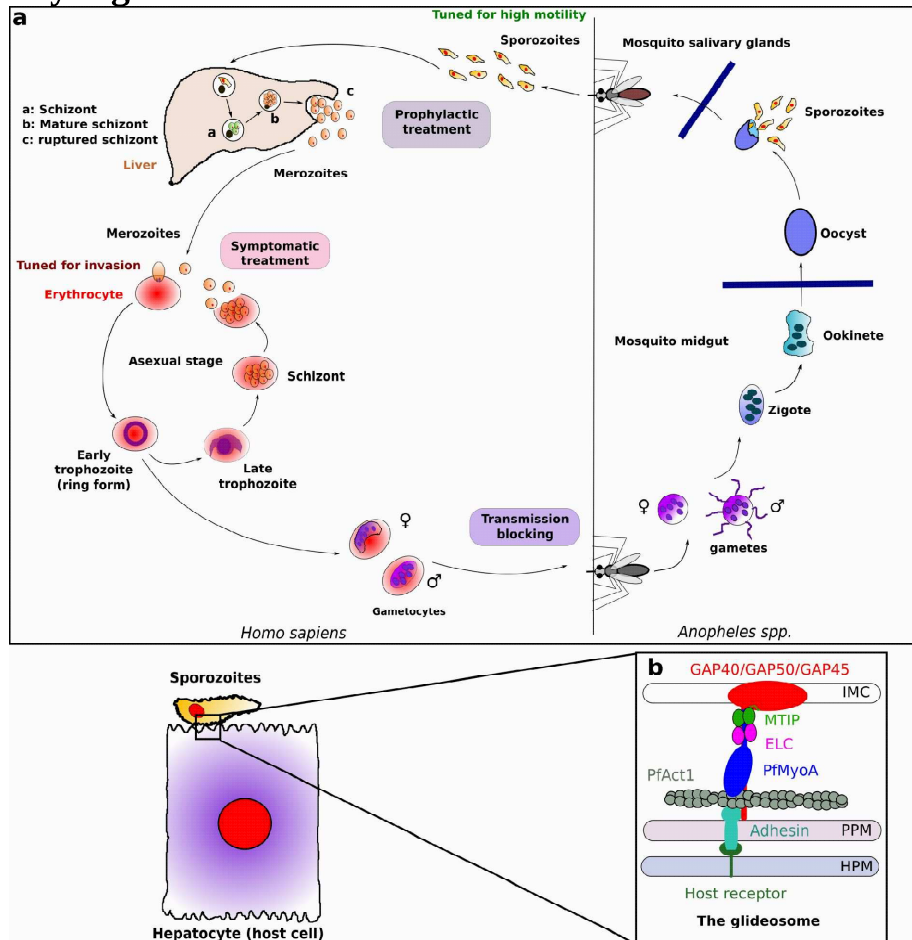


**Open Access** This article is licensed under a Creative Commons Attribution 4.0 International License, which permits use, sharing, adaptation, distribution and reproduction in any medium or format, as long as you give appropriate credit to the original author(s) and the source, provide a link to the Creative Commons license, and indicate if changes were made. The images or other third party material in this article are included in the article's Creative Commons license, unless indicated otherwise in a credit line to the material. If material is not included in the article's Creative Commons license and your intended use is not permitted by statutory regulation or exceeds the permitted use, you will need to obtain permission directly from the copyright holder. To view a copy of this license, visit <http://creativecommons.org/licenses/by/4.0/>.

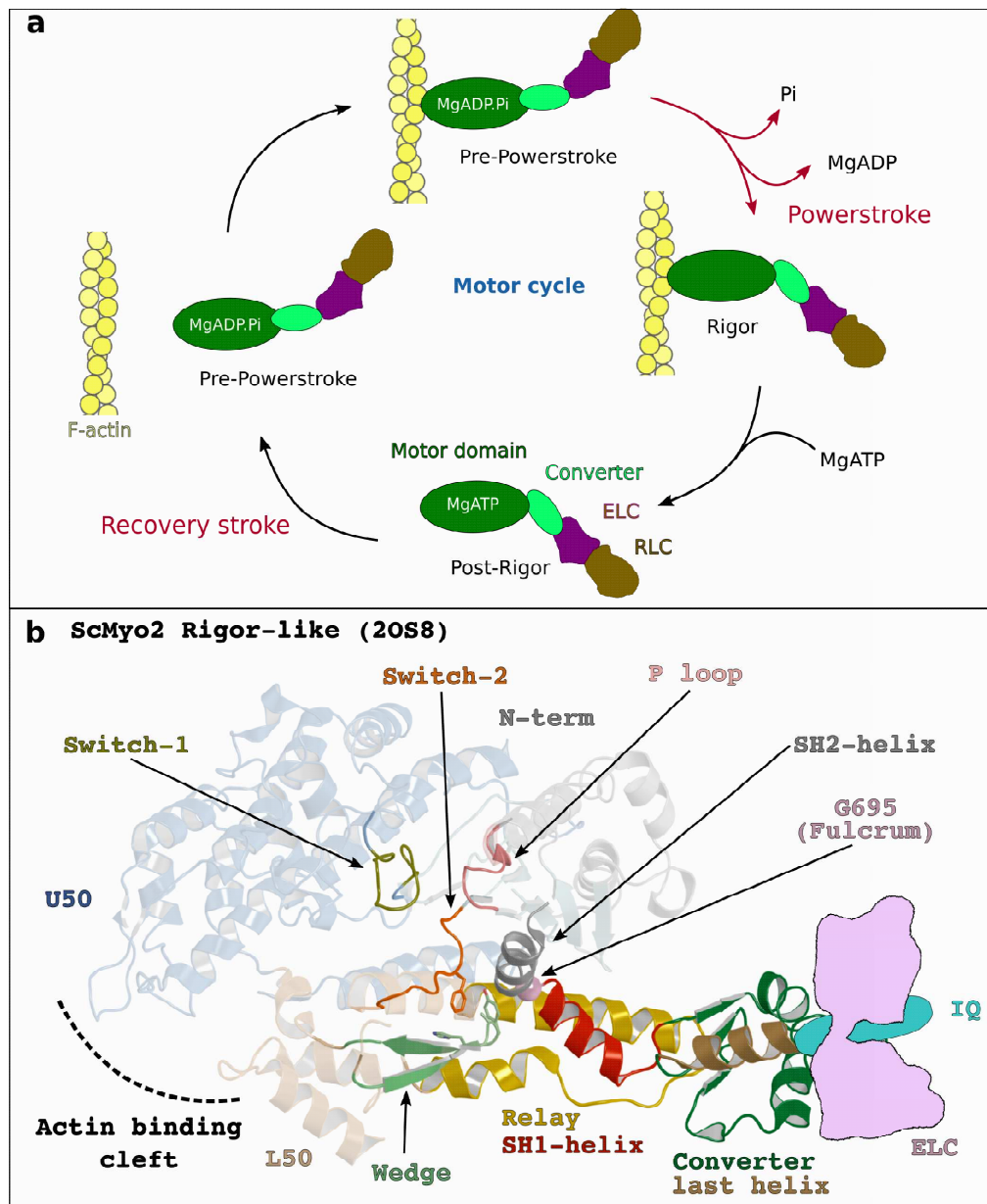
© The Author(s) 2019

**Supplementary Information**  
**Robert-Paganin *et al.*, 2019**

## Supplementary Figures



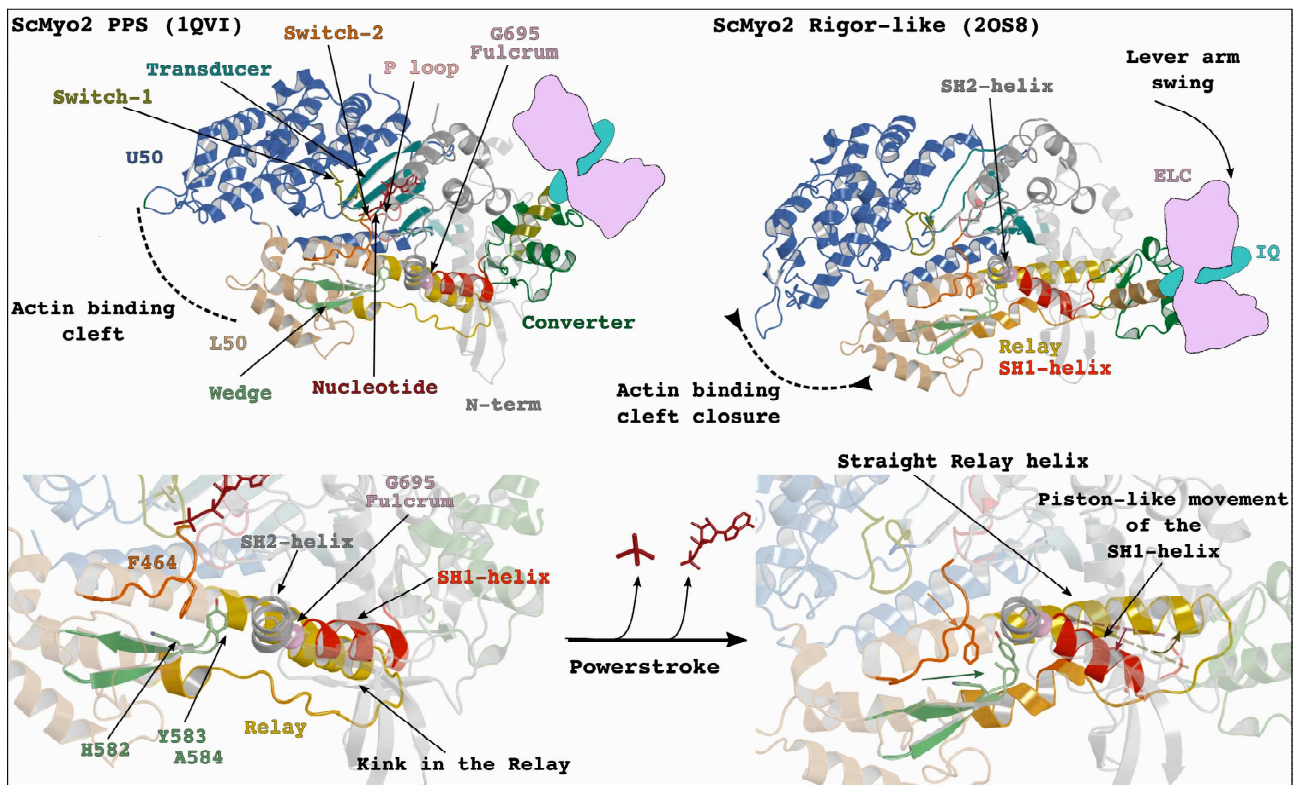
**Supplementary Figure 1 | *Plasmodium falciparum* life cycle and current treatments.** (a) The apicomplexan parasite *Plasmodium falciparum* displays a complex life-cycle with two hosts: mosquitos from the genus *Anopheles* and *Homo sapiens*. In the human host, the parasite alternates between highly motile stages called Sporozoites, able to use a substrate-dependent mode of locomotion broadly termed gliding motility ( $\sim 2 \mu\text{m/s}$ ) and immobile but invasive Merozoites. Merozoites invade blood cells, performing asexual reproduction until gametocytes appear, in order to perform sexual reproduction once they are collected via another mosquito bite. Current antimalarial therapeutics for malaria, targeting the *Plasmodium* parasite can be subdivided into three classes: (i) Prophylactic treatments aimed at blocking malarial infection in the early stages. Liver stage prophylaxis (Primaquine, Malarone) blocks hepatic invasion by sporozoites. Blood stage prophylaxis (Chloroquine, Mefloquine, Amodiaquine) blocks primary infection of the erythrocytes by the merozoites. These treatments are preventive but resistance by the parasite is already demonstrated<sup>1</sup>. (ii) Symptomatic treatments aim to eliminate the parasite in the asexual reproduction blood stages. The most important of these treatments are derivatives and combination therapies (ACTs) based on artemisinin which likely work in many ways such as via interfering with hemoglobin digestion by the parasite, thus blocking its development. Recent reports of resistant to ACTs suggests this frontline antimalarial is under threat. See<sup>2</sup> for review. (iii) Transmission blocking treatments which aim to block the transmission of the parasites in a population. Drugs in this class may target gametocytes or stages of development in the mosquito. For a review see<sup>3</sup>. (b) Schematic representation of the glideosome, the macromolecular complex responsible of gliding motility. Movement production relies on a specific actomyosin system comprising myosin A (PfMyoA) and actin 1 (PfAct1). PfMyoA contains the essential light chain (ELC) and the myosin tail domain interacting protein (MTIP). MTIP anchors PfMyoA to the inner membrane complex (IMC) via GAP proteins. Short and oriented PfAct1 filaments are anchored to the parasite plasma membrane (PPM) via adhesins that bind host receptors from the host plasma membrane (HPM).



**Supplementary Figure 2 | Motor cycle of a canonical myosin. (a)** During the mechanical cycle, myosins explore distinct structural states depending on the nucleotide bound. ATP binding in the myosin active site triggers detachment of the motor from F-actin while myosin adopts the Post-rigor state (PR) of poor affinity for F-actin and with a lever arm down. The recovery stroke allows priming of the lever arm (comprising the essential light chain (ELC) and the regulatory light chain (RLC)), leading to the pre-powerstroke state (PPS) in which ATP hydrolysis can occur. The PPS state has a low affinity for F-actin but its association with F-actin triggers rearrangements during the powerstroke that couples the release of hydrolysis products and the swing of the lever arm. The nucleotide-free Rigor state has high affinity to F-actin. **(b)** Cartoon representation of scallop myosin II (ScMyo2) in the Rigor-like state (PDB code 2O88). The subdomains of the myosin are shown in transparency: N-terminal (N-term, grey); Upper 50 kDa (U50); Lower 50 kDa (L50); converter (green). The myosin lever arm is composed of the converter whose last helix extends to form a helical domain containing the IQ motifs to which light chains bind. Here the first IQ domain, (cyan), which binds an ELC (pale pink) is represented schematically. The active site loops and the connectors driving the lever arm swing during the powerstroke are represented in plain: P-loop (light pink); Switch-1 (olive); Switch-2 (orange); Relay (yellow); Wedge (pale green); SH1-helix (red); SH2-helix (grey) as well as the conserved SH2-SH1 glycine (fulcrum) (pink sphere). For detail on the rearrangements of these connectors during the powerstroke see [Supplementary Fig. 4](#).

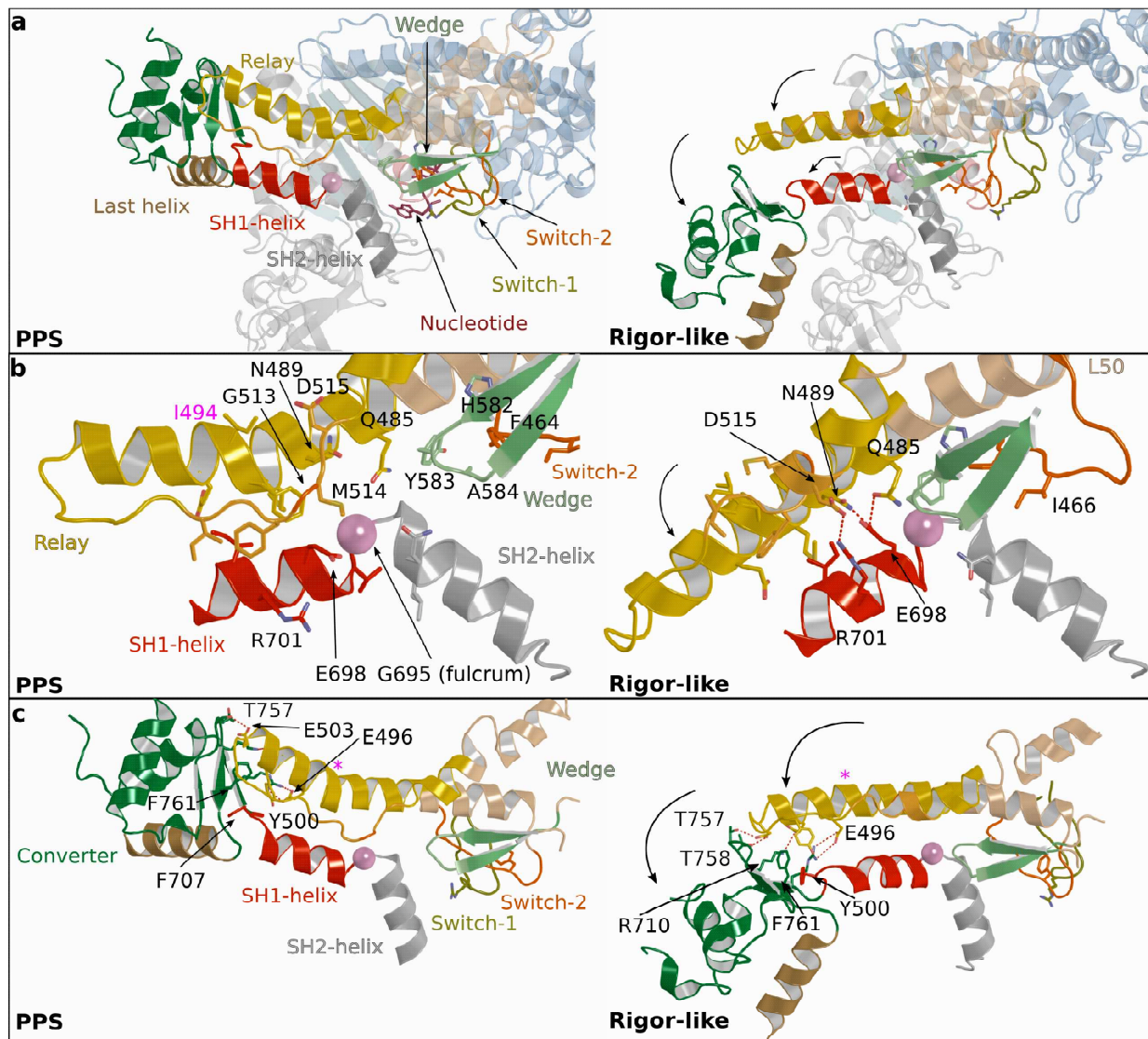




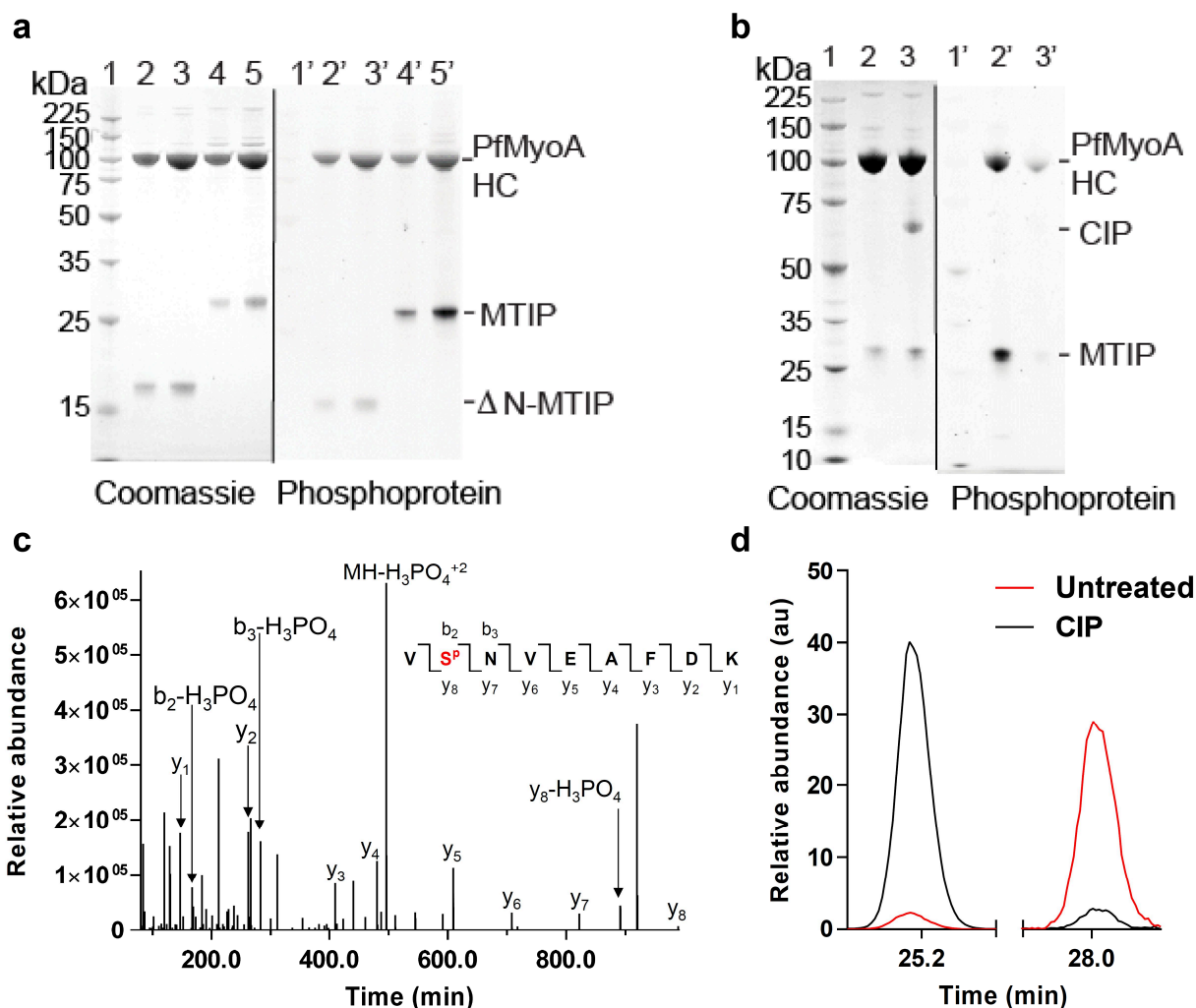


**Supplementary Figure 4 | Canonical structural rearrangements in a myosin motor domain.** Cartoon representation of scallop myosin II (ScMyo2) in the pre-powerstroke state (PPS) (PDB code 1QVI) and of scallop ScMyo2 in the Rigor-like state (PDB code 2OS8). **(Top)**, an overall view of the motor domain is presented to show the canonical structural elements of conventional myosin. **(Bottom)**, a zoom on the Wedge shows the allosteric transduction within the motor domain. During the powerstroke, sequential release of the hydrolysis products triggers global rearrangements of the motor domain. Changes in the Switch-2 conformation push the Wedge near the Relay/SH1-helix since they interact via conserved hydrophobic interactions between <sup>Switch-2</sup>F464 and <sup>Wedge</sup>H582, <sup>Wedge</sup>Y583 and <sup>Wedge</sup>A584. The bulky side chain of <sup>Wedge</sup>Y583 participates in the release of the Relay kink and in the piston-like movement of the SH1-helix, triggering the lever arm swing.

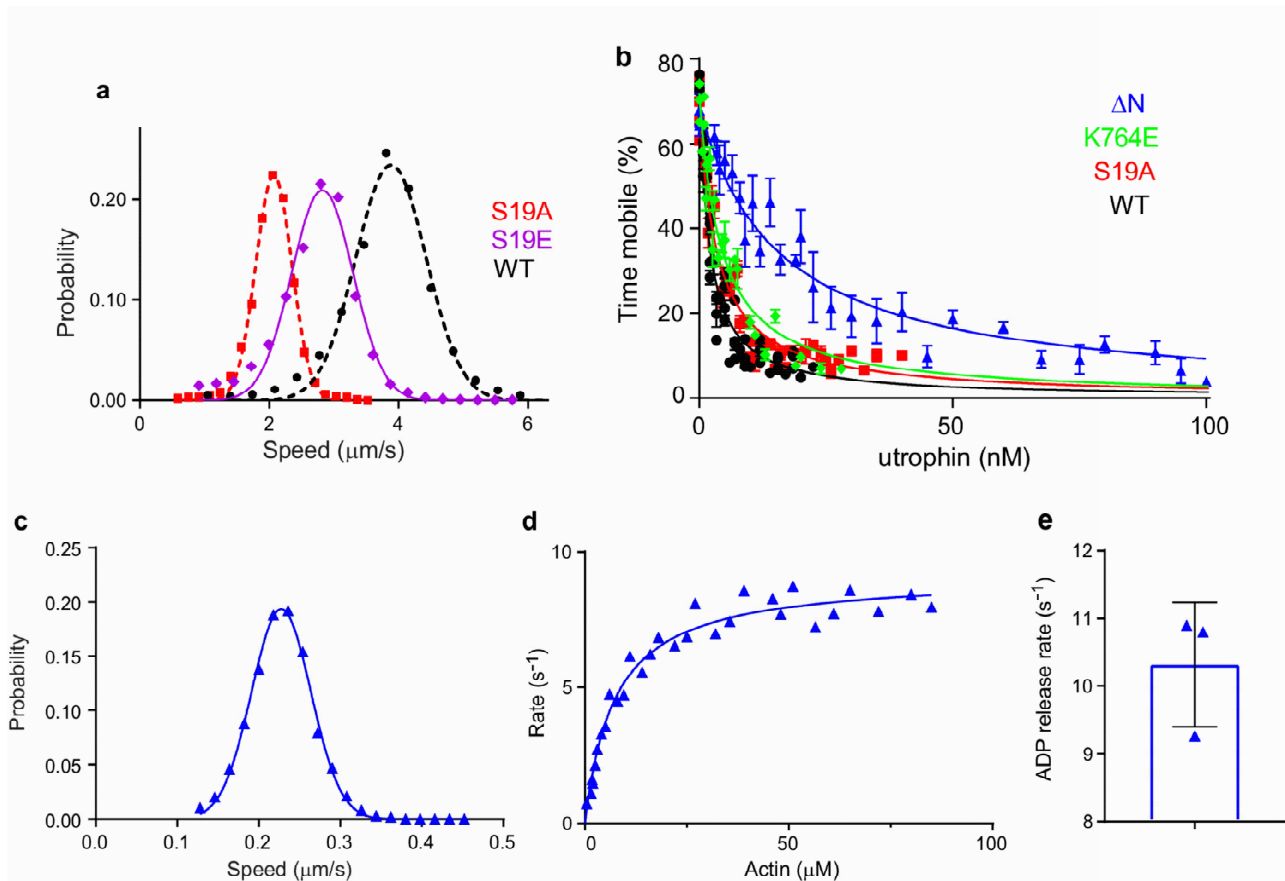




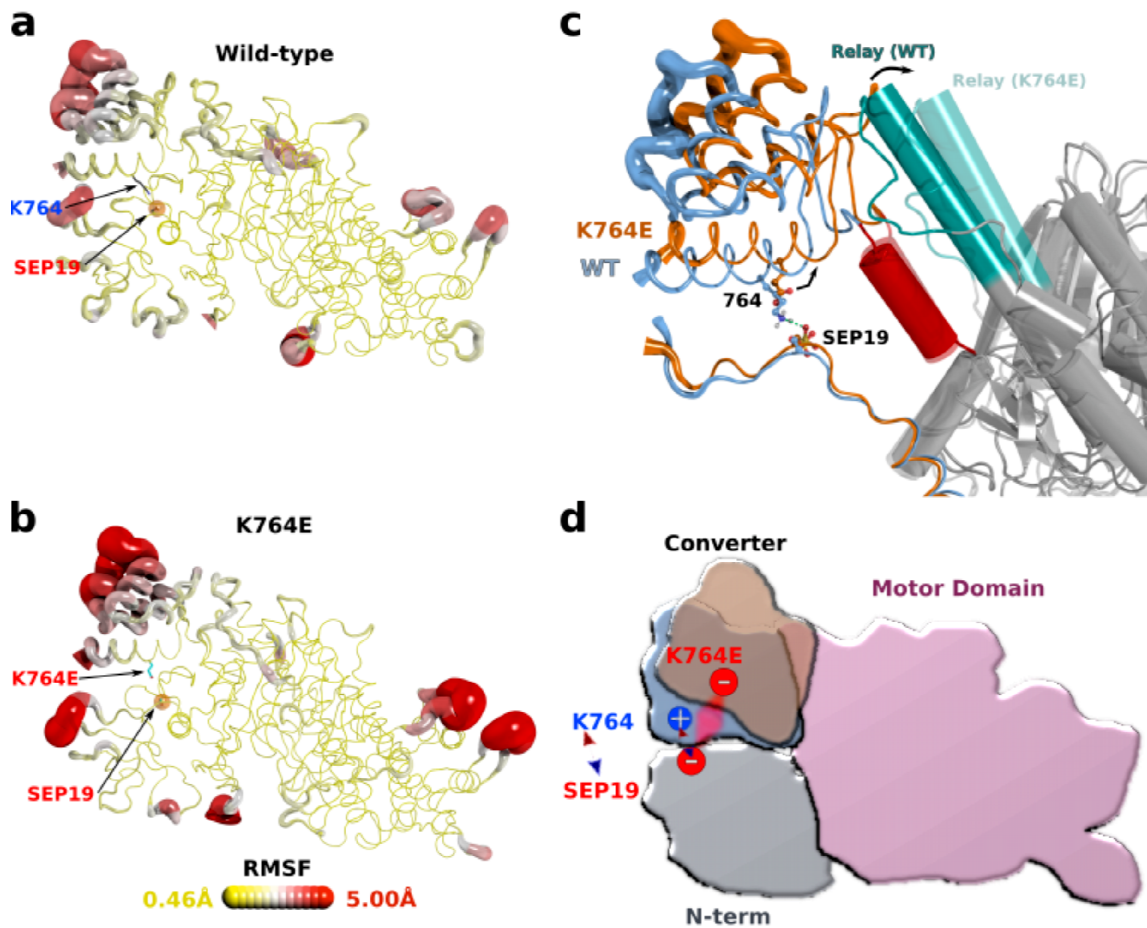
**Supplementary Figure 5 | The mechanism of force production by a conventional myosin II (scallop myosin II, ScMyo2).** Here the key elements in allosteric communication during the powerstroke of a conventional myosin II are presented. The structure of the pre-powerstroke state (PPS) of scallop myosin II (PDB code 1QVI) and the structure of the Rigor-like state of scallop Myo2 (PDB code 2OS8) have been used for the figures. **(a)** In the PPS state of conventional myosins, the Relay is in a primed position and it establishes a network of hydrophobic interactions with the SH1-helix. The Wedge is in a distal position from these elements. Release of hydrolysis products triggers a reorganization of Switch-2 and thus a cascade of events favoring the lever arm swing (arrows). **(b)** During the powerstroke, Switch-2 rearrangements displaces the Wedge close to the Relay and the SH1-helix. To avoid steric hindrance with the aromatic side chain of <sup>Wedge</sup>Y583, a piston-like movement of the SH1-helix occurs coordinated with the straightening of the kink in the Relay while the network of interactions between these two elements is remodeled. The piston-like movement of the SH1-helix is allowed by the presence of a deformable connector at the SH2-SH1 junction called the fulcrum (G695) (shown as a pink ball). As with PfMyoA (see [Fig. 5b](#)), in Myo2, a conserved aromatic residue from Switch-2 (F464) interacts with hydrophobic residues of the Wedge in both the PPS and Rigor-like state. This conserved interaction drives the movement of the Wedge during the powerstroke and positions it close to the Relay. The view in **(b)** is rotated  $\sim 45^\circ$  anticlockwise compared to **(a)**. **(c)** Similar figure as in **(a)** in which now the major interactions between the converter and both the Relay and the SH1-helix are shown. These interactions transmit and amplify the structural rearrangements of the motor domain. Thus, the piston-like movement of the SH1-helix and the straightening of the Relay kink trigger the swing of the converter.



**Supplementary Figure 6 | Gel and mass spectrometry-based analyses of PfMyoA phosphorylation state.** (a) 12% SDS-PAGE of PfMyoA expressed with full-length MTIP or truncated ΔN-MTIP (starts at residue Ser61), stained with Coomassie (left panel) or ProQ Diamond (Invitrogen, P33300) phosphoprotein stain (right panel). Lanes 1, 1', molecular mass markers; lanes 2, 2', 3, 3', two loads of PfMyoA-ΔN-MTIP; lanes 4, 4', 5, 5', two loads of PfMyoA-MTIP. The heavy chain and full-length MTIP were phosphorylated, but ΔN-MTIP was not. (b) 4-12% SDS-PAGE of PfMyoA expressed with full-length MTIP and stained with Coomassie (left panel) or ProQ Diamond phosphoprotein stain (right panel). Lanes 1, 1', molecular mass markers; lanes 2, 2' PfMyoA as expressed in *Sf9* cells; lanes 3, 3' following dephosphorylation with calf intestinal phosphatase (CIP; New England Biolabs, M0290S). Both the heavy chain and MTIP were dephosphorylated by CIP. (c) PfMyoA bands were excised from the 4-12% SDS-PAGE gels, digested with trypsin to produce peptides and analyzed by liquid chromatography mass spectrometry (LCMS). LCMS MS fragmentation spectra of the VSpNVEAFDK phosphopeptide containing PfMyoA serine 19. The sequence identity and position of phosphate were confirmed by the continuum of fragment ions (y- and b-ions). Similar mass spec analyses identified the sites of phosphorylation on MTIP as Ser 51, 55, 58 and 61<sup>6</sup>. (d) LCMS peptide elution profiles for the non-phosphorylated VSNVEAFDK (RT = 25.2 min; m/z = 504.7535) and phosphorylated VSpNVEAFDK (RT = 28.0 min; m/z = 544.7366) peptides found in the untreated and CIP-treated PfMyoA samples. Y-axis for the right panel was increased 40-fold to account for the difference in the intrinsic ionization efficiency between the non-phosphorylated and phosphopeptides (right panel). 96 ± 1% (± SD, n = 6, 2 independent preparations) of the peptides found in the untreated sample were phosphorylated at serine 19 and CIP treatment removed almost all of the phosphate from the peptide.

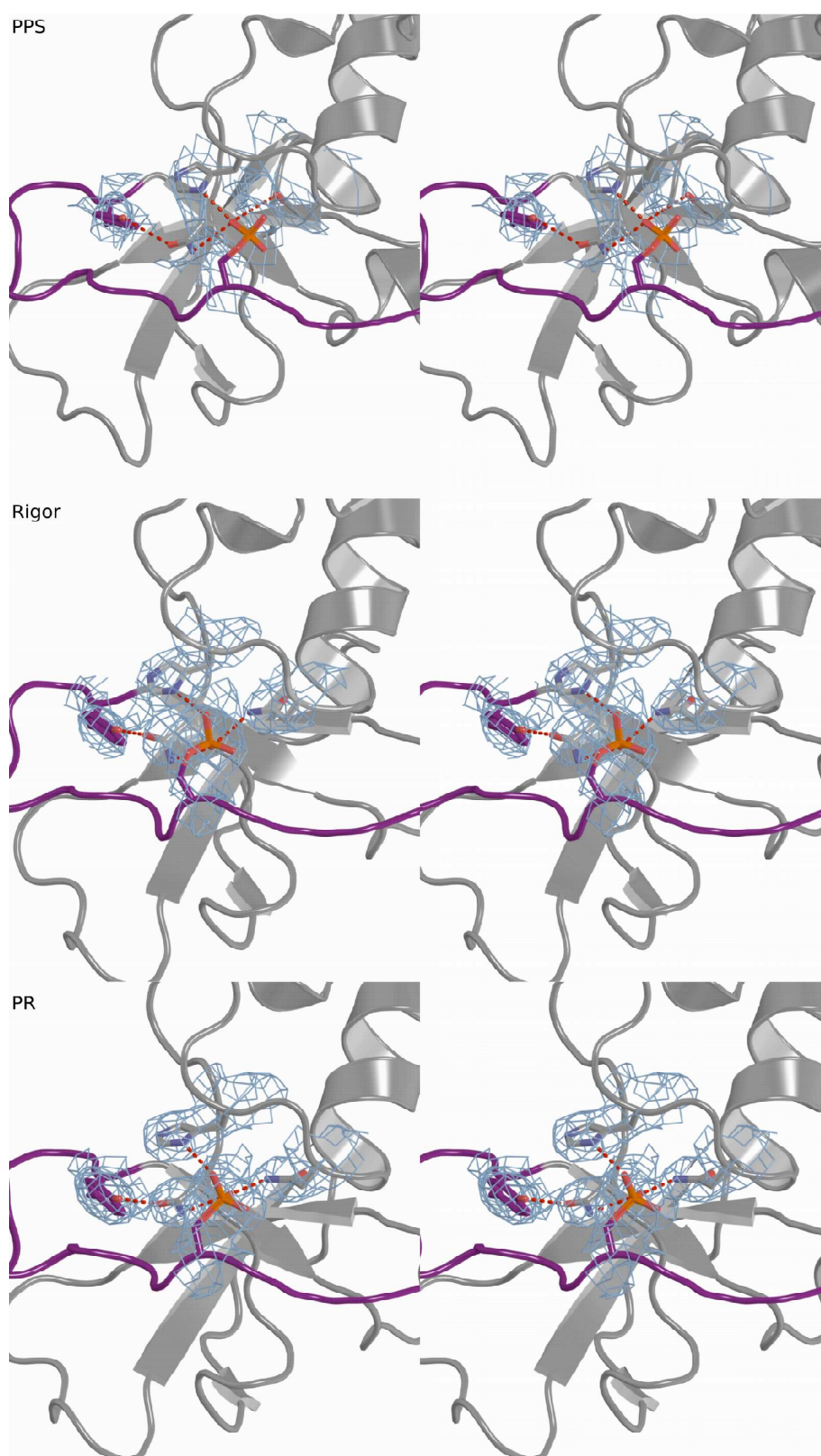


**Supplementary Figure 7 | Phospho-mimic S19E does not recapitulate phosphorylation, ensemble force data shown in Fig. 5e extended to higher utrophin concentrations, and data for  $\Delta\text{N}$  with expanded y-axis scale compared with Fig. 5b-d. (a)** Speed distributions from a representative *in vitro* motility assay showing that the phospho-mimic S19E does not recapitulate phosphorylation. WT (black),  $3.88 \pm 0.54 \mu\text{m/sec}$  ( $n=4294$  filaments); S19A (red),  $2.07 \pm 0.28 \mu\text{m/sec}$  ( $n=5291$  filaments); S19E (purple),  $2.82 \pm 0.47 \mu\text{m/sec}$  ( $n=4213$  filaments). Values are mean  $\pm$  SD. **(b)** Ensemble force fits from Fig. 5e with data at higher utrophin concentrations shown. **(c)** *In vitro* motility speed for  $\Delta\text{N}$ , **(d)** actin-activated ATPase activity for  $\Delta\text{N}$ , and **(e)** ADP release rate for  $\Delta\text{N}$ , each with expanded y-axis scales compared with Fig. 5b-d. Source data are provided as Source Data File.

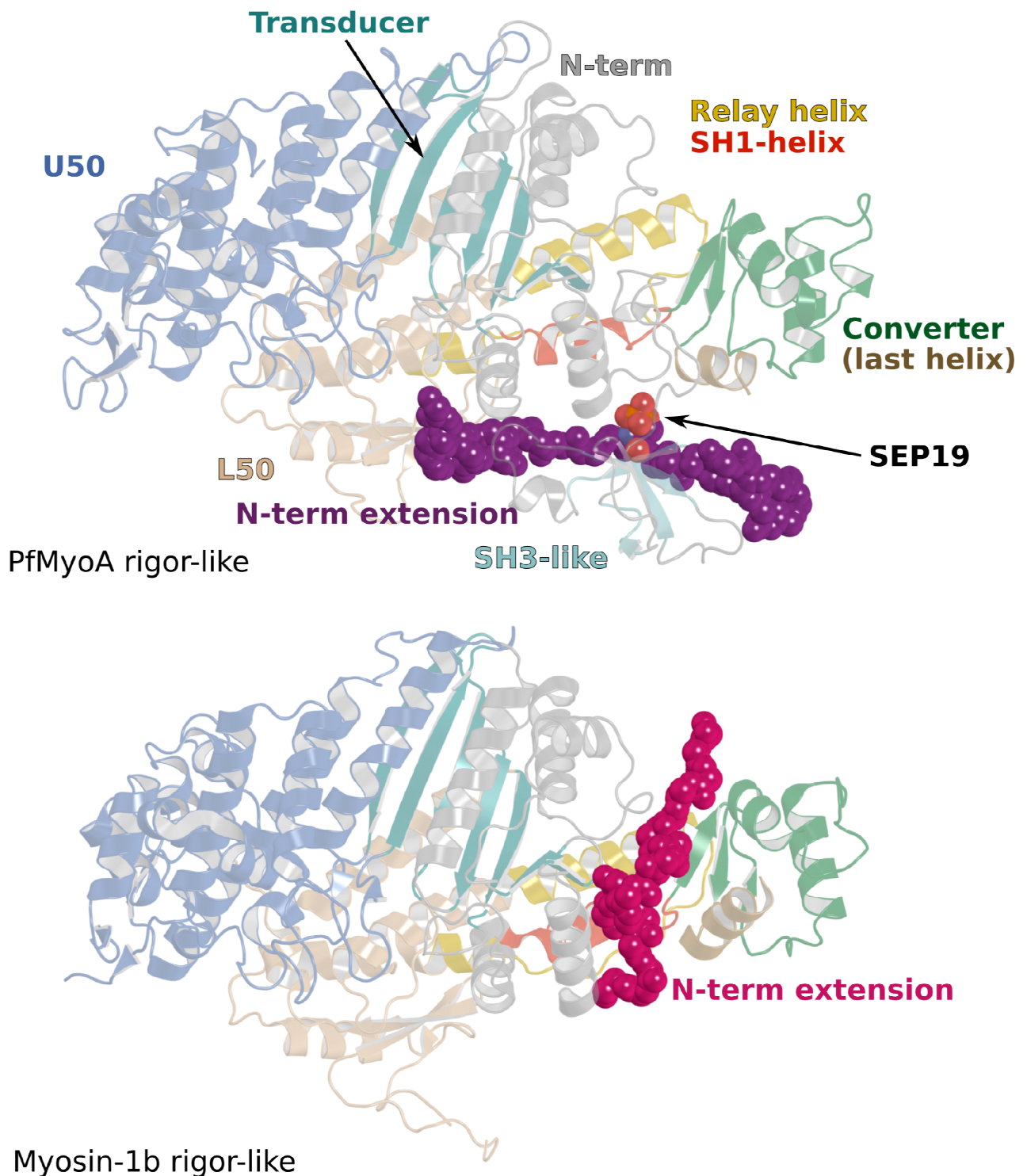


**Supplementary Figure 8 | Molecular dynamics of the phosphorylated wild-type (WT) and K764E mutant.** The mutant K764E in the Rigor state has been studied *in silico* to analyze the effect of introducing a repulsive interaction instead of the electrostatic bond between Converter<sup>K764</sup> and SEP19 from the N-term extension. On the left (**a** and **b**), a “putty representation” of the PfMyoA motor domain in the Rigor state (aa 1-768) represents the RMS fluctuations observed during 60 ns simulations with RMS scale ranging from 0.6 Å (yellow) to 4.8 Å (red). (**a**) WT, (**b**) K764E. In (**c**), superimposition on the N-term subdomain of the two putty representations. In the WT, during the entire duration of the dynamics, the converter stays in position and the electrostatic bond established between SEP19 and K764 is maintained. In contrast, the electrostatic repulsion introduced in the K764E mutant fails to maintain the converter in position. It is progressively displaced from its original position together with the Relay but not with the SH1-helix that maintains its position. (**d**) Schematic representation of the molecular dynamics results: the motor domain is represented in pale purple, the N-term in light grey, the WT converter in light blue and the K764E converter in light orange. In the WT, the converter establishes an electrostatic bond with SEP19 from the N-term extension via K764, this stabilizes the Rigor-like conformation of PfMyoA. When the mutation K764E is introduced, the converter is no longer stabilized in its rigor conformation and is progressively exploring positions that are further away from the N-terminal subdomain and its WT position.

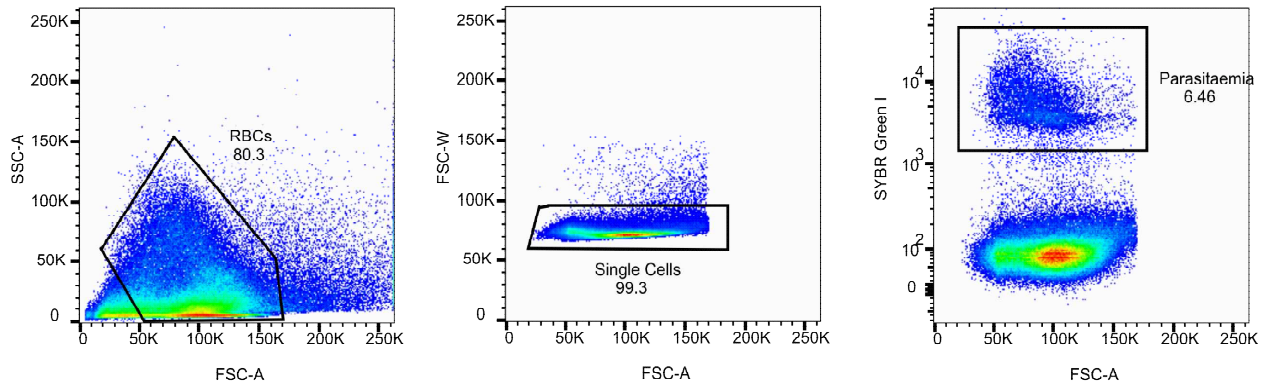




**Supplementary Figure 9 | Stereo view of the electron-density map for the phosphoserine SEP19 in the three PfMyoA structural states.** The 2Fo-Fc electron density map contoured at 1.0  $\sigma$  is presented for each state. The structures of the Rigor and the Post-rigor (PR) states comes from the asymmetric unit of the same crystal (crystal type 1) and have been solved at a resolution of 2.82 Å. The structure of the pre-powerstroke state (PPS) has been solved at 3.49 Å (crystal type 2). Despite the lower resolution for the PPS state, the electron density map is well-defined for SEP19 and for the interacting residues. See [Supplementary Tables 1 & 2](#) for data processing and refinement statistics.



**Supplementary Figure 10 | N-terminus extension in PfMyoA and Myosin-1b.** (a) Cartoon representation of the Rigor-like state of PfMyoA (top) and of Myosin-1b (Myo1b) (bottom, PDB code 4L79). The N-term extension of PfMyoA and Myo1b are represented as spheres and colored in purple and hotpink respectively. The comparison between the two structures illustrates the differences in terms of location and orientation between the N-term extensions of these two myosins. Note that Class 1 myosins do not have a SH3-like domain as part of their N-term sequence as most other class do (shown in cyan for PfMyoA). Color code: N-term (grey), U50 (marine blue), L50 (wheat tint), Relay helix (yellow), SH1-helix (red), transducer (deepteal cyan), converter (green), last helix of the converter (yellow sand).



**Supplementary Figure 11 | flow cytometry plots showing the gating strategy used to produce data for Fig 1B.** RBCs were gated out, then single cells, then infected RBCs as DNA-positive cells.



## Supplementary Tables

**Supplementary Table 1. Data collection and refinement statistics of crystal type 1 (Rigor-like and PR states).** PDB code 6I7D.

	Rigor-like and PR MD PfMyoA
<b>Data collection</b>	
Space group	$P2_1$
Cell dimensions	
$a, b, c$ (Å)	63.52, 258.73, 103.09
$\alpha, \beta, \gamma$ (°)	90 92.08 90
Resolution (Å)	44.22-2.82 (2.921-2.82)*
$R_{\text{meas}}$	0.1163 (0.8961)
$I / \sigma I$	12.54 (1.97)
CC <sub>1/2</sub> (%)	99.7 (70.5)
Completeness (%)	98.75 (96.41)
Redundancy	5.1 (5.0)
<b>Refinement</b>	
Resolution (Å)	44.22-2.82
No. reflections	403,952 (total), 78757 (unique)
$R_{\text{work}} / R_{\text{free}}$ (%)	18.70/24.10
No. atoms	
Protein	23,917
Ligand/ion	14
Water	423
$B$ -factors	
Protein	71.85
Ligand/ion	57.10
Water	53.64
R.m.s. deviations	
Bond lengths (Å)	0.015
Bond angles (°)	1.82

\*Values in parentheses are for highest-resolution shell.

**Supplementary Table 2. Data collection and refinement statistics of crystal type 2 (PPS state). PDB code 6I7E.**

PPS MD PfMyoA	
<b>Data collection</b>	
Space group	$P6_1 2 2$
Cell dimensions	
$a, b, c$ (Å)	197.460, 197.460, 175.144
$\alpha, \beta, \gamma$ (°)	90 90 120
Resolution (Å)	171.005-3.492 (3.735-3.492)*
$R_{\text{meas}}$ (all I+ and I-)	0.186 (2.456)
$R_{\text{meas}}$ (within I+/I-)	0.201 (2.490)
$I / \sigma I$	12.10 (1.40)
$CC_{1/2}$ (%)	99.9 (69.4)
Completeness (%)	59.5 (16.50) <sup>#</sup>
(Spherical)	
Completeness (%)	94.7 (66.4) <sup>#</sup>
(Ellipsoidal)	
Redundancy	22.6 (21.8) <sup>#</sup>
<b>Refinement</b>	
Resolution (Å)	25.17-3.492 (3.615-3.492)
No. reflections	31114 (total), 15557 (unique)
$R_{\text{work}} / R_{\text{free}}$ (%)	19.50/23.30
No. atoms	
Protein	6061
Ligand/ion	33
Water	0
$B$ -factors	
Protein	150.76
Ligand/ion	140.47
Water	
R.m.s. deviations	
Bond lengths (Å)	0.017
Bond angles (°)	1.88

\*Values in parentheses are for highest-resolution shell.

Data collection values obtained after using StarAniso.

**Supplementary Table 3. *In vitro* motility speed distributions of various PfMyoA constructs.**

<b>PfMyoA construct</b>	<b>mean (μm/s)</b>	<b>±SD (μm/s)</b>	<b>Number of Filaments</b>
WT	3.84	0.55	4408
	3.92	0.53	5475
	3.82	0.59	3748
	3.90	0.47	6600
	3.89	0.66	3634
S19A	2.07	0.33	6441
	2.04	0.35	6072
	1.99	0.26	5039
	2.02	0.26	5250
	2.07	0.28	5260
K764E	1.76	0.29	3962
	1.70	0.24	5555
	1.73	0.32	3079
	1.75	0.23	5962
ΔN	0.23	0.04	2310
	0.26	0.04	3485
	0.25	0.03	2474
	0.23	0.03	1696
	0.22	0.04	2046

WT, 5 technical replicates, 3 protein preparations; S19A, 5 technical replicates, 2 protein preparations; K764E, 4 technical replicates, 2 protein preparations; ΔN, 5 technical replicates, 2 protein preparations. Conditions: 25 mM imidazole, pH 7.5, 150 mM KCl, 1 mM EGTA, 4 mM MgCl<sub>2</sub>, 10 mM DTT, 2 mM MgATP, 0.5% (w/v) methylcellulose, 25 μg/ml PfELC, 25 μg/ml PfMTIP and oxygen scavengers (50 μg/ml catalase, 125 μg/ml glucose oxidase, and 3 mg/ml glucose. 30°C. SD, standard deviation.

**Supplementary Table 4. Rate of ADP release from actomyosin at various temperatures.**

PfMyoA construct	20°C (s <sup>-1</sup> )	25°C (s <sup>-1</sup> )	30°C (s <sup>-1</sup> )
WT	79.4 ± 0.6	171.5 ± 0.9	285.9 ± 2.3
	98.0 ± 0.5	188.2 ± 1.2	320.4 ± 2.5
	131.4 ± 1.2	266.0 ± 2.2	384.4 ± 6.0
	93.1 ± 0.7	186.2 ± 1.2	333.2 ± 3.1
	114.2 ± 1.0	233.1 ± 3.4	347.8 ± 4.8
S19A	30.2 ± 0.1	-	111.5 ± 0.2
	29.8 ± 0.1	58.4 ± 0.2	107.7 ± 0.3
	39.1 ± 0.1	72.9 ± 0.3	128.2 ± 0.6
K764E	18.1 ± 0.1	43.2 ± 0.2	95.2 ± 0.6
	26.8 ± 0.1	56.2 ± 0.3	112.3 ± 0.9
	20.2 ± 0.2	45.1 ± 0.4	103.0 ± 1.2
ΔN	1.64 ± 0.01	3.78 ± 0.01	9.26 ± 0.01
	2.10 ± 0.01	5.03 ± 0.01	10.90 ± 0.01
	1.99 ± 0.01	4.79 ± 0.01	10.80 ± 0.02

Data from 3-5 protein preparations are shown for each construct.  
Conditions: 10 mM HEPES, pH 7.5, 50 mM KCl, 4 mM MgCl<sub>2</sub>,  
1 mM EGTA, and 1 mM DTT.

## References

1. Schwartz, E. Prophylaxis of malaria. *Mediterr. J. Hematol. Infect. Dis.* **4**, e2012045–e2012045 (2012).
2. Martin, R. E., Shafik, S. H. & Richards, S. N. Mechanisms of resistance to the partner drugs of artemisinin in the malaria parasite. *Curr. Opin. Pharmacol.* **42**, 71–80 (2018).
3. Sinden, R. E. Targeting the Parasite to Suppress Malaria Transmission. *Adv. Parasitol.* **97**, 147–185 (2017).
4. Powell, C. J. *et al.* Structural and mechanistic insights into the function of the unconventional class XIV myosin MyoA from *Toxoplasma gondii*. *Proc. Natl. Acad. Sci. U. S. A.* **115**, E10548–E10555 (2018).
5. Waterhouse, A. *et al.* SWISS-MODEL: homology modelling of protein structures and complexes. *Nucleic Acids Res.* **46**, W296–W303 (2018).
6. Bookwalter, C. S. *et al.* Reconstitution of the core of the malaria parasite glideosome with recombinant *Plasmodium* class XIV myosin A and *Plasmodium* actin. *J. Biol. Chem.* **292**, 19290–19303 (2017).

# Full-length *Plasmodium falciparum* myosin A and essential light chain PfELC structures provide new anti-malarial targets

Dihia Moussaoui<sup>1</sup>, James P Robblee<sup>2</sup>, Daniel Auguin<sup>3</sup>, Elena B Krementsova<sup>2</sup>, Silvia Haase<sup>4</sup>, Thomas CA Blake<sup>4</sup>, Jake Baum<sup>4</sup>, Julien Robert-Paganin<sup>1\*</sup>, Kathleen M Trybus<sup>2\*</sup>, Anne Houdusse<sup>1\*</sup>

<sup>1</sup>Structural Motility, Institut Curie, Paris Université Sciences et Lettres, Sorbonne Université, CNRS UMR144, Paris, France; <sup>2</sup>Department of Molecular Physiology and Biophysics, University of Vermont, Burlington, United States; <sup>3</sup>Laboratoire de Biologie des Ligneux et des Grandes Cultures (LBLGC), Université d'Orléans, INRAE, USC1328, Orléans, France; <sup>4</sup>Department of Life Sciences, Imperial College London, South Kensington, London, United Kingdom

**Abstract** Parasites from the genus *Plasmodium* are the causative agents of malaria. The mobility, infectivity, and ultimately pathogenesis of *Plasmodium falciparum* rely on a macromolecular complex, called the glideosome. At the core of the glideosome is an essential and divergent Myosin A motor (PfMyoA), a first order drug target against malaria. Here, we present the full-length structure of PfMyoA in two states of its motor cycle. We report novel interactions that are essential for motor priming and the mode of recognition of its two light chains (PfELC and MTIP) by two degenerate IQ motifs. Kinetic and motility assays using PfMyoA variants, along with molecular dynamics, demonstrate how specific priming and atypical sequence adaptations tune the motor's mechano-chemical properties. Supported by evidence for an essential role of the PfELC in malaria pathogenesis, these structures provide a blueprint for the design of future anti-malarials targeting both the glideosome motor and its regulatory elements.

**\*For correspondence:**

julien.robert-paganin@curie.fr (JR-P);

Kathleen.Trybus@med.uvm.edu (KMT);

Anne.Houdusse@curie.fr (AH)

**Competing interests:** The

authors declare that no competing interests exist.

**Funding:** See page 20

**Received:** 30 June 2020

**Accepted:** 17 September 2020

**Published:** 13 October 2020

**Reviewing editor:** Adam Frost, University of California, San Francisco, United States

© Copyright Moussaoui et al. This article is distributed under the terms of the [Creative Commons Attribution License](https://creativecommons.org/licenses/by/4.0/), which permits unrestricted use and redistribution provided that the original author and source are credited.

## Introduction

Parasites from the genus *Plasmodium*, the causative agents of malaria, are responsible for half of a million deaths per year ([WHO, 2018](#)). Despite significant effort and money having been devoted for developing vaccines and new preventive treatments, the malaria parasites are becoming resistant to current artemisinin-based therapies ([Haldar et al., 2018](#)). The global death rate from malaria has recently started to rise after many years of decrease ([WHO, 2018](#)), emphasizing the necessity to develop new interventions, particularly because climate change may further expand the range of *Anopheles* mosquitoes ([Hertig, 2019; Ryan et al., 2020](#)).

The mosquito-borne parasite *P. falciparum*, the deadliest species that infects humans, alternates between motile and non-motile stages. Locomotion of apicomplexan parasites occurs by a process called gliding motility (reviewed in [Frénal et al., 2017](#)). This mode of displacement and the infectivity of the parasite rely on a macromolecular assembly called the glideosome that is anchored in an inner membrane complex located ~25 nm below the parasite plasma membrane (PPM). The core of the glideosome consists of an atypical class XIV myosin A (PfMyoA) and a divergent actin (PfAct1). PfMyoA is a short myosin with a conserved globular motor domain and a lever arm that binds two light chains: an essential light chain (PfELC) and myosin tail interacting protein (MTIP) ([Green et al.,](#)

2017; Bookwalter et al., 2017). The N-terminal extension of MTIP binds to integral membrane proteins called GAPs (glideosome associated proteins), which anchors the myosin so that it can interact cyclically with actin (Jones et al., 2012; Figure 1a) (reviewed in Frénel et al., 2017). PfMyoA is a critical molecule in the parasite life-cycle because it powers the fast motility ( $\sim 2 \mu\text{m.s}^{-1}$ ) required during motile sporozoite stages (Münter et al., 2009), and is essential for providing the force (up to 40 pN) needed for non-motile merozoites to invade erythrocytes (Crick et al., 2014; Robert-Paganin et al., 2019).

The molecular motor myosin has a conserved ATPase cycle in which the state of hydrolysis of the nucleotide drives both the association with actin and movements of the lever arm. Structural reorganization initiated at the active site is transmitted allosterically by connectors, and amplified by the lever arm (Figure 1—figure supplement 1a, c and d) (reviewed by Robert-Paganin et al., 2020). We recently solved the X-ray structures of the *P. falciparum* MyoA motor domain in three states of this ATPase cycle (Robert-Paganin et al., 2019), which revealed how the lack of consensus residues in the connectors is compensated by the presence of a unique N-terminal extension of the heavy chain (Figure 1—figure supplement 1d). Phosphorylation of Ser19 within this extension directly tunes speed and force production (Robert-Paganin et al., 2019). The motor moves actin at high-speed and exerts low ensemble force when phosphorylated; conversely, it produces more force at the expense of slower speed when unphosphorylated (Robert-Paganin et al., 2019; Figure 1—figure supplement 1b). According to this model, phosphorylated PfMyoA would allow the parasite to move at high velocity during motile stages such as the sporozoites, and when unphosphorylated, would provide the high force necessary for merozoites to enter erythrocytes in invasive stages (Robert-Paganin et al., 2019).

The motor domain is not the only region of PfMyoA lacking myosin consensus sequences. The lever arm typically contains 'IQ motifs' (consensus sequence IQxxxRGxxxR) that binds light chains or calmodulin. In PfMyoA, both the first IQ motif and the PfELC that binds to it are so degenerate in their sequence that the existence of an essential light chain was only recently recognized (Green et al., 2017; Bookwalter et al., 2017; Figure 1a). The structure of MTIP in complex with a Plasmodium IQ2 peptide is the only structural information available for the PfMyoA lever arm (Bosch et al., 2006; Bosch et al., 2007; Douse et al., 2012). Further structures are required to establish how interactions between the motor domain and the lever arm influence the overall dynamics and properties of the motor.

Here, we present the X-ray structures of full-length (FL) PfMyoA complexed to PfELC and MTIP in two states of the motor cycle. These structures, together with molecular dynamics and small-angle X-ray scattering (SAXS), reveal the specific orientation of the lever arm in the pre-powerstroke state (PPS). This atypical priming, which enables a larger powerstroke, is stabilized by the converter and PfELC forming specific interactions with the motor domain. Kinetic and motility assays on mutant PfMyoA constructs show how the specific priming and unique sequence adaptations tune the motor properties of this atypical myosin. The lever arm structure explains how the PfELC and MTIP light chains evolved to recognize degenerate IQ motifs. The PfELC, a weak link in forming a fully functional motor, is shown here to be essential for red blood cell invasion, thus providing a novel target for the design of anti-malarial compounds.

## Results

### FL structures of PfMyoA reveal a specific priming of the lever arm

We determined the crystal structures of FL PfMyoA with two light chains bound (PfMyoA/PfELC/MTIP- $\Delta\text{n}$ ) in the post-rigor (PfMyoA•FL-PR) and in the pre-powerstroke (PfMyoA•FL-PPS) states at 2.5 Å and 3.9 Å resolution, respectively (Supplementary file 1a; Figure 1b and c). To investigate the structural consequences of the deletion of the N-terminal extension (N-ter) of the PfMyoA heavy chain (HC), we also crystallized the truncated construct (PfMyoA- $\Delta\text{Nter}$ /PfELC/MTIP- $\Delta\text{n}$ ). The structure was solved in the post-rigor (PR) state at 3.3 Å resolution (PfMyoA- $\Delta\text{Nter}$ -PR) (Figure 1—figure supplement 2a and b). In all the constructs, MTIP was truncated and lacking the N-terminal extension (residues 1–60) because this extension is predicted to be intrinsically disordered. For all three structures, the electron density was well-defined for the motor domain and the lever arm, in

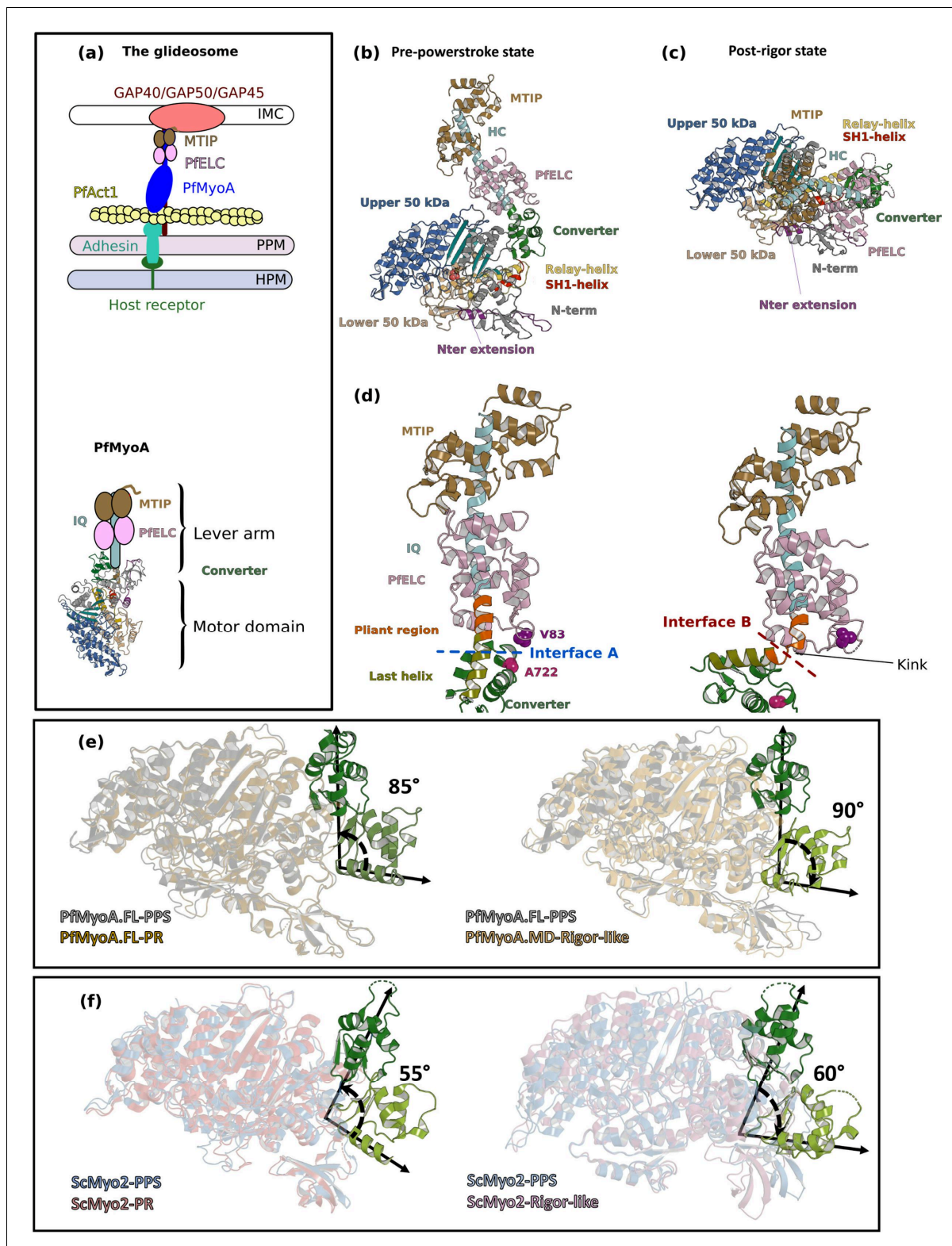


**Figure 1.** Crystal structures of PfMyoA in the Post-rigor (PR) and the Pre-Powerstroke (PPS) states. (a) (Left) The PfMyoA motor is located in the intermembrane space of the parasite. PfMyoA (blue) binds two light chains, PfELC and myosin tail interacting protein (MTIP). MTIP connects the motor to the glideosome-associated proteins (GAP) complex, which is anchored in the inner membrane complex (IMC). PfMyoA cyclically interacts with PfAct1 filaments, which are bound to adhesins from the parasite plasma membrane (PPM); these adhesins also bind receptors from the host cell plasma

Figure 1 continued on next page



Figure 1 continued

membrane (HPM). The displacement of PfAct1 filaments by PfMyoA drives parasite gliding motility. (Right) The crystal structure of the motor domain of PfMyoA has been solved (Robert-Paganin et al., 2019), but the lever arm structure was not known. (b,c) Overall structures of the full-length PfMyoA motor in the PPS and PR states, displayed so that their N-terminal subdomains adopt a similar orientation. As expected, the orientation of the converter and lever arm differs in these two states. (d) The lever arm has been built in these two states of the motor, revealing the structure of the two bound light chains, PfELC and MTIP, displayed here in a similar orientation. The kink in the lever arm helix at the end of the converter (pliant region in orange; last helix of the converter in deep olive green) induces different converter/PfELC interfaces in the PPS (interface A, left) compared to the PR state (interface B, right). To illustrate that the two interfaces are different, two reporter residues are displayed as spheres, A722 from the converter and V83 from PfELC. These residues are the part of interface A but not the part of interface B. (e) and (f) represents the recovery stroke (left) and the powerstroke (right) for PfMyoA and scallop myosin 2 (ScMyo2), respectively. Structures of ScMyo2 used: PR (PDB code 1S5G); PPS (PDB code 1QVI). The online version of this article includes the following figure supplement(s) for figure 1:

**Figure supplement 1.** The atypical and tunable mechanical cycle of PfMyoA.

**Figure supplement 2.** The crystal structure of the PfMyoA-PR state displays a kink at the pliant region.

**Figure supplement 3.** Electron density in the PfMyoA structures.

**Figure supplement 4.** The orientation of the lever arm of PfMyoA in PPS differs in the structures of the MD and of the FL.

particular for the interfaces between the HC and the PfELC and the interface between the two light chains (Figure 1—figure supplement 3).

These structures allow the description of the lever arm that was not present in the previously published PfMyoA motor domain (MD) structures (Robert-Paganin et al., 2019). When comparing the PR and PPS states, the overall fold of both the IQ region of the HC/PfELC/MTIP and converter regions are highly similar. Major differences are located at the ELC/converter interface when the PR and the PPS are compared (Figure 1d), predominantly due to a sharp kink in the pliant region (Houdusse et al., 2000) observed in the PR structures that promotes contacts between the ELC and the motor domain (Figure 1—figure supplement 2c). SAXS experiments demonstrate that this ‘folded-back’ position of the lever arm is not primarily populated in solution and is selected by crystal contacts. In solution, the lever arm adopts an extended conformation as seen in other myosins (Figure 1—figure supplement 2d and e–h).

The converter orientation is the same in both the motor domain (PfMyoA•MD-PR) (Robert-Paganin et al., 2019) and the FL (PfMyoA•FL-PR) post-rigor structures (Figure 1—figure supplement 4a). In the PPS states, crystallized with ADP and Pi analogs, however, the converter orientation is less primed by ~30° in the MD structure compared with that found in the FL structure (Robert-Paganin et al., 2019; Figure 1—figure supplement 4b). SAXS experiments validated that the PPS of PfMyoA adopts the more primed orientation in solution (Figure 1—figure supplement 2e). The MD structure with ADP.VO<sub>4</sub> bound thus likely corresponds to an intermediate state populated during the recovery stroke, close to that of the fully primed PPS (Figure 1—figure supplement 4c and d). Interestingly, the priming of the lever arm in the TgMyoA•MD-PPS structure (Powell et al., 2018) is identical to that of the PfMyoA•FL-PPS structure (Figure 1—figure supplement 4e). No major difference is found in the motor domain when the FL and MD structures are compared (Figure 1—figure supplement 4f). Notably, the lever arm is more primed in the PPS state of PfMyoA compared with that of conventional myosins, leading to a larger powerstroke than most myosins.

The FL structures of PfMyoA can be used to define the lever arm swing occurring during the PfMyoA motor cycle. The converter is reoriented ~90° during the powerstroke (Figure 1e). In conventional myosins, such as ScMyo2, the converter is reoriented only ~60° during the powerstroke (Figure 1f). In comparison, Myo10 undergoes a large ~140° swing during the powerstroke (Ropars et al., 2016) linked to both a highly primed lever arm orientation in its PPS state and an unusual rigor converter position. Specific structural features of PfMyoA thus control the lever arm repriming and larger swing amplitude during the powerstroke.

## Sequence adaptations tune distinct transitions of the cycle

Specific sequence differences in PfMyoA do not alter the global positioning of subdomains compared with conventional myosins, but instead affect the stability of structural states the motor explores and tune the kinetics of transitions between these states. Deletion of the Nter enhanced the duty-ratio (time spent strongly bound to actin) by greatly slowing ADP release to the extent that it rate-limited the overall ATPase cycle, which is ~14 fold slower than WT (Robert-Paganin et al.,

2019). The similarity of the  $\Delta$ Nter heavy chain and WT PfMyoA structures (rmsd of 0.415 Å on 993 atoms) (**Figure 1—figure supplement 2b**) strongly argues that the dramatic kinetic differences observed between these two constructs are due to an altered equilibrium between the states of the motor cycle (**Robert-Paganin et al., 2019**).

We previously showed that Serine 19 phosphorylation (SEP19) accelerates ADP release by stabilizing the converter in its rigor orientation through a polar interaction with <sup>converter</sup>K764 but other residues likely modulate these motor properties. In the Rigor state, <sup>Nter-extension</sup>E6 establishes cation- $\pi$  stacking interactions with <sup>Switch-2</sup>F476 and <sup>Switch-1</sup>R241 from the Switch-2 and Switch-1 elements of the active site (**Robert-Paganin et al., 2019; Figure 2a**). The charge reversal E6R mutant was designed to disrupt the interaction seen in the rigor state, a state the motor needs to populate to release ADP. The effects of the E6R mutation are similar to that observed with mutants disrupting the polar bond between SEP19 and the converter (S19A and K764E) (**Robert-Paganin et al., 2019**): ~2 fold reduced maximal actin-activated ATPase, ~2 fold reduced rate of ADP release that is correlated with a reduced speed of moving actin, ~3 fold increased ensemble force, and ~2.5 fold faster dissociation of acto-PfMyoA by MgATP (**Figure 2b–f, Supplementary file 1b**). All these results are consistent with E6 stabilizing the rigor state in WT via its interactions with Switches-1 and -2.

Two residues that are conserved in most myosins but not in PfMyoA were mutated to further investigate the role of sequence differences that are unique to PfMyoA (S691G and T586F). These residues are part of the environment between the Relay and SH1 helix, two critical connectors for the control of converter repriming and the powerstroke (**Figure 2a**). The presence of S691 at the base of the SH1 helix, which is typically a glycine in all other myosins, restrains the mobility of the SH1 helix. S691G is the only mutant to date that showed faster in vitro motility and faster ADP release than WT, implying that the mutation destabilizes the strong-ADP state (**Figure 2b–d, Supplementary file 1b**). The enhanced speed could be attributed to an increased flexibility of the SH1 helix or a decrease in steric hindrance that favors converter movement, resulting in faster ADP release. The maximal actin-activated ATPase activity was half that of WT and not rate-limited by ADP release (**Figure 2e, Supplementary file 1b**). S691 is involved in the communication between the Relay and the SH1 helices by maintaining an electrostatic bond with <sup>Relay</sup>Q494, which is part of the sequence compensation specific to PfMyoA. This bond is formed in the PR and PPS states but must be lost during the powerstroke. The absence of this bond in the mutant could reduce actin-activated ATPase because of altered communication between the connectors that affects the kinetics of the transitions in the motor cycle, introducing a slower step most likely early in the powerstroke. The nine-fold higher basal ATPase activity in the absence of actin (**Supplementary file 1b**) indicates that the pre-powerstroke (PPS) state of the mutant is less stable than WT, while the similar rate of dissociation of acto-PfMyoA by MgATP implies that the stability of the rigor state and the transition to PR are like WT (**Supplementary file 1b**). The mutant retains the ability to undergo conformational transitions when bound to actin under strain, with a modestly enhanced ensemble force (1.4-fold) compared with WT (**Figure 2f, Supplementary file 1b**). The role Ser691 plays in PfMyoA is thus to stabilize the PPS state and to slow the steps that are involved in rearrangements on F-actin to control the powerstroke.

Thr586 from the Wedge was replaced by the bulkier aromatic residue Phe that is present in conventional myosins (T586F). The wedge guides the movement of the relay-helix and the SH1-helix connectors depending on L50 subdomain movements that result from events in the active site (**Figure 1—figure supplement 1c**). This mutation had relatively little effect on in vitro motility speed or on ADP-release rates compared with WT (**Figure 2b–d, Supplementary file 1b**), despite the fact that the bulkier Phe would likely reduce the mobility around the wedge due to steric hindrance and thus impede the communication between the active site and the lever arm during the lever arm swing. The rate-limiting step for motility is not the first transition of the powerstroke that leads to the strong-ADP state on actin, but the following ADP-release step, which is not affected by this mutation. Rearrangements near the wedge thus play a minor role for ADP release, consistent with previous structural results (**Mentes et al., 2018**). The ~40% faster transition to the PR state suggests that rigor is slightly destabilized, while the elevated basal ATPase indicates a reduced stability of the PPS state (**Supplementary file 1b**). The reduced maximal actin-activated ATPase activity of the mutant indicates that other transitions in the motor cycle have slowed (**Figure 2e, Supplementary file 1b**). Similar to the other two point mutants (E6R and S691G), its ability to

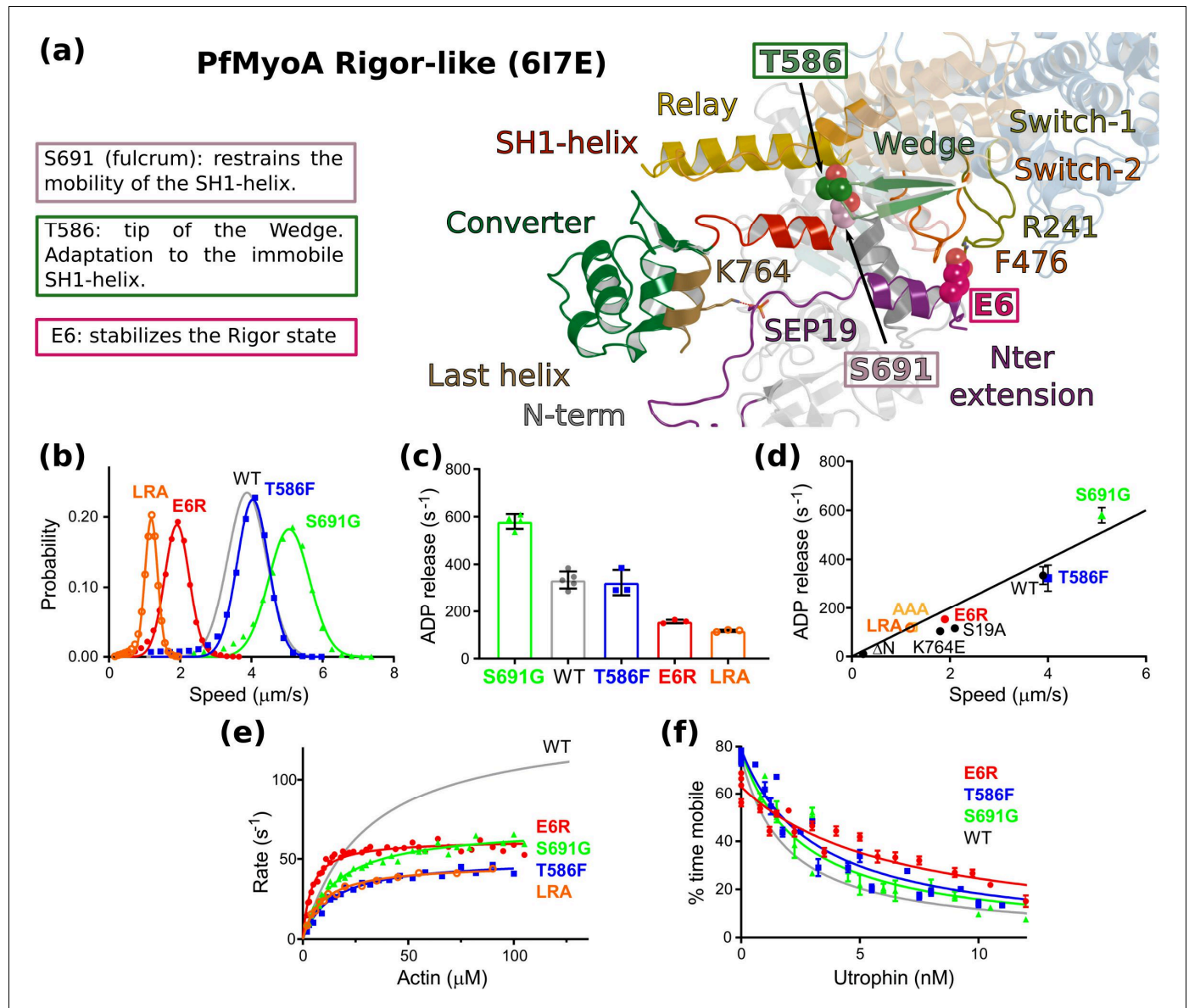


**Figure 2.** Sequence adaptations tune distinct transitions of the cycle. (a) Location and function of three mutated residues. (b) Speed distributions from representative in vitro motility assays. **Supplementary file 1b** shows values from additional experiments. (c) ADPrelease rates from acto-PfMyoA. WT data are from **Robert-Paganin et al., 2019**. Data for LRA (three experiments, two protein preparations); E6R (three experiments, three protein preparations); T586F (three experiments, two protein preparations); S691G (four experiments, three protein preparations). Values, mean  $\pm$  SD. (d) Correlation of ADP -release rates and in vitro motility speed. (e) Actin-activated ATPase activity. WT data are from **Robert-Paganin et al., 2019**. Data from at least two protein preparations and two experiments for each construct were fitted to the Michaelis-Menten equation. Error, SE of the fit. (f) Ensemble force measurements using a utrophin-based loaded in vitro motility assay. A myosin that produces more force requires higher utrophin concentrations to slow motion: E6R,  $4.02 \pm 0.31$  nM; T586F,  $2.38 \pm 0.18$  nM; S691G,  $1.99 \pm 0.19$  nM; WT,  $1.40 \pm 0.08$  nM. WT data are from **Robert-Paganin et al., 2019**. Error, SE of the fit. Data from two protein preparations and three experiments for each mutant construct. **Figure 6—figure supplement 1d** shows additional data with an expanded x-axis. Skeletal actin was used for all experiments. Temperature, 30°C. See also **Supplementary file 1b** for values.

The online version of this article includes the following source data for figure 2:

**Source data 1.** Source data for kinetic experiments presented in **Figure 2**.

generate motion under force was better than WT, implying more time spent in actin-bound states of the powerstroke (**Figure 2f, Supplementary file 1b**). Thr586, which is an adaptation to the immobile SH1 helix, contributes to stabilizing both the PPS and Rigor states.

The FL structures are consistent with the model previously proposed for the atypical and tunable mechanism of force production (**Robert-Paganin et al., 2019**). The new mutants analyzed here validate the idea that the sequence compensations observed in the SH1-helix, the Wedge and the Nter are key-elements that not only maintain the allosteric communication between the different myosin connectors, but also tune the motor properties.

### Specific recognition of the degenerate IQ motifs in the atypical PfMyoA lever arm

PfMyoA, like other class XIV myosins, is short and lacks a tail domain (**Foth et al., 2006**). The C-terminal region of PfMyoA consists of two degenerate IQ motifs (PflQ1 and PflQ2) that deviate from the consensus IQ sequence (IQxxxRGxxxR) but are recognized by the native light chains, PfELC and MTIP. The recognition of PflQ2 by MTIP has already been described (**Bosch et al., 2006; Bosch et al., 2007; Douse et al., 2012**) and involves several residues from the consensus IQ motif sequence (**Figure 3—figure supplement 1a–e**).

The FL structures allow the description of how PfELC binds to the lever arm and the interactions it forms with the motor domain. PfELC interacts with the long HC  $\alpha$ -helix with its N-lobe in a closed conformation and its C-lobe in a semi-open conformation, as it is the case for other ELCs (**Figure 3; Houdusse and Cohen, 1995**). While the structure of the N-lobe is mostly conserved compared to other ELCs (**Figure 3a and b; Houdusse and Cohen, 1996**), the C-lobe contains an extremely short  $\alpha 5$  helix, which consists of only one turn ( $\alpha 5^*$ ) followed by a short linker in which a small inserted helix turn forms ( $\alpha 5'^*$ ) (**Figure 3c and d**). In addition, the inter-lobe linker is shorter than canonical ELCs and forms an internal hairpin-like structure, that interacts strongly with the N-lobe and does not contact residues of the HC helix (**Figure 3e and f**). This unusual feature for an inter-lobe linker prevents the PfELC from fully surrounding the HC helix.

The sequence of the first IQ motif is adapted to the atypical features of PfELC. PflQ1 is highly degenerate, containing none of the consensus IQ motif residues (IQxxxRGxxxR) (**Figure 4a; Figure 4—figure supplement 1a, b and c**). In particular, PflQ1 lacks the glutamine and the proximal arginine that makes specific polar interactions with the C-lobe intra-lobe linker (between  $\alpha 6$  and  $\alpha 7$ ) in other myosins (**Houdusse and Cohen, 1996; Figure 4b**). In PfMyoA, these two residues are replaced by a valine (V781) and a glutamate (E785), respectively (**Figure 4c**). While they also bind the intra-lobe linker of the semi-open C-lobe, the change in the nature of these interactions (**Figure 4b and c**) results in a shift of the position of the intra-lobe linker relative to the HC helix (**Figure 3e and f**). Interestingly, compared to other myosins, the IQ1 motif starts one residue earlier in the PfMyoA HC sequence because a HC residue is missing in the pliant region at the end of the converter. This feature, in addition to a kink in the pliant region itself, contributes to a different orientation of the PflQ1 HC helix (and thus the PfELC C-lobe) compared with other myosins when the converter regions are superimposed (**Figure 4—figure supplement 2**). A different converter/ELC interface is thus established (**Figure 4—figure supplement 2b and c**) and specific recognition of the semi-open C-lobe occurs both by its interaction with the converter and with the HC helix. An atypical Trp (W777) in this helix strengthens the hydrophobic interactions between PflQ1 and PfELC (**Figure 4d and e**). Conventional myosins have a smaller side chain (I782) that interacts weakly with the C-lobe (**Figure 4d**). In PfMyoA, W777 is sandwiched between the  $\alpha 5^*$ ,  $\alpha 5'^*$  and  $\alpha 6$  helices, thus interacting with the hydrophobic core of the PfELC C-lobe (**Figure 4e**). These interactions between W777 and the  $\alpha 5^*$  and  $\alpha 5'^*$  helices are not present in the folded-back PR structure that displays a much larger kink at the pliant region and thus moves W777 away. The absence of electron density for the two helical turns of  $\alpha 5^*$  and  $\alpha 5'^*$  in this crystal structure indicates that lack of stabilization by the converter and the W777 side chain affects the fold of these atypical PfELC structural elements (**Figure 1—figure supplement 2c, Figure 4—figure supplement 1d, Figure 5a**). These results demonstrate how the degenerate PflQ1 motif is adapted to the peculiar structural features of PfELC, promoting specific recognition.



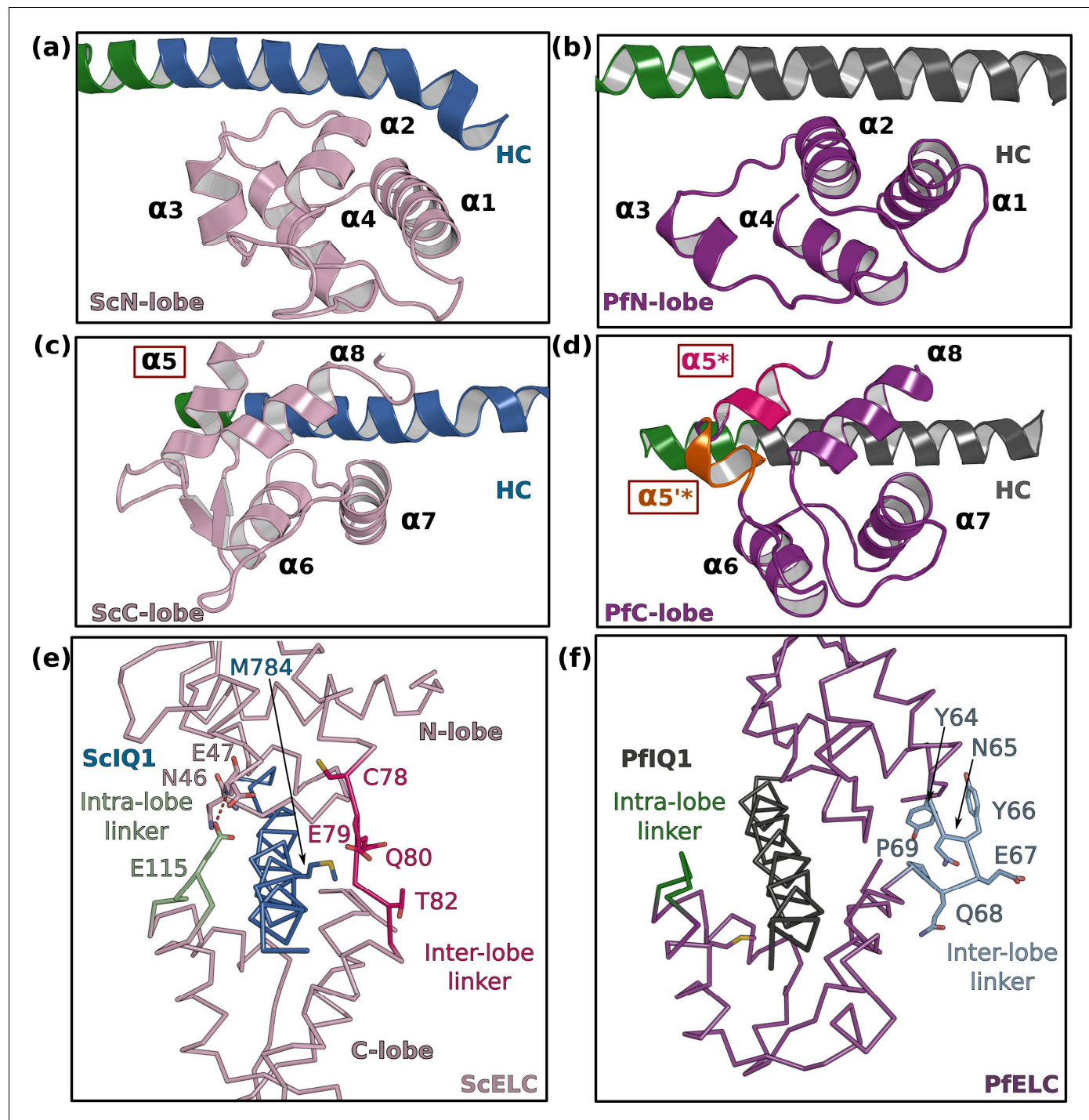


**Figure 3.** PfELC adopts an atypical fold. (a) The N-lobe of scallop myosin 2 ELC (ScMyo2) is compared to (b) the N-lobe of PfELC. The two lobes are conserved in structure, and adopt a closed conformation. In contrast, the C-lobe of ScMyo2 ELC (c) and PfELC (d) differ. The most divergent feature is the much shorter  $\alpha 5^*$  helix (comprised of only one turn) and the presence of the short  $\alpha 5'^*$  helix in PfMyoA. (e) shows the elongated inter-lobe linker of ScELC (red) compared with (f) the kinked, hairpin-like inter-lobe linker of PfELC (light blue). The specific structure of the inter-lobe linker makes the PfELC structure more compact than canonical ELCs and no direct interaction can occur between the lobes in PfMyoA to encircle the heavy chain, contrary to what is seen in the case of ScMyo2.

The online version of this article includes the following figure supplement(s) for figure 3:

**Figure supplement 1.** MTIP bound to PfMyoA.

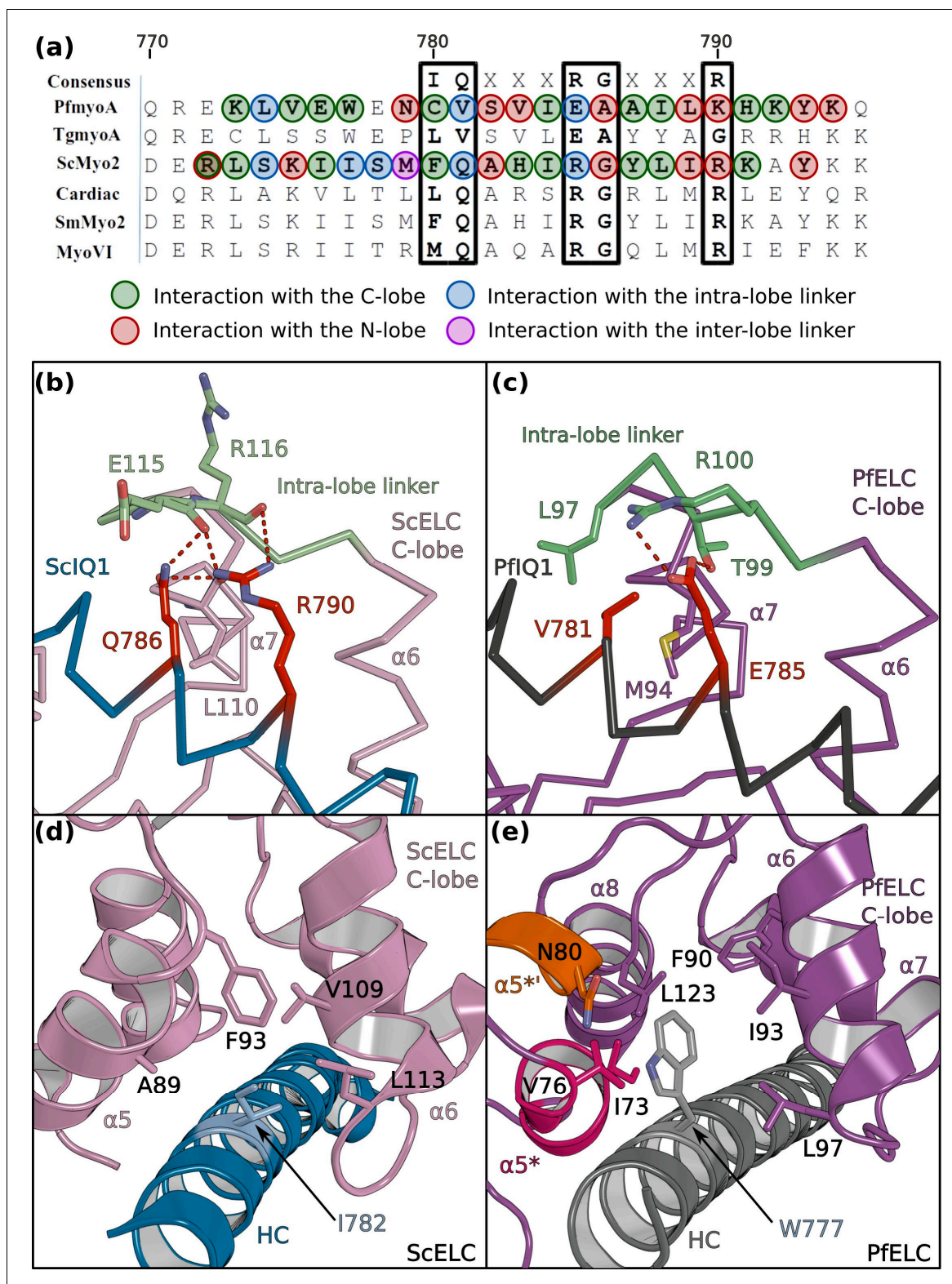


**Figure 4.** PfELC binds a degenerate IQ motif. (a) Sequence alignment of PfMyoA IQ1 to the consensus IQ motif and IQ motifs from other myosins: MyoA from *Toxoplasma gondii* (TgmyoA); bay scallop (*Argopecten irradians*) myosin 2 (ScMyo2); human (*Homo sapiens*)  $\beta$ -cardiac myosin 2 (Cardiac); human smooth muscle myosin 2 (SmMyo2); human myosin 6 (MyoVI). Consensus residues are contoured by a black box. (b) The intra-lobe linker of the scallop C-lobe interacts with the HC consensus residues with polar contacts. (c) In contrast, the intra-lobe linker of the Pf C-lobe is predominantly

Figure 4 continued on next page



Figure 4 continued

bound to the HC with apolar contacts. (d,e) Intra-lobe interactions maintain the semi-open C-lobe. Specificity in the recognition of the PfELC occurs via the W777 residue in PfMyoA. (d) In conventional myosins such as ScMyo2, a small side chain (I782) is found at the equivalent position, contributing to few interactions within the semi-open lobe. (e) In PfMyoA the bulky Trp (W777) is sandwiched between the  $\alpha 5^*$ ,  $\alpha 5'^*$  and  $\alpha 6$  helices, increasing the hydrophobic interactions with the PfELC C-lobe.

The online version of this article includes the following figure supplement(s) for figure 4:

**Figure supplement 1.** Interaction between the IQ1 motif and the ELC.

**Figure supplement 2.** The converter/ELC interface differs in PfMyoA and in ScMyo2.

## Compliance and hinge flexibility in the PfMyoA lever arm

The so-called pliant region between the converter and the lever arm (Houdusse et al., 2000) and the interfaces between light chains are hinges promoting lever arm flexibility (Pylypenko and Houdusse, 2011; Robert-Paganin et al., 2018). The numerous differing structural features of the PfMyoA lever arm described above change these hinges of flexibility. We describe below the converter/PfELC interface (interface A) seen in the PfMyoA•FL-PPS crystal structure, which is similar to the solution structure (Figure 1—figure supplement 2e–h).

The shift in the PfELC position as compared with other myosins (Figure 4—figure supplement 2) results in a different converter/ELC interface (Figure 5a and b). In canonical myosins, the converter/ELC interface is established between residues from the converter and the  $\alpha 5$  helix and includes mainly polar and few apolar interactions (Figure 5b). In PfMyoA, a more rigid interface forms because it involves mainly hydrophobic contributions from the  $\alpha 5^*$ ,  $\alpha 5'^*$ , and  $\alpha 6$  helices whose conformations are stabilized by W777 (Figure 5a). The PfELC/MTIP interface is also mainly hydrophobic, involving residues from the MTIP  $\alpha 5$  and  $\alpha 6$  helices (H150, F151, I167, W171) and residues from the PfELC  $\alpha 1$  helix and the following loop1 (Figure 3—figure supplement 1f). Interestingly, this interaction is possible only after the formation of a  $\sim 130^\circ$  kink in the HC helix between the two IQs motifs of the PfMyoA lever arm. The kink is facilitated by proline ( $^{\text{HC}}\text{P802}$ ) and is similar in all molecules of the asymmetric units of the structural states we crystallized (Figure 3—figure supplement 1g). The contacts at the MTIP/PfELC interface contribute to stabilizing the kink and providing a specific conserved feature for this rather rigid lever arm.

To further investigate the dynamics of the PfMyoA lever arm, we performed molecular dynamics with explicit solvent on the PfMyoA•FL-PPS structure, an approach successfully used to investigate other myosins (Robert-Paganin et al., 2018; Robert-Paganin et al., 2019). The first insight from this experiment is that priming of the PfMyoA lever arm is maintained throughout the time course. Even if the lever arm position slightly diverges at the beginning of the simulation, the priming is restored quickly and thus stays stable during the entire simulation (Video 1). As expected, the converter/PfELC and PfELC/MTIP interfaces are rigid. All the hydrophobic interactions between PfELC and MTIP are maintained during the simulation and the Converter/PfELC interface is more rigid as compared with conventional myosins (Videos 1 and 2). In  $\beta$ -cardiac myosin, the converter/ELC interface displays a controlled dynamic driven by labile polar interactions, the so-called ‘musical chairs’ (Robert-Paganin et al., 2018). These interactions between charged residues are located at the pliant region, and involve the  $\alpha 5$  helix of the ELC and the specific top-loop of the converter (Figure 5a and b, Video 2). The dynamic associations between the musical chairs govern the flexibility of the converter/ELC interface and the conformations allowed for the top-loop (Robert-Paganin et al., 2018). In contrast, in PfMyoA, most of the converter/ELC interface is hydrophobic and the bulky W777 introduces rigidity at this interface. The only musical chairs of the PfMyoA lever arm are located in two regions. Charged residues from the top-loop (E725 and D726) interact alternatively with residues of the  $\alpha 6$  helix ( $^{\text{PfELC}}\text{D88}$ ,  $^{\text{PfELC}}\text{N89}$ ), restricting the top-loop conformation. Other musical chairs involve residues from the converter (D720; K773 and E776) with polar residues from the  $\alpha 5^*$  and  $\alpha 5'^*$  helices ( $^{\alpha 5^*}\text{N75}$ ;  $^{\alpha 5'^*}\text{N77}$ ;  $^{\alpha 5^*}\text{E78}$ ;  $^{\alpha 5'^*}\text{Q79}$ ) (Figure 5a; Video 2). We conclude that the priming seen in the PfMyoA•FL-PPS crystal structure is stable, and that the PfMyoA lever arm is more rigid than in conventional myosins.

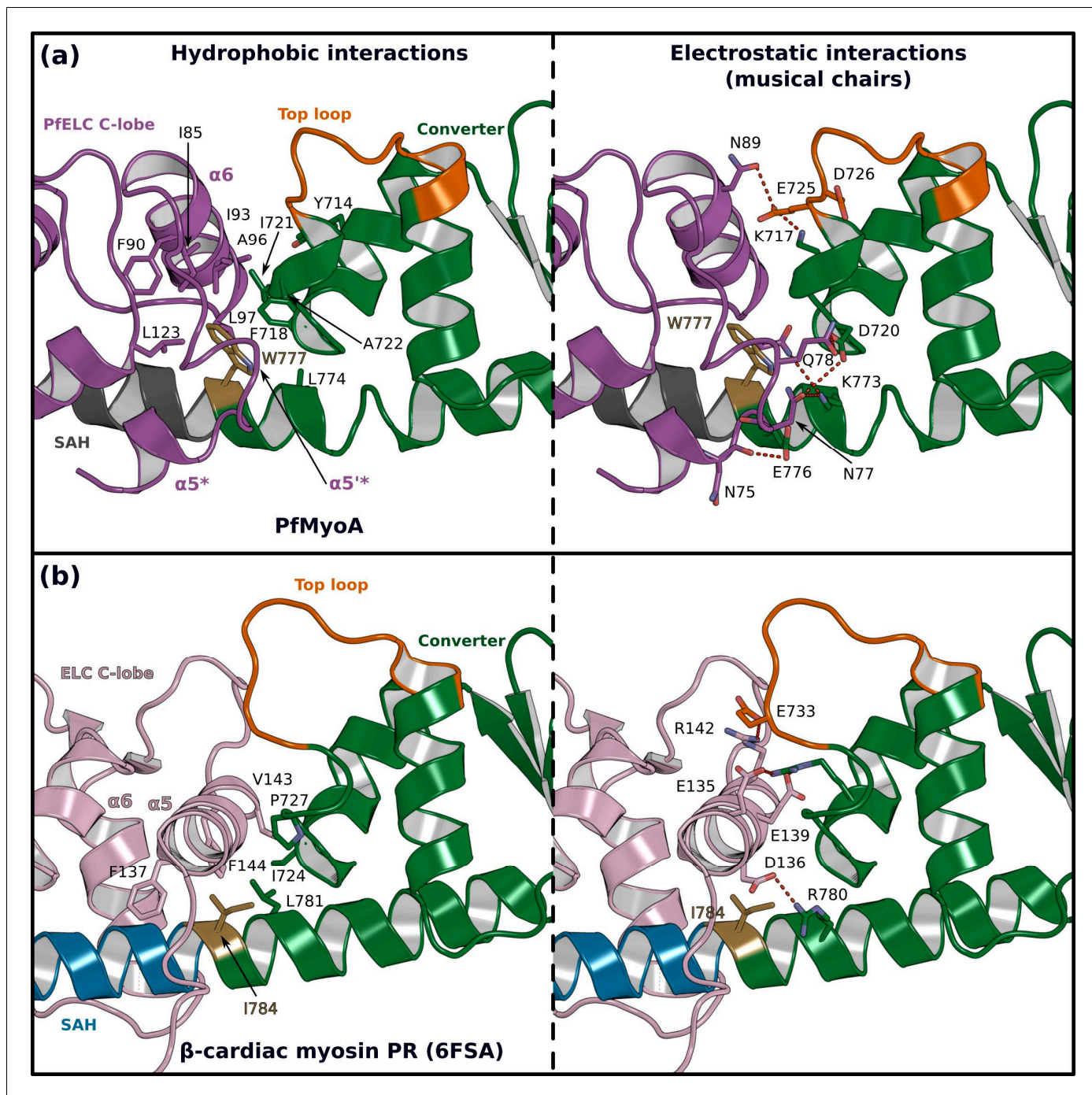
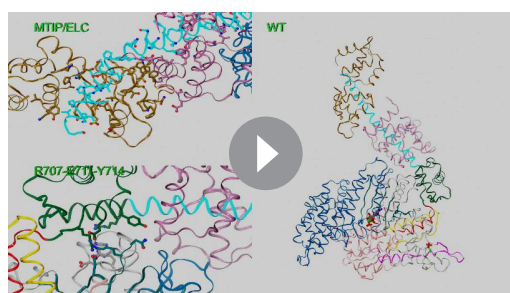


**Figure 5.** The atypical PfELC/Converter interface. Comparison of the converter/ELC interface of (a) PfMyoA and (b)  $\beta$ -cardiac myosin. (Left), hydrophobic contacts are displayed. (Right), polar residues responsible for the contacts identified as 'musical chairs' in molecular dynamics experiments (Robert-Paganin et al., 2018) are labeled.

### Motor domain/lever arm interactions stabilize the atypical PfMyoA priming

The atypical priming of the PfMyoA lever arm in the PPS state results from several interactions between the lever arm and the motor domain that are not present in conventional myosins. Conformational changes at the end of the SH1 helix are required to allow an additional Converter rotation



**Video 1.** Molecular dynamics performed on the structure of full-length (FL) PfMyoA in the PPS state (wild-type). Zooms show the interface between PfELC (light pink) and MTIP, and the interface between the lever arm and the motor domain.

<https://elifesciences.org/articles/60581#video1>



**Video 2.** Molecular dynamics performed on the structure of full-length (FL) PfMyoA in the PPS state (wild type). Zoom at the interface between the converter and PfELC showing the musical chairs.

<https://elifesciences.org/articles/60581#video2>

so that it can reach the PfMyoA motor domain surface with which it interacts (**Figure 1—figure supplement 4d**). These interactions involve two interfaces: interactions of PfELC with Loop-1 and the  $\beta$ -bulge and a specific interface between the Converter and the N-terminal subdomain (N-term) (**Figure 6a and b**). Interestingly, interactions between PfELC, loop-1 and the  $\beta$ -bulge are highly labile during molecular dynamics (**Video 1**), but the interface between the Converter and the N-term subdomain is highly stable and maintained throughout the time course (**Video 1**).

The converter/N-term subdomain interface can be subdivided into two regions. The first region involves a set of two polar interactions involving  $\text{Converter}^{\text{R707}}/\text{Nterm}^{\text{N177}}/\text{Transducer}^{\text{E660}}$  and  $\text{Converter}^{\text{E711}}/\text{Nterm}^{\text{K183}}$  and also hydrophobic interactions established between  $\text{Converter}^{\text{Y714}}$  and  $\text{Nterm}^{\text{V181}}$  and  $\text{Nterm}^{\text{N182}}$  (**Figure 6b**). These interactions are maintained throughout the duration of the molecular dynamics (**Video 1**). While the position of  $\text{Converter}^{\text{Y714}}$  shifts, it remains part of the interface. The second region consists in cation/ $\pi$ -stacking interactions between  $\text{Converter}^{\text{R771}}$  from the last helix of the Converter and  $\text{Nterm}^{\text{H160}}$ . This interaction is also stable throughout the time course of the dynamics, while  $\text{Converter}^{\text{R771}}$  occasionally establishes an interaction with  $\text{Nterm}^{\text{D159}}$  (**Video 1**).

To test the hypothesis that this Converter/N-term interface is key for stabilization of the atypical priming of PfMyoA in the PPS state, we designed the triple mutant R707A/E711A/Y714A in silico. As expected, molecular dynamics show that the three mutations destabilize the Converter/Nterm subdomain interface and cause a loss of priming, demonstrating that this interface stabilizes the atypical priming of PfMyoA in the PPS state (**Figure 6c**, **Videos 3 and 4**).

The consequences of this atypical priming on the motor properties of PfMyoA were tested with two triple mutants: R707A/E711A/Y714A and R707L/E711R/Y714A (priming AAA and LRA mutants). The two sets of mutations are expected to disrupt the converter/MD interface and thus to reduce the priming of the PPS. Both triple mutants greatly impact and tune the properties of the motor similarly: they reduce the maximum actin-activated ATPase to  $\sim 30\%$  of WT, and decrease both in vitro motility speed and the ADP release rate to a similar extent ( $\sim 35\%$  of WT) (**Figure 2b–e**, **Figure 6—figure supplement 1a–d**, **Supplementary file 1b**). The decreased ADP-release rate implies that these converter residues play a role in the stability of the strong-ADP state the motor populates when attached to actin. It is likely that a smaller step size also contributes to the reduced speed at which the mutant motor moves actin, because in silico studies show that the AAA mutant fails to maintain the WT lever arm orientation, although the Converter stays oriented in a primed orientation (**Figure 6c**).

## The PfELC is essential for *Plasmodium* invasion

As described above, the PfELC is uniquely suited to bind to the degenerate IQ motif and is also engaged in stabilizing the unusual priming of this motor, as well as being an essential element to maintain the rigidity of the lever arm. To validate this essential role and to test whether alternate



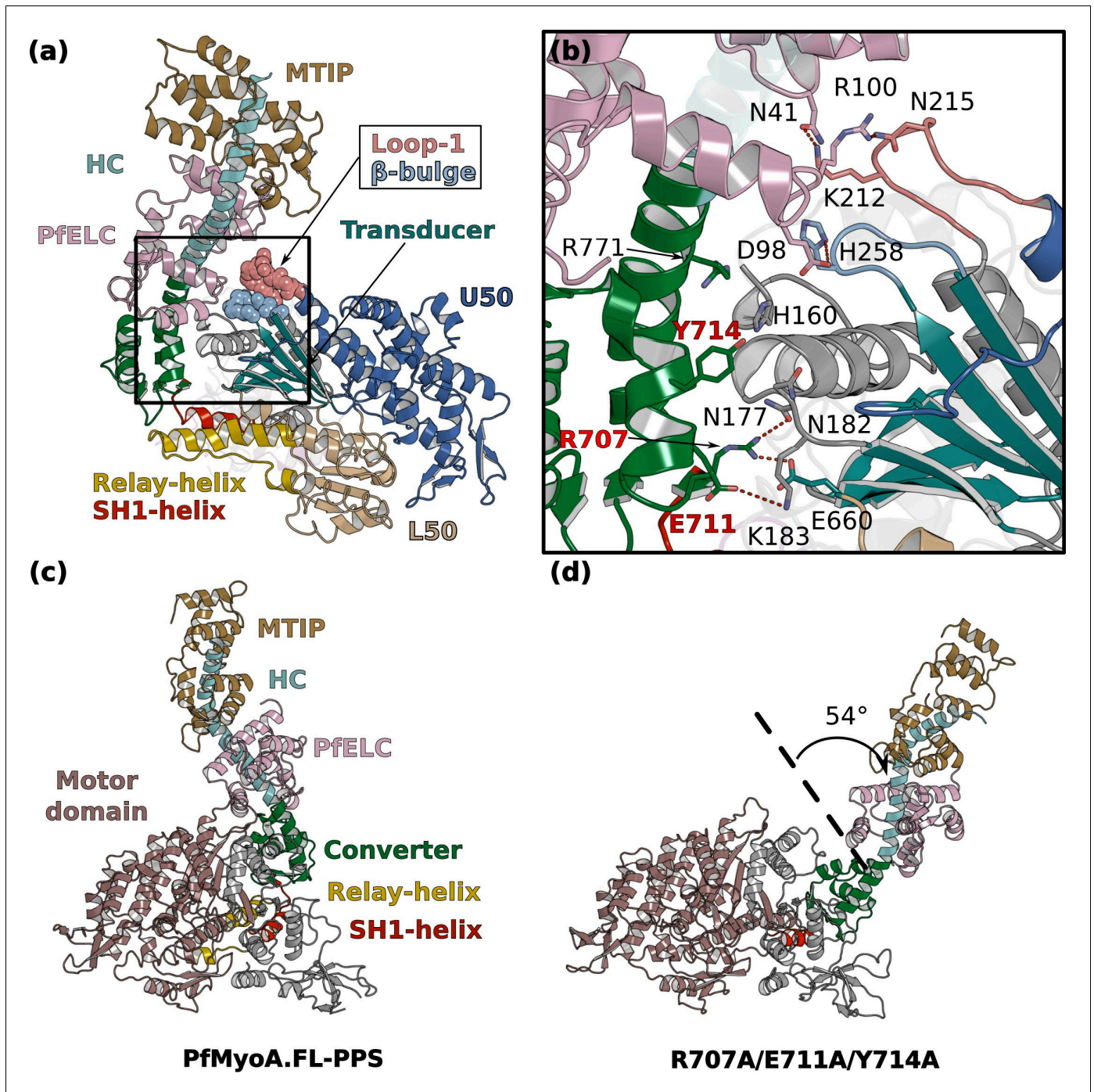
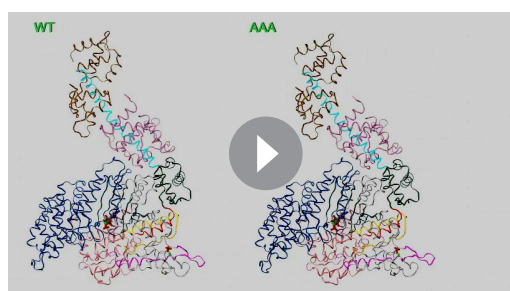


**Figure 6.** Interactions stabilizing the priming of the PfMyoA PPS state. (a) Overall structure of PfMyoA-FL-PPS. The priming of the lever arm is stabilized by interactions between elements of the lever arm and the motor domain (boxed in black). (b) Zoom on the lever arm/motor domain interface. The residues involved in the interaction are labeled. Key residues that have been mutated to disrupt the interface (see d) are labeled red. (c,d) MD simulations comparing the WT and triple mutant R707A/E711A/Y714A. (c) The primed PPS state is stable during the entire duration of the simulation (320 ns). (d) In contrast, the priming is lost with the triple R707A/E711A/Y714A mutant and the position of the lever arm deviates by up to 54°. The online version of this article includes the following source data and figure supplement(s) for figure 6:

**Figure supplement 1.** Transient kinetics and genetic engineering of the parasite.

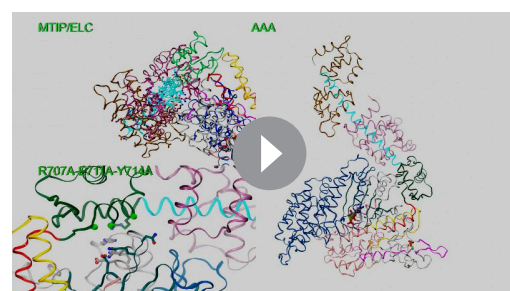
**Figure supplement 1—source data 1.** Source data for kinetic experiments presented in **Figure 6—figure supplement 1**.

**Figure supplement 2.** Interactions between the motor domain (MD) and the lever arm stabilizing the priming in PPS in different myosins.



**Video 3.** Comparison of the dynamics on the structure of the molecular dynamics performed on the structures of full-length (FL) PfMyoA in the PPS state wild-type (WT) and of the in silico generated AAA mutant (R707A/E711A/Y714A).

<https://elifesciences.org/articles/60581#video3>



**Video 4.** Comparison of the dynamics on the structure of the molecular dynamics performed on the structures of FL PfMyoA in the PPS state wild-type (WT) and of the in silico generated AAA mutant (R707A/E711A/Y714A).

<https://elifesciences.org/articles/60581#video4>

light chains might compensate for PfELC function (as exists in *T. gondii* [Williams et al., 2015]), we generated a conditional knockout (cKO) for the *PfELC* gene in *Plasmodium falciparum*. Using a combined process of drug selection-linked integration and engineering of artificial Cre recombinase sites into the *PfELC* gene via synthetic introns (Jones et al., 2016; Birnbaum et al., 2017; Figure 7—figure supplement 1a), we were able to selectively induce PfELC truncation at the protein C-terminus (lacking amino acids 93–134, predicted to render it non-functional). Integration of the introns did not affect parasite asexual growth (Figure 7a). Treatment with rapamycin, inducing DiCre dimerization and gene excision, led to gene truncation (as validated by PCR Figure 7—figure supplement 1b). Truncation was also confirmed by immunoblot and immunofluorescence assay (Figure 7b, c and d). Analysis of rapamycin-treated parasites was associated with a near complete ablation of red blood cell invasion over 60 hr of an asexual growth cycle, on a par with inhibition levels seen with the non-specific invasion inhibitor heparin (Boyle et al., 2010; Figure 7e). Further analysis over a single 48 hr or double 96 hr cycle showed that this inhibition of invasion was near total (Figure 7f and g) suggesting residual invasion after a single cycle is likely the result of incomplete gene excision. The level of invasion retardation following loss of PfELC suggests that, like the heavy chain PfMyoA (Robert-Paganin et al., 2019), PfELC is essential for asexual blood-stage life-cycle progression. Unlike *T. gondii*, there is no evidence for redundancy in essential light chains. Both PfMyoA motor domain and PfELC thus represent attractive targets for arresting parasite invasion in pathogenic blood stages.

## Discussion

The FL PfMyoA structures reveal how the atypical lever arm of this myosin is part of the adaptations tuning its motor cycle. This information could not be extracted from the previous PfMyoA-MD (Robert-Paganin et al., 2019) and TgMyoA-MD (Powell et al., 2018) structures that lacked the IQ region bound to its specific light chains. The PPS-FL structure of the PfMyoA motor reveals how critical adaptations in the converter and PfELC play a central role in defining and stabilizing the PPS lever arm orientation.

Unexpectedly, the lever arm of PfMyoA is ~30° more primed upon reattachment to the actin track than it is in conventional class II myosins. Designed from structural insights, in vitro and in silico experiments reveal that specific interactions stabilize the priming of PfMyoA and define specific adaptations tuning the properties of this motor. These interactions are not present in ScMyo2 (Figure 6—figure supplement 2). Myo10 and Myo1c are two motors for which the lever arm priming position is also large in the PPS (Ropars et al., 2016), (Münnich et al., 2014), but their lever arm orientation is stabilized by a different set of interactions when compared with PfMyoA (Figure 6—figure supplement 2). The contribution of the transducer in the stabilization of the primed lever arm also differs in the three myosins. It is thus tempting to speculate that the nature of these interactions will tune each motor for its specific functions. Increasing the amplitude of the lever

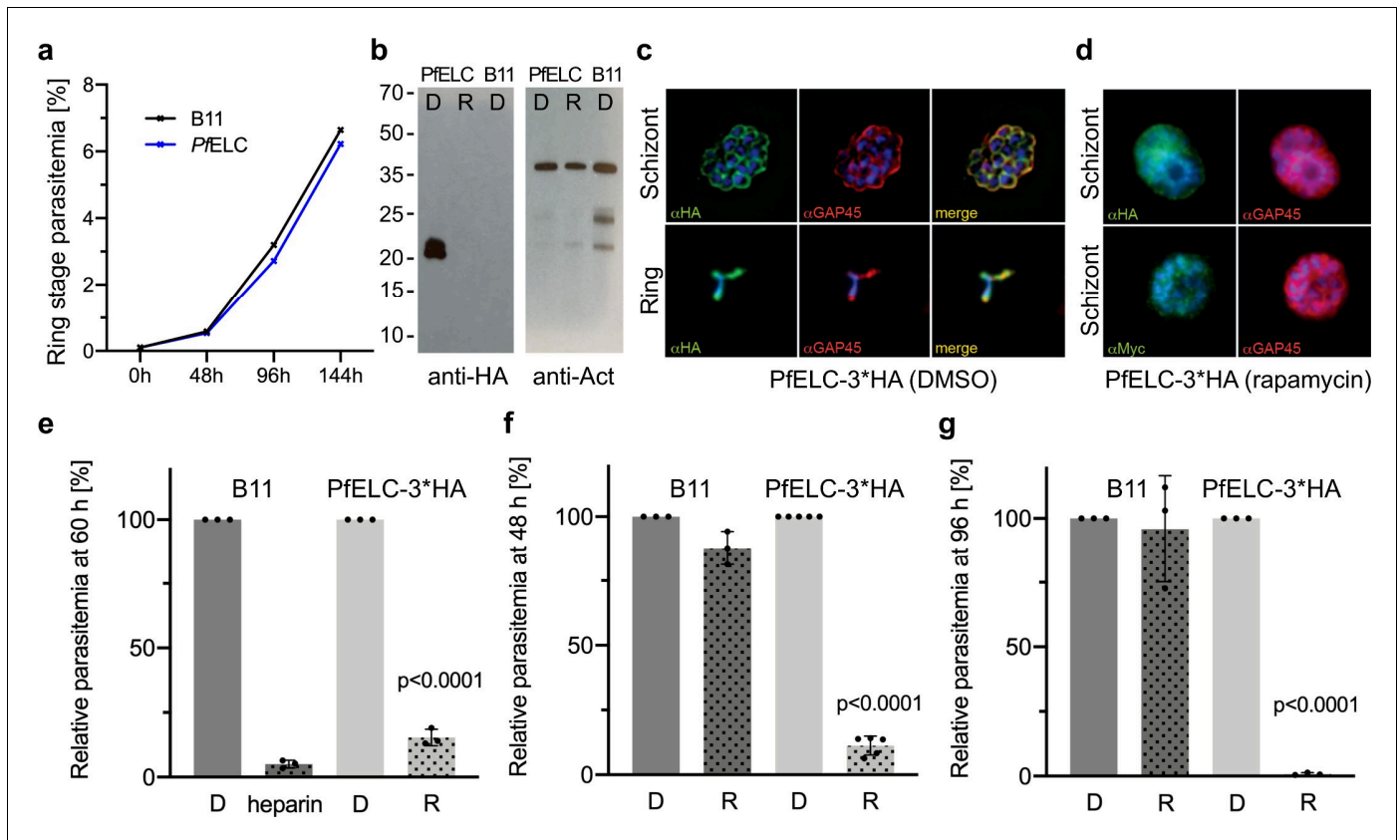


**Figure 7.** PfELC is essential for parasite invasion of the red blood cell. (a) Growth curve comparing wildtype (B11) and PfELC-3xHA parasites over the course of three cycles indicates no detrimental effect of genetic modification in the *pfelc* locus. Mean ring-stage parasitemia is shown of two biological replicates as determined by flow cytometry. (b) Western blot analysis of parasite extracts separated by SDS-PAGE probed with anti-HA and anti-actin antibodies as a loading control. PfELC-3xHA runs at the expected MW of ~21 kDa in mock DMSO-treated samples (D) and the HA signal is lost upon treatment with rapamycin (R), indicating successful excision. (c–d) Representative immunofluorescence assays (IFAs) of schizont and ring-stage parasites co-labeled with the IMC marker GAP45. Peripheral staining is lost after treatment with rapamycin and a diffuse/punctate pattern is seen with anti-cMyc antibodies. (e) R-treated PfELC-3xHA parasites are significantly impaired in invading red blood cells as determined by flow cytometry analysis of ring-stage parasites over 60 hr, comparable to that seen with the non-specific inhibitor heparin. A small amount of residual invasion seen after 48 hr (f) disappears after 96 hr post-treatment (g) suggesting that the absence of PfELC results in complete ablation of invasion. D-treated parasites show no invasion defect. Parasitemias were normalized to D-treated for each line, bars show mean  $\pm$  S.D.

The online version of this article includes the following source data and figure supplement(s) for figure 7:

**Source data 1.** Source data for parasitology experiments presented in **Figure 7**.

**Figure supplement 1.** Genetic integration of LoxP Cre recombinase sites into the *Pfelc* gene of *Plasmodium falciparum*.

arm priming could be a way to lengthen the step size of the motor and thus to increase the speed at which it can move actin. This is consistent with the reduced speed of in vitro motility obtained with PfMyoA mutants designed to reduce the priming of the lever arm as well as data for Myo10 indicating that this motor is tuned for performing large steps on actin bundles (Ropars et al., 2016). Specific interactions with the transducer may also be involved in enlarging the stroke and tuning the orientation of the powerstroke for high duty-ratio motors able to resist rearwards load, as with the Myo1b motor that anchors the cell membrane to the cytoskeleton (Clark et al., 2005). As it is the case for class I myosins (Shuman et al., 2014), (Greenberg et al., 2015), the duty-ratio of PfMyoA is regulated by a specific N-terminal HC extension (Robert-Paganin et al., 2019). The observation that converter mutations involved in priming PfMyoA also decrease the ADP-release rate suggests that these converter residues might be involved in facilitating the transitions occurring during the PfMyoA powerstroke.



Atomic structures of the PfMyoA lever arm indicate how degenerate IQ motifs of the HC are recognized by PfELC and MTIP, as well as how unusual apolar interactions occur between PfELC and the converter. These unusual features could not have been predicted from recently solved TgMyoA structures of the lever arm bound to TgELC or TgELC2 (Pazicky *et al.*, 2019), because TgELC is a poor model for PfELC considering the low sequence identity (20% and 21% between PfELC and TgELC and TgELC2, respectively). Interestingly, TgELC1 and TgELC2 are homologous to classical ELCs and do not display the specific inter-lobe linker nor the atypical  $\alpha 5^*$  and  $\alpha 5'^*$  helices found in PfELC, which are also part of the interface with the Converter. This structural difference illustrates again that Myosin A from different organisms differ in detail due to the high divergence of the different taxa from the Apicomplexa phylum. The structure of PfELC and its specific association with the HC and MTIP also explains the cooperative binding of these elements and why PfELC does not bind to the HC in the absence of MTIP (Bookwalter *et al.*, 2017). Indeed, the structures reveal a sequence shift near the pliant region resulting in a specific orientation of the HC helix to stabilize the converter/PfELC interface (Figure 4—figure supplement 2). The PfELC  $\alpha 5^*$  and  $\alpha 5'^*$  helices are involved in this interface but may not be properly folded prior to its establishment. In addition, PfELC cannot surround the IQ1 motif due to its unusual inter-lobe linker, which may contribute to diminishing a stable association with the HC. According to this hypothesis, PfMTIP may need to bind first to the IQ2 motif and its presence could add stabilizing interactions to cooperatively recruit PfELC to the PfIQ1 motif via formation of the interfaces with PfMTIP and the Converter, allowing stabilization of the PfELC  $\alpha 5^*$  and  $\alpha 5'^*$  helices. PfELC is thus a weak point in the assembly of the fully functional motor complex, and compounds targeting PfELC may be a good strategy for decreasing motor activity. PfMyoA lacking the ELC moves actin at half the speed of the motor containing both light chains (Bookwalter *et al.*, 2017). Surprisingly, the ensemble force of PfMyoA lacking the PfELC is comparable to that of the motor with both light chains (Figure 6—figure supplement 1e). This is in contrast to what was seen with skeletal muscle myosin, in which the absence of the ELC results in a twofold reduction in isometric force (VanBuren *et al.*, 1994). One possibility is that the atypical priming of the PfMyoA lever arm in the PPS state, which results from several interactions that are not present in conventional myosins, is responsible for allowing force to remain high in the absence of the ELC. It should be noted that video microscopy showed that PfELC cKO merozoites can still deform red blood cells, unlike cKO of PfMyoA heavy chain (Blake *et al.*, 2020). Nonetheless, cKO of either PfMyoA or PfELC left merozoites entirely incapable of invasion. The reduced speed of PfMyoA in vitro without PfELC may thus be sufficient to disrupt invasion. Alternative possibilities are that in vivo other factors need to be considered that are not assessed by the in vitro assays. In vivo, the lack of the PfELC may result in proteolysis that would effectively decrease the number of functional motors. In addition, the shortened neck in the absence of the PfELC may not allow the motor to reach the actin filaments as effectively as the WT does, within the constraints of the space between the plasma membrane and inner membrane complex.

Taken together, the data presented here reveal important new findings about the PfMyoA motor, and how the lever arm is involved in tuning the specific mechano-properties of this atypical myosin. While the N-terminal HC extension of PfMyoA is involved in regulating the transition between the strong -ADP and the rigor states, the sequence adaptations located in the relay, the SH1-helix or the wedge (Robert-Paganin *et al.*, 2019) influence other structural transitions essential for motor function. We show that the overall stabilization of the PPS differs in this myosin compared with all other myosins in the superfamily. Control of the recovery and powerstroke transitions differ in detail although the overall sequence allows conservation of the essential properties of a motor: the ability to couple the lever arm priming with ATP hydrolysis and control of the powerstroke via interaction with F-actin, associated with sequential controlled release of the products phosphate and ADP.

Lastly, we have also demonstrated that PfELC, like PfMyoA (Robert-Paganin *et al.*, 2019), is essential in parasite asexual invasion of the red blood cell and therefore a second attractive target within the glideosome for targeting malaria parasite asexual replication, where absence of either alone or in combination would block red blood cell entry. While strategies to disrupt the glideosome have already been investigated (Perrin *et al.*, 2018), inhibition of the PfMyoA motor (Robert-Paganin *et al.*, 2019) or the association of the PfELC light chain opens up new strategies toward therapeutic solutions. Importantly, the structures described here provide a precise blueprint for designing just such small molecules that could prevent binding of PfELC or target PfMyoA full-length

motor activity and thus diminish glideosome function. These results inform the design of new therapies that specifically target life-cycle progression in the pathogenic blood stages of *Plasmodium*.

## Materials and methods

### Expression constructs

Full-length PfMyoA heavy chain (PlasmoDB ID PF3D7\_1342600/GenBank accession number XM\_001350111.1), with Sf9 cell preferred codons, was cloned into the baculovirus transfer vector pFastBac (pFB) (Thermo Fisher). A 13 amino acid linker separates the C-terminus of the PfMyoA heavy chain from an 88 amino acid segment of the *Escherichia coli* biotin carboxyl carrier protein (Cronan, 1990), which gets biotinylated during expression in Sf9 cells, followed by a C-terminal FLAG tag for purification via affinity chromatography. Heavy chain mutants (point mutants E6R, T586F, S691G; triple mutants R707A/E711A/Y714A and R707L/E711R/Y714A) were generated on this backbone using site directed mutagenesis. An N-terminal truncation of MTIP (MTIP- $\Delta$ n, residues 1-E60 deleted and an N-terminal HIS tag), and an N-terminal truncation of the heavy chain ( $\Delta$ N-terminal HC extension ( $\Delta$ Nter), residues 1-S20 deleted) were also cloned for use in constructs that were crystallized. Recombinant baculovirus was produced using the Bac-to-Bac Baculovirus expression system (Thermo Fisher). The mouse utrophin (NP\_035812) clone was a gift from Kathleen Ruppel and James Spudich. It was modified so that utrophin residues 1-H416 were followed by C-terminal biotin and FLAG tags. It was cloned into pFastbac for production of recombinant baculovirus and subsequent expression in Sf9 cells.

### Myosin expression and purification

For biochemical characterization, FL PfMyoA heavy chain mutant constructs were co-expressed with the chaperone PUNC and the light chains (PfMTIP and PfELC) in Sf9 cells as described in Bookwalter et al., 2017. Two constructs were expressed for crystallization. In one, the WT heavy chain, PfELC, and MTIP- $\Delta$ n were co-expressed with the chaperone PUNC. In the second,  $\Delta$ Nter heavy chain, PfELC, and MTIP- $\Delta$ n were co-expressed with the chaperone PUNC. The cells were grown for 72 hr in medium containing 0.2 mg/ml biotin, harvested and lysed by sonication in 10 mM imidazole, pH 7.4, 0.2M NaCl, 1 mM EGTA, 5 mM MgCl<sub>2</sub>, 7% (w/v) sucrose, 2 mM DTT, 0.5 mM 4-(2-aminoethyl)benzenesulfonyl fluoride, 5  $\mu$ g/ml leupeptin, 2 mM MgATP. An additional 2 mM MgATP was added prior to a clarifying spin at 200,000  $\times$  g for 40 min. The supernatant was purified using FLAG-affinity chromatography (Sigma). The column was washed with 10 mM imidazole pH 7.4, 0.2M NaCl, and 1 mM EGTA and the myosin eluted from the column using the same buffer plus 0.1 mg/ml FLAG peptide. The fractions containing myosin were pooled and concentrated using an Amicon centrifugal filter device (Millipore), and dialyzed overnight against 10 mM imidazole, pH 7.4, 0.2M NaCl, 1 mM EGTA, 55% (v/v) glycerol, 1 mM DTT, and 1  $\mu$ g/ml leupeptin and stored at  $-20^{\circ}\text{C}$ . Utrophin purification was essentially the same as for myosin but without the MgATP steps. Skeletal muscle actin was purified from chicken skeletal muscle tissue essentially as described in Pardee and Spudich, 1982.

### Biochemical assays

Unloaded and loaded in vitro motility assays, actin-activated ATPase assays, and transient kinetic measurements were performed as described in Robert-Paganin et al., 2019. Skeletal muscle actin was used for all in vitro assays.

### Crystallization and data processing

Crystals of PfMyoA•FL-PR (10 mg.ml<sup>-1</sup>) (Type A) were obtained at 4°C by the hanging drop vapor diffusion method from a 1:1 (v:v) of protein with 2 mM MgADP and precipitant containing 1.9M ammonium sulfate, 0.1M sodium HEPES pH 6.8, 2% PEG400. Crystals of PfMyoA•FL-PPS (Type B) were obtained at 17°C by the sitting drop vapor diffusion method from a 1:1 mixture of protein (10 mg.ml<sup>-1</sup>) with 2 mM MgADP.VO<sub>4</sub> and precipitant containing 1M Na Citrate tribasic; 0.01M Na Borate pH 8.0. Crystals of PfMyoA• $\Delta$ Nter-PR were obtained at 4°C by the hanging drop vapor diffusion method from a 1:1 mixture of protein (10 mg.ml<sup>-1</sup>) with 2 mM MgADP and precipitant containing 2.0M Ammonium sulfate, 0.1M Sodium HEPES pH 7.5, 6% PEG400.

Crystals were transferred in the mother liquor containing 30% glycerol before and flash freezing in liquid nitrogen. X-ray diffraction data were collected at the SOLEIL synchrotron, on PX1 beamline ( $\lambda = 0.906019$  Å for type A,  $\lambda = 0.978570$  Å for type B,  $\lambda = 0.978570$  Å for type C), at 100 K. Diffraction data were processed using the XDS package (Kabsch, 2010) and AutoPROC (Vonnrhein et al., 2011). Crystals type A and C belong to the  $P2_12_12_1$  space group, crystals type B belong to the  $P2_12_12$  space group, with one molecule per asymmetric unit for type A and C and two molecules per asymmetric unit for type B. The data collection and refinement statistics for these crystals are presented in (Supplementary file 1a).

## Structure determination and refinement

Molecular replacement was performed with the PfMyoA motor domain coordinates (21-768) (PDB code 6I7E for the PPS; PDB code 6I7D chain A for the PR [Robert-Paganin et al., 2019]) with Phaser (McCoy et al., 2007). The structure in the PR state (PDB code 6I7D, chain A) without ligand and water was used as a target model for type A and C crystals. PfMyoA motor domain in the PPS state (PDB code 6I7E) was used as a target model for type B crystals. Manual model building was achieved using Coot (Emsley and Cowtan, 2004), the structure of MTIP complexed with the cognate IQ motif peptide (PDB code 4OAM (Douse et al., 2012) was used to rebuild MTIP). Refinement was performed using Buster (Bricogne, 2017). The statistics for most favored, allowed and outlier in Ramachandran angles are for each crystal type respectively (in %): 96.40, 3.41, 0.19 for PfMyoA•FL-PR; 91.93, 6.80 and 1.27 for PfMyoA•FL-PPS; 93.12, 5.92, 0.96 for PfMyoA•ΔNter-PR.

## SAXS experiments

SAXS data were collected at the SOLEIL synchrotron, on the SWING beamline ( $\lambda = 1.03319947498$  Å). Purified PfMyoA/ELC/MTIP-Δn was extensively dialyzed against 10 mM HEPES pH 7.4, 100 mM NaCl, 1 mM DTT, 1 mM NaN<sub>3</sub> (without any ATP) in order to remove nucleotide. We prepared two samples PfMyoA-PR and PfMyoA-PPS. Both were subsequently incubated with 2 mM MgADP for 20 min on ice, and then we added 2 mM vanadate for PfMyoA-PPS, but not for PfMyoA-PR. All samples were centrifuged at  $20,000 \times g$  for 10 min at 4°C prior to the analysis. 40 μl of the protein at 2, 5 and 9 mg.ml<sup>-1</sup> (17, 41 and 75 μM, respectively) were injected between two air bubbles using the auto-sampler robot. Thirty-five frames of 1.5 s exposure were averaged and buffer scattering was subtracted from the sample data. As all 2, 5 and 9 mg ml<sup>-1</sup> curves displayed no traces of aggregation, only the 9 mg.ml<sup>-1</sup> curve was used for further analysis because of the higher signal/noise ratio. The theoretical SAXS curves were calculated with CRY SOL and compared based on the quality of their fits against the different experimental curves. We computed the SAXS envelopes of the two samples with GASBOR, two programs from the ATSAS suite (Franke et al., 2017). The analysis and the fit of the computed SAXS envelopes and the X-ray structures were performed with FoXS (Schneidman-Duhovny et al., 2016). Furthermore, to analyze if we have a mixed population of PR-Closed and PR-open conformations of PfMyoA-PR in solution we used Oligomer (Franke et al., 2017). The model of PR-open conformation used in this study was generated by Swiss model (Waterhouse et al., 2018) after manual positioning of the lever arm, as found in the PPS structure in which the pliant region is not kinked.

## Molecular dynamics

Molecular dynamics experiments were performed with a procedure close to Robert-Paganin et al., 2018. All the systems (WT + mutants) were built with the CHARM-GUI (Brooks et al., 2009; Jo et al., 2017), with the Solution Builder module. The entire proteins were relaxed in a box containing explicit water (TIP3P) and salt (150 mM KCl) at 310.15 K in the CHARMM36m force field (Huang et al., 2017). The duration of the simulations was 320 ns in GROMACS (version 2018.3) (Abraham et al., 2015).

## Generation of the PfELC<sub>loxP</sub> construct

A gene fragment (GeneArt) was synthesized comprising a 454 bp targeting sequence of the *pfelc* gene (3D7\_1017500), a loxP module replacing the second intron and the last 126 bp (codon-optimized) exon, encoding the C-terminal end of PfELC (Ile93 to Ile134) and a triple hemagglutinin tag. The fragment was cloned into the NotI/AvrII site of a modified version of the conditional KO vector

(Tibúrcio *et al.*, 2019), containing the SLI elements (Birnbaum *et al.*, 2017) and a cMyc/FLAG tag. The resulting plasmid was purified from *E. coli* using the Qiagen Plasmid Maxi kit.

### ***P. falciparum* culture and transfection**

*P. falciparum* B11 parasites expressing the DiCre recombinase (Perrin *et al.*, 2018) were cultured in RPMI 1640 medium containing 0.5% w/v AlbumaxII and at 4% hematocrit using human erythrocytes (blood group O<sup>+</sup>) according to standard procedures (Trager and Jensen, 1976). Ring-stage parasites were synchronized with 5% sorbitol (w/v) and transfected with 100 µg of purified pARL PfELC<sub>loxP</sub> plasmid. Transgenic parasites harbouring the episomal plasmid were initially selected with 2.5 nM WR99210 (Jacobus Pharmaceuticals) for 7 days and integration into the genomic locus was achieved by G418 treatment (400 µg/ml) for 10 days.

DiCre-mediated excision was achieved by treating synchronized ring-stage parasites with 100 nM rapamycin (Sigma) in DMSO for 14–16 hr. Additionally, parasites were mock-treated with 1% (v/v) DMSO as a negative control. Cultures were washed three times with culture media to remove rapamycin and DMSO, respectively. Treated parasites were transferred into 96-well plates at 0.1% parasitemia (in triplicate) containing fresh red blood cells at 0.1% hematocrit and were allowed to proceed to the next ring-stage cycle for FACS analysis. Samples for gDNA extraction and PCR amplification, western blot and immunofluorescence analysis were taken toward the end of the treatment cycle or subsequent cycles. Parallel assays were carried out with a negative control, B11 parasites treated with heparin throughout (Pfizer, 1:25). For these assays, parasites were treated with rapamycin and washed as above, then transferred to 48-well plates at 1% parasitaemia (in triplicate) containing fresh red blood cells at 5% hematocrit and parasitaemia was analyzed as above, at around 60 hr post-treatment.

### **Genotyping, western blot analysis and immunofluorescence assays**

DNA was extracted using the PureLink Genomic DNA Mini kit (Invitrogen) for genotyping by PCR using primers P1 5' CATTACTTTAATTTTATACTACTGTTTATTTTACAGTAC 3', P2 5' CTAATCC TATTATTT AAATATTTTCATATTTTAAACATAGATGG 3', P3 5' GGCCAGCCACGATAGCCGCGC TGCCTCG 3', P4 5' CTTGTCGTCATCGTCTTTGTAGTCCTTGTC 3' and P5 5' CAGGAAACA GCTA TGACCATG 3' and KOD Hot Start DNA Polymerase (Millipore).

Schizonts were lysed with 0.2% saponin/PBS, washed three times with PBS (supplemented with cOmplete EDTA-free protease inhibitors, Roche) and resuspended in 1x SDS loading dye. Proteins were separated on NuPAGE Novex 4–12% Bis-Tris protein gels in MES buffer (Life Technologies) and were transferred onto nitrocellulose membranes using the iBlot system (Life Technologies). Membranes were blocked in 5% skim milk/PBS (w/v) and probed with the following antibodies diluted in 5% skim milk/PBS (w/v): anti-HA (1:4000, clone C29F4, Cell Signaling), anti-cMyc (1:100, clone 9E10, Invitrogen) and rabbit anti F-actin (Angrisano *et al.*, 2012)(1:1000), Horseradish peroxidase-conjugated goat anti-rabbit and goat anti-mouse antibodies were used as secondary antibodies and diluted 1:10,000 (Jackson IR).

Late stage parasites were treated with cysteine protease inhibitor E64 (10 µM) for 4 hr prior to fixation with 4% PFA/0.0025% glutaraldehyde/PBS for 1 hr. Fixed cells were permeabilised with 0.1% TX-100/PBS for 15 min, blocked in 3% BSA and probed with anti-HA (clone 12CA5, Roche), anti-cMyc (clone 9E10, Invitrogen) and anti-GAP45 (Baum *et al.*, 2006) antibodies at 1:500 in 3% BSA/PBS for 1 hr, followed by three washes in PBS. Secondary Alexa Fluor conjugated antibodies (Invitrogen) and DAPI (4',6-diamidino-2-phenylindole) were diluted at 1:4000 and incubated for 1 hr, followed by three washes in PBS. Images were acquired with an OrcaFlash4.0 CMOS camera using a Nikon Ti Microscope (Nikon Plan Apo 100 × 1.4 N.A. oil) and Z-stacks were deconvolved using the EpiDEMIC plugin with 80 iterations in Icy (de Chaumont *et al.*, 2012). Images were processed in Fiji/Image J (Schindelin *et al.*, 2012) Representatives of 3–5 biological replicates are shown. Significance was assessed by unpaired t-test, two tailed.

### **Growth analysis by FACS**

Tightly synchronized ring-stage parasites were diluted to 0.1% parasitemia (in triplicate) for growth curves and transferred into 96-well plates containing fresh red blood cells at 0.1% hematocrit. Parasites were allowed to proceed to the next ring-stage cycle, were stained with SYBR Green (1:10,000,



Sigma) for 10 min and washed three times with PBS prior to collection by flow cytometry using a BD LSRFortessa. A 100,000 cells were counted and FCS vs SSC was used to gate for red blood cells, SSC-A vs SSC-W for singlets and FSC-H vs SYBR-A was applied to gate for infected red blood cells. Flow cytometry data were analyzed in FlowJo. Biological replicates are indicated in the figures.

## Acknowledgements

We are grateful to beamline scientists of PX1 (SOLEIL synchrotron) for excellent support during data collection. We thank Margaret A Titus for critical reading of the manuscript. This work was supported by National Institutes of Health multi-PI grant AI 132378 to KMT and AH and Human Frontier Science Program grant to JB and AH (RGY0066/2016). Parasite work was funded through an Investigator Award to JB (100993/Z/13/Z) and PhD studentship to TCAB (109007/Z/15/A) both from Wellcome. The AH team is part of the Labex CeTisPhyBio:11-LBX-0038, which is part of the IDEX PSL (ANR-10-IDEX-0001-02 PSL).

## Additional information

### Funding

Funder	Grant reference number	Author
National Institute for Health Research	AI 132378	Kathleen M Trybus Anne Houdusse
Human Frontier Science Program	RGY0066/2016	Jake Baum Anne Houdusse
Wellcome Trust	100993/Z/13/Z	Jake Baum
Wellcome Trust	109007/Z/15/A	Thomas C A Blake

The funders had no role in study design, data collection and interpretation, or the decision to submit the work for publication.

### Author contributions

Dhia Moussaoui, Visualization, Data curation, Formal analysis, Investigation, Methodology, Writing - original draft, Writing - review and editing; James P Robblee, Data curation, Formal analysis, Investigation, Writing - review and editing; Daniel Auguin, Data curation, Formal analysis, Validation, Investigation, Visualization, Methodology, Writing - review and editing; Elena B Krementsova, Data curation, Formal analysis, Investigation, Methodology; Silvia Haase, Data curation, Formal analysis, Investigation; Thomas CA Blake, Data curation, Formal analysis, Methodology, Writing - review and editing; Jake Baum, Formal analysis, Validation, Visualization, Methodology, Writing - review and editing; Julien Robert-Paganin, Data curation, Formal analysis, Supervision, Validation, Visualization, Methodology, Writing - original draft, Project administration, Writing - review and editing; Kathleen M Trybus, Conceptualization, Data curation, Formal analysis, Supervision, Funding acquisition, Validation, Investigation, Methodology, Project administration, Writing - review and editing; Anne Houdusse, Conceptualization, Data curation, Formal analysis, Supervision, Funding acquisition, Validation, Methodology, Writing - original draft, Project administration, Writing - review and editing, Visualization

### Author ORCIDs

Dhia Moussaoui  <https://orcid.org/0000-0002-1605-9619>

Thomas CA Blake  <https://orcid.org/0000-0002-8534-0025>

Jake Baum  <http://orcid.org/0000-0002-0275-352X>

Julien Robert-Paganin  <https://orcid.org/0000-0001-6102-2025>

Kathleen M Trybus  <https://orcid.org/0000-0002-5583-8500>

Anne Houdusse  <https://orcid.org/0000-0002-8566-0336>

## Decision letter and Author response

Decision letter <https://doi.org/10.7554/eLife.60581.sa1>Author response <https://doi.org/10.7554/eLife.60581.sa2>

## Additional files

## Supplementary files

- Supplementary file 1. Supplementary tables. (a) Data collection and refinement statistics (molecular replacement). (b) Kinetic and motility parameters of PfMyoA mutants. (c) Dissociation of acto-PfMyoA by MgATP at 20°C.

## Data availability

The atomic models are available in the PDB under accession numbers PDB 6YCX, 6YCY and 6YCZ for the PfMyoA•FL-PR, PfMyoA•FL-PPS and PfMyoA•ΔNter-PR, respectively.

The following datasets were generated:

Author(s)	Year	Dataset title	Dataset URL	Database and Identifier
Moussaoui D, Robblee JP, Auguin D, Krementsova EB, Robert-Paganin J, Trybus KM, Houdusse A	2020	<i>Plasmodium falciparum</i> Myosin A full-length, post-rigor state	<a href="https://www.rcsb.org/structure/6YCY">https://www.rcsb.org/structure/6YCY</a>	RCSB Protein Data Bank, 6YCY
Moussaoui D, Robblee JP, Auguin D, Krementsova EB, Robert-Paganin J, Trybus KM, Houdusse A	2020	<i>Plasmodium falciparum</i> Myosin A delta-Nter, Post-Rigor state	<a href="https://www.rcsb.org/structure/6YCZ">https://www.rcsb.org/structure/6YCZ</a>	RCSB Protein Data Bank, 6YCZ
Moussaoui D, Robblee JP, Auguin D, Krementsova EB, Robert-Paganin J, Trybus KM, Houdusse A	2020	PfMyoA•FL-PR	<a href="https://www.rcsb.org/structure/6YCX">https://www.rcsb.org/structure/6YCX</a>	RCSB Protein Data Bank, 6YCX

## References

- Abraham MJ**, Murtola T, Schulz R, Páll S, Smith JC, Hess B, Lindahl E. 2015. GROMACS: high performance molecular simulations through multi-level parallelism from laptops to supercomputers. *SoftwareX* **1-2**:19–25. DOI: <https://doi.org/10.1016/j.softx.2015.06.001>
- Angrisano F**, Riglar DT, Sturm A, Volz JC, Delves MJ, Zuccala ES, Turnbull L, Dekiwadia C, Olshina MA, Marapana DS, Wong W, Mollard V, Bradin CH, Tonkin CJ, Gunning PW, Ralph SA, Whitchurch CB, Sinden RE, Cowman AF, McFadden GI, et al. 2012. Spatial localisation of actin filaments across developmental stages of the malaria parasite. *PLOS ONE* **7**:e32188. DOI: <https://doi.org/10.1371/journal.pone.0032188>, PMID: 22389687
- Baum J**, Richard D, Healer J, Rug M, Krnajska Z, Gilberger TW, Green JL, Holder AA, Cowman AF. 2006. A conserved molecular motor drives cell invasion and gliding motility across malaria life cycle stages and other apicomplexan parasites. *Journal of Biological Chemistry* **281**:5197–5208. DOI: <https://doi.org/10.1074/jbc.M509807200>, PMID: 16321976
- Birnbaum J**, Flemming S, Reichard N, Soares AB, Mesén-Ramírez P, Jonscher E, Bergmann B, Spielmann T. 2017. A genetic system to study *Plasmodium falciparum* protein function. *Nature Methods* **14**:450–456. DOI: <https://doi.org/10.1038/nmeth.4223>, PMID: 28288121
- Blake TCA**, Haase S, Baum J. 2020. Actomyosin forces and the energetics of red blood cell invasion by the malaria parasite *Plasmodium falciparum*. *bioRxiv*. DOI: <https://doi.org/10.1101/2020.06.25.171900>
- Bookwalter CS**, Tay CL, McCrorie R, Previs MJ, Lu H, Krementsova EB, Fagnant PM, Baum J, Trybus KM. 2017. Reconstitution of the core of the malaria parasite glideosome with recombinant *Plasmodium* class XIV myosin A and *Plasmodium* actin. *Journal of Biological Chemistry* **292**:19290–19303. DOI: <https://doi.org/10.1074/jbc.M117.813972>, PMID: 28978649



- Bosch J, Turley S, Daly TM, Bogh SM, Villasmil ML, Roach C, Zhou N, Morrissey JM, Vaidya AB, Bergman LW, Hol WG. 2006. Structure of the MTIP-MyoA complex, a key component of the malaria parasite invasion motor. *PNAS* **103**:4852–4857. DOI: <https://doi.org/10.1073/pnas.0510907103>, PMID: 16547135
- Bosch J, Turley S, Roach CM, Daly TM, Bergman LW, Hol WG. 2007. The closed MTIP-myosin A-tail complex from the malaria parasite invasion machinery. *Journal of Molecular Biology* **372**:77–88. DOI: <https://doi.org/10.1016/j.jmb.2007.06.016>, PMID: 17628590
- Boyle MJ, Richards JS, Gilson PR, Chai W, Beeson JG. 2010. Interactions with heparin-like molecules during erythrocyte invasion by *Plasmodium falciparum* merozoites. *Blood* **115**:4559–4568. DOI: <https://doi.org/10.1182/blood-2009-09-243725>, PMID: 20220119
- Bricogne G. 2017. BUSTER. 2.10.2. Glob Phasing Ltd. <https://www.globalphasing.com/buster/wiki/index.cgi?BusterCite>
- Brooks BR, Brooks CL, Mackerell AD, Nilsson L, Petrella RJ, Roux B, Won Y, Archontis G, Bartels C, Boresch S, Caflisch A, Caves L, Cui Q, Dinner AR, Feig M, Fischer S, Gao J, Hodoscek M, Im W, Kuczera K, et al. 2009. CHARMM: the biomolecular simulation program. *Journal of Computational Chemistry* **30**:1545–1614. DOI: <https://doi.org/10.1002/jcc.21287>, PMID: 19444816
- Clark R, Ansari MA, Dash S, Geeves MA, Coluccio LM. 2005. Loop 1 of transducer region in mammalian class I myosin, Myo1b, modulates actin affinity, ATPase activity, and nucleotide access. *Journal of Biological Chemistry* **280**:30935–30942. DOI: <https://doi.org/10.1074/jbc.M504698200>, PMID: 15980431
- Crick AJ, Theron M, Tiffert T, Lew VL, Cicuta P, Rayner JC. 2014. Quantitation of malaria parasite-erythrocyte cell-cell interactions using optical tweezers. *Biophysical Journal* **107**:846–853. DOI: <https://doi.org/10.1016/j.bpj.2014.07.010>, PMID: 25140419
- Cronan JE. 1990. Biotination of proteins in vivo. A post-translational modification to label, purify, and study proteins. *The Journal of Biological Chemistry* **265**:10327–10333. PMID: 2113052
- de Chaumont F, Dallongeville S, Chenouard N, Hervé M, Pop S, Provoost T, Meas-Yedid V, Pankajakshan P, Lecomte T, Le Montagner Y, Lagache T, Dufour A, Olivo-Marin JC. 2012. Icy: an open bioimage informatics platform for extended reproducible research. *Nature Methods* **9**:690–696. DOI: <https://doi.org/10.1038/nmeth.2075>, PMID: 22743774
- Douse CH, Green JL, Salgado PS, Simpson PJ, Thomas JC, Langsley G, Holder AA, Tate EW, Cota E. 2012. Regulation of the *Plasmodium* motor complex: phosphorylation of myosin A tail-interacting protein (MTIP) loosens its grip on MyoA. *The Journal of Biological Chemistry* **287**:36968–36977. DOI: <https://doi.org/10.1074/jbc.M112.379842>, PMID: 22932904
- Emsley P, Cowtan K. 2004. Coot: model-building tools for molecular graphics. *Acta Crystallographica. Section D, Biological Crystallography* **60**:2126–2132. DOI: <https://doi.org/10.1107/S0907444904019158>, PMID: 15572765
- Foth BJ, Goedecke MC, Soldati D. 2006. New insights into myosin evolution and classification. *PNAS* **103**:3681–3686. DOI: <https://doi.org/10.1073/pnas.0506307103>, PMID: 16505385
- Franke D, Petoukhov MV, Konarev PV, Panjkovich A, Tuukkanen A, Mertens HDT, Kikhney AG, Hajizadeh NR, Franklin JM, Jeffries CM, Svergun DI. 2017. ATSAS 2.8: a comprehensive data analysis suite for small-angle scattering from macromolecular solutions. *Journal of Applied Crystallography* **50**:1212–1225. DOI: <https://doi.org/10.1107/S1600576717007786>, PMID: 28808438
- Frénal K, Dubremetz JF, Lebrun M, Soldati-Favre D. 2017. Gliding motility powers invasion and egress in apicomplexa. *Nature Reviews Microbiology* **15**:645–660. DOI: <https://doi.org/10.1038/nrmicro.2017.86>, PMID: 28867819
- Green JL, Wall RJ, Vahokoski J, Yusuf NA, Ridzuan MAM, Stanway RR, Stock J, Knuepfer E, Brady D, Martin SR, Howell SA, Pires IP, Moon RW, Molloy JE, Kursula I, Tewari R, Holder AA. 2017. Compositional and expression analyses of the glideosome during the *plasmodium* life cycle reveal an additional myosin light chain required for maximum motility. *Journal of Biological Chemistry* **292**:17857–17875. DOI: <https://doi.org/10.1074/jbc.M117.802769>, PMID: 28893907
- Greenberg MJ, Lin T, Shuman H, Ostap EM. 2015. Mechanochemical tuning of myosin-I by the N-terminal region. *PNAS* **112**:E3337–E3344. DOI: <https://doi.org/10.1073/pnas.1506633112>, PMID: 26056287
- Haldar K, Bhattacharjee S, Safeukui I. 2018. Drug resistance in *Plasmodium*. *Nature Reviews Microbiology* **16**:156–170. DOI: <https://doi.org/10.1038/nrmicro.2017.161>, PMID: 29355852
- Hertig E. 2019. Distribution of Anopheles vectors and potential malaria transmission stability in Europe and the Mediterranean area under future climate change. *Parasites & Vectors* **12**:18. DOI: <https://doi.org/10.1186/s13071-018-3278-6>
- Houdusse A, Szent-Gyorgyi AG, Cohen C. 2000. Three conformational states of scallop myosin S1. *PNAS* **97**:11238–11243. DOI: <https://doi.org/10.1073/pnas.200376897>, PMID: 11016966
- Houdusse A, Cohen C. 1995. Target sequence recognition by the calmodulin superfamily: implications from light chain binding to the regulatory domain of scallop myosin. *PNAS* **92**:10644–10647. DOI: <https://doi.org/10.1073/pnas.92.23.10644>, PMID: 7479857
- Houdusse A, Cohen C. 1996. Structure of the regulatory domain of scallop myosin at 2 Å resolution: implications for regulation. *Structure* **4**:21–32. DOI: [https://doi.org/10.1016/S0969-2126\(96\)00006-8](https://doi.org/10.1016/S0969-2126(96)00006-8), PMID: 8805510
- Huang J, Rauscher S, Nawrocki G, Ran T, Feig M, de Groot BL, Grubmüller H, MacKerell AD. 2017. CHARMM36m: an improved force field for folded and intrinsically disordered proteins. *Nature Methods* **14**:71–73. DOI: <https://doi.org/10.1038/nmeth.4067>
- Jo S, Cheng X, Lee J, Kim S, Park SJ, Patel DS, Beaven AH, Lee KI, Rui H, Park S, Lee HS, Roux B, MacKerell AD, Klauda JB, Qi Y, Im W. 2017. CHARMM-GUI 10 years for biomolecular modeling and simulation. *Journal of Computational Chemistry* **38**:1114–1124. DOI: <https://doi.org/10.1002/jcc.24660>, PMID: 27862047

- Jones ML, Collins MO, Goulding D, Choudhary JS, Rayner JC. 2012. Analysis of protein palmitoylation reveals a pervasive role in *Plasmodium* development and pathogenesis. *Cell Host & Microbe* **12**:246–258. DOI: <https://doi.org/10.1016/j.chom.2012.06.005>, PMID: 22901544
- Jones ML, Das S, Belda H, Collins CR, Blackman MJ, Treeck M. 2016. A versatile strategy for rapid conditional genome engineering using loxP sites in a small synthetic intron in *Plasmodium falciparum*. *Scientific Reports* **6**: 21800. DOI: <https://doi.org/10.1038/srep21800>, PMID: 26892670
- Kabsch W. 2010. XDS. *Acta Crystallographica. Section D, Biological Crystallography* **66**:125–132. DOI: <https://doi.org/10.1107/S0907444909047337>, PMID: 20124692
- Kad NM, Patlak JB, Fagnant PM, Trybus KM, Warshaw DM. 2007. Mutation of a conserved glycine in the SH1-SH2 Helix affects the load-dependent kinetics of myosin. *Biophysical Journal* **92**:1623–1631. DOI: <https://doi.org/10.1529/biophysj.106.097618>, PMID: 17142278
- Kinose F, Wang SX, Kidambi US, Moncman CL, Winkelmann DA. 1996. Glycine 699 is pivotal for the motor activity of skeletal muscle myosin. *The Journal of Cell Biology* **134**:895–909. DOI: <https://doi.org/10.1083/jcb.134.4.895>, PMID: 8769415
- McCoy AJ, Grosse-Kunstleve RW, Adams PD, Winn MD, Storoni LC, Read RJ. 2007. Phaser crystallographic software. *Journal of Applied Crystallography* **40**:658–674. DOI: <https://doi.org/10.1107/S0021889807021206>, PMID: 19461840
- Mentes A, Huehn A, Liu X, Zwolak A, Dominguez R, Shuman H, Ostap EM, Sindelar CV. 2018. High-resolution cryo-EM structures of actin-bound myosin states reveal the mechanism of myosin force sensing. *PNAS* **115**: 1292–1297. DOI: <https://doi.org/10.1073/pnas.1718316115>, PMID: 29358376
- Münnich S, Taft MH, Manstein DJ. 2014. Crystal structure of human myosin 1c—the motor in GLUT4 exocytosis: implications for Ca<sup>2+</sup> regulation and 14-3-3 binding. *Journal of Molecular Biology* **426**:2070–2081. DOI: <https://doi.org/10.1016/j.jmb.2014.03.004>, PMID: 24636949
- Münter S, Sabass B, Selhuber-Unkel C, Kudryashev M, Hegge S, Engel U, Spatz JP, Matuschewski K, Schwarz US, Frischknecht F. 2009. Plasmodium sporozoite motility is modulated by the turnover of discrete adhesion sites. *Cell Host & Microbe* **6**:551–562. DOI: <https://doi.org/10.1016/j.chom.2009.11.007>
- Pardee JD, Spudich JA. 1982. Purification of muscle actin. *Methods in Enzymology* **85**:9. DOI: [https://doi.org/10.1016/0076-6879\(82\)85020-9](https://doi.org/10.1016/0076-6879(82)85020-9), PMID: 7121269
- Pazicky S, Dhamotharan K, Kaszuba K, Mertens H, Gilberger T, Svergun D, Kosinski J, Weininger U, Löw C. 2019. Structural role of essential light chains in the apicomplexan glideosome. *bioRxiv*. DOI: <https://doi.org/10.1101/867499>
- Perrin AJ, Collins CR, Russell MRG, Collinson LM, Baker DA, Blackman MJ. 2018. The actinomyosin motor drives malaria parasite red blood cell invasion but not egress. *mBio* **9**:e00905-18. DOI: <https://doi.org/10.1128/mBio.00905-18>, PMID: 29970464
- Powell CJ, Ramaswamy R, Kelsen A, Hamelin DJ, Warshaw DM, Bosch J, Burke JE, Ward GE, Boulanger MJ. 2018. Structural and mechanistic insights into the function of the unconventional class XIV myosin MyoA from *Toxoplasma gondii*. *PNAS* **115**:E10548–E10555. DOI: <https://doi.org/10.1073/pnas.1811167115>, PMID: 30348763
- Preller M, Bauer S, Adamek N, Fujita-Becker S, Fedorov R, Geeves MA, Manstein DJ. 2011. Structural basis for the allosteric interference of myosin function by reactive thiol region mutations G680A and G680V. *Journal of Biological Chemistry* **286**:35051–35060. DOI: <https://doi.org/10.1074/jbc.M111.265298>, PMID: 21841195
- Pylypenko O, Houdusse AM. 2011. Essential “ankle” in the myosin lever arm: Fig. 1. *PNAS* **108**:5–6. DOI: <https://doi.org/10.1073/pnas.1017676108>
- Robert-Paganin J, Auguin D, Houdusse A. 2018. Hypertrophic cardiomyopathy disease results from disparate impairments of cardiac myosin function and auto-inhibition. *Nature Communications* **9**:4019. DOI: <https://doi.org/10.1038/s41467-018-06191-4>, PMID: 30275503
- Robert-Paganin J, Robblee JP, Auguin D, Blake TCA, Bookwalter CS, Kremenstova EB, Moussaoui D, Previs MJ, Jousset G, Baum J, Trybus KM, Houdusse A. 2019. Plasmodium myosin A drives parasite invasion by an atypical force generating mechanism. *Nature Communications* **10**:3286. DOI: <https://doi.org/10.1038/s41467-019-11120-0>, PMID: 31337750
- Robert-Paganin J, Pylypenko O, Kikuti C, Sweeney HL, Houdusse A. 2020. Force generation by myosin motors: a structural perspective. *Chemical Reviews* **120**:5–35. DOI: <https://doi.org/10.1021/acs.chemrev.9b00264>, PMID: 31689091
- Ropars V, Yang Z, Isabet T, Blanc F, Zhou K, Lin T, Liu X, Hissier P, Samazan F, Amigues B, Yang ED, Park H, Pylypenko O, Cecchini M, Sindelar CV, Sweeney HL, Houdusse A. 2016. The myosin X motor is optimized for movement on actin bundles. *Nature Communications* **7**:12456. DOI: <https://doi.org/10.1038/ncomms12456>, PMID: 27580874
- Ryan SJ, Lippi CA, Zermoglio F. 2020. Shifting transmission risk for malaria in Africa with climate change: a framework for planning and intervention. *Malaria Journal* **19**:170. DOI: <https://doi.org/10.1186/s12936-020-03224-6>, PMID: 32357890
- Schindelin J, Arganda-Carreras I, Frise E, Kaynig V, Longair M, Pietzsch T, Preibisch S, Rueden C, Saalfeld S, Schmid B, Tinevez JY, White DJ, Hartenstein V, Eliceiri K, Tomancak P, Cardona A. 2012. Fiji: an open-source platform for biological-image analysis. *Nature Methods* **9**:676–682. DOI: <https://doi.org/10.1038/nmeth.2019>, PMID: 22743772
- Schneidman-Duhovny D, Hammel M, Tainer JA, Sali A. 2016. FoXS, FoXSDock and MultiFoXS: single-state and multi-state structural modeling of proteins and their complexes based on SAXS profiles. *Nucleic Acids Research* **44**:W424–W429. DOI: <https://doi.org/10.1093/nar/gkw389>, PMID: 27151198

- Shuman H**, Greenberg MJ, Zwolak A, Lin T, Sindelar CV, Dominguez R, Ostap EM. 2014. A vertebrate myosin-I structure reveals unique insights into myosin mechanochemical tuning. *PNAS* **111**:2116–2121. DOI: <https://doi.org/10.1073/pnas.1321022111>, PMID: 24469830
- Tibúrcio M**, Yang ASP, Yahata K, Suárez-Cortés P, Belda H, Baumgarten S, van de Vegte-Bolmer M, van Gemert GJ, van Waardenburg Y, Levashina EA, Sauerwein RW, Treeck M. 2019. A novel tool for the generation of conditional knockouts to study gene function across the *Plasmodium falciparum* life cycle. *mBio* **10**:e01170-19. DOI: <https://doi.org/10.1128/mBio.01170-19>, PMID: 31530668
- Trager W**, Jensen JB. 1976. Human malaria parasites in continuous culture. *Science* **193**:673–675. DOI: <https://doi.org/10.1126/science.781840>, PMID: 781840
- VanBuren P**, Waller GS, Harris DE, Trybus KM, Warshaw DM, Lowey S. 1994. The essential light chain is required for full force production by skeletal muscle myosin. *PNAS* **91**:12403–12407. DOI: <https://doi.org/10.1073/pnas.91.26.12403>, PMID: 7809049
- Vonrhein C**, Flensburg C, Keller P, Sharff A, Smart O, Paciorek W, Womack T, Bricogne G. 2011. Data processing and analysis with the autoPROC toolbox. *Acta Crystallographica. Section D, Biological Crystallography* **67**:293–302. DOI: <https://doi.org/10.1107/S0907444911007773>, PMID: 21460447
- Waterhouse A**, Bertoni M, Bienert S, Studer G, Tauriello G, Gumienny R, Heer FT, de Beer TAP, Rempfer C, Bordoli L, Lepore R, Schwede T. 2018. SWISS-MODEL: homology modelling of protein structures and complexes. *Nucleic Acids Research* **46**:W296–W303. DOI: <https://doi.org/10.1093/nar/gky427>, PMID: 29788355
- WHO**. 2018. *World Malaria Report 2018*: World Health Organization.
- Williams MJ**, Alonso H, Enciso M, Egarter S, Sheiner L, Meissner M, Striepen B, Smith BJ, Tonkin CJ. 2015. Two essential light chains regulate the MyoA lever arm to promote *Toxoplasma* gliding motility. *mBio* **6**:e00845. DOI: <https://doi.org/10.1128/mBio.00845-15>, PMID: 26374117

**Supplementary Information**  
**Moussaoui *et al.*, 2020**

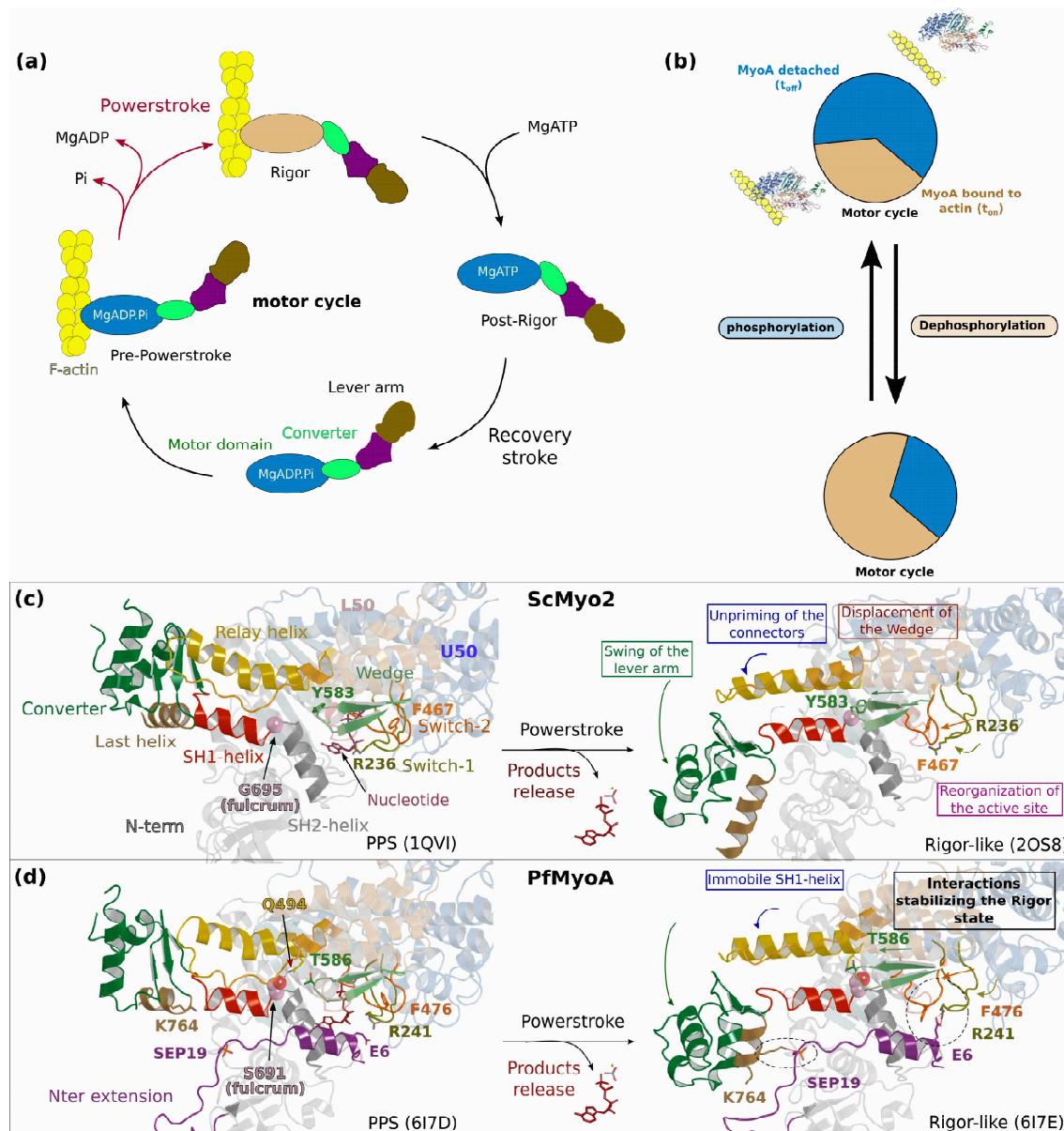


**Figure 1-figure supplement 1 The atypical and tunable mechanical cycle of PfMyoA.** **(a)** Motor cycle of myosin motors. The nucleotide free state, strongly bound to actin, is called Rigor. Binding of ATP in the Rigor state detaches the head from actin. Upon detachment, the motor first populates the Post-Rigor state (PR) with ATP bound. Isomerization towards the Pre-Powerstroke state allows ATP hydrolysis. This state binds weakly to actin. The sequential release of the products of hydrolysis drives the lever arm swing and thus the powerstroke, which generates force. Detachment of the motor upon ATP binding starts a new cycle. **(b)** PfMyoA properties are tuned by a phosphorylation in the N-terminal extension of the motor domain (SEP19). When the motor is phosphorylated, it moves actin with a high velocity spending a short fraction of the cycle strongly bound to actin. When the motor is dephosphorylated, it produces more force at the expense of speed. **(c)** and **(d)** show the mechanism of force production in Scallop myosin 2 (ScMyo2) and PfMyoA respectively. In ScMyo2 the mobility of the SH1-helix is a key element for the mechanism driving the powerstroke of most myosins and requires the presence of a conserved glycine (G695), the so-called fulcrum, at the basis of the SH1-helix<sup>12,13,14</sup>. In PfMyoA, the SH1-helix is immobile, due to the presence of a Serine at the fulcrum (S691). The lack of mobility of the fulcrum is compensated by a phosphorylatable N-terminal extension (SEP19) and sequence adaptations in the connector.



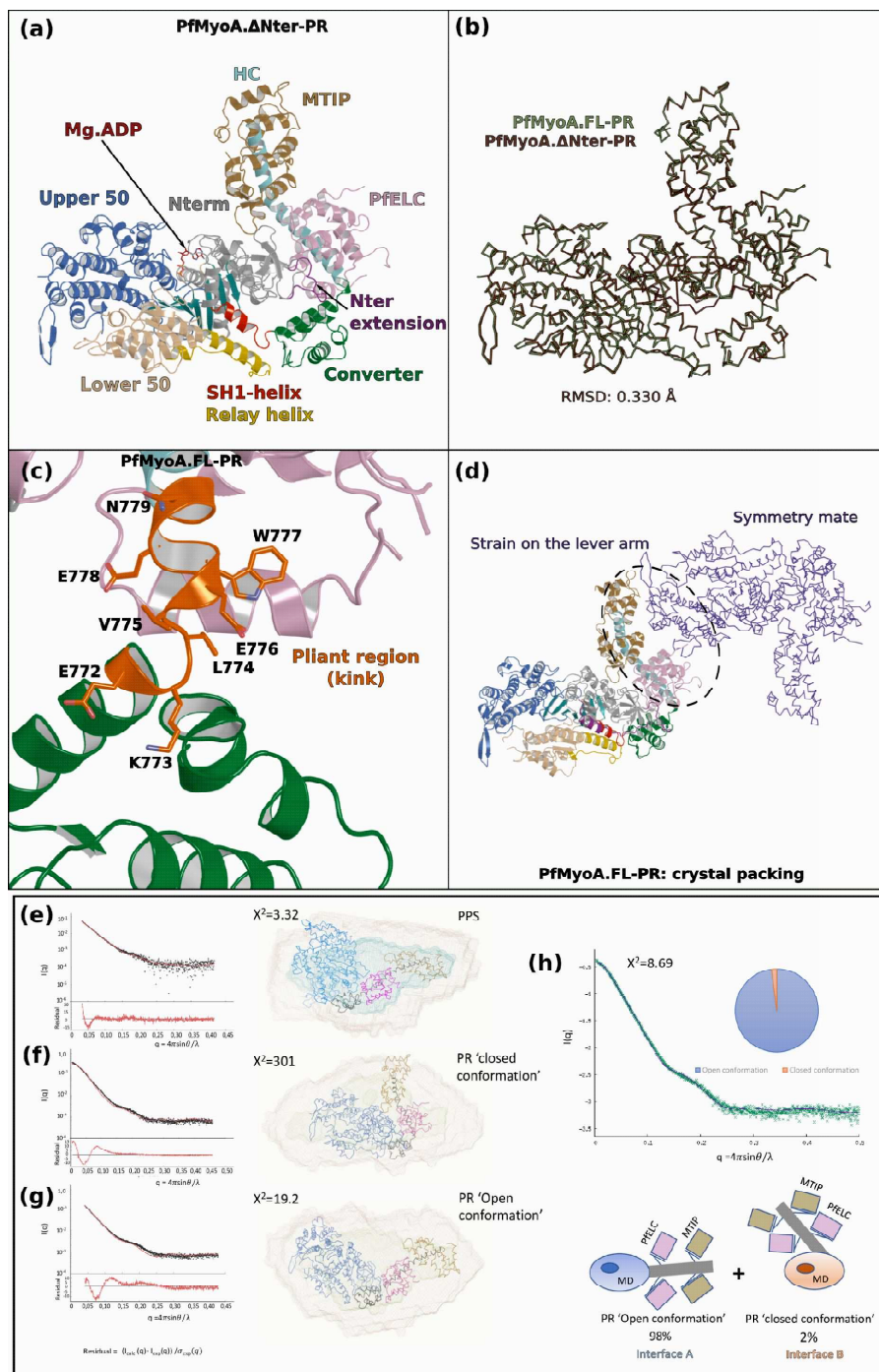


**Figure 1-figure supplement 2 – The crystal structure of the PfMyoA PR state displays a kink at the pliant region. (a)**

Overall structure of PfMyoA•ΔNter-PR. **(b)** PfMyoA•ΔNter-PR and PfMyoA•FL-PR superimpose perfectly (rmsd 0.330 Å), indicating that the deletion does not change or alter the protein fold.

**(c)** The PR state of PfMyoA•FL displays a kink in the lever arm at the pliant region (orange). The Converter thus becomes far from the  $\alpha 5^*$  and  $\alpha 5'^*$  helices which are destabilized (not modeled since no density is indicated in the electron density map). **(d)** Crystal

packing shows that the kinked lever arm is involved in a large surface of the crystal packing. **(e), (f), (g)** Small-Angle X-ray Scattering experiment investigating the conformation of PfMyoA in solution. **(e)** When the motor is bound to ADP and Pi analogs, the theoretical curve computed from the

PfMyoA•FL-PPS structure (chain A) fits well to the SAXS experimental curve ( $\chi^2 = 3.32$ ).

**(f)** When the motor is bound to MgADP, the experimental curve fits poorly to the theoretical curve from the kinked PfMyoA•FL-PR crystal structure ( $\chi^2 = 302$ ), **(g)** The SAXS experimental curve fits better to the theoretical curve obtained from a model of the PR state in which no kink occurs at the end of the Converter (open conformation) ( $\chi^2 = 19.2$ ). **(h)** A fit of the theoretical curve in the PR condition with the software Oligomer<sup>4</sup>. The fit has been performed with the closed PfMyoA•FL-PR structure obtained from the crystal with a kink at the pliant region (interface A) and a computed open PfMyoA•FL-PR structure (interface B from the PfMyoA•FL-PPS structure) (see Figure 1). Calculations predict 98% of the sample in the open conformation ( $\chi^2 = 8.69$ ).

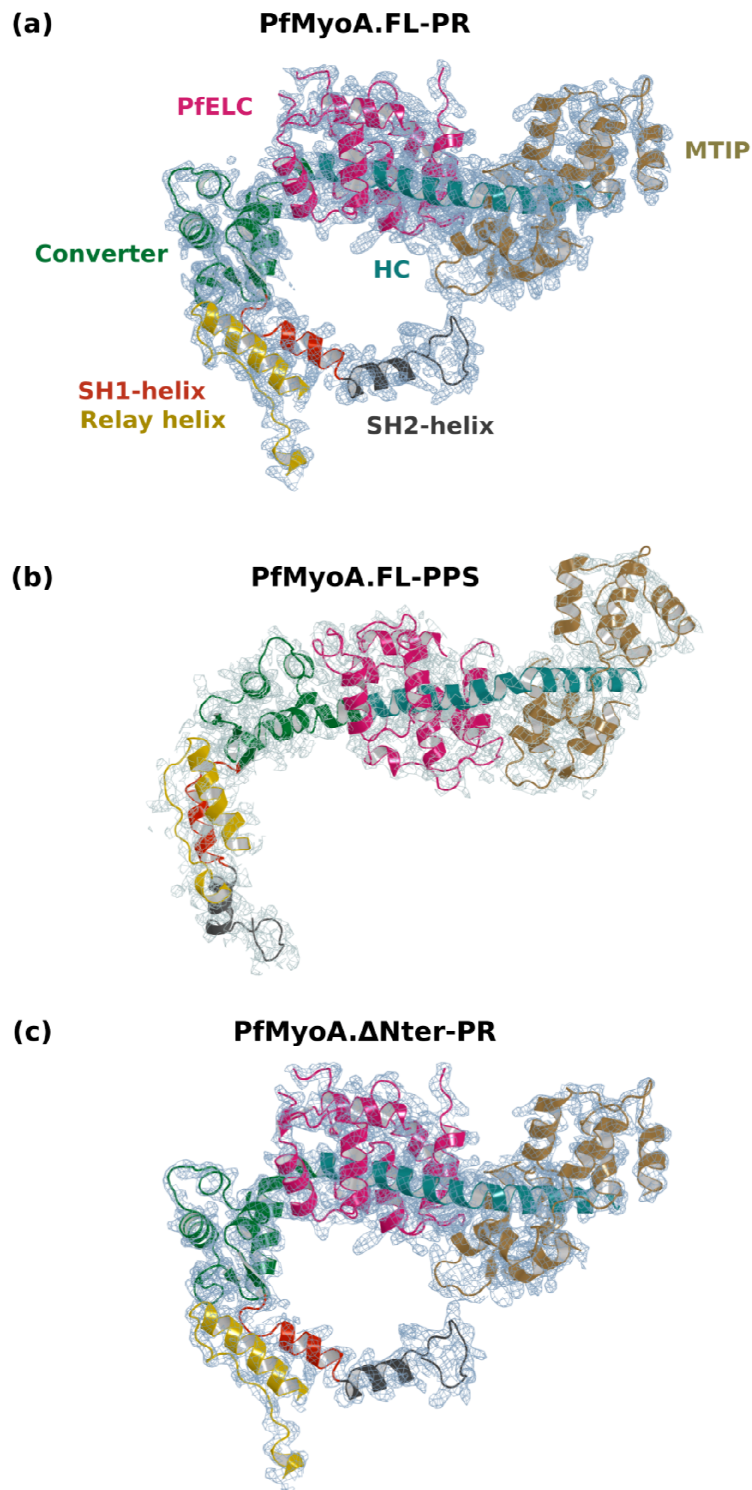


*Figure 1-figure supplement 3 - **Electron density in the PfMyoA structures.** For all structures, the lever arm and the connectors are displayed and the 2Fo-Fc map is shown, contoured at 1.0  $\sigma$ . (a) PfMyoA•FL-PR at 2.5 Å resolution. (b) PfMyoA•FL-PPS at 3.9 Å resolution. (c) PfMyoA•ΔNter-PR at 3.3 Å resolution.*

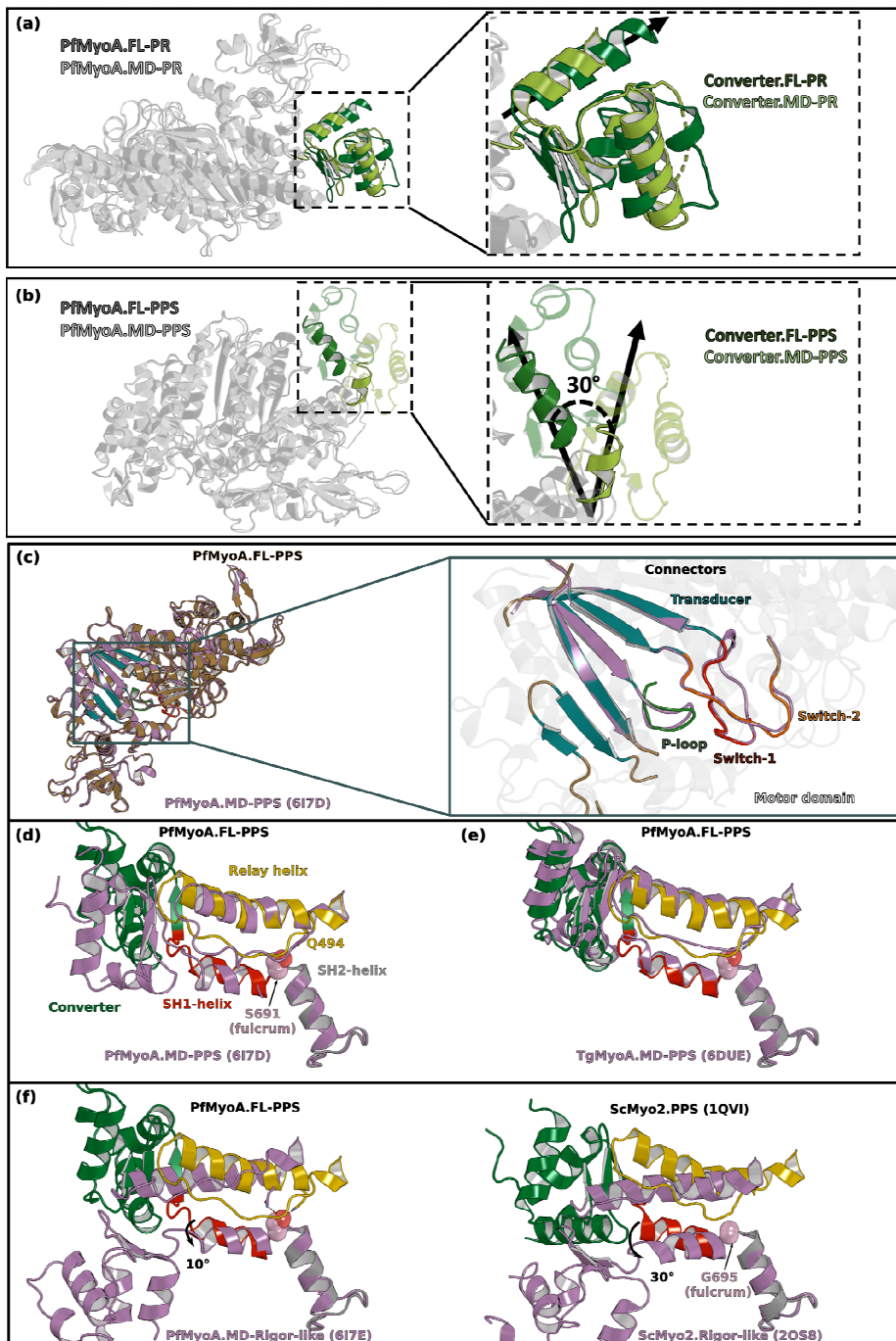


Figure 1-figure supplement 4 – **The orientation of the lever arm of PfMyoA in PPS differs in the structures of the MD and of the FL.**

**(a)** The orientation of the Converter in the Post-Rigor state (PR) of PfMyoA is identical in the structures of the full-length (FL) and of the motor domain (MD) constructs (PDB code 6I7D chain A). **(b)** In the Pre-Powerstroke state (PPS), the lever arm is 30° more primed in the FL structure compared to that found in the MD structure (PDB code 6I7E).

**(c)** Superimposition on the N-terminal subdomain of PfMyoA.FL-PPS and PfMyoA.MD-PPS. On the left, overall view showing that the conformation of the motor domain is similar for the two structures. On the right, zoom on the transducer and on the connectors of the active site (P-loop, Switch-1 and Switch-2) show that the conformation of these elements, which is characteristic of the state, is highly similar.

On the following panels, all the structures are superimposed on the SH2-helix. **(d)** The positions of both the Relay-helix and the Converter (also shown in Supplementary Fig. 6) vary between the FL and the MD constructs. Since the SH1-helix was reported to be immobile in PfMyoA<sup>5</sup>, its position only slightly differs between the two constructs. **(e)** The priming of PfMyoA.FL-PPS is identical to the priming of TgMyoA.MD-PPS (PDB code 6DUE). The communication described between the SH1- and the Relay helices (polar bond between S691 and Q494)<sup>5</sup> is similar as well as the orientation of the lever arm. **(f)** Comparison of the position of the connectors between the PPS and the Rigor-like states in PfMyoA (**Left**), and ScMyo2 (**Right**). The priming described in the PfMyoA.FL-PPS structure indicates that the SH1-helix remains mostly immobile: this connector is only rotated 10° during the powerstroke. This rotation is of smaller amplitude compared to that of conventional myosins such as ScMyo2 (~30°).



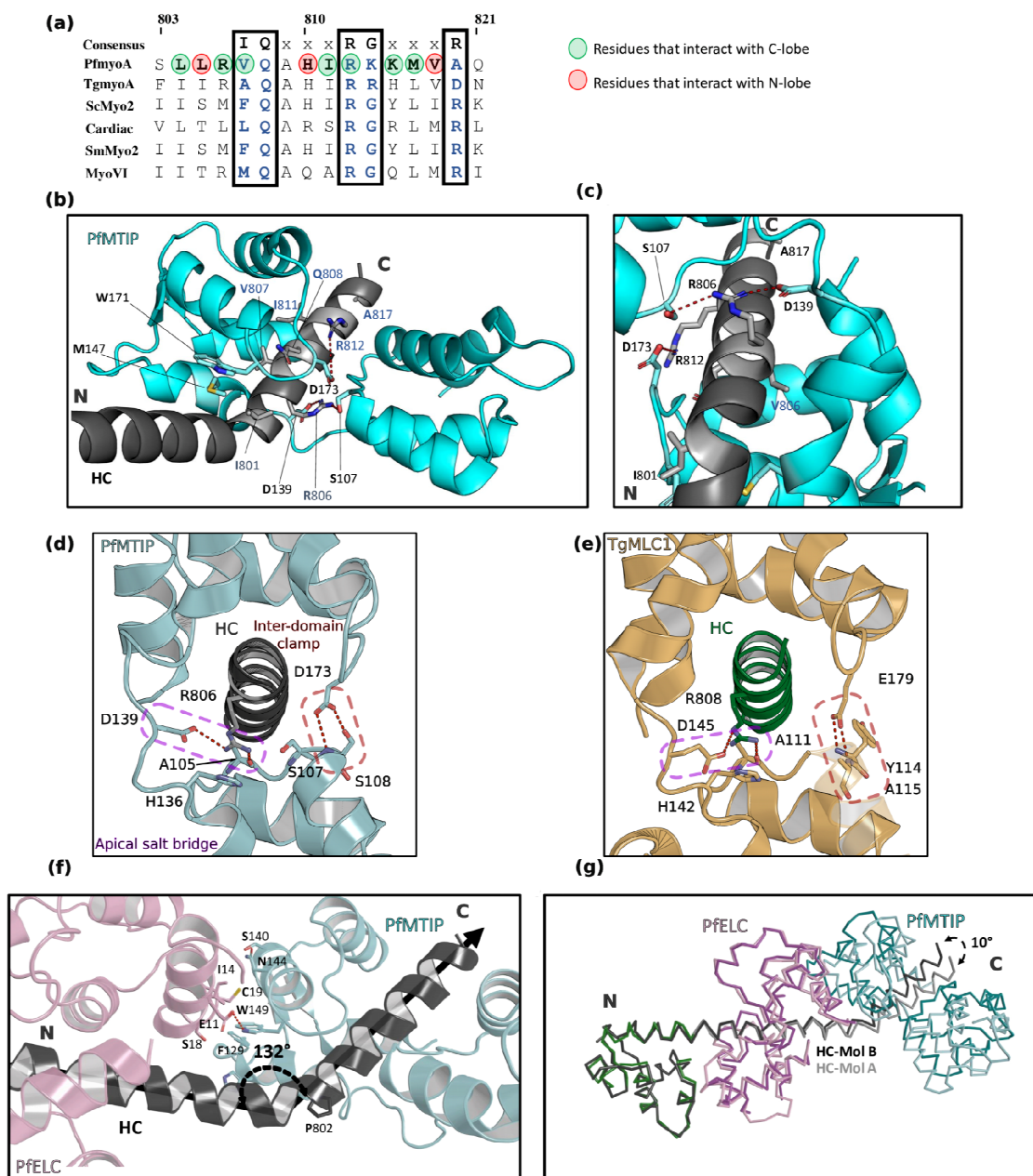


**Figure 3-figure supplement 1 – MTIP associated to PfMyoA.** **(a)** Sequence alignment of PfMyoA IQ2 with conventional IQ motifs. Residues at consensus positions are colored in blue. **(b)** MTIP is bound to the heavy chain (HC) in a similar manner as a conventional ELC. Several residues from the consensus are conserved in PflQ2. **(c)** Zoom on the specific contacts involved in the MTIP/PfMyoA recognition. **(d, e)** The recognition of the HC by MTIP is highly similar to the recognition of the HC by TgMLC1 (PDB 5VT9) and the residues involved in the apical salt bridge and the inter-lobe clamp (dotted lines)<sup>6</sup> are conserved. **(f)** and **(g)** Interface between PfELC and MTIP. **(f)** The interface between PfELC and MTIP is hydrophobic and includes two aromatic residues (<sup>PfMTIP</sup>H150, <sup>PfMTIP</sup>W171) that maintain the relative positioning of the two light-chains. A 132° angle occurs between the two HC helices that contain the PflQ1 and PflQ2 motifs. The kink is facilitated by the presence of a proline at the hinge (P802). **(g)** Alignment of the two molecules of the asymmetric unit in the PfMyoA•FL-PPS crystal structure. The hinge at the PfELC/MTIP interface is a restricted point of compliance since ~10° difference is found for the orientation of the PflQ2 motif HC helices for these two molecules, when the structures are aligned using the PflQ1 motif residues.

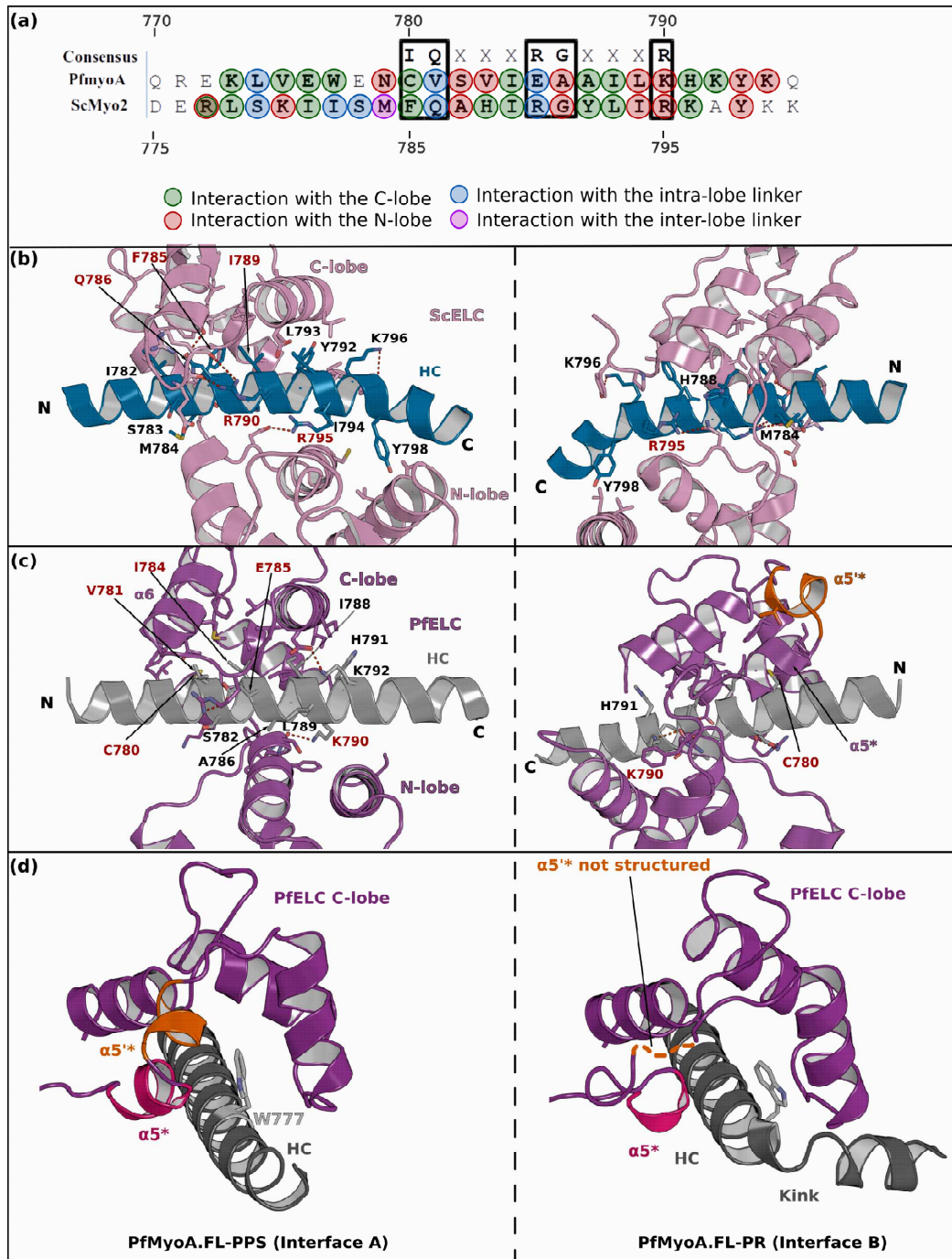


**Figure 4-figure supplement 1 – Interaction between the IQ1 motif and the ELC.** **(a)** Sequence alignment of the IQ1 motif from ScMyo2 and PfMyoA. Residues interacting with the ELCs are contoured following the same color code as defined in **Fig. 4**. **(b, c)** Two different orientations (180° rotation around the y axis) are shown to depict all residues involved in the IQ1 motif/ELC complex recognition, in order to compare **(b)** ScMyo2 and **(c)** PfMyoA. Residues at consensus positions are labeled in red. **(d)** The tryptophan W777 stabilizes the  $\alpha 5^*$  and  $\alpha 5'^*$  helices. The left and the right panels show W777 and its environment in the structures of PfMyoA•FL-PPS and PfMyoA•FL-PR, respectively. Note the change in position of the W777 side chain due to its position at the kink of the pliant region. In PfMyoA•FL-PPS, W777 interacts with the  $\alpha 5^*$  and  $\alpha 5'^*$  helices stabilizing their structure. In PfMyoA•FL-PR, the interaction between W777 and the  $\alpha 5^*$  and  $\alpha 5'^*$  helices are lost due to the kink at the pliant region, and a loss of interaction of these helices with the Converter. These helices become disordered.



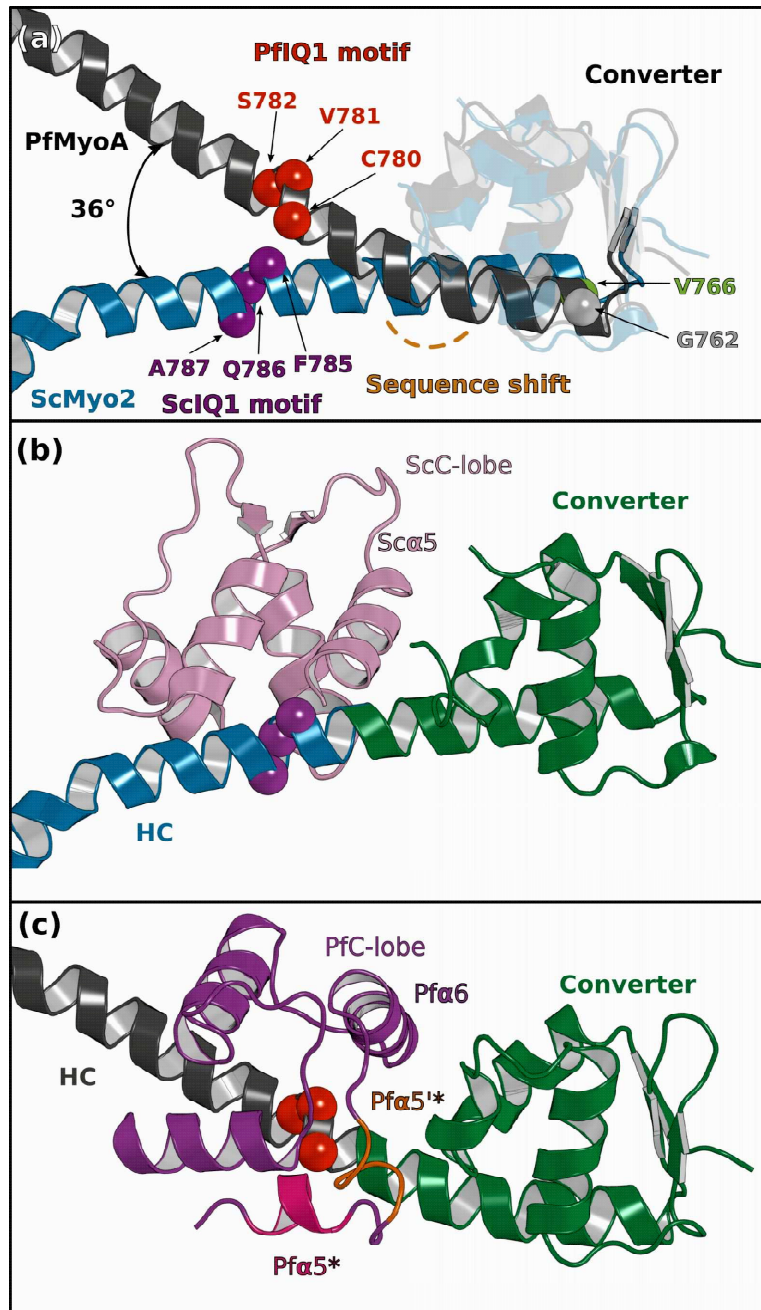


**Figure 4-figure supplement 2 –The Converter/ELC interface differs in PfMyoA and in ScMyo2.** **(a)** The first IQ motif residues of PfMyoA starts one residue downstream to that of ScMyoA (PDB code 1QVI), resulting in a sequence shift in the pliant region and different orientation for the consensus IQ1 motif residues (balls). A difference in the kink at the pliant region accentuates the difference in position of the IQ1 residues in the two lever arms. **(b, c)** The C-lobe of PfELC and ScELC bound to the IQ1 motif are shown for comparison. The difference in the position of the HC consensus residues result in a different Converter/ELC interface in **(b)** ScMyo2 compared with **(c)** PfMyoA (see **Fig. 6** for details of the interactions).

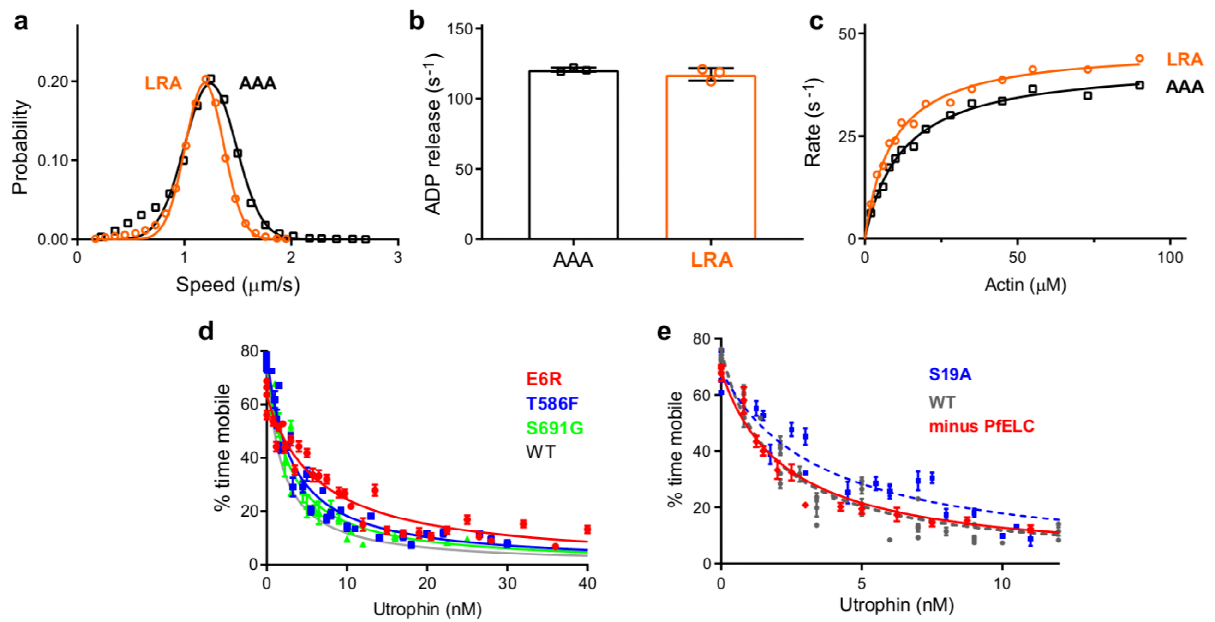


**Figure 6-figure supplement 1 – Transient kinetics and genetic engineering of the parasite. (a) (e)** Triple mutants that affect the atypical priming of PfMyoA. Speed, ADP release rate, and actin-activated ATPases for LRA (see also data presented in **Fig. 2**) compared with the AAA mutant (LRA: R707L/E711R/Y714A; AAA: R707A/E711A/Y714A). **(a)** Speed distributions from a representative in vitro motility assay for LRA ( $1.19 \pm 0.18 \mu\text{m/s}$ ,  $n = 4092$ ) and AAA ( $1.24 \pm 0.24 \mu\text{m/s}$ ,  $n = 3030$ ). **(b)** ADP release rates from ActoPfMyoA for LRA ( $117 \pm 4 \text{ s}^{-1}$ ) and AAA ( $122 \pm 2 \text{ s}^{-1}$ ). 3 experiments, 1 protein preparation of AAA. **(c)** Actin-activated ATPase activity for LRA ( $V_{\text{max}} = 46.8 \pm 1.0 \text{ s}^{-1}$ ;  $K_{\text{m}} = 9.1 \pm 0.6 \mu\text{M}$ ) and AAA ( $V_{\text{max}} = 42.7 \pm 0.9 \text{ s}^{-1}$ ;  $K_{\text{m}} = 12.3 \pm 0.8 \mu\text{M}$ ). Error, SE of the fit. 2 experiments, 1 protein preparation of AAA. **(d)** Ensemble force measurements using a utrophin-based loaded in vitro motility assay, showing more data and an expanded x-axis compared with the main **Fig. 2f**. Temperature,  $30^\circ\text{C}$ . **(e)** Ensemble force measurement of full-length PfMyoA with only MTIP light chain bound. A myosin that produces more force requires higher utrophin concentrations to slow motion. Minus PfELC:  $1.57 \pm 0.18 \text{ nM}$  (red diamonds and solid red line fit); WT,  $1.40 \pm 0.08 \text{ nM}$ ; S19A,  $2.42 \pm 0.17 \text{ nM}$ . WT and S19A data are from<sup>5</sup>. Error, SE of the fit. Data for minus PfELC are from one protein preparation and 2 experiments. Skeletal actin was used for all experiments. Temperature,  $30^\circ\text{C}$ .

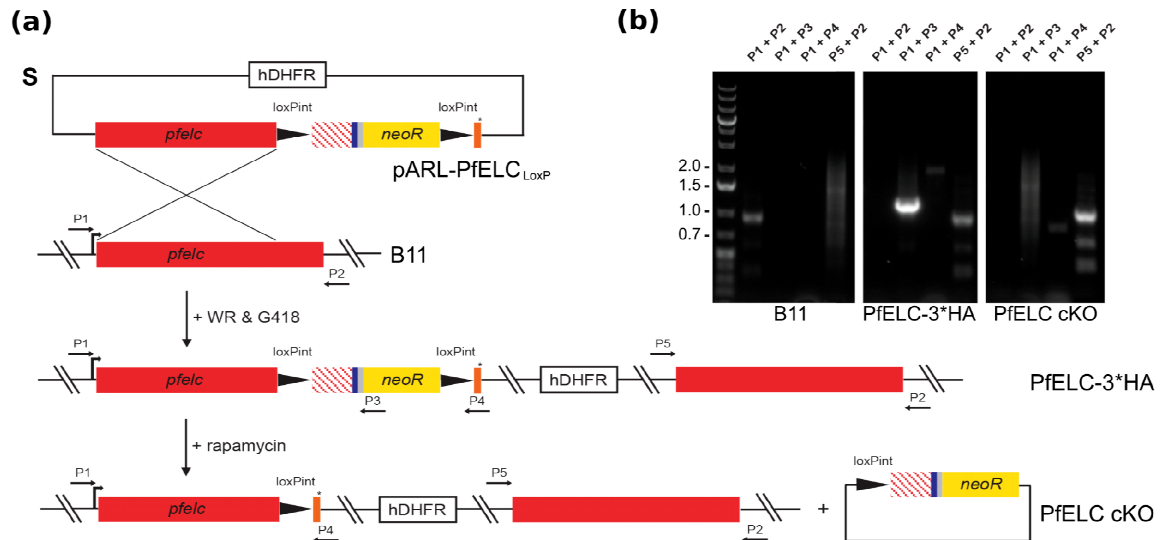


**Figure 7-figure supplement 1 Genetic integration of LoxP Cre recombinase sites into the *Pfelc* gene of *Plasmodium falciparum*.** **(a)** Schematics of the targeting plasmid (pARL PfELC<sub>LoxP</sub>), expected selection linked integration (SLI) into the *pfelc* locus leading to C-terminally tagged PfELC 3xHA and the DiCre-mediated recombinase event resulting in the PfELC conditional KO (cKO). The recodonised version of the *pfelc* gene is shown as a red striped box, the 3x HA tag is depicted in blue, the T2A skip peptide in gray and the cMyc/Flag tag in orange. The stop codon is indicated by an asterisk and primers used for genotyping are indicated by numbered arrows. **(b)** PCR analysis and confirmation of integration into the *pfelc* locus in transgenic PfELC 3x HA parasites as evidenced by loss of the wild-type band at ~1 kb (P1 & P2) and amplification of an ~1.2 kb (P1 & P3), ~1.9 kb (P1 & P4) and ~1 kb (P5 & P2) product. Successful rapamycin-induced excision results in the expected loss of the ~1.2 kb band and size reduction of the ~1.9 kb product leading to PfELC cKO.

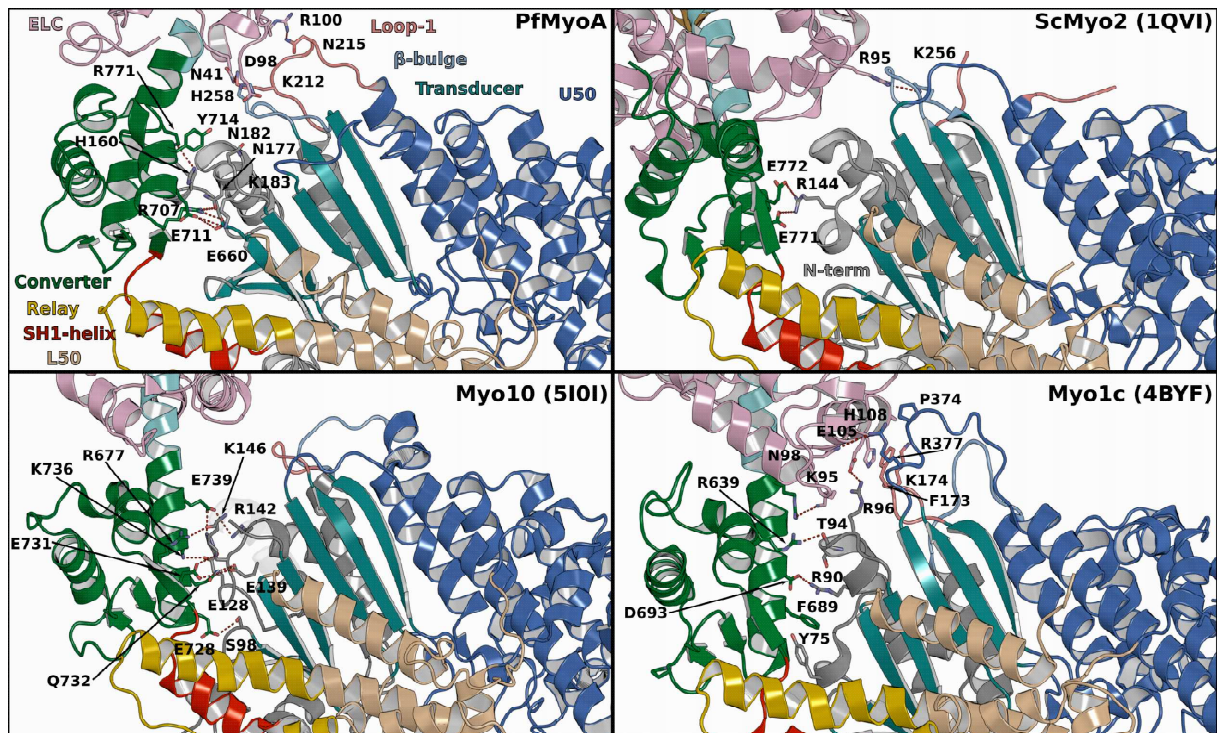


**Figure 6-figure supplement 2 Interactions between the motor domain (MD) and the lever arm stabilizing the priming in PPS in different myosins.** Important interactions occur in PfMyoA between the Converter and the N-terminal subdomain while the PfELC is involved in interactions with Loop1 and the  $\beta$ -bulge of the Transducer. In comparison, limited interactions occur in ScMyo2 consistent with smaller priming of the lever arm. Myo10 is another highly primed myosin but the interactions involve mainly the Converter with the N-terminal subdomain, without contribution from the Transducer. The priming of another highly primed PPS structure from Myo1c requires interaction of the CaM light chain with Loop1 and the HO-linker of the Transducer.

**Supplementary file 1a. Data collection and refinement statistics  
(molecular replacement)**

	<b>PfMyoA•FL-PR</b>	<b>PfMyoA•FL-PPS</b>	<b>PfMyoA•ΔNter-PR</b>
<b>Data collection</b>			
Space group	P 2 <sub>1</sub> 2 <sub>1</sub> 2 <sub>1</sub>	P 2 <sub>1</sub> 2 <sub>1</sub> 2	P 2 <sub>1</sub> 2 <sub>1</sub> 2 <sub>1</sub>
Cell dimensions			
<i>a</i> , <i>b</i> , <i>c</i> (Å)	89.67 114.69 169.46	168.24 287.43 78.61	90.08 114.43 170.70
α, β, γ (°)	90 90 90	90 90 90	90 90 90
Resolution (Å)	25.6-2.55(2.641-2.55)*	48.4-3.99 (4.133-3.99)	48.3-3.27 (3.387-3.27)
<i>R</i> <sub>merge</sub>	0.169 (1.918)	0.4443 (2.491)	0.3707 (2.157)
<i>I</i> / σ <i>I</i>	10.57 (0.83)	4.19 (0.64)	9.02 (1.68)
CC <sub>1/2</sub>	0.998 (0.505)	0.989 (0.319)	0.992 (0.553)
Completeness (%)	99.62 (97.94)	99.49 (96.58)	99.88 (99.85)
Redundancy	11.2 (11.5)	10.3 (10.1)	12.8 (12.9)
<b>Refinement</b>			
Resolution (Å)	25.57-2.55 (2.62-2.55)	48.4-3.99 (4.11-3.99)	48.3-3.27 (3.39-3.27)
No. reflections	641 293 (total)	343 030 (total)	358 945 (total)
	57 507 (unique)	33 243 (unique)	27 977
<i>R</i> <sub>work</sub> / <i>R</i> <sub>free</sub>	0.199 / 0.248	0.237 / 0.273	0.184 / 0.232
No. atoms			
Protein	8571	17 386	8490
Ligand/ion	47	66	51
Water	290	0	4
<i>B</i> -factors			
Protein	79.82	70.84	92.81
Ligand/ion	83.16	23.55	78.44
Water	69.70		63.85
R.m.s. deviations			
Bond lengths (Å)	0.014	0.014	0.015
Bond angles (°)	1.82	1.65	1.82

\*Number of crystals for each structure should be noted in footnote. \*Values in parentheses are for highest-resolution shell.



## Supplementary file 1b. Kinetic and motility parameters of PfMyoA mutants

PfMyoA construct	In vitro motility speed ( $\mu\text{m/s} \pm \text{SD}$ )*	ADP release rate ( $\text{s}^{-1} \pm \text{SD}$ )*	ATPase $V_{\text{max}}$ ( $\text{s}^{-1} \pm \text{SE}$ )*	ATPase $K_m$ ( $\mu\text{M} \pm \text{SE}$ )*	Rate of acto-PfMyoA dissociation by MgATP ( $\text{s}^{-1}$ ) <sup>5*</sup>	Basal ATPase ( $\text{s}^{-1}$ )*	Ensemble force (nM utrophin $\pm \text{SE}$ )*
<b>WT</b> <sup>1</sup>	3.88 $\pm$ 0.54 (1)	334 $\pm$ 36 (1)	138 $\pm$ 4 (1)	30.3 $\pm$ 2.3 (1)	326 $\pm$ 9 (1)	0.3 (1)	1.40 $\pm$ 0.08 (1)
E6R	1.91 $\pm$ 0.35 (0.49)	157 $\pm$ 8 (0.47)	61.8 $\pm$ 0.9 (0.45)	4.1 $\pm$ 0.3 (7.39)	857 $\pm$ 22 (2.62)	0.5 (1.67)	4.02 $\pm$ 0.31 (2.9)
S691G	5.06 $\pm$ 0.58 (1.30)	580 $\pm$ 31 (1.74)	70.3 $\pm$ 1.4 (0.51)	15.4 $\pm$ 1.0 (1.97)	348 $\pm$ 7 (1.07)	2.7 (9)	1.99 $\pm$ 0.19 (1.4)
T586F	4.04 $\pm$ 0.44 (1.04)	323 $\pm$ 54 (0.97)	50.1 $\pm$ 1.4 (0.36)	13.6 $\pm$ 1.3 (2.23)	471 $\pm$ 27 (1.44)	2.1 (7)	2.38 $\pm$ 0.18 (1.7)
<b>LRA</b> <sup>2</sup>	1.19 $\pm$ 0.18 (0.31)	117 $\pm$ 4 (0.35)	46.8 $\pm$ 1.0 (0.34)	9.1 $\pm$ 0.6 (3.33)	472 $\pm$ 35 (1.45)	0.7 (2.3)	n.d.
<b>AAA</b> <sup>3</sup>	1.24 $\pm$ 0.24 (0.32)	121 $\pm$ 2 (0.36)	42.7 $\pm$ 0.9 (0.31)	12.3 $\pm$ 0.8 (2.46)	n.d.	0.5 (1.67)	n.d.
minus PfELC	1.75 $\pm$ 0.32 <sup>4</sup> (0.45)	n.d.	n.d.	n.d.	n.d.	n.d.	1.57 $\pm$ 0.18 (1.1)

\*Values inside parentheses are normalized relative to WT as 1.

<sup>1</sup> Data from<sup>5</sup>

<sup>2</sup> LRA: R707L/E711R/Y714A

<sup>3</sup>AAA: R707A/E711A/Y714A

<sup>4</sup>Data from<sup>7</sup>

<sup>5</sup>Temperature, 20°C. See **Supplementary file 1c** for additional values.

n.d., not determined

**Supplementary file 1c. Dissociation of acto-PfMyoA by MgATP at 20°C.**

<b>PfMyoA construct</b>	<b><math>V_{\max}</math> (<math>s^{-1}</math>)</b>	<b><math>K_m</math> (<math>\mu M</math>)</b>
WT	$326 \pm 9$	$240 \pm 18$
E6R	$857 \pm 52$	$351 \pm 51$
K764E	$801 \pm 54$	$257 \pm 38$
$\Delta N$	$616 \pm 45$	$103 \pm 25$
S19A	$592 \pm 40$	$227 \pm 44$
S691G	$348 \pm 7$	$201 \pm 12$
T586F	$471 \pm 27$	$364 \pm 50$
LRA	$472 \pm 35$	$198 \pm 42$

Fits to Michaelis-Menten equation  $\pm$  SE of the fit.

## **Chapter III: PfMyoA motor domain**

## 1. The conservation of the adaptations in Apicomplexa Phylum

One of the remaining issues of our work is the conservation of the adaptations described in PfMyoA in Myosin A of other organisms from the Apicomplexa phylum and in other myosin from the class XIV. In order to address this question, I have made a comparison of PfMyoA with another myosin A from another organism, *T. gondii* (TgMyoA). I also extended the analysis to Myosin B from *P. falciparum* (PfMyoB), another member of class XIV. Data on the function of PfMyoB in invasion have been obtained only recently by our collaborators ([Blake et al., 2020](#)): PfMyoB drives the first stage of internalization of the parasite. Even if PfMyoB is not essential to invasion, it is close to PfMyoA in sequence (35% of sequence identity and 59% of sequence similarity, NCBI Blast).

If the structure of *Toxoplasma gondii* Myosin A (TgMyoA) motor domain construct was solved in the PPS state at the same time ([Powell et al., 2018](#)), this structure was lacking the N-term extension. Interestingly, several phosphorylations were reported in the N-terminus of TgMyoA, but they could not be visualized in the structure ([Powell et al., 2018](#)). In order to complete the structure of TgMyoA, I generated a homology model of TgMyoA in the Rigor-like state with Swissmodel and PfMyoA in the Rigor-like state as a template (PDB code 6I7D). I used the same strategy to generate a homology model of the motor domain of PfMyoB in the Rigor-like state. I used a combination of sequence alignments and structural analysis of the homology models in order to study the conservation of the unique features of the motor domain of PfMyoA described in our two articles ([Robert-Paganin et al., 2019](#); [Moussaoui et al., 2020](#)).

## 2. The Glycine that plays a role of fulcrum is also replaced by a Serine in PfMyoB and TgMyoA

As explained previously, the force production in myosins relies on small changes in the active site (site of ATP hydrolysis) which are transmitted via connectors to the lever arm, involving the interaction between the Switch-2 and the Wedge (structural elements from L50 subdomain). In conventional myosins such as Scallop Myosin II the swing movement of the lever arm is coordinated by two connectors: The Relay helix kink and the piston-like movement of the SH1-Helix. The presence of a highly-conserved Glycine at the basis of the SH1-helix which plays the role of fulcrum promotes the piston-like movement. Unlike conventional myosins, in PfMyoA this Glycine is not conserved and it is replaced by Serine. This is

surprising since the mutation of this Glycine in conventional myosins impedes force production (Preller et al., 2010). Surprisingly, PfMyoA is still able to produce force and to move on actin filament. That means a new mechanism of force production that was described by our team (Robert-Paganin et al., 2019). Based on structural and sequence alignment this Glycine G<sup>SH1-SH2</sup> that promotes the mobility of the SH1 in conventional myosins is also absent in both PfMyoB and TgMyoA (as shown in **table 1**) and replaced by S673 and S693, respectively (**Figure 13**). which leads us to think that the SH1-helix of PfMyoB and TgMyoA is unable to perform the piston-like movement during the cycle. Given the fact that these myosins are both able to produce force, this implies compensatory mechanism, as it is the case for PfMyoA.

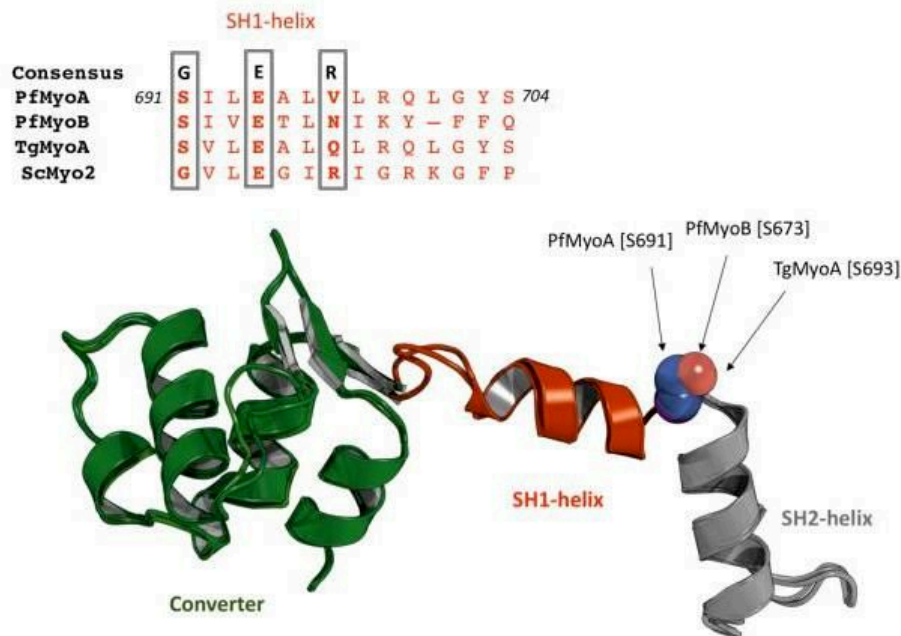


**FIGURE 13- Non-conservation of the fulcrum at the basis of the SH1-helix**

At the top of the panel the sequence alignment of SH1-helix of PfMyoA, PfMyoB, TgMyoA and ScMyo2. At the bottom of the panel the structural alignment of the converter (green), the SH2-helix (red) and the SH1-helix (gray) of PfMyoA-B, TgMyoA. The glycine that plays a role of fulcrum is replaced in PfMyoA-B, TgMyoA by a Serines, Serine S691, S673 and S693, respectively. This is expected to reduce the flexibility of the fulcrum.



### 3. Sequence alignment of PfMyoA, PfMyoB and TgMyoA

CLUSTAL O(1.2.4) multiple sequence alignment

```

PfMyoB      --MVNKINELNNY--F--RINSTFINKSENESENFYVWTYKSPNVDLYPDLVFFKCQVL53
PfMyoA      --MAVTNEEIKTASKIVRRVSNVEAFDKSGSVFKGYQIWTDISPTIENDPNIMFVKCVVQ58
TgMyoA      MASKTTSEELKTATALKKRSSDVHAVDHSNGVYKGFQIWTDLAPSVKEEPLDMFAKCIVQ60
              . :*:..      :      .:.* .   .: :**  :*..  *:::* ** *

PfMyoB      NING-DNY-EVKEISPETNSVYTVKKEHLFNCNNMVNINSH-RLNDMVHQNSAEVLNTLA110
PfMyoA      QGSKKEKLTVVQIDPPGTGTPYDIDPTHAWNCNSQVDPMSFGDIGLLNHTNIPCVLDFLK118
TgMyoA      AGTDKGNLTCVQIDPPGFDEPFVEPQANAWNNSLIDPMTYGDIGMLPHTNIPCVLDFLK120
              .   :   * :   * .   : :   : :* * . : :   . :   : * *   ** : *

PfMyoB      LRYEKNIYITIAEPLISVNPHYVIDTDMNEYKNKS-----TDLLPPHVYTYAKDAMLDF165
PfMyoA      HRYLKNQIYTTAVPLIVAINPYKDLGNTTNEWIRRYRDTADHTKLPHPVFTCAREALSNL178
TgMyoA      VRFMKNQIYTTADPLVVAINPFRDLGNTTLDWIVRYRDTFDLSKLAPHVFTARRALDNL180
              * :  **  *** *  *:::***: :..      : :      *  ***:  * :  * :  :

P Loop
PfMyoB      INTKNSQSIIISGESGSGKTEASKLVIKFYLSGVRED--NDISKTLWDSNFILEAFGNAK223
PfMyoA      HGVNKSQTIIVSGESGAGKTEATKQIMRYFASSKSGNMDLRIQTAIMAANPVLEAFGNAK238
TgMyoA      HAVNKSQTIIVSGESGAGKTEATKQIMRYFAAAKTGSMDLRIQNAIMAANPVLEAFGNAK240
              . : ** : ** : *** : * : : : : : : : : : : .   .   * . : :   : * : *****

Switch1
PfMyoB      TVKNNNSSRYGKYIKIQLDENQNIVSSSIEIFLLEKIRVVSQEPDERCYHIFYEILKGMN283
PfMyoA      TIRNNNSSRFGRFMQLVISHEGGIRYGSVVAFLLEKSRIITQDDNERSYHIFYQFLKGAN298
TgMyoA      TIRNNNSSRFGRFMQLDVGREGGIKFGSVVAFLLEKSRLVTQDEQERSYHIFYQMCKGAD300
              * : : ***** : : : : : : : : . * . : *  * * : : : : : * . ***** : * :

PfMyoB      DEMKKKYKIKSEEDYKYISNKSINIPeIDDAKDFENLMISFDKMKMSDLK-DDLFLTLSG342
PfMyoA      STMKSKFGLKGVTEYKLLNPNSTEVSGVDDVKDFEEVIESLKNMELSESIEVIFSVIVAG358
TgMyoA      AAMKERFHILPLSEYKYINPLCLDAPGIDDAEFHEVCESFRSMNLTEDEVASVWSIVSG360
              ** : : :      : ** . .   :      : ** . : * : :   * : . * : : .   : :   : : *

PfMyoB      LLLLGNIQFNGIEKGGKSNCSLDDENLEVNEASELLGIDYESLKNLSLVITEKSIANQK402
PfMyoA      ILTLGNVRLIEKQEAGLSDAAIMDEDMGVFNKACELMYLDPELIKREILIKVTVAGGTK418
TgMyoA      VLLLGNV EVTATKDGIDDAAAIEGKNLEVFKKACGLLFLDAERIREELTVKVS YAGNQE420
              : *  *** : ..      . . * . : : : : : : : * : : * . * : : : : : . .   . .   :

Switch2
PfMyoB      IEIPLSIEESLSICRSISKDIYNKIFYITKRINNFLNNKELENFIGILDIFGFEIFVK462
PfMyoA      IEGRWNKNDAEVLKSSLCKAMYELFLWIIIRHLNSRIEPEGGFKTFMGMLDIFGFEVFNK478
TgMyoA      IRGRWKQEDGMDLKSSLAKAMYDKLFMWIIIAVLNRSIKPPGGFKIFMGMLDIFGFEVFNK480
              * .   .   : : .   : * : . * : * : * : *   *   * : :   : : * : : ***** : * :

Relay Helix      Relay Loop
PfMyoB      NSLEQLLINIANEEIHNIYLFVVYKEKNLYKKEGIIIESVKYTNNESIIDLLRGK-TSI521
PfMyoA      NSLEQLFINITNEMLQKNFVDIVFERESKLYKDEGISTAE LKYTSNKEVINVLCEKGKSV538
TgMyoA      NSLEQFFINITNEMLQKNFVDIVFDRESKLYRDEGVSSKELIFTSNAEVIKILTAKNNSV540
              ***** : *** : * * : : : : : * : * : * : : : : : : . : : * . * . : : * * . : * :

Wedge
PfMyoB      ISILEDNCLAPGKKDESIVSVYTNKFSKNEHYSVCKKNITESFVIKHTVSDVTYSISNFI581
PfMyoA      LSYLEDQCLAPGGTDEK FVSSCATNLKENNKFTPAKVASNKNFI IQHTIGPIQYCAESFL598
TgMyoA      LAALEDQCLAPGGSDEKFLSTCKNALKGTTKFKPAKVSPNINFLISHTVGD IQYNAEGFL600
              : :  *** : ***** . ** : : * .   .   . : : . *   . * : * . ** : . : *   . : * :

PfMyoB      SKNKDILSPNILKLLKVSNNKLIQNLYDDAEVT-DSLGRKNLITYKYLENLKKICSYLKS640
PfMyoA      LKNKDVLRGDLVEVIKDSNPPIVQQLFEGQVIEKGKIAKGLSIGSFLNQLTSLMNLINS658
TgMyoA      FKNKDVLRAEIMEIVQQSKNPVVAQLFAGIVMEKGKMAKGQLIGSQFLSQLQSLMELINS660
              * * * : * : : : : : : * * : : * : .   :   . : : : : . **  : * : * : . .   : : *

```

**SH1**

PfMyoB TNIYFIKCIKPNETKEKNFNPKKVYPQLFSL**SIVETLNIKY-FFQYKYTFASFLSYQY**699  
PfMyoA TEPHFIRCIKPNNKKPLEWCEPKILIQHLAL**SILEALVLRQLGYSYRRTFEELYQYKF**718  
TgMyoA TEPHFIRCIKPNDTKKPLDWVP SKMLIQLHAL**SVLEALQLRQLGYSYRRPFKEFLQFKF**720  
\*: \*\*:\*\*\*\*\*.:\*: :: \*: \*.::\*\*:\*: : .\*: \* .\*\* ::

PfMyoB LDIAVSNDSSLDEKTKVTM-LLERNFDKDSYKVGHTMVFLKKEAVHKIRDIINSLNKCYR**758**  
PfMyoA VDIAAAEDSSVENQNKC VNILKL SGLSESMYKIGKSMVFLKQEGAKILT KIQREKLVEWE**778**  
TgMyoA IDLSASENP NLDPEKAALRL LKSKLPSEEYQLGKT MVFLKQTGA KELTQIQRECLSSWE**780**  
\*:\*:\*:\*:\*: :\*: : \* : .. \*:\*:\*\*:\*\*\*\*\*: .. : .\* .. \* :.

IQ1 IQ2

PfMyoB NLCCIT**SALIMK**IKKKRIVEENIKNLQA**QAAYFRKYKI**KEHE----- 801  
PfMyoA NCVSVIE**EAILK**HKYKQKVNNKPI SLRL**VQAHIRKKMVA**Q----- 818  
TgMyoA PLVSVLE**AYYAG**RRHKKQLLKLTPTFIIR**QAQHIRRHLVD**NNVSPATVQPAF 831  
:\*. \* :\*: :\*:\*:\*: :\*:\*:\*: : \*

ScMyoII	PfMyoA	PfMyoB	TgMyoA	The interface role
Y583	Not Conserved replaced by T586	Not Conserved replaced by T569	Not Conserved replaced by T588	Interaction with M514 <sup>Relay</sup> and E698 <sup>SH1-Helix</sup> => lever arm swing
E698 <sup>SH1-Helix</sup>	Conserved interact with I587	Conserved interact with V570	Conserved interact with V589	
M514 <sup>Relay</sup>	Not Conserved replaced by T522	Not Conserved replaced by T506	Not Conserved replaced by T524	
-	Sep19	S16	S21	Sep19 <sup>N-terminal extension</sup> interact with K764 further stabilize the Rigor like
G768	K764	Not Conserved replaced by Histidine	K766	
Y583	T586	Conserved	Conserved	Replace the aromatic and the bulky wedge
G513	T522	Conserved	Conserved	Replace the methionine residue from the relay
Q485	Q494 <sup>Relay</sup>	Conserved	Not conserved replaced by Histidine	Q494 <sup>Relay/</sup> S691 Interaction present in PPS and Rigor like
G694 <sup>SH1-SH2 (fulcrum)</sup>	Not Conserved replaced by S691	Not Conserved replaced by S693	Not Conserved replaced by S673	G <sup>SH1-SH2</sup> promotes the mobility of the SH1
A583	I587 <sup>Wedge</sup>	Not conserved replaced by valine	Not conserved replaced by valine	F473 <sup>Switch2</sup> interact with I587 <sup>Wedge</sup> Stabilize the Rigor like
F464	F473 <sup>Switch2</sup>	Conserved	Conserved	
I466	V475 <sup>Switch2</sup>	Not conserved replaced by Isoleucine	Conserved	V475 <sup>Switch2</sup> interact with H688 <sup>SH2</sup> Stabilize the Rigor like
Q692	H688 <sup>SH2</sup>	Not conserved replaced by F	Conserved	
R236	R241 <sup>Switch1</sup>	Not conserved replaced by K	Conserved	R241 <sup>Switch1</sup> interact with

				F476 <sup>Switch2</sup> additional interaction further stabilize the Rigor like
F467	F476 <sup>Switch2</sup>	Conserved	Conserved	

**TABLE 2-Comparison of critical residues that play important role in force production of PfMyoA, PfMyoB and TgMyoA.**

#### 4. Stabilization of the Converter by the N-term extension

In order to study the sequence adaptations in class XIV, we have made a structural alignment of the motor domain PfMyoA with complete homology models of PfMyoB and TgMyoA. We found that the N-terminal extension discovered in PfMyoA (residues 1-35) tunes the mechanical proprieties of this motor ([Robert-Paganin et al., 2019](#)) is present in both PfMyoB (residues 1-30) and TgMyoA (residues 1-37) but their helices are shorter than that of PfMyoA N-terminal extension. In addition to being divergent from each other, these N-terminal extensions present some structural differences. PfMyoB N-terminal extension contains an additional turn helix 19-INK-21 and TgMyoA N-terminal extension is more extended and less compact.

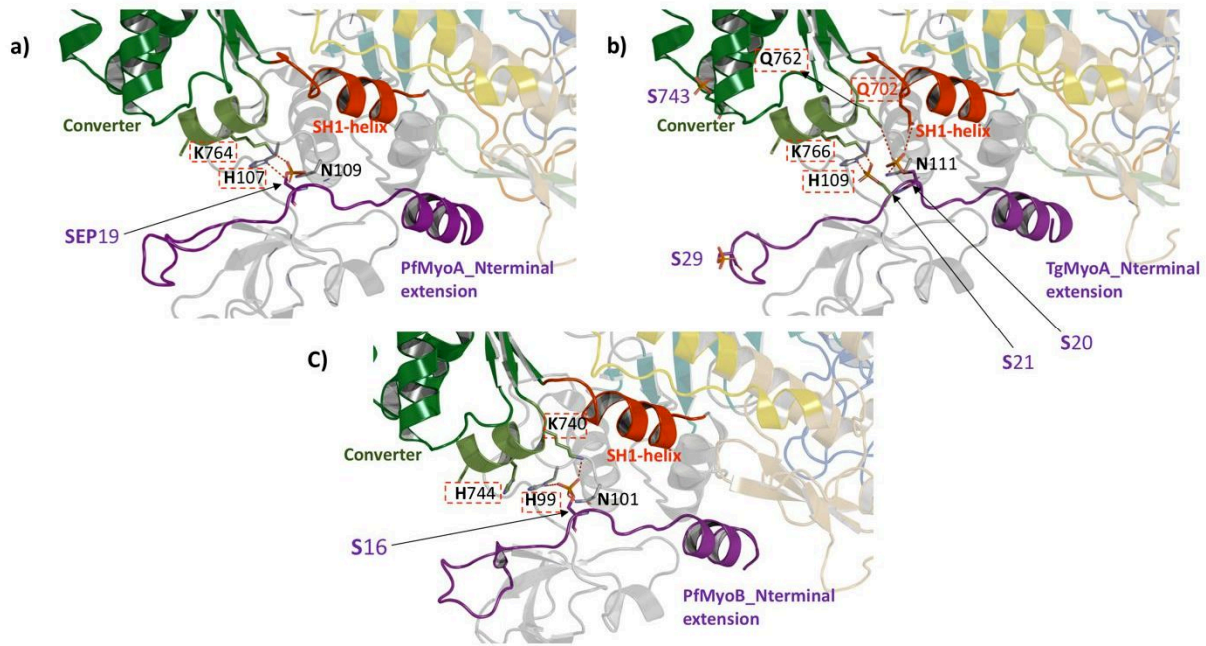


**FIGURE 14-Interactions that stabilize the rigor state in *PfMyoA* may be conserved in *TgMyoA* and *PfMyoB***

The converter/motor domain interfaces of *PfMyoA* (PDB code: 6I7D), *PfMyoB* (model generated by Phye2) and *TgMyoA* (PDB code: 6DUE) are represented. Residues that could be involved in the stabilizing the Rigor state are boxed with red dashed lines. The phosphorylated Serine seems to be conserved in all these myosins, also the contacts that stabilized the rigor are mainly conserved especially, the Lysine in the last helix of the converter that establish electrostatic contact with the phosphorylated N-terminal extension.

The phosphorylated Serine S19 present in *PfMyoA* and which is the key of the new mechanism discovered for *PfMyoA* (Robert-Paganin et al., 2019) is also present in the same location in space in *TgMyoA* S21, this phosphorylation which was demonstrated with other phosphorylations S20 and S29 in the N-terminal extension and S743 in the converter to be essential for fast motility and host cell egress of *T.gondii* Tachyzoites (which is equivalent to merozoites stages in *P.falciparum*) (Tang et al., 2014; Gaji et al., 2015; Powell et al., 2018). According to previous studies, phosphomimetic mutants of the three serines in the N-term extension leads to an increase of the speed of the protein in *in vitro* motility assays, which is not the case for a phosphomimetic of S743 (Powell et al., 2018). At the time of the study, Boulanger and coworkers could not explain the role of the phosphorylations of the N-term extension since the region was missing from the structure of *TgMyoA*, and hypothesized they were necessary to stabilize the N-term subdomain. Thanks to the homology model of the Rigor-like state of *TgMyoA* containing the N-term extension, we can model the three phosphoserines and their interactions in the Rigor-like state. Interestingly, the serine homologous the *PfMyoA*SEP19, *TgMyoA*SEP20 is oriented to interact with *TgMyoA*K766, which is the equivalent to

$PfMyoA$ K764 (**Figure 14**). A second phosphorylation of  $TgMyoA$ S21 is also oriented to interact with  $TgMyoA$ K766, which would strengthen the interactions with the converter, and thus induces additional stability of the Rigor-like state (**Figure 14**). The third phosphorylation from the N-term extension, SEP is not oriented to interact with the Converter  $TgMyoA$ SEP29, it may be involved in the stability of the N-terminal extension of the N-terminal subdomain of  $TgMyoA$  (**Figure 14**). Finally, the phosphorylation from the Converter,  $TgMyoA$ SEP743, is far from the N-terminal extension and has no impact on the motility when  $TgMyoA$  is complexed to  $TgELC1$  (Powell et al 2018). Interestingly, this phosphorylation is close to the Converter/ELC interface, it may be an element of regulation governing the association with  $TgELC1$  and 2 (**Figure 14b**). The authors have only evaluated the effect on mobility and stability of the complex  $TgMyoA/TgELC1/TgMLC1$ , but nothing has been done with  $TgELC2$  and transient kinetics experiments to evaluate other parameters than motility are still to be done.

However, my analysis suggests that the N-term extension of  $TgMyoA$  is also involved in electrostatic interactions stabilizing the Rigor-like conformation. Interestingly, contrarily to  $PfMyoA$  that displays only one phosphorylation in the N-terminal extension,  $TgMyoA$  displays two additional phosphorylated serines. The fact that the phosphorylation of these three serines gradually increases both the stability and the motility of the motor is interesting. As we concluded in our first study, this may come from the biology of *T. gondii*. Indeed, Tachyzoites from *T. gondii* are all more or less mobile depending on the stage of the cycle, the phosphorylation state of  $TgMyoA$  N-term extension may be an element of regulation allowing to tune the motor to different ratio of force production/mobility in order to fit the needs of the parasite in the different stages (Robert-Paganin et al., 2019). On the other hand, the phosphorylation from the Converter has no impact on motility and may have an effect on the association with the  $TgELCs$ .

In  $PfMyoB$ , the N-term extension is highly divergent in sequence compared to  $TgMyoA$  and  $PfMyoA$ . Interestingly, there is a serine at an equivalent position compared to  $PfMyoA$ SEP19:  $PfMyoB$ S16. This serine could be phosphorylated and interact with the last helix of the Converter in the Rigor-like state (**Figure 14**). If there is no equivalent for the lysine from  $MyoA$ ,  $PfMyoB$ SEP16 could interact with the residue at the equivalent position  $PfMyoB$ H744 and another residue from the last helix of the Converter,  $PfMyoB$ K740. This suggests that the N-term extension of  $PfMyoB$  may be involved in stabilizing the orientation of the Converter in the Rigor state of  $PfMyoB$ , but with a different set of interactions.



According to this analysis, we can hypothesize that the N-term extension in both TgMyoA and PfMyoB has a function to stabilize the Rigor-like conformation with phosphorylated serines. However, the position and the number of these serines, but also the residues from the last helix of the Converter involved in the interaction as well seem to vary. This may be another level of regulation present in the class XIV from Apicomplexa. Future studies on TgMyoA and PfMyoB will determine if these hypotheses are right and conclude if the tuning of the force production mechanism by phosphorylations of the N-term extension could be generalized to all the members of class XIV.

PfMyoB remains the most divergent and both the unknown structure of the N-term extension and the absence of lysine in the last helix from the Converter suggest some differences that may result from a different function. Future structural and functional studies on PfMyoB will allow to study its mechanism of force production and evaluate how the adaptations differ from PfMyoA and TgMyoA.

## **5. Conservation of the adaptations stabilizing the Rigor conformation**

In conventional myosins the release of hydrolysis products induces structural rearrangements of critical elements of the active site. Along with the phosphorylations, another residue of the N-term extension, PfMyoA E6, participates to the stabilization of the Rigor state, interacting with the Switch-1 and Switch-2 ([Robert-Paganin et al., 2019](#); [Moussaoui et al., 2020](#)). The stabilization of the Rigor-like state is mediated by a cation- $\pi$  interaction between N-term extension E6, Switch-1 R241 and Switch-2 F476 in PfMyoA. A similar interaction is observed in the homology model of TgMyoA between N-term extension E8, Switch-1 R243 and Switch-2 F478, demonstrating that this interaction is likely to be conserved. Conversely, in PfMyoB the glutamate from the N-term extension is not conserved, so this interaction is not conserved, suggesting that this adaptation is not present or may involve different residues (**Figure 15**).

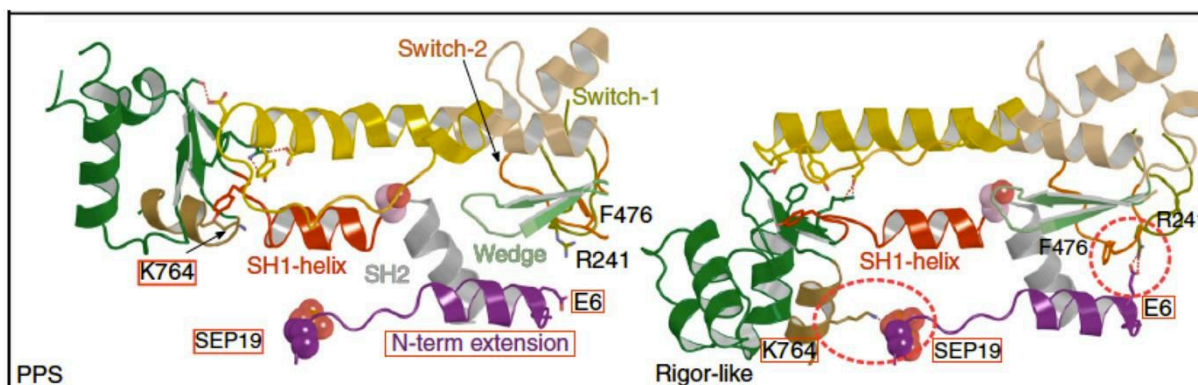


**FIGURE 15-*PfMyoA* force generation**

Taken from (Robert-Paganin et al., 2019). Overall view of the additional interactions established between the N-terminal extension and the motor domain connectors involving the Switch-1 and the Switch-2. We highlight how this N-terminal extension stabilizes the Rigor-like and compensates the immobility of the SH1-helix during the powerstroke.

## 6. Conservation of the adaptations within the connectors

As we have demonstrated in our work, major sequence differences are present within the connectors of PfMyoA compared to conventional myosines (Robert-Paganin et al., 2019). Transient kinetics demonstrated the importance of these differences in force production of this atypical motor, leading to the conclusion that they constitute some adaptation to the atypical mechanism of PfMyoA (Moussaoui et al., 2020).

In conventional myosins, the conserved aromatic residue at the tip of the wedge (Y583<sup>Wedge</sup> ScMyoII) favors the unpriming of the Relay and the piston-like movement of the SH1-helix in the motor domain. Rearrangements of these connectors are induced by steric clashes between the aromatic residue and M514<sup>Relay</sup> and E698<sup>SH1-helix</sup> (Robert-Paganin et al., 2019). Thus, the movements of the Relay and the SH1-helix which interact strongly with the Converter are associated with the lever arm swing. In all cases PfMyoA, PfMyoB and TgMyoA the aromatic residue from the wedge (Tyrosine 583 in ScMyoII) is replaced by a Threonine: T586<sup>Wedge</sup>, T569<sup>Wedge</sup> and T588<sup>Wedge</sup>, respectively. In the case of PfMyoA, this has been studied in depth because the presence of this Threonine instead of Tyrosine is not trivial, it causes less steric clash in PfMyoA which allows the wedge to establish contact with the Relay during the powerstroke and is an adaptation to the immobility of the SH1-helix (Robert-Paganin et al., 2019). To further study this adaptation in PfMyoA, we mutated T586<sup>Wedge</sup> by Phenylalanine that is supposed to increase the steric hindrance with the Relay and the SH1-helix, thus reduces

the mobility around the Wedge. Interestingly, there is no major effect on the motility and ADP-release of PfMyoA (Moussaoui et al., 2020). This mutation increased the transition to the PR state by 40% faster suggests that Rigor is slightly destabilized. The mutant T586F would likely destabilizes the PPS state, justified by the increase in basal ATPase (Moussaoui et al., 2020). This loss of stability more likely due to additional steric hindrance that alters the communication between the connectors, as shown by our structural analysis...

In PfMyoA, this adaptation of the Wedge is accompanied by adaptation in the SH1-helix and in the Relay. E698<sup>SH1-helix</sup> is conserved in PfMyoA, PfMyoB and TgMyoA but not the M514<sup>Relay</sup> which is replaced in all of PfMyoA, PfMyoB and TgMyoA by T522<sup>Relay</sup>, T506<sup>Relay</sup> and T524<sup>Relay</sup>, respectively.

These adaptations of the Wedge and of the communication between the Relay and the SH1-helix all result from the immobility of the SH1-helix in PfMyoA due to the replacement of the conserved glycine by a serine at the fulcrum. Since both TgMyoA and PfMyoB have a serine at the fulcrum, and consequently an immobile SH1-helix, some adaptations in the Wedge and in the communication between the Relay and the SH1-helix were expected. The fact that the specific adaptations described in PfMyoA are conserved in both TgMyoB and PfMyoA is fully consistent with our model.

## **Chapter IV: PfMyoA Full Length**

## 1. The resolved atomic structures of PfMyoA in PR and PPS

The study of the full-length (FL) structure of PfMyoA complexed to its two light chains PfELC1 and MTIP revealed an atypical priming of the lever arm in the PPS state (Moussaoui et al., 2020). Moreover, our study reveals how specific contacts between the converter and the motor domain, but also the interaction between atypical light chains and degenerated IQs stabilizes the priming and maintain the lever arm. In this part, I have tried to determine if the specific features of the lever arm of PfMyoA are conserved in TgMyoA and PfMyoB. For this purpose, I have generated homology models of both FL TgMyoA and PfMyoB and compared the adaptations. The homology models have been generated with SwissModel, with the FL structure of PfMyoA in PPS as a search model (PDB code 6YCX).

## 2. The interface that stabilizes the priming of the lever arm

Our structural study of the priming of the PfMyoA lever arm (Moussaoui et al., 2020) revealed an interface between the converter and the motor with mainly hydrophobic and polar contacts between the converter on one side and the N-term subdomain and the Transducer on the other side (Figure 16a, 16b). We subdivided these interfaces into two regions: i) region that involves a set of two polar interactions involving Converter<sup>R707</sup>/Nterm<sup>N177</sup>/Transducer<sup>E660</sup> and Converter<sup>E711</sup>/Nterm<sup>K183</sup> and also hydrophobic interactions established between Converter<sup>Y714</sup> and Nterm<sup>V181</sup> and Nterm<sup>N182</sup> ii) The second region consists in cation/ $\pi$ -stacking interactions between Converter<sup>R771</sup> from the last helix of the Converter and Nterm<sup>H160</sup> (Moussaoui et al., 2020).

To further study the effect of this interface on the stability of the lever arm priming, we designed triple mutant E711A +Y714A +R707A (mutant AAA) and we performed transient kinetic studies coupled with molecular dynamic (Moussaoui et al., 2020). Finally, we found that this interface drastically affects the stability of the lever arm priming and the functionality of the motor. Here, I study the conservation of this interface in both PfMyoB and TgMyoA, based on the structural analysis of this atypical interface (not present in conventional myosin). The structure of the PPS state of TgMyoA is already known (Powell et al., 2018) and displays the same priming as that found for PfMyoA. Interestingly, there are equivalent residues



maintaining the interface (**Table 2, Figure 16c**) showing that the structural features underlying TgMyoA and PfMyoA priming are similar in the two motors.

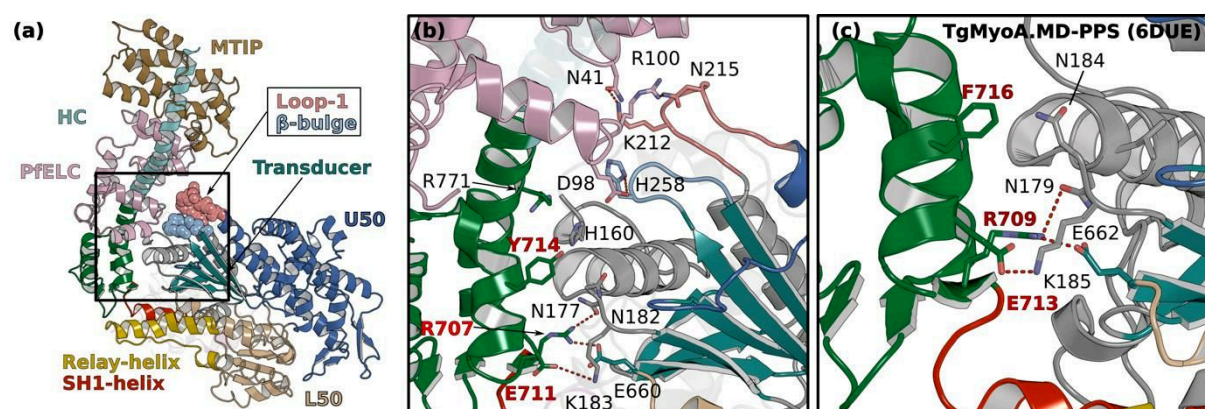


**FIGURE 16-Interface that promotes the priming of the PfMyoA lever arm**

Taken from (Moussaoui et al., 2020). **(a)** Overall structure of PfMyoA.FL-PPS. The priming of the lever arm is stabilized by interactions between elements of the lever arm and the motor domain (boxed in black). **(b)** Zoom on the lever arm/motor domain interface. The residues involved in the interaction are labeled. **(c)** MD/Converter interface in the structure of the motor domain of TgMyoA in PPS (PDB code 6DUE), the equivalent key-residues are colored in red.

In PfMyoB, the interface is completely degenerated but has adaptations that could maintain the stability of this interface, including polar interactions between the converter and the Nterm subdomain (See the **Table 3**). These interactions may stabilize the same lever arm priming as observed for PfMyoA, but the structure will be needed to conclude on the priming of PfMyoB.

PfMyoA	PfMyoB	TgMyoA
E711	S692	E713
Y714	S695	F716
R707	Y688	R709
V181	T168 interacts with S692	V183
N177	D164 interacts with Y688	N179
K183	N170 interacts with S692	K185
N182	K169	N184

**TABLE 3-Critical elements of the interface that stabilizes the lever arm priming**

### 3. Recognition of light chains (LCs) by IQ motifs

In myosins, the lever arm is constituted of the Converter, followed by an elongated single alpha helix, located downstream to the motor domain. It recognizes light chains such as calmodulins or calmodulins-like that stabilize it. Light chains recognize specific sequences called the IQ motifs (usually two or more IQ motifs are found in myosins): in conventional myosins from class II, the ELC (essential light chain) bind to the N-terminal region of the lever arm, while the RLC (Regulatory Light Chain) binds to the C-terminal part of the lever arm ([Anne Houdusse & Carolyn Cohen. 1996](#)). Unlike PfMyoA, TgMyoA has two ELCs including TgELC1 and TgELC2 that are able to recognize the first IQ motif. MLC1 (which is equivalent to MTIP in PfMyoA), interacts with the second IQ motif. The N-terminus of the MLC1 interacts with the GAP protein (glideosome-associated protein) complex, thus establishing the crucial link between the glideosome and the parasite motor ([Powell et al., 2017](#)). MTIP and MLC1 play a dual role as (1) adaptors which act on the structural characteristics of the motor and (2) as regulators that they recruit these motors to the inner membrane of the complex ([Frénal et al., 2010](#)).

In PfMyoA, MTIP is also important to promote the docking of PfELC to the lever arm ([Bookwalter et al., 2017](#)). Indeed, PfELC does not bind to the lever arm in the absence of MTIP ([Bookwalter et al., 2017](#)). Interestingly, in TgMyoA, MLC1 requires the association of TgELC1 or 2 to the lever arm to bind ([Pazicky et al., 2019](#)). This is surprising because the first IQ of TgMyoA and PfMyoA are very close in sequence (**Figure 17a**). This may be due to a difference in the interfaces TgELC/MLC1 and PfELC/MTIP or the differences in the structures of the ELC.

In PfMyoA, the contacts between MTIP and PfELC are mainly hydrophobic, so the interface ELC/MTIP is more rigid than in conventional myosins ([Moussaoui et al., 2020](#)). This interface is supported by a kink, which is facilitated by a Proline (P802) ([Moussaoui et al., 2020](#)) (**Figure 17d**). We found also in the same position Proline in TgMyoA (P804) in the homology model, the presence of the proline suggests the presence of the kink between TgELC and MLC1 in TgMyoA (**Figure 17d**). Sequence alignments of PfELC and *T. gondii* TgELC1 and TgELC2 the ELCs reveal how these light chains are divergent from conventional ELCs and from each other (see **Table 3**). A recent preprint described different structures of the lever arm of TgMyoA bound to TgELC1 or 2 and MLC1 ([Pazicki et al., 2019](#)). Surprisingly, TgELC1

and 2 have a structure that is similar to that described previously for conventional calmodulin-like ELCs, suggesting that they display specific sequence adaptations in order to recognize the degenerated IQs. Since the work from Pazicki and coworker is not reviewed and that the PDBs are not available, I could not make a direct comparison of structures, but this will have to be investigated in the future and may explain why the association of the light chains is different in PfMyoA and TgMyoA.

The lever arm of PfMyoB is predicted to be very divergent since its IQ motif does not conserve any element of the consensus and is highly different in sequence from Class XIV MyoA (**Figure 17a**). PfMyoB is deprived of the proline mentioned above, suggesting that the angle between the two IQs may be different than found in PfMyoA (**Figure 17c**). These findings are consistent with preliminary results from Jake Baum's laboratory: co-expression of the PfMyoB FL with both PfELC and MTIP does not allow co-purification of the PfELC light chain, indicating that this light chain does not bind to PfMyoB (Jake Baum, unpublished results).

According to my analysis, even if there is a different behavior of the light chains in PfMyoA and TgMyoA, the IQs are quite conserved and suggest a lever arm with sequence similarities such as the kink between the IQs. PfMyoB seems to be more divergent. In order to understand why PfMyoB is not capable to bind the PfELC, a close look at the conservation of the crucial residues involved in the anchoring of the PfELC is needed (see **Table 3**).

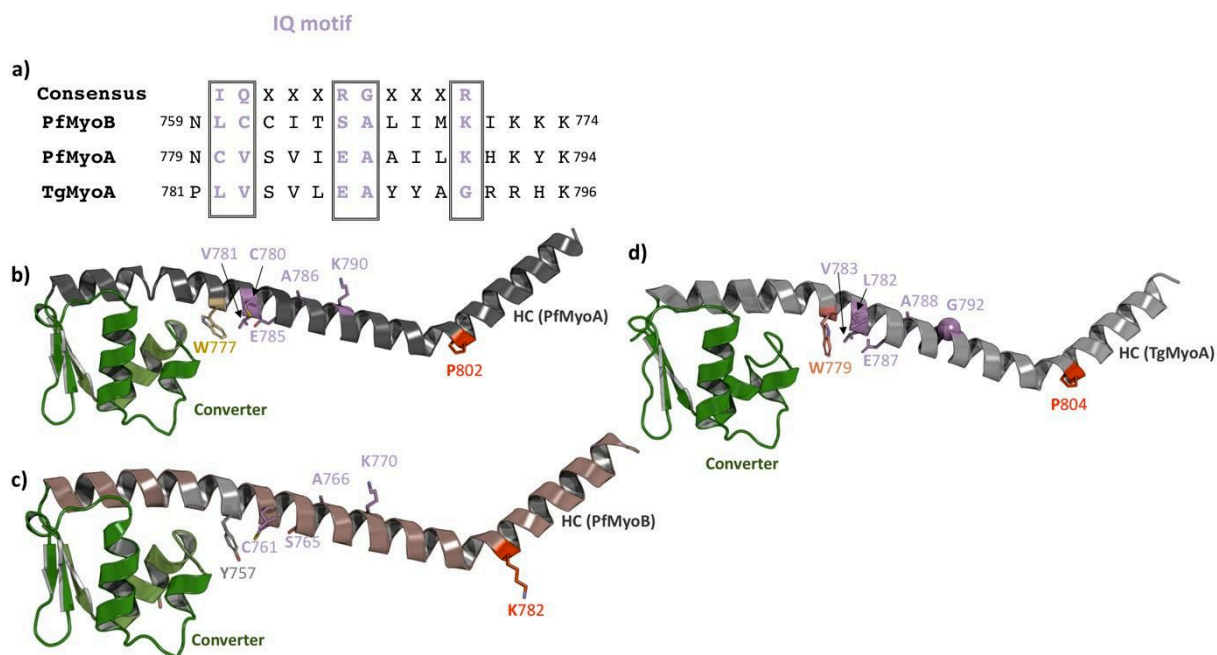


**FIGURE 17-Degeneration of IQ motif**

(a) The sequence alignment of the IQ1 from PfMyoA, PfMyoB and TgMyoA with the elements from the consensus. The Proline that facilitates the kink of the lever arm P802 (red) in PfMyoA (b) is replaced by K782 in PfMyoB (c) but conserved in TgMyoA (d).

PfMyoA	PfMyoB	TgMyoA
E725 Top-loop	N706 Top-loop	E727 Top-loop
D726 Top-loop	D707 Top-loop	N728 Top-loop
D720 Converter	D701 Converter	D722 Converter
K773 Converter	N753 Converter	C775 Converter
E776 Converter	C756 Converter	S778 Converter

**TABLE 4-The conservation of the residues that maintain the interactions between the ELC and the Heavy chain helix of the lever arm**

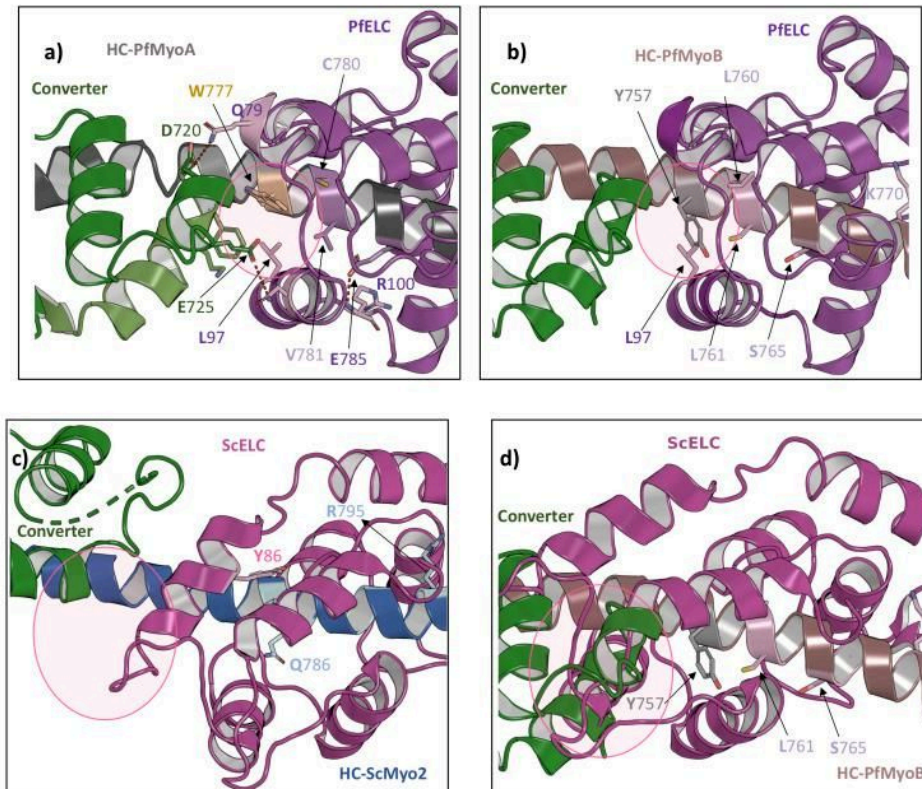


**FIGURE 18- Model of the PfMyoB and analysis of why PfELC is not interacting strongly on the 1<sup>st</sup> IQ motif.**

(a) The heavy chain/PfELC interface, residues allowing the anchoring of the PfELC to the PfMyoA lever arm are shown. (b) Alignment and superimposition of the PfELC was done with the generated model of the PfMyoB lever arm. We noticed that the aromatic residue Y757 is facing down and might hinder the binding of the PfELC to the PfMyoB lever arm. In addition, the contacts that are crucial to the interaction with PfELC are not conserved in the PfMyoB lever arm. (c) The Converter / ScELC interface in Scallop myosin II (d) we have done the same comparison with ScELC and PfMyoB lever arm but the converter is oriented differently, therefore the comparison is not reliable.

#### 4. Why cannot PfMyoB associate with PfELC?

Preliminary experiments performed by our collaborator Jake Baum suggest that PfMyoA and PfMyoB does not share the same light chain, PfELC. Indeed, they demonstrated that PfELC is not able to bind PfMyoB (Pr. Jake Baum, unpublished results). According to these results, PfMyoB should have a distinct ELC.

As described in our study, the PfELC structure in itself is divergent from the conventional ELCs that are usually more similar to calmodulin with conventional EF-hands helices (Moussaoui et al., 2020). The PfELC binds the PfMyoA lever arm in a similar conformation than other ELCs: the PfELC N-lobe interacts with the heavy chain in a closed conformation while PfELC C-lobe binds the heavy chain in a semi-open conformation. Major



differences are located in the C-lobe and in the interlobe linker. The  $\alpha 5$  helix is shorter and followed by an additional small turn helix that we called  $\alpha 5'$ . Due to a smaller interlobe linker, PfELC is more compact compared to other ELCs. These specificities allow PfELC to recognize the first IQ of PfMyoA specifically (**Figure 18a, 18c**) (Moussaoui et al., 2020).

Based on the analysis of the IQs of PfMyoA, PfMyoB and TgMyoA by sequence alignment, we found that the IQ motif of PfMyoB is highly divergent from the consensus IQxxxRGxxxR (no element is conserved), and also differs from the IQ motif of PfMyoA (only two residues are conserved).

In addition, the residues from the converter (D720, K773, E776) and E725, D726 from the top-loop participate to the anchoring of the PfELC (**Table 3, Figure 18a**). We found that these residues are not conserved in PfMyoB (see **table 4**) except for two residues: <sup>Conv</sup>D701 and <sup>top-loop</sup>D707. More importantly, the aromatic bulky W777 that stabilizes the PfELC is replaced by a Tyrosine (Y757) in PfMyoB (**Figure 18b**). Y757 like W777 is sandwiched by helices of the C-lobe, but with a different orientation, that may interfere with the binding of PfELC. Possible steric clashes between Y757 and L97 would indeed prevent this association (**Figure 18d**). This analysis could explain why PfELC does not bind PfMyoB but also suggests that the ELC of PfMyoB may recognize its IQ differently than found for the PfMyoA myosin. In turn, this could also result in promoting a different ELC/Converter interface and a different ELC/MTIP interface.

## 5. MTIP recruits PfMyoA to the plasma membrane of the complex

Myosin tail-domain interacting protein (MTIP) is a protein of 24 KDa discovered in 2002 by Bergman et al., 2003. It interacts with the C-terminal region of the lever arm. In Bergman, et al., 2003, they showed by yeast two-hybrid screen assays that the 15-amino acid of MyoA C-terminal are involved in the interaction with MTIP. MTIP consists of four degenerated EF-hand motifs but none of these motifs have been shown to coordinate  $\text{Ca}^{2+}$  as it is the case of Myosin light chain1 (MLC1) (Bosch et al., 2005).

The PfMyoA sequence stops after the second IQ motif and is thus devoided of a tail sequence. It is thus addressed to the inner plasma membrane of the parasite by the interaction of MTIP with GAPs proteins. MTIP in complex with PfMyoA adopts a compact conformation

(Bosch et al., 2007). Mutagenesis and structural studies in Bosch et al., 2007 have shown that the K813 residue in the PfMyoA lever arm is crucial in maintaining the compact conformation of MTIP by interacting with <sup>MTIP</sup>G103 and <sup>MTIP</sup>Q204 (**Figure 19a**) (Bosch et al., 2007). We found that the residue equivalent in PfMyoB is K793, possibly indicating that the MTIP homologue that binds the second IQ motif of PfMyoB may use in part similar interactions.

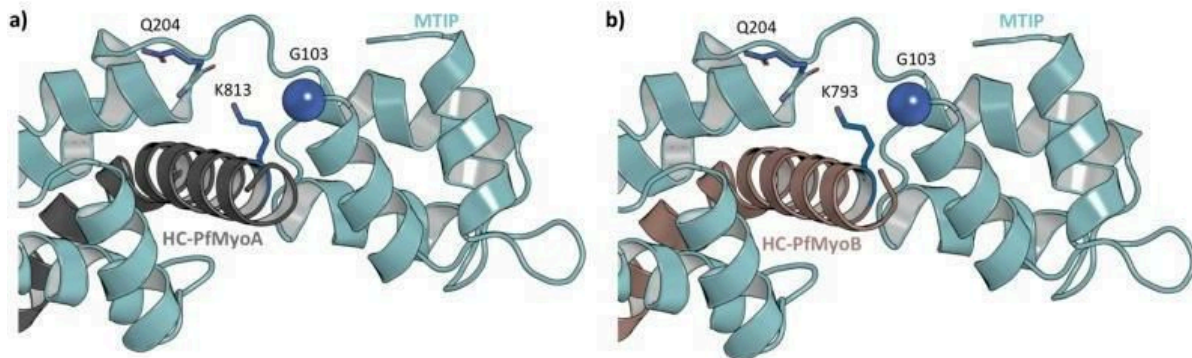


**FIGURE 19-Interaction MTIP-lever arm**

(a) Cartoon representation of how MTIP anchors the PfMyoA IQ2, we highlight the role of K813 in the maintaining of the MTIP compact conformation. (b) Superimposition of MTIP with the IQ2 from PfMyoB (generated model by Phyre2), the lysine is conserved in PfMyoB (K793) and is predicted to interact with both Q204 and G103 as it is the case in PfMyoA.

Based on the assumption that PfMyoA and PfMyoB may have a redundant function, Hernandez et al., 2018 had the idea to study the interaction between PfMyoB and MTIP (the light chain of PfMyoA). They used both molecular docking predictions (Hernandez et al., 2017) and *in vitro* protein–protein interaction assays using far western blot (FWB) and *in vitro* pulldown (Hernandez et al., 2018). Based on these experiments, their conclusion was that PfMyoB may have some redundant function with PfMyoA at some stages of the cycle, such as merozoite invasion. In fact, these results are not surprising considering that the lysine K813 that is crucial for the binding of MTIP is conserved in PfMyoB. In addition, the H810 which is also important in the interaction between MTIP and PfMyoA is replaced by Tyrosine Y790 in PfMyoB which could establish the same interactions than H810 especially, the electrostatic interaction with D139 of MTIP (**Figure 20a, 20b**). Thus, nothing major indicates why MTIP would not associate with PfMyoB. However, this interaction characterized *in silico* or *in vitro* may not make sense in the *in vivo* context since PfMyoB has not been found to be associated to MTIP or to the glideosome in co-immunoprecipitation assays (Yusuf et al., 2015). Interestingly, *in vivo* experiments reported the interaction of PfMyoB with a novel CaM-like

protein that was called MLC-B (Yusuf et al., 2015). MLC-B was shown to interact with the second IQ of PfMyoB and comprises a long helical N-terminal extension that may be involved in addressing PfMyoB (Yusuf et al., 2015). Further investigations will be needed to identify precisely the light chain(s) specifically binding to the second IQ motif of PfMyoB and how this is regulated and linked to the biological function of this myosin.

MTIP has a N-terminal extension (residues 1-74) (Tardieux and Baum, 2016). In *T. gondii*, MLC1, the analog of MTIP, is also binding TgGAP45, and this association occurs through the N-terminal extension (Frénal et al., 2010). Based on sequence alignment (see **Figure 23**), MTIP and its analog from *T. gondii* MLC1 share 57 % sequence identity and 73% sequence similarity in their N-terminal region (**Figure 21**). Given the similarity of the N-terminal extension of these two light-chains, it is tempting to speculate that MTIP also associate to PfGAP45 through its N-terminal extension as it is the case in *T. gondii*, even if this is still to be demonstrated.

Interestingly, phosphorylations have been demonstrated to govern the association of MTIP to the heavy chain of PfMyoA. S107 and/or S108 are the only residues from MTIP to be phosphorylated *in vivo* (Douse et al., 2012; Jacot et al., 2014). The analyzing of our structure shown that <sup>MTIP</sup>S107 and <sup>MTIP</sup>S108 are oriented outside of the lobe, so that they interact with R806 and L805 from the lever arm , respectively.

*In vitro*, phosphomimetic mutants on these sites reduce the affinity of MTIP to PfMyoA (Douse et al., 2012; Jacot et al., 2014). These phosphorylations are thus able to modulate the interaction between MTIP and PfMyoA. There is only one serine at this site in MLC1 (S113) and it corresponds to <sup>MTIP</sup>S107. Surprisingly, the phosphomimetic mutation of this residue does not affect the interaction with TgMyoA *in vitro* (Jacot et al., 2014). However, in the same paper the authors identified other phosphorylations of MLC1, S92 and S97 whose role is not yet known. As long as the role of these phosphorylations remains unknown, we cannot say if these interactions are involved in the association to TgMyoA or even TgGAP45.

Given the key-role of MTIP and MLC1 in connecting the Myosin A to GAP45, it is tempting to speculate that they may be involved in the regulation of the function of the glideosome. The presence of specific phosphorylations in MTIP disrupting the interaction with PfMyoA is a strong argument in favor of this idea. Future studies will be necessary to decipher the role of this putative regulation and how it may be different with MLC1 that has different

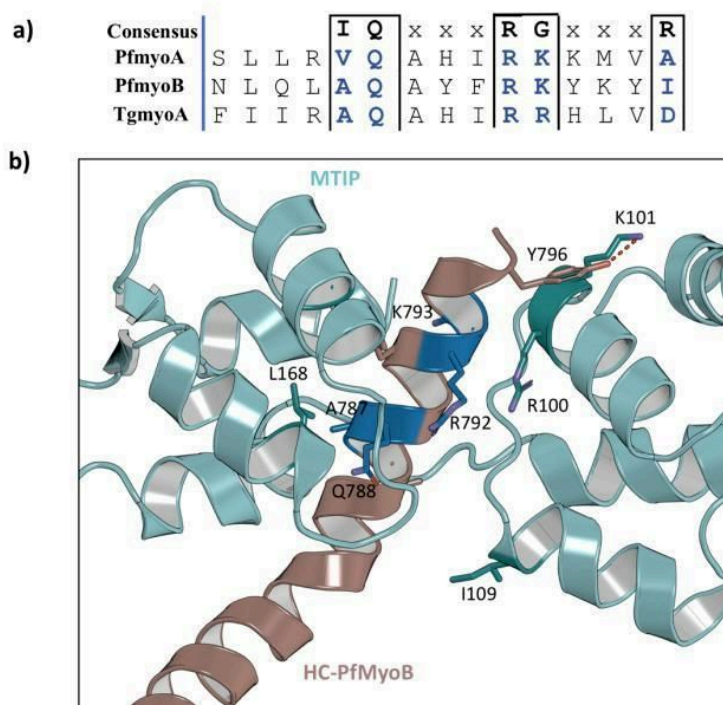


**FIGURE 20-*MTIP* may anchor *PfMyoB***

**(a)** Sequence alignment of IQ2 from PfMyoA, PfMyoB and TgMyoA, most of the element from PfMyoA consensus are conserved in PfMyoB. **(b)** Superimposition of MTIP with the lever arm from PfMyoB showing the potential ability of MTIP to bind PfMyoB



— N-terminal region  
— Linker between N- and C- lobe

Sequence identity (42%)  
Sequence similarity (62%)

**FIGURE 21-Sequence alignment of MTIP from *P.falciparum* and MLC1 from *T.gondii*.**

## 6. Towards the production of a minimal glideosome

The critical missing piece to reconstitute a minimal glideosome (**Figure 22**) in our study are GAPs proteins (GAP45, GAP40 and GAP50). GAP45 were first described in *Toxoplasma gondii* (Gaskins et al., 2004; Ridzuan et al., 2012). GAP40 and GAP50 were later identified in the IMC (Inner Membrane Complex) (Ridzuan et al., 2012). In the case of TgMyoA, the C-terminal region of TgGAP45 recruits MLC1-TgMyoA to the IMC (Frénal et al., 2010). In this same paper, they showed that TgGAP45 is essential in gliding, invasion and egress in *Toxoplasma gondii*. The glideosome model is built by identifying the proteins that compose it. It is localized in the region between the PM and the IMC of the parasite (Keeley & Soldati, 2004) (See **Figure 24**). The GAP complex allows to anchor the specific PfMyoA motor that interacts with the polymerized actin 1 (PfAct1) (Wetzel et al., 2003) to the glideosome, by interactions with MLC1 or MTIP, specific light chain of the motor (Bergman et al., 2003; Herm-Götz et al., 2002; Frénal et al., 2010).

Interestingly, GAP45 displays several post-translational and co-translational modifications in GAP45, including a set of phosphorylations (Gilk et al., 2009; Ridzuan et al., 2012). The reconstitution of a complex between PfGAP45 and PfMyoA was initially an aim of my PhD, in order to reconstitute a minimal glideosome. Unfortunately, we could not purify GAP45, the protein was not soluble and could not be produced either alone or by co-purification with PfMyoA (Kathleen Trybus, unpublished results). The other complication also lies in the fact that despite that we solved the full length structure of PfMyoA associated to its light chains ELC and MTIP, we still lack the structural information of the MTIP N-terminal region. We will explain later our analysis and the strategies that we will adopt to study this region of MTIP, which could be the key for the formation of a minimal glideosome.



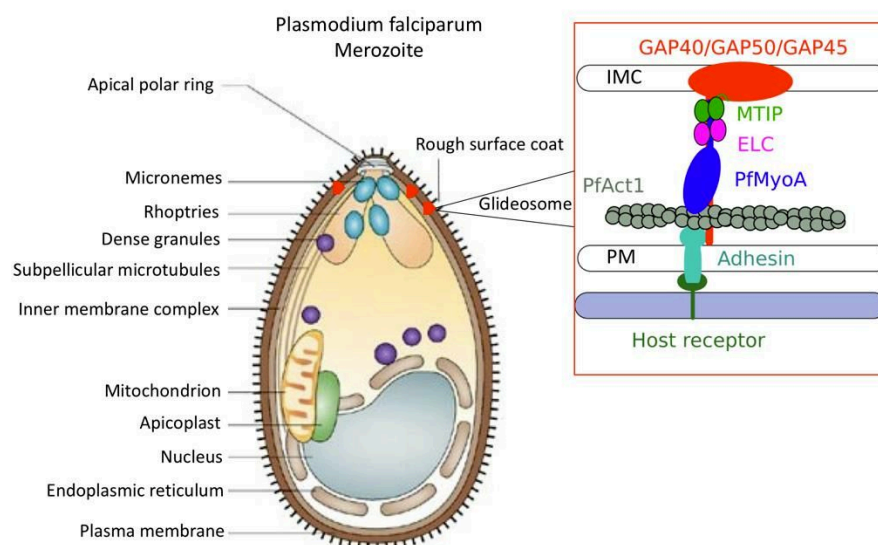


**FIGURE 22-Glideosome localization in merozoite**

Modified from [Baum et al., 2006](#).

As I already mentioned in the methods section, the laboratory of our collaborator Kathleen Trybus succeeded in producing the PfMyoA full length with its two light chains. One major goal of my PhD was to find crystallization conditions for PfMyoA in different nucleotide states. However, in our constructs, the N-terminal region of MTIP was truncated because it was predicted unstructured by HCA analysis (see below). Generally, the unstructured regions of a protein make its crystallization difficult or even impossible. MTIP was first analyzed by hydrophobic cluster analysis (HCA), a method that aims to predict the disordered regions of proteins based on sequence analysis ([Callebaut et al., 1997](#)) (see **Figure 23**). Based on the HCA of MTIP we found that the MTIP N-terminal region could be unstructured (1-74 amino acids) since this region is rich in proline and charged residues, upstream of this region, some hydrophobic residues could play important roles in the interaction with GAP proteins. Another argument that was in favor of the deletion of the N-terminal region was that this region is missing in all the crystal structures of MTIP to date ([Bosch et al., 2007](#); [Douse et al., 2015](#)). However, the understanding of the structural features governing the association of GAP45 with both MTIP and the IMC is crucial to reconstitute a minimal glideosome.



## 8. GAP45 phosphorylations and glideosome assembly

As explained earlier, GAP45 displays a set of phosphorylations. The calcium-dependent protein kinase (CDPK1) of *P. falciparum*, has been proposed to phosphorylate both PfGAP45 and MTIP, but also their homologs in *T. gondii* TgGAP45 and MLC1 (Ridzuan et al., 2012; Jacot et al., 2014). PfGAP45 was reported also to be phosphorylated *in vitro* by the protein kinase B (PfPKB) (Vaid et al., 2008; Thomas et al., 2012). Whereas, pulse-chase analysis showed that GAP45 is phosphorylated before its association with GAP50 in the IMC (Rees-Channer et al., 2006; Ridzuan et al., 2012).

The role of the phosphorylations of GAP45 has been studied in *T. gondii*. S163 and S167 control the association of TgGAP45 with TgGAP50 (Gilk et al., 2009; Ridzuan et al., 2012). The expression of phosphomimetic mutants abolished the association of TgGAP45 with TgGAP50 (Gilk et al., 2009; Jacot et al., 2014). Interestingly, these two phosphorylated serines are not conserved in PfGAP45, <sup>TgGAP45</sup>S163 is replaced by an aspartic acid and <sup>TgGAP45</sup>S167 is replaced by a Threonine in PfGAP45 (Figure 24). In PfGAP45, residues S89, S103 and S149 from PfGAP45 were reported to be phosphorylated *in vitro* by PfCDPK1 (Vaid et al., 2008; Green et al., 2008; Ridzuan et al., 2012). In this same paper, the authors show that the mutation of the phosphorylated serines S89 and S103 in PfGAP45 by Alanine do not affect the localization to the IMC or the formation of the complex. Further studies demonstrated that these phosphorylation sites may not be involved directly in glideosome complex formation (Thomas et al., 2012). Further studies are required to establish the role of the phosphorylations of PfGAP45 in the function of the parasite.

The role of GAP45 phosphorylations will require further studies to be elucidated. However, in TgGAP45, two of these phosphorylations seem to be involved in glideosome assembly, regulating the association of GAP complex. Here again, the position, the number and the role of the phosphorylations differ between GAP45 from *T. gondii* and *P. falciparum*. These phosphorylations may be another component of the fine regulation of the function of the glideosome. If this is true, this regulation may be different in *P. falciparum* and in *T. gondii*, this is another example of the differences existing among the phylae of the Apicomplexan parasites. Future investigations will shed light on these mechanisms and we will have to study specifically how the phosphorylation sites could impact binding of PfGAP45 to MTIP in order to reconstitute the complex and assemble a minimal glideosome.





## 9. Approaches for the treatment against malaria

As we mentioned previously, the parasite develop resistance against all antimalarial treatments discovered to date (**Figure 25, Table 5**) (Sinha et al., 2014). The first synthetic antimalarial drug that had a great success was chloroquine which was discovered around 1934 (Wellems and Plow. 2001). Unfortunately, this success did not continue since several cases of parasite resistance against chloroquine appeared in South-East Asia around 1957, then it was spread to all the countries affected by malaria. (Wellems and Plow. 2001; Pazhayam et al., 2019). Another treatment recommended by WHO, 2001 is Artemisinin-based Combination Therapies (ACTs) which is an important class of antimalarial medication (Yeung et al., 2004). This treatment had the same fate as the treatment mentioned above. First cases of ACTs resistance were observed in Western Cambodia and then in all malaria endemic countries (Amaratunga et al., 2014; Phyo et al., 2012; Ashley et al., 2012; Huang et al., 2013). Efforts are being made by researchers to find new therapeutic approaches and elaborate vaccines against malaria. Among the drugs against malaria developed these last years, the proton pump inhibitors (PPIs), esomeprazole magnesium and omeprazole (Pazhayam et al., 2019) are described as promising, safe and orally administrated but needs further studies to anticipate a potential treatment resistance (Manickam et al., 2018; Das et al., 2018; Pazhayam et al., 2019). In addition, several vaccines are in clinical phase 2b (see **Table 5**), and the most advanced candidate vaccine to date is RTS,S/AS01 completed the clinical phase 3. This vaccine received a favorable opinion from the European Medicines Agency (Laurens. 2018).

Interestingly, all the treatments currently available target elements of the metabolism of the parasite. Given the high mutability of the unicellular parasites such as *Plasmodium*, it is not surprising that they can develop resistance strategies. Once the machinery that powers the gliding motility was discovered, it is naturally that researchers started to study it deeply to understand the different interactions that stabilize it and understand the mechanism of its regulation. Among the inhibitor targets that are currently studied, one can cite the junction between AMA 1 and RON protein complex, inhibitors of actin dynamics, peptides that target the interface between MyoA and MTIP. Targeting the acto-myosin system that fuels parasite motility and infectivity would be a solution to resistance since actin has very low variability and that single point mutations in the myosins are often associated with severe motor dysfunctions (Robert-Paganin et al., 2018; reviewed by Robert-Paganin et al., 2020).



Our collaborator Jake Baum showed that divergent PfMyoA is essential in both motility and red blood cell invasion ([Robert-Paganin et al., 2019](#)), which gives us an evidence that PfMyoA is an excellent therapeutic target. Later, we demonstrated ([Moussaoui et al., 2020](#)) the essentiality of the PfELC in the invasion mechanism of the parasite. Based on our results, we can thus propose different strategies targeting the acto-myosin complex of *P. falciparum*: (i) treatments specifically blocking/inhibiting the motor function of PfMyoA; (ii) treatments blocking the association of the light chain with the lever arm (iii) treatments that could block the interaction between PfMyoA and the actin filament.

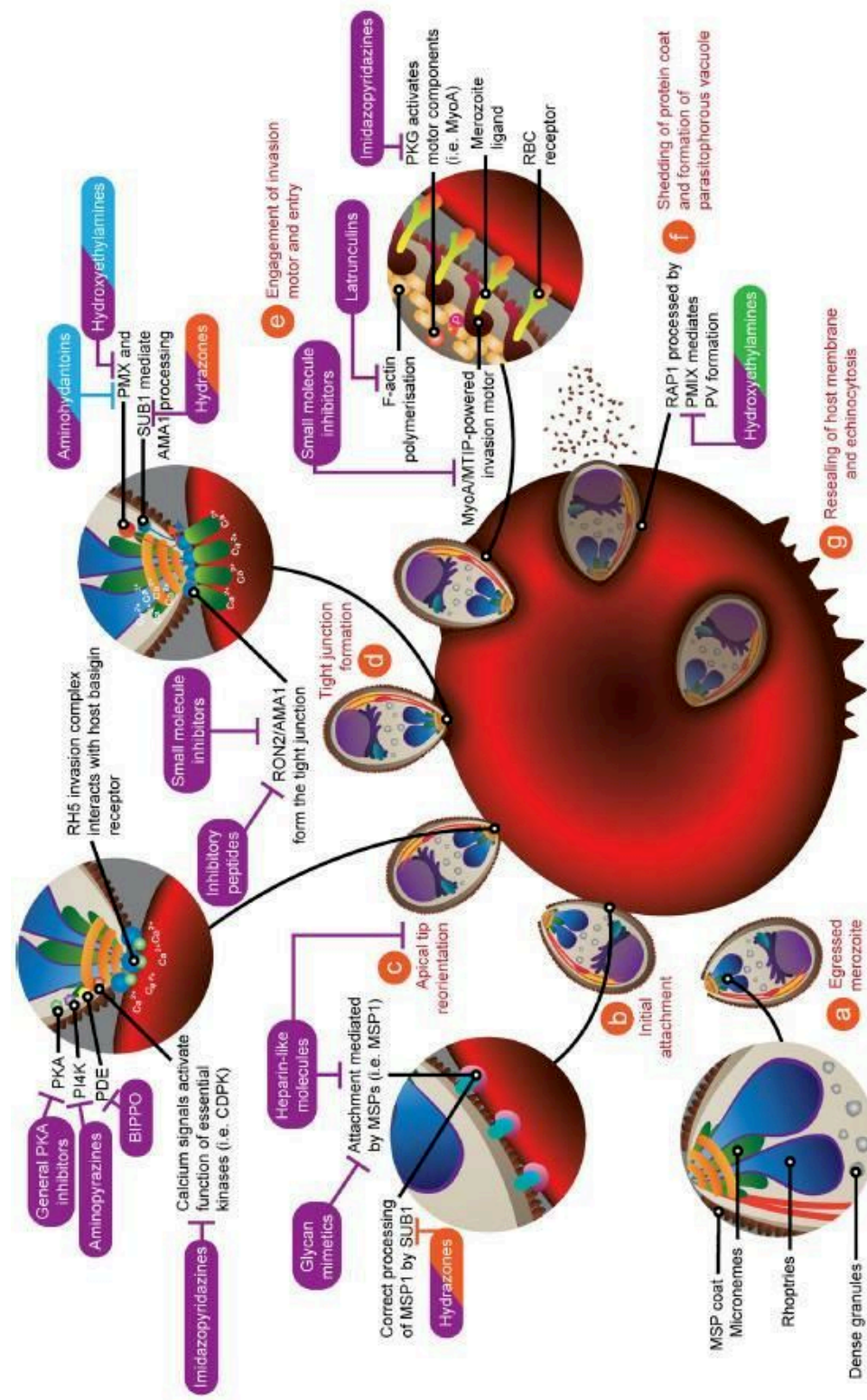


**FIGURE 25- Existing treatments against malaria and different kind of novel approaches that are under development. (Taken from Burns et al., 2019)**

Antigen	Vaccine mechanism	Most advanced status
<i>Plasmodium falciparum</i>		
RTS,S (CSP fused to HBsAg)	Inhibits sporozoite motility, prevents hepatocyte invasion	Pilot implementation, phase 4 Pharmacovigilance baseline
RTS,S fractional dose (CSP fused to HBsAg)	Inhibits sporozoite motility, prevents hepatocyte invasion	Phase 2b clinical testing in endemic areas
ChAd63/MVA, ME-TRAP	Inhibits sporozoite motility, prevents hepatocyte invasion	Phase 2b clinical testing in endemic areas
PfSPZ (radiation-attenuated whole-organism sporozoites)	Inhibits sporozoite motility, prevents hepatocyte invasion	Phase 2b clinical testing in endemic areas
PfCelTOS	Inhibits sporozoite motility, prevents hepatocyte invasion	Phase 1 clinical testing
R21 (CSP-HBsAg fusion protein)	Inhibits sporozoite motility, prevents hepatocyte invasion	Phase 1 clinical testing
Recombinant CSP	Inhibits sporozoite motility, prevents hepatocyte invasion	Preclinical testing
EBA175	Targets merozoite ligand that mediates erythrocyte invasion	Phase 1 clinical testing
Genetically attenuated whole-organism sporozoites	Inhibits sporozoite motility, prevents hepatocyte invasion	Phase 1 clinical testing

**TABLE 5-Current malaria vaccines stages**

Modified from Matthew B. Laurens, 2018.

## 10. Three strategies to develop treatments targeting the actomyosin complex of *P. falciparum*

The "Structural Motility" team and its collaborators are involved in the search of developing new treatments against malaria, with PfMyoA as a target. The team is interested in defining how specific modulators of myosin activity can be used for the treatment of human diseases, but also to investigate the mechanism of these allosteric modulators. Identifying specific modulators for the inhibition of PfMyoA activity will open a door for the development of a new generation of anti-malarial drugs.

Structure-based drug discovery approaches like docking have significantly contributed to the identification of hit compounds in the Pharma industry (Kitchen et al., 2004). However, in the case of allosteric proteins such as myosin, several problems arise. First, the protein adopts multiple structural states during the motor cycle that are not all characterized at atomic

resolution, which is key to understand in which of them the ligand may bind. Transient kinetics and relevant structures of myosin/drug complexes provide this information (Planelles-Herrero et al., 2017). The Structural Motility team has shown that allosteric inhibitors can bind to pockets that only transiently exist in the absence of ligands (e.g. SMM2 in complex with CK571 (Sirigu et al., 2016), which cannot be guessed without co-crystallization. Once visualized, however, these pockets can be exploited to search for new scaffolds that might bind and thus modulate motor activity. Third, the design of inhibitors versus activators in allosteric proteins is challenging per se. It requires an understanding of how a compound may allow or prevent a functional transition, and this remains an unsolved problem.

Search for inhibitors will be performed thanks to the combined expertise of our laboratory and members or an international consortium of experts (Figure 26). Libraries of compounds will be screened in a miniaturized ATPase assays in order to identify potential modulators of the activity of PfMyoA. The precise effect of the selected compounds on ATPase activity will be evaluated by coupled enzyme assays in order to calculate the inhibition constant ( $K_i$ ). In parallel, transient kinetics and *in vitro* motility assays performed in the team of Kathleen Trybus will determine which transitions are affected by the compounds in the motor cycle. The structure of PfMyoA complexed to each compound will be solved by X-ray crystallography to decipher the mechanism of action of the drug candidates. The structure analysis and SAR studies will allow to optimize the compound and thus perform rational drug design. Iterative cycles of optimization will be performed if necessary. Finally, the effect of the most promising and efficient inhibitors will be tested directly on the parasite in the lab of Jake Baum (Imperial College, London, UK) (Figure 26).

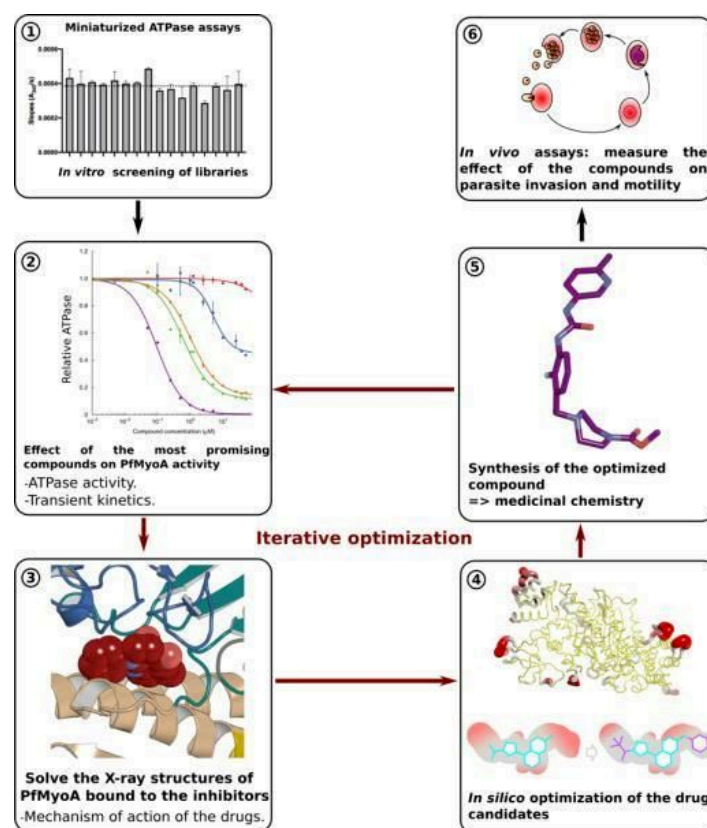


**FIGURE 26-Global strategy to target *PfMyoA*.**

(1) First step is to do screening with miniaturized ATPase assays, once promising effectors will be identified (from libraries), the specificity and efficiency of these compounds in inhibiting ATPase activity will be performed as well as transient kinetics (Dr. Kathleen Trybus laboratory) (2) the most promising compounds will be co-crystallized with PfMyoA (3) Structural information will guide the optimization of the compounds by structure activity relationship (4) and synthesis of most promising optimized compounds will be performed (5). In addition, *in vivo* assays will be performed to measure the effect of these compounds on invasion and motility of the parasite (6).

### 10.1 Inhibition of PfMyoA activity

As already mentioned in the section of motor effectors, (Chapter I, 1.7) several small molecules have been identified that target specifically Myosin I, II, V and VI. These small molecules interact in different ways with the motor domain of target myosins and have not the same effect on the motor cycle. Some of these drugs affect the rate of transitions between states of the motor cycle (Kawas et al., 2017; Planelles-Herrero et al., 2017), others are able to block intermediate states (Sirigu et al., 2016).

Four binding sites (pockets) have so far been identified by structural studies (Allingham et al., 2005; Fedorov et al., 2009; Preller et al., 2011b; Sirigu et al., 2016; Planelles-Herrero et al., 2017). These pockets share a hydrophobic nature with some polar and apolar contacts that are involved in the interaction with the small molecules. They are distributed in the vicinity of



critical regions for the mechanochemical properties of the motor domain such as connectors (Manstein & Preller, 2020). Thus, each modulator has different properties and acts differently on the myosin force production cycle (Manstein & Preller, 2020).

In this chapter I will detail the properties of the best characterized myosin inhibitors, and why this strategy can be promising against malaria.

### 10.1.1 Blebbistatin – a myosin inhibitor

Blebbistatin binds in a pocket that is located between the U50 and L50 subdomains. The drug fits in the pocket as found in the pre-powerstroke state. It thus is compatible with ATP hydrolysis but myosin is then blocked in the PPS state (Allingham et al., 2005; Kovács et al., 2004; Ramamurthy et al., 2004). Blebbistatin is a specific inhibitor of the Myosin II class. It inhibits muscle myosins (skeletal and cardiac) as well as non-muscle myosins (NMM2a, NMM2B), with an IC<sub>50</sub> between 0.5  $\mu$ M and 5  $\mu$ M (Limouze et al., 2004; Zhang et al., 2017).

I studied the conservation of the residues of the Blebbistatin binding pocket in PfMyoA. I found that both <sup>MyoII</sup>L262 and <sup>MyoII</sup>G240 that interact with Blebbistatin are conserved in PfMyoA (<sup>PfMyoA</sup>L271 and <sup>PfMyoA</sup>G249). In addition, the tyrosine <sup>MyoII</sup>Y261 that stacks the Blebbistatin is replaced by another aromatic residue (<sup>PfMyoA</sup>F270). However, the <sup>MyoII</sup>S456 is replaced by <sup>PfMyoA</sup>F471 which could cause a steric hindrance with Blebbistatin binding (Figure 27). The presence of <sup>PfMyoA</sup>F471 reduces the pocket and makes it unable to bind Blebbistatin derivatives.

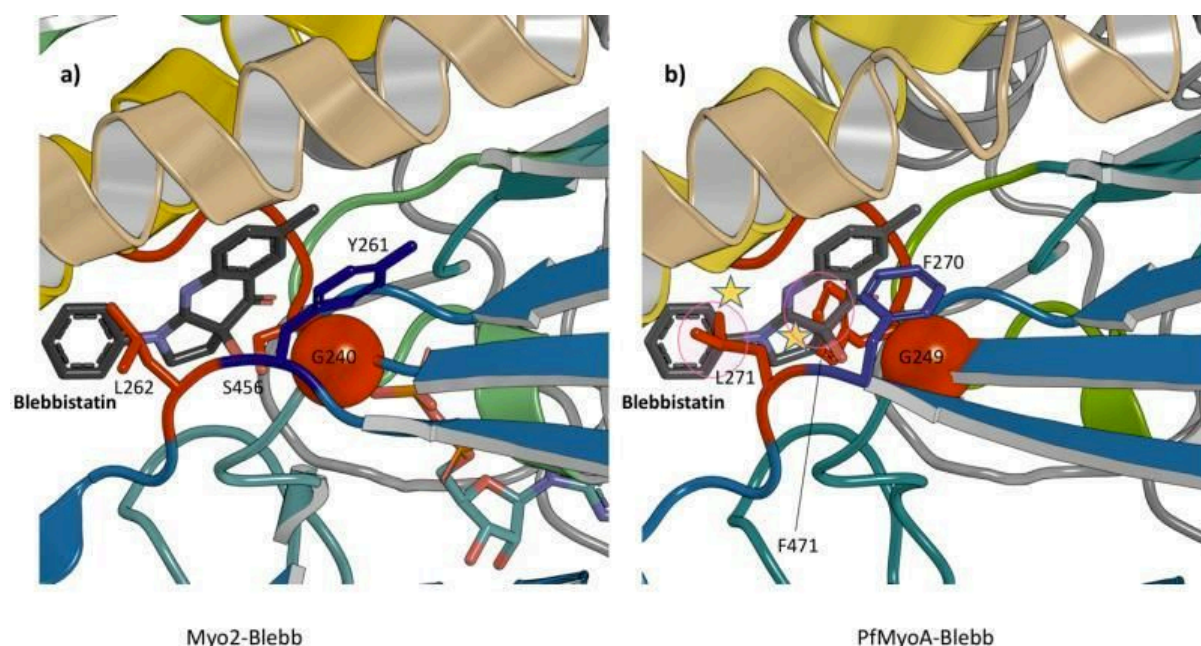


### FIGURE 27-The *Blebbistatin* pocket in *PfMyoA*

(a) The binding of Blebbistatin in Myo2 with crucial residues of its binding labeled. (b) Blebbistatin in the equivalent binding pocket of PfMyoA, most of the essential residues for the binding of Blebbistatin are conserved in PfMyoA pocket, except the serine S456 which is replaced by F471 and is predicted to cause steric hindrance with the Blebbistatin, explaining why Blebbistatin cannot target PfMyoA.

#### 10.1.2 CK-571 – a myosin inhibitor

CK-571 is another inhibitor that targets specifically the smooth muscle myosin (SMM) with an IC<sub>50</sub> of 9 nM. It targets also other class II myosin such as cardiac, skeletal myosin and NM2b but with a high IC<sub>50</sub> compared to SMM (Sirigu et al., 2016). CK-271 has been proposed as a treatment against asthma. The effect of this small molecule has been characterized by a California-based pharmaceutical company, *Cytokinetics Inc*, engaged in the discovery and development of small therapeutic molecules targeting muscle proteins, especially myosins. This inhibitor prevents motor domain binding of Actin SMM and promotes relaxation of smooth muscle *in vitro* and *in vivo* (Sirigu et al., 2016). Unlike the Blebbistatin, CK-571 prevents hydrolysis of MgATP, blocking the conformational changes required for the interaction of the motor domain with actin (Sirigu et al., 2016). It targets a novel pocket that opens during the ‘recovery stroke’ (Sirigu et al., 2016). So, CK-571 blocks Myosin II in an intermediate state of the recovery stroke (Sirigu et al., 2016). These results show that two inhibitors, such as Blebbistatin and CK-571, target different allosteric pockets and inhibit myosin with different mechanisms.

#### 10.1.3 Halogenated pseudilins – myosin inhibitors

Pentachloropseudilin (PCIP), pentabromopseudilin (PBP) and Tribromodichloropseudilin (TBDCIP) are three small molecules sharing a similar molecular structure. They inhibit myosin I (IC<sub>50</sub> = 1.0 μM), myosin Va (IC<sub>50</sub> = 1.2 μM) and myosin II (IC<sub>50</sub> = 47.2 μM), respectively (Fedorov et al., 2009; Chinthalapudi et al., 2011; Preller et al., 2011; Manstein and Preller, 2020).

These small molecules target myosins in yet another novel allosteric binding pocket, which is located below the subdomain U50 and close to the actin interaction region. The binding of these small molecules in the pocket reduces the ATPase activity of myosins by inhibiting the

rate of hydrolysis of ATP and affect a global protein dynamics (Fedorov et al., 2009; Chinthalapudi et al., 2011; Manstein and Preller. 2020).

#### **10.1.4 Mavacamten – a myosin inhibitor**

Mavacamten is a specific inhibitor of  $\beta$ -cardiac myosin. Mavacamten decreases the contractility of the heart and suppresses cardiomyocyte disarray specific of cardiomyopathies in mice (Green et al., 2015). On a kinetic point of view, Mavacamten decreases the Pi release rate and is able to increase the proportion of cardiac myosin heads in the inactive auto-inhibited state (Kawas et al., 2017; Anderson et al., 2018).

Mavacamten is currently in clinical trials phase 3 against obstructive hypertrophic cardiomyopathies (<https://clinicaltrials.gov/ct2/show/NCT03470545>). The structure of cardiac myosin complexed to Mavacamten is not yet available but will be mandatory to describe its mode of action.

#### **10.1.5 Omecamtive mecarbil (OM) – a myosin activator**

OM is an activator specifically targeting  $\beta$ -cardiac myosin. OM is currently in phase 3 clinical trials against heart failure (<https://cytokinetix.com/omecamtiv-mecarbil/>) and has been suggested as a treatment against dilated cardiomyopathy (DCM) (Utter et al., 2015). The oral administration of OM increases cardiac contractility with no side effects on calcium concentration or oxygen consumption of the cardiomyocytes (Shen et al., 2010; Malik et al., 2011).

The effects of OM on the kinetics and mechanical properties of  $\beta$ -cardiac myosin have been extensively studied. OM increases both the rate of the Pi release, but also the time spent by the motor on actin (Malik et al., 2011; Cleland et al., 2011; Swenson et al., 2017).

The crystal structure of the S1 fragment of  $\beta$ -cardiac myosin complexed to OM allowed to decipher the molecular mechanism of the activator (Planelles-Herrero et al., 2017). OM binds to a pocket located at the interface of the Converter, the relay helix and the N-terminal domain (Planelles-Herrero et al., 2017) and thus stabilizes the PPS conformation. This explains the mode of action of OM that increases the proportion of myosin heads in PPS, that are available to produce a powerstroke in systole thus increasing the force output of the sarcomere (Planelles-Herrero et al., 2017).

### 10.1.6 Specificity and efficiency of inhibitors against PfMyoA

Several small-molecules specifically modulating the activity of myosins are currently in clinical trials. The fact that such molecules are able to modulate specifically the activity of myosins when they are administrated orally is a proof of concept that these molecules could be used as efficient treatments. The maximum tolerated doses and the efficiency of OM as an oral treatment have been intensively studied ([Kaplinsky & Mallarkey, 2018](#)).

Interestingly, the structure revealed why OM targets specifically  $\beta$ -cardiac myosin ([Planelles-Herrero et al., 2017](#)), which could be surprising since myosin from class II are all very close in sequence ( $\beta$ -cardiac myosin and skeletal myosin with 80% identity and 88% similarity). We are thus confident that small-molecules can be found that target specifically PfMyoA which belongs to a class specific to the Apicomplexan, absent in humans. In fact, PfMyoA is highly divergent from human myosins (~30% identity with myosin from class II).

For all these reasons and because this approach is currently studied in the lab for other myosins, the development of small molecules to inhibit specifically PfMyoA activity is the most promising at the moment (**Figure 28a**).

## 10.2 Inhibiting the association of the light chains

As it was revealed in our work, PfMyoA binds two specific light chains: PfELC and MTIP ([Moussaoui et al., 2020](#)). PfELC was shown to be essential for the invasion mechanism of the parasite in Jake Baum's laboratory, our collaborator ([Moussaoui et al., 2020](#)), and MTIP is essential for connecting PfMyoA to the glideosome ([Frénal et al., 2010](#)). Blocking the association of the light chains with PfMyoA is thus a promising approach to develop antimalarial approaches. However, depending on which light chain is targeted, the aim is slightly different (i) in the case the adaptor protein MTIP is targeted, the assembly of a functional glideosome is altered, (ii) in the case PfELC is targeted, PfMyoA will not be sufficiently functional to support efficient invasion.

The interaction between PfMyoA and MTIP is essential for the invasion of erythrocytes ([Bosch et al., 2006](#)). Another argument for MTIP to be a viable therapeutic target is its divergence from any human homologs (**Figure 28c**) ([Bosch et al., 2006](#); [Burns et al., 2019](#)). A strategy has already been described to identify small molecule inhibitors preventing the

MTIP/MyoA association in a library of 300 000 compounds (Kortagere. 2010; Burns et al., 2019). An interesting compound was identified C416 with an IC<sub>50</sub> of 0.145  $\mu$ M. Structure-based screening identified several derivatives of C416 (C2-1 and C3-21) with IC<sub>50</sub> of 0,047  $\mu$ M and 0,385  $\mu$ M, respectively. Whereas, C3-21 was found to inhibit gliding motility of mosquito stage sporozoites (Kortagere 2010; Burns et al., 2019).

In our published work (Moussaoui et al., 2020), we showed also the crucial role of PfELC in the invasive stage of the parasite. The inhibition of the expression of PfELC leads to the drastic drop of the erythrocytes invasion by the merozoites. For all these reasons, we believe that PfELC is an interesting therapeutic target against malaria (Figure 28b).

### 10.3 Inhibiting the association of PfMyoA to the actin

The divergent acto-myosin system is responsible of the gliding motility and the invasion of the erythrocytes (Soldati et al., 2004). The acto-myosin actively pulls on the actin filament bound to the adhesins establishing tight junctions with the receptors of the host erythrocyte. This results in wrapping of the merozoite in the membrane of the erythrocyte and invasion (Soldati et al., 2004; Tardieux & Baum 2016).

The importance of actin in the invasion of erythrocytes has been demonstrated, using the cytochalasins which disrupts the polymerization of the actin and blocks totally the invasion of the erythrocytes (Miller et al., 1979; Cooper 1987; Johnson et al., 2015). To further study and investigate how we can block myosin association to actin by targeting the interface, structural studies are requested. So far, this strategy has not been investigated for myosin motors. The availability of the CryoEM structure of the PfActo-myosin complex, solved recently in the team by CryoEM at high resolution, (Robert-Paganin et al., submitted to PNAS), could provide a basis for drug design for such a strategy, allowing identification of specific inhibitors preventing the association of this divergent and specific acto-myosin complex.

So, three approaches could be adopted in our laboratory to design a new generation of anti-malarial drugs, targeting distinct elements of the glideosome core (Figure 28d).



## A hope for the birth of novel anti-malarial treatments

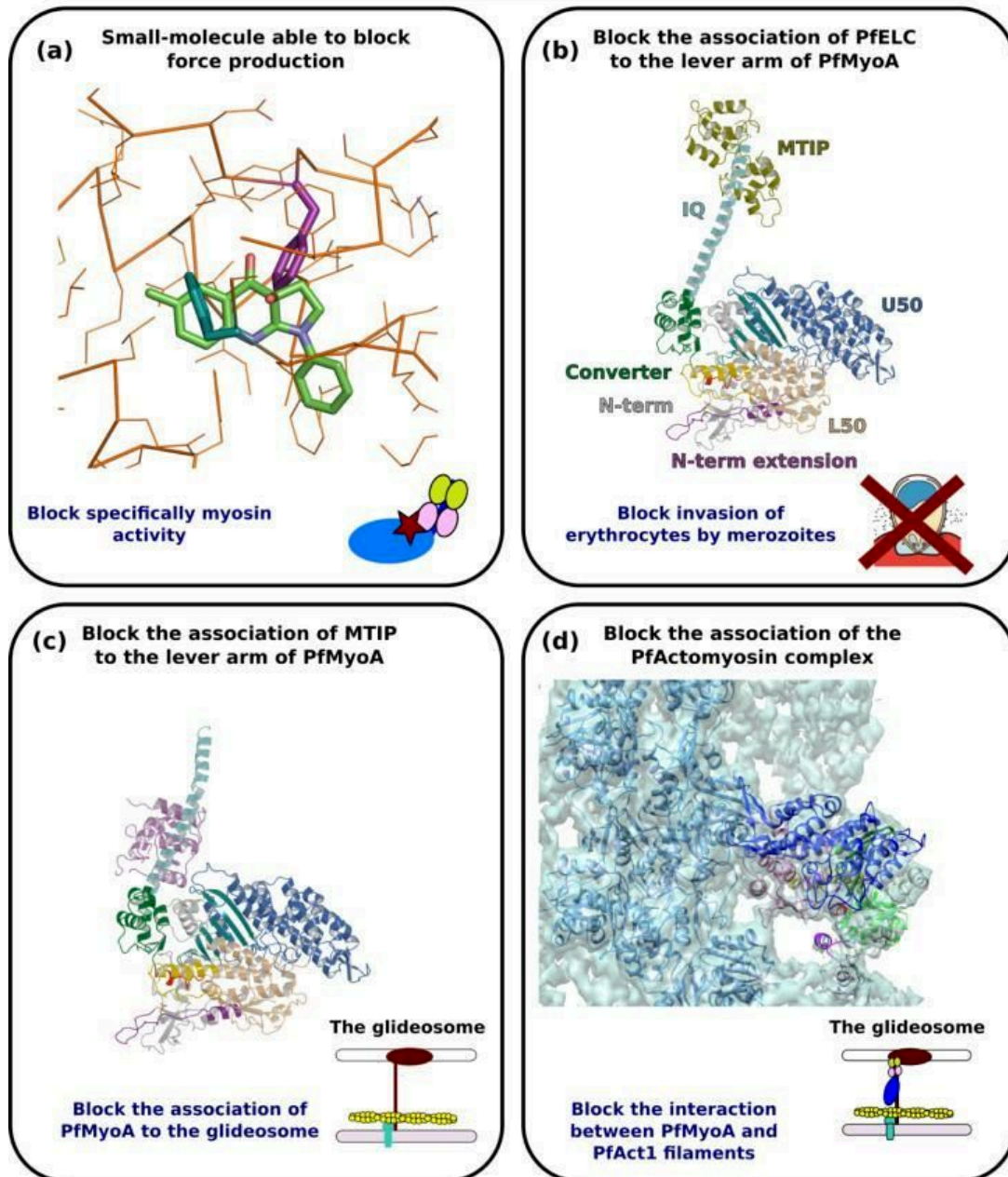


FIGURE 28-Strategies to block the parasite infectivity.

(a) Identify small molecules that are able to block PfMyoA force production. (b)(c) By blocking the association of the light chains MTIP or ELC to the lever arm of PfMyoA. (d) Disrupting the association of the PfActo-myosin.

## Conclusions

The work presented in this thesis allowed a complete description of PfMyoA properties and unique mechanism of force production. Thanks to the solved atomic structures of PfMyoA motor domain we were able to explain the crucial role of the phosphorylated N-terminal extension, which in fact compensates the immobility of the connector SH1 helix. We also showed in this work that a phosphorylated serine in the N-terminal extension not only plays a role in the force production mechanism of Myosin A but tunes directly its properties. For a motor that stays longer on the actin filament, thus produces more force at the expense of the speed or a motor that moves at high speed on the actin filament with lower produced force. The two collaborations with the teams of Pr. K. Trybus and Pr. J. Baum permitted to perform complementary and interdisciplinary studies and thus to investigate the atypical and tunable mechanism of PfMyoA at different scales, from the atomic level to the organism. We finally proposed a model that explains the role of Myosin A both in the invasion and in the motility of the parasite. On a more fundamental point of view, this work brings a new understanding on the function of the N-terminal region of myosins since it provides another example of N-terminus extension allowing to directly tune the function of a specific myosin. Such a function for N-terminal extension was already described in myosin-1b ([Greenberg et al., 2015](#); [Mentes et al., 2018](#)) All these results allowed us to write and publish a paper in Nature Communications journal ([Robert-Paganin et al., 2019](#)).

In our publication [Moussaoui et al., 2020](#), we complete the study with the description of the lever arm of PfMyoA associated with its light chains. We solved the atomic structure of PfMyoA Full Length with its light chains PfELC and MTIP in PR and PPS states at 2.5 Å and 3.9 Å, respectively. This is a first structure of a myosin Full Length. We explained how these lights chains anchor the lever arm and why MTIP is so important for the binding and the stabilization of the ELC. The atomic structures of PfMyoA FL in PPS and PR allowed us to study the orientation of the lever arm in each state and to compare it with the orientation of the lever arm of conventional myosins. By studying the structure, we realized that some features of this myosin could explain its high velocity and its atypical mechanism of force production. Our study revealed the important role of the ELC for parasite invasion, but also specific interactions between the lever arm and the motor domain stabilize the priming in PPS. This work was published in *eLife* journal ([Moussaoui et al., 2020](#)).

Our results provided an entire study of PfMyoA, a myosin of unknown structure at the beginning of my PhD, for which the mechanism was mysterious. The structures allowed us to reveal the unique features of PfMyoA and to compare it with other myosins from class XIV such as myosin B for example. The example of PfMyoA is unique and provides an unforeseen example of divergent myosin able to tune its motor properties in order to satisfy the physiological needs of the parasite. Moreover, the tools developed by us and our collaborators will be useful to investigate the role of the other myosins from *P. falciparum*. On a therapeutic point of view, the structures described in this work will be mandatory for the rational design of specific inhibitors and open the road to novel anti-malarial treatments.

## Perspectives

### I. Other *P.falciparum* myosins

The comparison of the sequences of PfMyoA and PfMyoB revealed that myosin B seem to also have a divergent force production mechanism with some differences compared to myosin A. During my thesis, I worked on the study of myosin B which is important for the invasion of erythrocytes but not essential ([Blake et al., 2020](#)). However, the function of PfMyoB has not yet been defined in detail. Future investigations will provide further information.

In the last months of my PhD, I started to work on PfMyoB in order to solve its structure at atomic resolution. I received cells (Sf9) with expressed PfMyoB, I succeeded in optimizing the constructs and the purification protocol of this myosin which was initially poorly soluble, then I characterized PfMyoB by DLS to be sure that it is not aggregated. Following these encouraging results, I started to crystallize PfMyoB and I obtained promising hits. Unfortunately, I could not continue because of lack of time and limitation of the of protein amount.

Currently, our collaborators are working on the expression of PfMyoB in order to continue these experiments.

### II. PfMyoA effectors

Regarding the drugs that target PfMyoA, we are still in the first phase of our study, we are looking for the best way to obtain them quickly. We aim to apply the strategies already used

in our laboratory to identify small molecules capable of binding myosin and affecting its mechanics. Some collaborations are planned in order to screen libraries and get some hits. Once small molecules are identified, we will directly test the effects of the compounds of interest on the ATPase activity of PfMyoA.

The most promising compounds will be co-crystallized with PfMyoA in our laboratory. For that purpose, the structures solved in my PhD and the crystallization conditions will be essential. Since many compounds target the PPS state, the crystallization assays will start with the PPS conditions described in this work. Together with transient kinetic experiments, the structural information of how and where these small molecules target PfMyoA will allow us to describe the mechanism of action of the drug. The next step will be to collaborate with chemists to improve the specificity of these modulators. Finally, thanks to our collaboration with Pr. Jake Baum, it will be possible to directly test the effect of the compounds on the parasite.

## References

- Al, B., Mg, D., Jm, B., Tf, de K.-W., Pr, G., Jg, B., Mj, B., & Dw, W. (2019, January 5). Targeting malaria parasite invasion of red blood cells as an antimalarial strategy. *FEMS Microbiology Reviews*; *FEMS Microbiol Rev.* <https://doi.org/10.1093/femsre/fuz005>
- Alano, P. (2007). *Plasmodium falciparum* gametocytes: Still many secrets of a hidden life. *Molecular Microbiology*, 66(2), 291–302. <https://doi.org/10.1111/j.1365-2958.2007.05904.x>
- Allingham, J. S., Smith, R., & Rayment, I. (2005). The structural basis of blebbistatin inhibition and specificity for myosin II. *Nature Structural & Molecular Biology*, 12(4), 378–379. <https://doi.org/10.1038/nsmb908>
- Alzahofi, N., Welz, T., Robinson, C. L., Page, E. L., Briggs, D. A., Stainthorp, A. K., Reekes, J., Elbe, D. A., Straub, F., Kallemijn, W. W., Tate, E. W., Goff, P. S., Sviderskaya, E. V., Cantero, M., Montoliu, L., Nedelec, F., Miles, A. K., Bailly, M., Kerkhoff, E., & Hume, A. N. (2020). Rab27a co-ordinates actin-dependent transport by controlling organelle-associated motors and track assembly proteins. *Nature Communications*, 11(1), 3495. <https://doi.org/10.1038/s41467-020-17212-6>
- Amaratunga, C., Witkowski, B., Khim, N., Menard, D., & Fairhurst, R. M. (2014). Artemisinin resistance in *Plasmodium falciparum*. *The Lancet. Infectious Diseases*, 14(6), 449–450. [https://doi.org/10.1016/S1473-3099\(14\)70777-7](https://doi.org/10.1016/S1473-3099(14)70777-7)
- Andenmatten, N., Egarter, S., Jackson, A. J., Jullien, N., Herman, J.-P., & Meissner, M. (2013). Conditional genome engineering in *Toxoplasma gondii* uncovers alternative invasion mechanisms. *Nature Methods*, 10(2), 125–127. <https://doi.org/10.1038/nmeth.2301>
- Anderson, R. L., Trivedi, D. V., Sarkar, S. S., Henze, M., Ma, W., Gong, H., Rogers, C. S., Gorham, J. M., Wong, F. L., Morck, M. M., Seidman, J. G., Ruppel, K. M., Irving, T. C., Cooke, R., Green, E. M., & Spudich, J. A. (2018). Deciphering the super relaxed state of human  $\beta$ -cardiac myosin and the mode of action of mavacamten from myosin molecules to muscle fibers. *Proceedings of the National Academy of Sciences of the United States of America*, 115(35), E8143–E8152. <https://doi.org/10.1073/pnas.1809540115>
- Anitei, M., & Hoflack, B. (2011). Bridging membrane and cytoskeleton dynamics in the secretory and endocytic pathways. *Nature Cell Biology*, 14(1), 11–19. <https://doi.org/10.1038/ncb2409>
- Ashley, E. A., Pyae Phy, A., & Woodrow, C. J. (2018). Malaria. *Lancet* (London, England), 391(10130), 1608–1621. [https://doi.org/10.1016/S0140-6736\(18\)30324-6](https://doi.org/10.1016/S0140-6736(18)30324-6)
- Baum, J., Papenfuss, A. T., Baum, B., Speed, T. P., & Cowman, A. F. (2006). Regulation of apicomplexan actin-based motility. *Nature Reviews. Microbiology*, 4(8), 621–628. <https://doi.org/10.1038/nrmicro1465>
- Behrmann, E., Müller, M., Penczek, P. A., Mannherz, H. G., Manstein, D. J., & Raunser, S. (2012). Structure of the rigor actin-tropomyosin-myosin complex. *Cell*, 150(2), 327–338. <https://doi.org/10.1016/j.cell.2012.05.037>
- Berg, J. S., Powell, B. C., & Cheney, R. E. (2001). A millennial myosin census. *Molecular Biology of the Cell*, 12(4), 780–794. <https://doi.org/10.1091/mbc.12.4.780>



- Berg, Jonathan S., & Cheney, R. E. (2002). Myosin-X is an unconventional myosin that undergoes intrafilopodial motility. *Nature Cell Biology*, 4(3), 246–250. <https://doi.org/10.1038/ncb762>
- Bergman, L. W., Kaiser, K., Fujioka, H., Coppens, I., Daly, T. M., Fox, S., Matuschewski, K., Nussenzweig, V., & Kappe, S. H. I. (2003). Myosin A tail domain interacting protein (MTIP) localizes to the inner membrane complex of *Plasmodium* sporozoites. *Journal of Cell Science*, 116(Pt 1), 39–49. <https://doi.org/10.1242/jcs.00194>
- Blake, T. C. A., Haase, S., & Baum, J. (2020). Actomyosin forces and the energetics of red blood cell invasion by the malaria parasite *Plasmodium falciparum*. *BioRxiv*, 2020.06.25.171900. <https://doi.org/10.1101/2020.06.25.171900>
- Bookwalter, C. S., Tay, C. L., McCrorie, R., Previs, M. J., Lu, H., Kremmentsova, E. B., Fagnant, P. M., Baum, J., & Trybus, K. M. (2017). Reconstitution of the core of the malaria parasite glideosome with recombinant *Plasmodium* class XIV myosin A and *Plasmodium* actin. *The Journal of Biological Chemistry*, 292(47), 19290–19303. <https://doi.org/10.1074/jbc.M117.813972>
- Bosch, J., Turley, S., Roach, C. M., Daly, T. M., Bergman, L. W., & Hol, W. G. J. (2007). The closed MTIP-myosin A-tail complex from the malaria parasite invasion machinery. *Journal of Molecular Biology*, 372(1), 77–88. <https://doi.org/10.1016/j.jmb.2007.06.016>
- Burns, A. L., Dans, M. G., Balbin, J. M., de Koning-Ward, T. F., Gilson, P. R., Beeson, J. G., Boyle, M. J., & Wilson, D. W. (2019). Targeting malaria parasite invasion of red blood cells as an antimalarial strategy. *FEMS Microbiology Reviews*, 43(3), 223–238. <https://doi.org/10.1093/femsre/fuz005>
- Buss, F., & Kendrick-Jones, J. (2008). How are the cellular functions of myosin VI regulated within the cell? *Biochemical and Biophysical Research Communications*, 369(1), 165–175. <https://doi.org/10.1016/j.bbrc.2007.11.150>
- Callebaut, I., Labesse, G., Durand, P., Poupon, A., Canard, L., Chomilier, J., Henrissat, B., & Mornon, J. P. (1997). Deciphering protein sequence information through hydrophobic cluster analysis (HCA): Current status and perspectives. *Cellular and Molecular Life Sciences: CMLS*, 53(8), 621–645. <https://doi.org/10.1007/s000180050082>
- Chinthalapudi, K., Taft, M. H., Martin, R., Heissler, S. M., Preller, M., Hartmann, F. K., Brandstaetter, H., Kendrick-Jones, J., Tsiavalariis, G., Gutzeit, H. O., Fedorov, R., Buss, F., Knölker, H.-J., Coluccio, L. M., & Manstein, D. J. (2011). Mechanism and specificity of pentachloropseudilin-mediated inhibition of myosin motor activity. *The Journal of Biological Chemistry*, 286(34), 29700–29708. <https://doi.org/10.1074/jbc.M111.239210>
- Chittenden, T. W., Pak, J., Rubio, R., Cheng, H., Holton, K., Prendergast, N., Glinskii, V., Cai, Y., Culhane, A., Bentink, S., Schwede, M., Mar, J. C., Howe, E. A., Aryee, M., Sultana, R., Lanahan, A. A., Taylor, J. M., Holmes, C., Hahn, W. C., ... Quackenbush, J. (2010). Therapeutic implications of GIPCI silencing in cancer. *PloS One*, 5(12), e15581. <https://doi.org/10.1371/journal.pone.0015581>
- Cleland, J. G. F., Teerlink, J. R., Senior, R., Nifontov, E. M., Mc Murray, J. J. V., Lang, C. C., Tsyrlin, V. A., Greenberg, B. H., Mayet, J., Francis, D. P., Shaburishvili, T., Monaghan, M., Saltzberg, M., Neyses, L., Wasserman, S. M., Lee, J. H., Saikali, K. G., Clarke, C. P., Goldman, J. H., ... Malik, F. I. (2011). The effects of the cardiac myosin activator, omecamtiv mecarbil, on cardiac function in systolic heart failure: A double-blind, placebo-controlled, crossover, dose-ranging phase 2 trial. *Lancet (London, England)*, 378(9792), 676–683. [https://doi.org/10.1016/S0140-6736\(11\)61126-4](https://doi.org/10.1016/S0140-6736(11)61126-4)

- Coluccio, L. (Ed.). (2020). *Myosins: A Superfamily of Molecular Motors* (2nd ed.). Springer International Publishing. <https://doi.org/10.1007/978-3-030-38062-5>
- Cooper, J. A. (1987). Effects of cytochalasin and phalloidin on actin. *The Journal of Cell Biology*, 105(4), 1473–1478. <https://doi.org/10.1083/jcb.105.4.1473>
- Coureux, P.-D., Wells, A. L., Ménétrey, J., Yengo, C. M., Morris, C. A., Sweeney, H. L., & Houdusse, A. (2003). A structural state of the myosin V motor without bound nucleotide. *Nature*, 425(6956), 419–423. <https://doi.org/10.1038/nature01927>
- Crick, A. J., Theron, M., Tiffert, T., Lew, V. L., Cicuta, P., & Rayner, J. C. (2014). Quantitation of malaria parasite-erythrocyte cell-cell interactions using optical tweezers. *Biophysical Journal*, 107(4), 846–853. <https://doi.org/10.1016/j.bpj.2014.07.010>
- Das, S., Saha, B., Hati, A. K., & Roy, S. (2018). Evidence of Artemisinin-Resistant *Plasmodium falciparum* Malaria in Eastern India. *The New England Journal of Medicine*, 379(20), 1962–1964. <https://doi.org/10.1056/NEJMc1713777>
- Dasgupta, S., Auth, T., Gov, N. S., Satchwell, T. J., Hanssen, E., Zuccala, E. S., Riglar, D. T., Toye, A. M., Betz, T., Baum, J., & Gompper, G. (2014). Membrane-wrapping contributions to malaria parasite invasion of the human erythrocyte. *Biophysical Journal*, 107(1), 43–54. <https://doi.org/10.1016/j.bpj.2014.05.024>
- Dhingra, S. K., Small-Saunders, J. L., Ménard, D., & Fidock, D. A. (2019). *Plasmodium falciparum* resistance to piperazine driven by PfCRT. *The Lancet. Infectious Diseases*, 19(11), 1168–1169. [https://doi.org/10.1016/S1473-3099\(19\)30543-2](https://doi.org/10.1016/S1473-3099(19)30543-2)
- Douse, C. H., Green, J. L., Salgado, P. S., Simpson, P. J., Thomas, J. C., Langsley, G., Holder, A. A., Tate, E. W., & Cota, E. (2012). Regulation of the *Plasmodium* motor complex: Phosphorylation of myosin A tail-interacting protein (MTIP) loosens its grip on MyoA. *The Journal of Biological Chemistry*, 287(44), 36968–36977. <https://doi.org/10.1074/jbc.M112.379842>
- Dubey, J. P. (2009). History of the discovery of the life cycle of *Toxoplasma gondii*. *International Journal for Parasitology*, 39(8), 877–882. <https://doi.org/10.1016/j.ijpara.2009.01.005>
- Dunn, T. A., Chen, S., Faith, D. A., Hicks, J. L., Platz, E. A., Chen, Y., Ewing, C. M., Sauvageot, J., Isaacs, W. B., De Marzo, A. M., & Luo, J. (2006). A novel role of myosin VI in human prostate cancer. *The American Journal of Pathology*, 169(5), 1843–1854. <https://doi.org/10.2353/ajpath.2006.060316>
- Ecken, J. von der, Heissler, S. M., Pathan-Chhatbar, S., Manstein, D. J., & Raunser, S. (2016). Cryo-EM structure of a human cytoplasmic actomyosin complex at near-atomic resolution. *Nature*, 534(7609), 724–728. <https://doi.org/10.1038/nature18295>
- Egarter, S., Andenmatten, N., Jackson, A. J., Whitelaw, J. A., Pall, G., Black, J. A., Ferguson, D. J. P., Tardieux, I., Mogilner, A., & Meissner, M. (2014). The toxoplasma Acto-MyoA motor complex is important but not essential for gliding motility and host cell invasion. *PloS One*, 9(3), e91819. <https://doi.org/10.1371/journal.pone.0091819>
- Engelhardt, W. A., & Liubimova, M. N. (1994). [Myosin and adenosine triphosphatase (*Nature*, 144, 688, Oct. 14, 1939)]. *Molekuliarnaia Biologiya*, 28(6), 1229–1230.
- Fedorov, R., Böhl, M., Tsiavaliaris, G., Hartmann, F. K., Taft, M. H., Baruch, P., Brenner, B., Martin, R., Knölker, H.-J., Gutzeit, H. O., & Manstein, D. J. (2009). The mechanism of

- pentabromopseudilin inhibition of myosin motor activity. *Nature Structural & Molecular Biology*, 16(1), 80–88. <https://doi.org/10.1038/nsmb.1542>
- Fejzo, M. S., Ginther, C., Dering, J., Anderson, L., Venkatesan, N., Konecny, G., Karlan, B., & Slamon, D. J. (2011). Knockdown of ovarian cancer amplification target *ADRM1* leads to downregulation of *GIPC1* and upregulation of *RECK*. *Genes, Chromosomes & Cancer*, 50(6), 434–441. <https://doi.org/10.1002/gcc.20868>
- Foth, B. J., Goedecke, M. C., & Soldati, D. (2006). New insights into myosin evolution and classification. *Proceedings of the National Academy of Sciences of the United States of America*, 103(10), 3681–3686. <https://doi.org/10.1073/pnas.0506307103>
- Fréchal, K., Dubremetz, J.-F., Lebrun, M., & Soldati-Favre, D. (2017). Gliding motility powers invasion and egress in Apicomplexa. *Nature Reviews. Microbiology*, 15(11), 645–660. <https://doi.org/10.1038/nrmicro.2017.86>
- Fréchal, K., Polonais, V., Marq, J.-B., Stratmann, R., Limenitakis, J., & Soldati-Favre, D. (2010). Functional dissection of the apicomplexan glideosome molecular architecture. *Cell Host & Microbe*, 8(4), 343–357. <https://doi.org/10.1016/j.chom.2010.09.002>
- Fréchal, K., & Soldati-Favre, D. (2013). [The glideosome, a unique machinery that assists the Apicomplexa in gliding into host cells]. *Medicine Sciences: M/S*, 29(5), 515–522. <https://doi.org/10.1051/medsci/2013295015>
- Gaji, R. Y., Johnson, D. E., Treeck, M., Wang, M., Hudmon, A., & Arrizabalaga, G. (2015). Phosphorylation of a Myosin Motor by TgCDPK3 Facilitates Rapid Initiation of Motility during *Toxoplasma gondii* egress. *PLoS Pathogens*, 11(11), e1005268. <https://doi.org/10.1371/journal.ppat.1005268>
- Gaskins, E., Gilk, S., DeVore, N., Mann, T., Ward, G., & Beckers, C. (2004). Identification of the membrane receptor of a class XIV myosin in *Toxoplasma gondii*. *The Journal of Cell Biology*, 165(3), 383–393. <https://doi.org/10.1083/jcb.200311137>
- Gilk, S. D., Gaskins, E., Ward, G. E., & Beckers, C. J. M. (2009). GAP45 Phosphorylation Controls Assembly of the *Toxoplasma* Myosin XIV Complex. *Eukaryotic Cell*, 8(2), 190–196. <https://doi.org/10.1128/EC.00201-08>
- Gordon, A. M., Homsher, E., & Regnier, M. (2000). Regulation of contraction in striated muscle. *Physiological Reviews*, 80(2), 853–924. <https://doi.org/10.1152/physrev.2000.80.2.853>
- Green, E. M., Wakimoto, H., Anderson, R. L., Evanchik, M. J., Gorham, J. M., Harrison, B. C., Henze, M., Kawas, R., Oslob, J. D., Rodriguez, H. M., Song, Y., Wan, W., Leinwand, L. A., Spudich, J. A., McDowell, R. S., Seidman, J. G., & Seidman, C. E. (2016). A small-molecule inhibitor of sarcomere contractility suppresses hypertrophic cardiomyopathy in mice. *Science (New York, N.Y.)*, 351(6273), 617–621. <https://doi.org/10.1126/science.aad3456>
- Green, J. L., Rees-Channer, R. R., Howell, S. A., Martin, S. R., Knuepfer, E., Taylor, H. M., Grainger, M., & Holder, A. A. (2008). The motor complex of *Plasmodium falciparum*: Phosphorylation by a calcium-dependent protein kinase. *The Journal of Biological Chemistry*, 283(45), 30980–30989. <https://doi.org/10.1074/jbc.M803129200>
- Greenberg, M. J., Lin, T., Shuman, H., & Ostap, E. M. (2015). Mechanochemical tuning of myosin-I by the N-terminal region. *Proceedings of the National Academy of Sciences of the United States of America*, 112(26), E3337–3344. <https://doi.org/10.1073/pnas.1506633112>

- Gross, S. P., Tuma, M. C., Deacon, S. W., Serpinskaya, A. S., Reilein, A. R., & Gelfand, V. I. (2002). Interactions and regulation of molecular motors in *Xenopus melanophores*. *The Journal of Cell Biology*, 156(5), 855–865. <https://doi.org/10.1083/jcb.200105055>
- Gurel, P. S., Kim, L. Y., Ruijgrok, P. V., Omabegho, T., Bryant, Z., & Alushin, G. M. (n.d.). Cryo-EM structures reveal specialization at the myosin VI-actin interface and a mechanism of force sensitivity. *ELife*, 6. <https://doi.org/10.7554/eLife.31125>
- Hanley, P. J., Xu, Y., Kronlage, M., Grobe, K., Schön, P., Song, J., Sorokin, L., Schwab, A., & Bähler, M. (2010). Motorized RhoGAP myosin IXb (*Myo9b*) controls cell shape and motility. *Proceedings of the National Academy of Sciences of the United States of America*, 107(27), 12145–12150. <https://doi.org/10.1073/pnas.0911986107>
- Hartman, M. A., Finan, D., Sivaramakrishnan, S., & Spudich, J. A. (2011). Principles of Unconventional Myosin Function and Targeting. *Annual Review of Cell and Developmental Biology*, 27(1), 133–155. <https://doi.org/10.1146/annurev-cellbio-100809-151502>
- Hartman, M. A., & Spudich, J. A. (2012). The myosin superfamily at a glance. *Journal of Cell Science*, 125(Pt 7), 1627–1632. <https://doi.org/10.1242/jcs.094300>
- Heissler, S. M., & Sellers, J. R. (2016). Various Themes of Myosin Regulation. *Journal of Molecular Biology*, 428(9 Pt B), 1927–1946. <https://doi.org/10.1016/j.jmb.2016.01.022>
- Heitner, S. B., Jacoby, D., Lester, S. J., Owens, A., Wang, A., Zhang, D., Lambing, J., Lee, J., Semigran, M., & Sehnert, A. J. (2019). Mavacamten Treatment for Obstructive Hypertrophic Cardiomyopathy: A Clinical Trial. *Annals of Internal Medicine*, 170(11), 741–748. <https://doi.org/10.7326/M18-3016>
- Herm-Götz, A., Weiss, S., Stratmann, R., Fujita-Becker, S., Ruff, C., Meyhöfer, E., Soldati, T., Manstein, D. J., Geeves, M. A., & Soldati, D. (2002b). *Toxoplasma gondii* myosin A and its light chain: A fast, single-headed, plus-end-directed motor. *The EMBO Journal*, 21(9), 2149–2158. <https://doi.org/10.1093/emboj/21.9.2149>
- Hernández, P. C., Morales, L., Castellanos, I. C., Wasserman, M., & Chaparro-Olaya, J. (2017). Myosin B of *Plasmodium falciparum* (PfMyoB): In silico prediction of its three-dimensional structure and its possible interaction with MTIP. *Parasitology Research*, 116(4), 1373–1382. <https://doi.org/10.1007/s00436-017-5417-y>
- Hernández, P. C., Wasserman, M., & Chaparro-Olaya, J. (2018). In vitro interaction between *Plasmodium falciparum* myosin B (PfMyoB) and myosin A tail interacting protein (MTIP). *Parasitology Research*, 117(11), 3437–3446. <https://doi.org/10.1007/s00436-018-6039-8>
- Houdusse, A., Szent-Györgyi, A. G., & Cohen, C. (2000). Three conformational states of scallop myosin S1. *Proceedings of the National Academy of Sciences*, 97(21), 11238–11243. <https://doi.org/10.1073/pnas.200376897>
- Houdusse, Anne, Gaucher, J.-F., Krementsova, E., Mui, S., Trybus, K. M., & Cohen, C. (2006). Crystal structure of apo-calmodulin bound to the first two IQ motifs of myosin V reveals essential recognition features. *Proceedings of the National Academy of Sciences*, 103(51), 19326–19331. <https://doi.org/10.1073/pnas.0609436103>
- Houdusse, Anne, Kalabokis, V. N., Himmel, D., Szent-Györgyi, A. G., & Cohen, C. (1999). Atomic Structure of Scallop Myosin Subfragment S1 Complexed with MgADP: A Novel Conformation of the Myosin Head. *Cell*, 97(4), 459–470. [https://doi.org/10.1016/S0092-8674\(00\)80756-4](https://doi.org/10.1016/S0092-8674(00)80756-4)

- Houdusse, Anne, & Sweeney, H. L. (2016). How Myosin Generates Force on Actin Filaments. *Trends in Biochemical Sciences*, 41(12), 989–997. <https://doi.org/10.1016/j.tibs.2016.09.006>
- Huang, Z., & Tatem, A. J. (2013). Global malaria connectivity through air travel. *Malaria Journal*, 12, 269. <https://doi.org/10.1186/1475-2875-12-269>
- Jacot, D., Fréchal, K., Marq, J.-B., Sharma, P., & Soldati-Favre, D. (2014). Assessment of phosphorylation in *Toxoplasma* glideosome assembly and function. *Cellular Microbiology*, 16(10), 1518–1532. <https://doi.org/10.1111/cmi.12307>
- Johnson, H. E., King, S. J., Asokan, S. B., Rotty, J. D., Bear, J. E., & Haugh, J. M. (2015). F-actin bundles direct the initiation and orientation of lamellipodia through adhesion-based signaling. *The Journal of Cell Biology*, 208(4), 443–455. <https://doi.org/10.1083/jcb.201406102>
- Jung, E. J., Liu, G., Zhou, W., & Chen, X. (2006). Myosin VI Is a Mediator of the p53-Dependent Cell Survival Pathway. *Molecular and Cellular Biology*, 26(6), 2175–2186. <https://doi.org/10.1128/MCB.26.6.2175-2186.2006>
- Kaplinsky, E., & Mallarkey, G. (2018). Cardiac myosin activators for heart failure therapy: Focus on omecamtiv mecarbil. *Drugs in Context*, 7, 212518. <https://doi.org/10.7573/dic.212518>
- Kaski, J. P., Syrris, P., Burch, M., Tomé-Esteban, M.-T., Fenton, M., Christiansen, M., Andersen, P. S., Sebire, N., Ashworth, M., Deanfield, J. E., McKenna, W. J., & Elliott, P. M. (2008). Idiopathic restrictive cardiomyopathy in children is caused by mutations in cardiac sarcomere protein genes. *Heart (British Cardiac Society)*, 94(11), 1478–1484. <https://doi.org/10.1136/hrt.2007.134684>
- Kawas, R. F., Anderson, R. L., Ingle, S. R. B., Song, Y., Sran, A. S., & Rodriguez, H. M. (2017). A small-molecule modulator of cardiac myosin acts on multiple stages of the myosin chemomechanical cycle. *The Journal of Biological Chemistry*, 292(40), 16571–16577. <https://doi.org/10.1074/jbc.M117.776815>
- Keeley, A., & Soldati, D. (2004a). The glideosome: A molecular machine powering motility and host-cell invasion by Apicomplexa. *Trends in Cell Biology*, 14(10), 528–532. <https://doi.org/10.1016/j.tcb.2004.08.002>
- Kitchen, D. B., Decornez, H., Furr, J. R., & Bajorath, J. (2004). Docking and scoring in virtual screening for drug discovery: Methods and applications. *Nature Reviews. Drug Discovery*, 3(11), 935–949. <https://doi.org/10.1038/nrd1549>
- Knudsen, B. (2006). Migrating with myosin VI. *The American Journal of Pathology*, 169(5), 1523–1526. <https://doi.org/10.2353/ajpath.2006.060712>
- Kortagere, S., Welsh, W. J., Morrissey, J. M., Daly, T., Ejigiri, I., Sinnis, P., Vaidya, A. B., & Bergman, L. W. (2010). Structure-based design of novel small-molecule inhibitors of *Plasmodium falciparum*. *Journal of Chemical Information and Modeling*, 50(5), 840–849. <https://doi.org/10.1021/ci100039k>
- Kovács, M., Tóth, J., Hetényi, C., Málnási-Csizmadia, A., & Sellers, J. R. (2004). Mechanism of blebbistatin inhibition of myosin II. *The Journal of Biological Chemistry*, 279(34), 35557–35563. <https://doi.org/10.1074/jbc.M405319200>
- Kühne, W. (1864). Untersuchungen über das Protoplasma und die Contractilität (pp. 1–192). W. Engelmann,. <https://doi.org/10.5962/bhl.title.46515>



- Langford, G. M. (1995). Actin- and microtubule-dependent organelle motors: Interrelationships between the two motility systems. *Current Opinion in Cell Biology*, 7(1), 82–88. [https://doi.org/10.1016/0955-0674\(95\)80048-4](https://doi.org/10.1016/0955-0674(95)80048-4)
- Laurens, M. B. (2018). The Promise of a Malaria Vaccine—Are We Closer? *Annual Review of Microbiology*, 72(1), 273–292. <https://doi.org/10.1146/annurev-micro-090817-062427>
- Limouze, J., Straight, A. F., Mitchison, T., & Sellers, J. R. (2004). Specificity of blebbistatin, an inhibitor of myosin II. *Journal of Muscle Research and Cell Motility*, 25(4–5), 337–341. <https://doi.org/10.1007/s10974-004-6060-7>
- Liu, K. C., Jacobs, D. T., Dunn, B. D., Fanning, A. S., & Cheney, R. E. (2012). Myosin-X functions in polarized epithelial cells. *Molecular Biology of the Cell*, 23(9), 1675–1687. <https://doi.org/10.1091/mbc.E11-04-0358>
- Ma, D., Zheng, B., Suzuki, T., Zhang, R., Jiang, C., Bai, D., Yin, W., Yang, Z., Zhang, X., Hou, L., Zhan, H., & Wen, J.-K. (2017). Inhibition of KLF5-Myo9b-RhoA Pathway-Mediated Podosome Formation in Macrophages Ameliorates Abdominal Aortic Aneurysm. *Circulation Research*, 120(5), 799–815. <https://doi.org/10.1161/CIRCRESAHA.116.310367>
- Malik, F. I., Hartman, J. J., Elias, K. A., Morgan, B. P., Rodriguez, H., Brejc, K., Anderson, R. L., Sueoka, S. H., Lee, K. H., Finer, J. T., Sakowicz, R., Baliga, R., Cox, D. R., Garard, M., Godinez, G., Kawas, R., Kraynack, E., Lenzi, D., Lu, P. P., ... Morgans, D. J. (2011). Cardiac myosin activation: A potential therapeutic approach for systolic heart failure. *Science (New York, N.Y.)*, 331(6023), 1439–1443. <https://doi.org/10.1126/science.1200113>
- Manickam, Y., Chaturvedi, R., Babbar, P., Malhotra, N., Jain, V., & Sharma, A. (2018). Drug targeting of one or more aminoacyl-tRNA synthetase in the malaria parasite *Plasmodium falciparum*. *Drug Discovery Today*, 23(6), 1233–1240. <https://doi.org/10.1016/j.drudis.2018.01.050>
- Maron, B. J. (2002). Cardiology patient pages. Hypertrophic cardiomyopathy. *Circulation*, 106(19), 2419–2421. <https://doi.org/10.1161/01.cir.0000034170.83171.0b>
- Marston, S. (2018). The Molecular Mechanisms of Mutations in Actin and Myosin that Cause Inherited Myopathy. *International Journal of Molecular Sciences*, 19(7). <https://doi.org/10.3390/ijms19072020>
- Meissner, M., Schlüter, D., & Soldati, D. (2002). Role of *Toxoplasma gondii* myosin A in powering parasite gliding and host cell invasion. *Science (New York, N.Y.)*, 298(5594), 837–840. <https://doi.org/10.1126/science.1074553>
- Mentes, A., Huehn, A., Liu, X., Zwolak, A., Dominguez, R., Shuman, H., Ostap, E. M., & Sindelar, C. V. (2018). High-resolution cryo-EM structures of actin-bound myosin states reveal the mechanism of myosin force sensing. *Proceedings of the National Academy of Sciences*, 115(6), 1292–1297. <https://doi.org/10.1073/pnas.1718316115>
- Miller, L. H., & Carter, R. (1976). A review. Innate resistance in malaria. *Experimental Parasitology*, 40(1), 132–146. [https://doi.org/10.1016/0014-4894\(76\)90075-8](https://doi.org/10.1016/0014-4894(76)90075-8)
- Morita, H., Rehm, H. L., Menesses, A., McDonough, B., Roberts, A. E., Kucherlapati, R., Towbin, J. A., Seidman, J. G., & Seidman, C. E. (2008). Shared genetic causes of cardiac hypertrophy in children and adults. *The New England Journal of Medicine*, 358(18), 1899–1908. <https://doi.org/10.1056/NEJMoa075463>

- Moussaoui, D., Robblee, J. P., Auguin, D., Kremontsova, E. B., Haase, S., Blake, T. C., Baum, J., Robert-Paganin, J., Trybus, K. M., & Houdusse, A. (2020). Full-length *Plasmodium falciparum* myosin A and essential light chain PfELC structures provide new anti-malarial targets. *ELife*, 9, e60581. <https://doi.org/10.7554/eLife.60581>
- Mukherjee, M., Ali, M. Y., Kikuti, C., Safer, D., Yang, Z., Sirkia, H., Ropars, V., Houdusse, A., Warshaw, D. M., & Sweeney, H. L. (2014). Myosin VI must dimerize and deploy its unusual lever arm in order to perform its cellular roles. *Cell Reports*, 8(5), 1522–1532. <https://doi.org/10.1016/j.celrep.2014.07.041>
- Müller, O., Lu, G. Y., & von Seidlein, L. (2019). Geographic expansion of artemisinin resistance. *Journal of Travel Medicine*, 26(4). <https://doi.org/10.1093/jtm/taz030>
- Münter, S., Sabass, B., Selhuber-Unkel, C., Kudryashev, M., Hegge, S., Engel, U., Spatz, J. P., Matuschewski, K., Schwarz, U. S., & Frischknecht, F. (2009). *Plasmodium* sporozoite motility is modulated by the turnover of discrete adhesion sites. *Cell Host & Microbe*, 6(6), 551–562. <https://doi.org/10.1016/j.chom.2009.11.007>
- Nemetski, S. M., Cardozo, T. J., Bosch, G., Weltzer, R., O'Malley, K., Ejigiri, I., Kumar, K. A., Buscaglia, C. A., Nussenzweig, V., Sinnis, P., Levitskaya, J., & Bosch, J. (2015). Inhibition by stabilization: Targeting the *Plasmodium falciparum* aldolase-TRAP complex. *Malaria Journal*, 14, 324. <https://doi.org/10.1186/s12936-015-0834-9>
- Núñez, C., Oliver, J., Mendoza, J. L., Gómez-García, M., Piñero, A., Taxonera, C., Díaz-Rubio, M., López-Nevot, M. A., de la Concha, E. G., Nieto, A., Urcelay, E., Martínez, A., & Martín, J. (2007). MYO9B polymorphisms in patients with inflammatory bowel disease. *Gut*, 56(9), 1321–1322. <https://doi.org/10.1136/gut.2007.121905>
- O'Connor, E., Phan, V., Cordts, I., Cairns, G., Hettwer, S., Cox, D., Lochmüller, H., & Roos, A. (2018). MYO9A deficiency in motor neurons is associated with reduced neuromuscular agrin secretion. *Human Molecular Genetics*, 27(8), 1434–1446. <https://doi.org/10.1093/hmg/ddy054>
- Odronitz, F., & Kollmar, M. (2007). Drawing the tree of eukaryotic life based on the analysis of 2,269 manually annotated myosins from 328 species. *Genome Biology*, 8(9), R196. <https://doi.org/10.1186/gb-2007-8-9-r196>
- Ouderkirk, J. L., & Krendel, M. (2014). Myosin 1e is a component of the invadosome core that contributes to regulation of invadosome dynamics. *Experimental Cell Research*, 322(2), 265–276. <https://doi.org/10.1016/j.yexcr.2014.01.015>
- Paludisme. (n.d.). Retrieved October 12, 2020, from /maladies-et-traumatismes/maladies-a-transmission-vectorielle/paludisme
- Pazhayam, N. M., Chhibber-Goel, J., & Sharma, A. (2019). New leads for drug repurposing against malaria. *Drug Discovery Today*, 24(1), 263–271. <https://doi.org/10.1016/j.drudis.2018.08.006>
- Pazicky, S., Dhamotharan, K., Kaszuba, K., Mertens, H. D. T., Gilberger, T., Svergun, D., Kosinski, J., Weininger, U., & Löw, C. (2020). Structural role of essential light chains in the apicomplexan glideosome. *Communications Biology*, 3(1), 1–14. <https://doi.org/10.1038/s42003-020-01283-8>
- Perrin, A. J., Collins, C. R., Russell, M. R. G., Collinson, L. M., Baker, D. A., & Blackman, M. J. (2018). The Actinomyosin Motor Drives Malaria Parasite Red Blood Cell Invasion but Not Egress. *MBio*, 9(4). <https://doi.org/10.1128/mBio.00905-18>

- Phyo, A. P., & von Seidlein, L. (2017). Challenges to replace ACT as first-line drug. *Malaria Journal*, 16(1), 296. <https://doi.org/10.1186/s12936-017-1942-5>
- Picariello, H. S., Kenchappa, R. S., Rai, V., Crish, J. F., Dovas, A., Pogoda, K., McMahon, M., Bell, E. S., Chandrasekharan, U., Luu, A., West, R., Lammerding, J., Canoll, P., Odde, D. J., Janmey, P. A., Egelhoff, T., & Rosenfeld, S. S. (2019). Myosin IIA suppresses glioblastoma development in a mechanically sensitive manner. *Proceedings of the National Academy of Sciences of the United States of America*, 116(31), 15550–15559. <https://doi.org/10.1073/pnas.1902847116>
- Planelles-Herrero, V. J., Hartman, J. J., Robert-Paganin, J., Malik, F. I., & Houdusse, A. (2017). Mechanistic and structural basis for activation of cardiac myosin force production by omecamtiv mecarbil. *Nature Communications*, 8(1), 190. <https://doi.org/10.1038/s41467-017-00176-5>
- Powell, C. J., Jenkins, M. L., Parker, M. L., Ramaswamy, R., Kelsen, A., Warshaw, D. M., Ward, G. E., Burke, J. E., & Boulanger, M. J. (2017). Dissecting the molecular assembly of the *Toxoplasma gondii* MyoA motility complex. *The Journal of Biological Chemistry*, 292(47), 19469–19477. <https://doi.org/10.1074/jbc.M117.809632>
- Powell, C. J., Ramaswamy, R., Kelsen, A., Hamelin, D. J., Warshaw, D. M., Bosch, J., Burke, J. E., Ward, G. E., & Boulanger, M. J. (2018). Structural and mechanistic insights into the function of the unconventional class XIV myosin MyoA from *Toxoplasma gondii*. *Proceedings of the National Academy of Sciences of the United States of America*, 115(45), E10548–E10555. <https://doi.org/10.1073/pnas.1811167115>
- Preller, M., Bauer, S., Adamek, N., Fujita-Becker, S., Fedorov, R., Geeves, M. A., & Manstein, D. J. (2011). Structural basis for the allosteric interference of myosin function by reactive thiol region mutations G680A and G680V. *The Journal of Biological Chemistry*, 286(40), 35051–35060. <https://doi.org/10.1074/jbc.M111.265298>
- Preller, M., & Manstein, D. J. (2013). Myosin structure, allostery, and mechano-chemistry. *Structure* (London, England: 1993), 21(11), 1911–1922. <https://doi.org/10.1016/j.str.2013.09.015>
- Provance, D. W., & Mercer, J. A. (1999). Myosin-V: Head to tail. *Cellular and Molecular Life Sciences: CMLS*, 56(3–4), 233–242. <https://doi.org/10.1007/s000180050425>
- Ramamurthy, B., Yengo, C. M., Straight, A. F., Mitchison, T. J., & Sweeney, H. L. (2004). Kinetic mechanism of blebbistatin inhibition of nonmuscle myosin IIb. *Biochemistry*, 43(46), 14832–14839. <https://doi.org/10.1021/bi0490284>
- Rayment, I. (1996). The structural basis of the myosin ATPase activity. *The Journal of Biological Chemistry*, 271(27), 15850–15853. <https://doi.org/10.1074/jbc.271.27.15850>
- Rees-Channer, R. R., Martin, S. R., Green, J. L., Bowyer, P. W., Grainger, M., Molloy, J. E., & Holder, A. A. (2006). Dual acylation of the 45 kDa gliding-associated protein (GAP45) in *Plasmodium falciparum* merozoites. *Molecular and Biochemical Parasitology*, 149(1), 113–116. <https://doi.org/10.1016/j.molbiopara.2006.04.008>
- Ridzuan, M. A. M., Moon, R. W., Knuepfer, E., Black, S., Holder, A. A., & Green, J. L. (2012). Subcellular location, phosphorylation and assembly into the motor complex of GAP45 during *Plasmodium falciparum* schizont development. *PloS One*, 7(3), e33845. <https://doi.org/10.1371/journal.pone.0033845>
- Robert-Paganin, J., Auguin, D., & Houdusse, A. (2018). Hypertrophic cardiomyopathy disease results from disparate impairments of cardiac myosin function and auto-inhibition. *Nature Communications*, 9(1), 4019. <https://doi.org/10.1038/s41467-018-06191-4>

- Robert-Paganin, J., Pylypenko, O., Kikuti, C., Sweeney, H. L., & Houdusse, A. (2020a). Force Generation by Myosin Motors: A Structural Perspective. *Chemical Reviews*, 120(1), 5–35. <https://doi.org/10.1021/acs.chemrev.9b00264>
- Robert-Paganin, J., Robblee, J. P., Auguin, D., Blake, T. C. A., Bookwalter, C. S., Krementsova, E. B., Moussaoui, D., Previs, M. J., Jousset, G., Baum, J., Trybus, K. M., & Houdusse, A. (2019). Plasmodium myosin A drives parasite invasion by an atypical force generating mechanism. *Nature Communications*, 10(1), 3286. <https://doi.org/10.1038/s41467-019-11120-0>
- Ross, J. L., Ali, M. Y., & Warshaw, D. M. (2008). Cargo transport: Molecular motors navigate a complex cytoskeleton. *Current Opinion in Cell Biology*, 20(1), 41–47. <https://doi.org/10.1016/j.ceb.2007.11.006>
- Shen, Y.-T., Malik, F. I., Zhao, X., Depre, C., Dhar, S. K., Abarzúa, P., Morgans, D. J., & Vatner, S. F. (2010). Improvement of cardiac function by a cardiac Myosin activator in conscious dogs with systolic heart failure. *Circulation. Heart Failure*, 3(4), 522–527. <https://doi.org/10.1161/CIRCHEARTFAILURE.109.930321>
- Siden-Kiamos, I., Pinder, J. C., & Louis, C. (2006). Involvement of actin and myosins in Plasmodium berghei ookinete motility. *Molecular and Biochemical Parasitology*, 150(2), 308–317. <https://doi.org/10.1016/j.molbiopara.2006.09.003>
- Sinha, N., & Balayla, G. (2020). Hydroxychloroquine and COVID-19. *Postgraduate Medical Journal*, 96(1139), 550–555. <https://doi.org/10.1136/postgradmedj-2020-137785>
- Sirigu, S., Hartman, J. J., Planelles-Herrero, V. J., Ropars, V., Clancy, S., Wang, X., Chuang, G., Qian, X., Lu, P.-P., Barrett, E., Rudolph, K., Royer, C., Morgan, B. P., Stura, E. A., Malik, F. I., & Houdusse, A. M. (2016). Highly selective inhibition of myosin motors provides the basis of potential therapeutic application. *Proceedings of the National Academy of Sciences of the United States of America*, 113(47), E7448–E7455. <https://doi.org/10.1073/pnas.1609342113>
- Soldati, D., & Meissner, M. (2004). Toxoplasma as a novel system for motility. *Current Opinion in Cell Biology*, 16(1), 32–40. <https://doi.org/10.1016/j.ceb.2003.11.013>
- Soulard, V., Bosson-Vanga, H., Lorthiois, A., Roucher, C., Franetich, J.-F., Zanghi, G., Bordessoulles, M., Tefit, M., Thellier, M., Morosan, S., Le Naour, G., Capron, F., Suemizu, H., Snounou, G., Moreno-Sabater, A., & Mazier, D. (2015). Plasmodium falciparum full life cycle and Plasmodium ovale liver stages in humanized mice. *Nature Communications*, 6, 7690. <https://doi.org/10.1038/ncomms8690>
- Straight, A. F., Cheung, A., Limouze, J., Chen, I., Westwood, N. J., Sellers, J. R., & Mitchison, T. J. (2003). Dissecting temporal and spatial control of cytokinesis with a myosin II Inhibitor. *Science (New York, N.Y.)*, 299(5613), 1743–1747. <https://doi.org/10.1126/science.1081412>
- Sweeney, H. L., & Houdusse, A. (2010). Myosin VI rewrites the rules for myosin motors. *Cell*, 141(4), 573–582. <https://doi.org/10.1016/j.cell.2010.04.028>
- Sweeney, H. L., Houdusse, A., & Robert-Paganin, J. (2020). Myosin Structures. *Advances in Experimental Medicine and Biology*, 1239, 7–19. [https://doi.org/10.1007/978-3-030-38062-5\\_2](https://doi.org/10.1007/978-3-030-38062-5_2)
- Swenson, A. M., Tang, W., Blair, C. A., Fetrow, C. M., Unrath, W. C., Previs, M. J., Campbell, K. S., & Yengo, C. M. (2017a). Omecamtiv Mecarbil Enhances the Duty Ratio of Human  $\beta$ -Cardiac Myosin Resulting in Increased Calcium Sensitivity and Slowed Force Development in Cardiac

- Muscle. *The Journal of Biological Chemistry*, 292(9), 3768–3778. <https://doi.org/10.1074/jbc.M116.748780>
- Tabb, J. S., Molyneaux, B. J., Cohen, D. L., Kuznetsov, S. A., & Langford, G. M. (1998). Transport of ER vesicles on actin filaments in neurons by myosin V. *Journal of Cell Science*, 111 ( Pt 21), 3221–3234.
- Tang, Q., Andenmatten, N., Hortua Triana, M. A., Deng, B., Meissner, M., Moreno, S. N. J., Ballif, B. A., & Ward, G. E. (2014). Calcium-dependent phosphorylation alters class XIVa myosin function in the protozoan parasite *Toxoplasma gondii*. *Molecular Biology of the Cell*, 25(17), 2579–2591. <https://doi.org/10.1091/mbc.E13-11-0648>
- Tardieux, I., & Baum, J. (2016). Reassessing the mechanics of parasite motility and host-cell invasion. *The Journal of Cell Biology*, 214(5), 507–515. <https://doi.org/10.1083/jcb.201605100>
- Teerlink, J. R., Clarke, C. P., Saikali, K. G., Lee, J. H., Chen, M. M., Escandon, R. D., Elliott, L., Bee, R., Habibzadeh, M. R., Goldman, J. H., Schiller, N. B., Malik, F. I., & Wolff, A. A. (2011). Dose-dependent augmentation of cardiac systolic function with the selective cardiac myosin activator, omecamtiv mecarbil: A first-in-man study. *Lancet (London, England)*, 378(9792), 667–675. [https://doi.org/10.1016/S0140-6736\(11\)61219-1](https://doi.org/10.1016/S0140-6736(11)61219-1)
- Thomas, A., Lee, P.-J., Dalton, J. E., Nomie, K. J., Stoica, L., Costa-Mattioli, M., Chang, P., Nuzhdin, S., Arbeitman, M. N., & Dierick, H. A. (2012). A Versatile Method for Cell-Specific Profiling of Translated mRNAs in *Drosophila*. *PLOS ONE*, 7(7), e40276. <https://doi.org/10.1371/journal.pone.0040276>
- Titus, M. A. (2018). Myosin-Driven Intracellular Transport. *Cold Spring Harbor Perspectives in Biology*, 10(3). <https://doi.org/10.1101/cshperspect.a021972>
- Utter, M. S., Ryba, D. M., Li, B. H., Wolska, B. M., & Solaro, R. J. (2015). Omecamtiv Mecarbil, a Cardiac Myosin Activator, Increases Ca<sup>2+</sup> Sensitivity in Myofilaments With a Dilated Cardiomyopathy Mutant Tropomyosin E54K. *Journal of Cardiovascular Pharmacology*, 66(4), 347–353. <https://doi.org/10.1097/FJC.0000000000000286>
- Vaid, A., Thomas, D. C., & Sharma, P. (2008). Role of Ca<sup>2+</sup>/calmodulin-PfPKB signaling pathway in erythrocyte invasion by *Plasmodium falciparum*. *The Journal of Biological Chemistry*, 283(9), 5589–5597. <https://doi.org/10.1074/jbc.M708465200>
- Wall, R. J., Zeeshan, M., Katris, N. J., Limenitakis, R., Rea, E., Stock, J., Brady, D., Waller, R. F., Holder, A. A., & Tewari, R. (2019). Systematic analysis of *Plasmodium* myosins reveals differential expression, localisation, and function in invasive and proliferative parasite stages. *Cellular Microbiology*, 21(10), e13082. <https://doi.org/10.1111/cmi.13082>
- Wellems, T. E., & Plowe, C. V. (2001). Chloroquine-resistant malaria. *The Journal of Infectious Diseases*, 184(6), 770–776. <https://doi.org/10.1086/322858>
- Wells, A. L., Lin, A. W., Chen, L. Q., Safer, D., Cain, S. M., Hasson, T., Carragher, B. O., Milligan, R. A., & Sweeney, H. L. (1999). Myosin VI is an actin-based motor that moves backwards. *Nature*, 401(6752), 505–508. <https://doi.org/10.1038/46835>
- Wetzel, D. M., Håkansson, S., Hu, K., Roos, D., & Sibley, L. D. (2003). Actin filament polymerization regulates gliding motility by apicomplexan parasites. *Molecular Biology of the Cell*, 14(2), 396–406. <https://doi.org/10.1091/mbc.e02-08-0458>



WHO | World malaria report 2018. (n.d.). WHO; World Health Organization. Retrieved October 12, 2020, from <http://www.who.int/malaria/publications/world-malaria-report-2018/en/>

World health statistics 2016: Monitoring health for the sustainable development goals SDGs. (2016).

Yoshida, H., Cheng, W., Hung, J., Montell, D., Geisbrecht, E., Rosen, D., Liu, J., & Naora, H. (2004). Lessons from border cell migration in the *Drosophila* ovary: A role for myosin VI in dissemination of human ovarian cancer. *Proceedings of the National Academy of Sciences*, 101(21), 8144–8149. <https://doi.org/10.1073/pnas.0400400101>

Yusuf, N. A., Green, J. L., Wall, R. J., Knuepfer, E., Moon, R. W., Schulte-Huxel, C., Stanway, R. R., Martin, S. R., Howell, S. A., Douse, C. H., Cota, E., Tate, E. W., Tewari, R., & Holder, A. A. (2015). The *Plasmodium* Class XIV Myosin, MyoB, Has a Distinct Subcellular Location in Invasive and Motile Stages of the Malaria Parasite and an Unusual Light Chain. *The Journal of Biological Chemistry*, 290(19), 12147–12164. <https://doi.org/10.1074/jbc.M115.637694>

Zhang, H.-M., Ji, H.-H., Ni, T., Ma, R.-N., Wang, A., & Li, X. (2017). Characterization of Blebbistatin Inhibition of Smooth Muscle Myosin and Nonmuscle Myosin-2. *Biochemistry*, 56(32), 4235–4243. <https://doi.org/10.1021/acs.biochem.7b00311>